

GEOLOGICA ULTRAIECTINA

**Mededelingen van de
Faculteit Aardwetenschappen der
Rijksuniversiteit te Utrecht**

No. 89

**PETROGENESIS OF THE MINERALIZED
GRANITIC INTRUSION NEAR
LOS SANTOS, WESTERN-SPAIN,
AND REMOTE SENSING AND DATA
INTEGRATION AS A TOOL IN
REGIONAL EXPLORATION FOR
GRANITE RELATED MINERALIZATION.**

MARC A. GOOSSENS

GEOLOGICA ULTRAIECTINA

**Mededelingen van de
Faculteit Aardwetenschappen der
Rijksuniversiteit te Utrecht**

No. 89

**PETROGENESIS OF THE MINERALIZED GRANITIC
INTRUSION NEAR LOS SANTOS, WESTERN-SPAIN,
AND REMOTE SENSING AND DATA INTEGRATION
AS A TOOL IN REGIONAL EXPLORATION FOR
GRANITE RELATED MINERALIZATION.**

MARC A. GOOSSENS

25 - 007

CIP-GEGEVENS KONINKLIJKE BIBLIOTHEEK, DEN HAAG

Goossens, Marc Antoine

Petrogenesis of the mineralized granitic intrusion near Los Santos, Western-Spain, and remote sensing and data integration as a tool in regional exploration for granite related mineralization / Marc Antoine Goossens.

- [Utrecht: Faculteit Aardwetenschappen der Rijksuniversiteit te Utrecht].

-(Geologica Ultraiectina, ISSN 0072-1026; no 89)

Proefschrift Rijksuniversiteit Utrecht. -Met lit. opg.-

Met samenvatting in het Nederlands.

ISBN 90-71577-43-0

Trefw.:graniet; mineralisatie / mineralisatie;
exploratie (geologie) / remote sensing; geologie.

**PETROGENESIS OF THE MINERALIZED GRANITIC
INTRUSION NEAR LOS SANTOS, WESTERN-SPAIN,
AND REMOTE SENSING AND DATA INTEGRATION
AS A TOOL IN REGIONAL EXPLORATION FOR
GRANITE RELATED MINERALIZATION.**

**PETROGENESE VAN DE GEMINERALISEERDE GRANIETISCHE
INTRUSIE NABIJ LOS SANTOS, WEST-SPANJE,
EN REMOTE SENSING EN DATA INTEGRATIE ALS
HULPMIDDEL BIJ REGIONALE EXPLORATIE NAAR
GRANIET GERELATEERDE MINERALISATIE**

(met een samenvatting in het Nederlands)

PROEFSCHRIFT

TER VERKRIJVING VAN DE GRAAD VAN DOCTOR AAN DE
RIJKSUNIVERSITEIT TE UTRECHT OP GEZAG VAN DE RECTOR
MAGNIFICUS, PROF.DR.J.A. VAN GINKEL, IN GEVOLGE HET
BESLUIT VAN HET COLLEGE VAN DEKANEN IN HET OPENBAAR
TE VERDEDIGEN OP MAANDAG 2 NOVEMBER 1992
DES NAMIDDAGS OM 12.45 UUR

DOOR

**MARC ANTOINE GOOSSENS
GEBOREN OP 29 APRIL 1959 TE 'S-GRAVENHAGE**

PROMOTOR: PROF.DR. R.D.SCHUILING
CO-PROMOTORES: DR.H.DE BOOORDER
DR.T.FINLOW BATES
DR.J.B.H.JANSEN

DIT PROEFSCHRIFT WERD MOGELIJK GEMAAKT MET FINANCIËLE STEUN
VAN BILLITON INTERNATIONAL METALS B.V.
EN BILITON RESEARCH ARNHEM

*Als ik het echt niet meer
weet kan ik nog altijd
Gissen.*

Eindelijk is het moment dan gekomen dat ik aan de laatste paginas van dit proefschrift kan beginnen. Dit doe ik dan ook met veel plezier, in het bijzonder omdat ik deze wil wijden aan de vele personen die op één of andere manier hebben bijgedragen tot de voltooiing ervan. Hun vertrouwen en steun waren vitale ingrediënten voor de bereiding van de volgende 160 bladzijden.

Daarom wil ik graag bedanken:

- Billiton International Metals BV, Billiton Research Arnhem en Billiton Española PRN SA voor het beschikbaar stellen van de nodige financiële en materiële voorzieningen. Met name wil ik Nigel Grant, David Hopgood en Chris Pointon bedanken voor hun persoonlijke bemoeienissen.
- Shell Internationale Petroleum Maatschappij, voor het beschikbaar stellen van hun GEM image processing system, zodat ook het laatste hoofdstuk verwezenlijkt kon worden.
- De vele mensen die zo vaak bereid waren om mij uit de brand te helpen wanneer er even snel wat geanalyseerd moest worden: Berta, Chiel, Theo, Vian, Angelique, Paul (Universiteit Utrecht) en Jan van Doesburg (Landbouw Universiteit Wageningen).
- De slijpkamer voor het maken van de talloze slijpplaatjes.
- De foto- en tekenkamer, met name Fred Trappenburg, die met zijn vele kunstzinnige ideen mij zeer heeft geholpen om mijn figuren in een presentabele vorm te gieten. Dat was soms nogal een klus.
- Mijn begeleiders, Olaf Schuiling, Hugo de Boorder en Terry Finlow Bates. Zij waren altijd bereid om mijn geklaag aan te horen. Telkens als ik weer eens van plan was de pijp aan Maarten te geven slaagden zij er wonderwel weer in om me daarvan te weerhouden. Ik wil hen ook bedanken voor de wijze waarop zij mij geholpen hebben de zaak op papier te krijgen zonder al te veel blunders. Met hun kritiek op mijn manuscripten was ik in eerste instantie meestal niet zo blij, maar naderhand des te meer. Hun steun bij het regelen van allerlei zaken was zondermeer onontbeerlijk.
- In het bijzonder wil ik Ben Jansen bedanken. Ben, jij raakte ongewild en onbedoeld verzeild in mijn onderzoek, op het moment dat ik stuurloos ronddreef in een grote plas van gegevens. Je hebt je vervolgens opgeworpen als inspirator en criticus op een wijze die bij mij zeer veel bewondering heeft afgedwongen. Hoewel ik soms wel in een hoekje kon gaan zitten janken om je niet aflatende stroom van kritiek, heb ik toch wel het gevoel dat ik er uiteindelijk bijzonder veel van heb kunnen leren.

- Ook wil ik graag Salle Kroonenberg bedanken. Jouw besmettelijke enthousiasme heeft enorm bijgedragen aan mijn begrip van de relaties tussen satellietbeeld en aardoppervlak. Tijdens het veldwerk heb je mij laten zien hoe boeiend het is om observaties op kleine schaal in een breder regionaal verband te plaatsen. Ik vond het erg leuk om met je samen te werken.

- I am very much obliged to the Enschedé ITC: Andrea Fabbri for his suggestions and comments related to my approach of the data integration problems; The Ilwis team - Ernst Schetselaar, Ben Gorte, Wim Koolhoven and Jelle Wind for their willingness to assist in technical problems, and the Delft ITC: Colin Reeves for allowing me to bother his staff time after time, Martin, Boudewijn, Phil, Hans, Peter, Sally and all others for their pleasant discussions, their friendship and support. To me it has always been an enormous pleasure to visit the ITC.

- Gerne möchte ich die Deutsche Forschungsanstalt für Luft- und Raumfahrt, insbesonders Frank Lehmann, danken dass sie mir erlaubt haben das Spektroradiometer zu benutzen.

- Nunca olvidaré el calor humano, la hospitalidad y la disposición de ayudar que encontré en España durante mi trabajo de campo. Estar con Santiago Jiménez fué siempre un placer. Siempre supo con exactitud donde había que comer y beber. Sus discusiones sobre geología valieron la pena. Me prestó una ayuda inestimable en la adquisición de todo tipo de información indispensable. A Javier Arnaiz (Empresa Nacional de Urano S.A.) le tengo que agradecer el poder disponer de los datos geofísicos de vuelo. Quiero agradecer al Prof. Ugidos y a la Dra. Pellitero Pascual por una gran cantidad de comentarios y sugerencias válidos. La Junta de Castilla y León me ha ayudado especialmente con información específica sobre las mineralizaciones en el área de estudio. La Dra. Carmen Antón Pacheco del Instituto Geotecnico y Minero de España, siempre estuvo dispuesta a discutir conmigo las posibles interpretaciones de las imágenes de satélite. La amistad de Luciano, María Jesús, Rosa, Abdón, Tinín, Las Petronillas y Pepa convirtió mi estancia en España en una experiencia muy agradable.

I am indebted to all others whose critical comments contributed to this thesis: Dr.Speer, Dr.Wörner, Dr.Holtz, anonymous reviewers, Dr. Bonham-Carter, James Baker, Enrique Ortega, Billy Loughlin, Cees Maijer, and of course, the examining committee: Prof.Dr. Oen Ing Soen, Prof.Dr.Fabbri, Prof.Dr.Kroonenberg, Dr.Westerhof and Dr.Garcia Sanchez.

En, last but certainly not least, allen die mij met hun vriendschap, geduld en vertrouwen zo enorm bijgestaan hebben.

Femke.

ABSTRACT

Ground based metal exploration is labour intensive and thus expensive. Data acquisition by satellite and aircraft, and subsequent image processing seem to offer a cheaper and attractive strategy to replace some of this effort, notably in the screening phase of a new project. However, realizing this promise requires considerably more than an image processing system and some satellite data. A vital component is a calibration area with known mineralization where the geology is sufficiently well known to permit a sound interpretation of the remote sensing data. This thesis studies the interpretation of remote sensing and data integration in regional exploration for granite related mineralization in Central Western Spain. The calibration area is located in the vicinity of the Los Santos tungsten skarn, at the N.W. Margin of the Hercynian Central System Batholith.

The Los Santos (1.5 million tonnes, 0.79%WO₃) garnet-pyroxene-scheelite skarn has formed by replacement of Cambrian limestones in an area where the contact aureole reaches its widest extent. The adjacent granite is strongly zoned, ranging from biotite bearing granodiorites in its core to muscovite and cordierite bearing monzogranites at its margins near Los Santos. The main REE variations in the intrusion are compatible with In Situ crystal fractionation of one magma. The regional zoning of the intrusion can be explained for an important part by gradual segregation of intercumulus melt during crystallization. Variations in biotite composition indicate that during differentiation the melt became progressively more peraluminous, reducing and enriched in volatiles. The most fractionated and volatile-enriched monzogranites are located adjacent to the Los Santos deposit. Locally, contamination processes have interfered with fractionation and obscured the diagnostic trace element patterns, in particular those for Ba and Sr. Enhanced Ba and Sr levels and depletion of Rb in the monzogranites near the Los Santos deposit, in combination with systematic Rb enrichment in the adjacent contact metamorphic rocks suggest exchange of magmatic fluid, possibly related to the mineralizing event.

The contact metamorphic setting is the main diagnostic feature that all mineralization in this area has in common. A significant correlation has been found between the degree of contact metamorphism and related features (mineralogy, volatile content and the Fe⁺⁺/Fe_{total} ratio), and the chemical and mineralogical composition of the overlying soils. Soils overlying the contact rocks are generally better developed than those on the surrounding granites and regional metamorphic sediments, and are richer in kaolinite and goethite. This is in turn reflected in more intense and diverse land use within the contact aureole. It is these features that can be related to spectral and textural variations in the Thematic Mapper image and therefore makes it possible to map contact metamorphic terrain using satellite data. Combined analysis of airborne radiometric thorium, uranium, potassium and total count data permitted adequate classification of the different granite types and of the sedimentary rocks, which in turn enabled mapping of the intrusive contact. The magnetic expression of the contact metamorphic rocks is different

compared to that of the regional metasediments, due to resetting of the remanent magnetism during heating. This particular feature enabled detection of metasedimentary rocks that underwent contact metamorphic heating, using airborne magnetic data.

It is a common experience that the results of remote sensing and data integration in mineral exploration are disappointing. In this study a number of important reasons for this are identified:

- 1) The basic relation between geology and the original data is often obscured by complex data manipulation, which obstructs the understanding of the final output.
- 2) The risk of removing potentially important information during the interpretation of the data is considerable, and very hard to control.
- 3) The decision criteria with respect to the correctness of classification and interpretation are often arbitrary and not quantifiable.
- 4) Error- and quality assessment is often subjective and therefore not reproducible under different circumstances.

No tailor-made solution can be presented for these problems, as this varies with each particular situation and depends on the nature of a particular data set. Nevertheless some rules of thumb can be presented. Concerning the first problem, it is very important that the link between the data, the interpretation and the geology is kept as direct as possible and soundly based on the experiences obtained in the calibration area. For example, the identified relation between metamorphic grade, soil composition and spectral signature is a feature that can be used for the detection of contact metamorphic soils with a minimum of statistical or other kinds of complicated data manipulation. The data manipulation should be very straightforward and aimed at the recognition of specific features that are known to be diagnostic for the setting in which the mineralization occurs.

The second problem is perhaps the most difficult to deal with, in particular when a large, poorly known area is investigated, as each step in the data processing, e.g. masking, filtering and classification, automatically implies loss of information. The potential damage can only be controlled by quantifying each step, so that all steps are reproducible. If, in the course of the investigation it turns out that relevant data may have been lost, the steps can be repeated with other parameters, and the results can still be compared.

With respect to the third problem it is important that the nature of the surrounding pixels of a certain classified pixel is involved in the decision whether the classification is correct. For example, in the case of mapping kaolinite pixels, using a TM image, one might use the concentration of classified pixels in a certain area as a criterion. A single classified pixel that is located close to other similarly classified pixels is more likely to be classified correctly than a single classified pixel that is far away from similarly classified pixels.

In the case of rock classification based on radiometric data, the size of a classified surface can be a

valuable criterion. The larger the size of a classified area, the greater is the chance that the classification is correct.

In order to deal with the fourth problem, weights have been assigned to the degrees of uncertainty within an interpretation. This is where the role of the calibration area is very important. For example, the pixels classified as kaolinitic are not unique for the contact aureole, as they also occur elsewhere. However, their concentration is much larger inside the aureole than outside. By contouring the classified image, a concentration map has been obtained. The range in concentrations was divided into several classes, and weights were given to each of these classes. As high concentrations were most typical for the contact zone, these classes were assigned the highest weights. The classes with the lowest concentrations, that were more typical for the area outside the contact aureole, were thus assigned low weights.

The subsequent integration of the data into a map that expresses for each location the probability that mineralization will be present, is a very important step, because the result is that pixels, that were misclassified for some reason in one data set, will not be confirmed by other data. They will therefore end up with low probabilities in the final map.

The ultimate aim of the study was to develop a data integration methodology that is a powerful tool in the regional phase of exploration for granite related mineralization. Therefore the methodology, developed for the calibration area, was tested on a regional scale (approximately 200*150km), in order to: 1) determine the nature of the complications that can be expected if the methodology is applied to a large area with little ground information; 2) examine whether known mineralization could have been predicted using this methodology and; 3) investigate whether new prospective areas can be proposed. Apart from the fact that the only ground information available was a 1:200.000 geological map, which made interpretation of the data much more complicated, a number of additional problems were encountered:

1) information that was relatively unique for the contact aureole in the calibration area turned out not to be unique on a regional scale. For example, the spectral signature of Tertiary sediments and associated soils is very similar to that of the kaolinite rich soils overlying the contact metamorphic rocks; 2) The quality of the results of the satellite data interpretation depend strongly on the acquisition date of the TM scene; 3) On a regional scale, situations were encountered that were not present in the calibration area. For example, certain granite types and parts of the Tertiary terrain had similar radiometric signatures; 4) The quality of the airborne survey was poor. For example, there are indications that the coordinate system of the airborne data set is not correct, causing a shift of the data of at least 2km to the north.

However, the methodology of data integration proved to be very efficient for dealing with these problems, as most of the larger known deposits coincide with zones that are mapped as very

prospective. In addition a number of other zones with good prospectivity are mapped. Clearly these require follow-up fieldwork.

In conclusion it can be said that this study demonstrates that remote sensing and data integration can indeed be valuable tools for identification of target areas in mineral exploration, provided that a sound understanding is available, on the basis of properly identified rock- and oreforming processes, concerning the variations in remotely sensed data that can be expected in relation to the diagnostic features one is searching for.

SAMENVATTING

Mineraal exploratie is arbeidsintensief en dus duur. Remote Sensing en beeldverwerkings-technieken lijken een goedkoper en aantrekkelijk alternatief te bieden om een deel van dit werk te vervangen, vooral in de verkenningsfase van een nieuw project. Om dit waar te maken, is echter heel wat meer nodig dan alleen een beeldverwerkings systeem en wat satellietgegevens. Essentieel is de beschikbaarheid van een calibratiegebied met bekende mineralisatie, waar de geologie goed genoeg van bekend is om een degelijke interpretatie om de remote sensing data te kunnen uitvoeren. Dit proefschrift bestudeert interpretatie van Remote Sensing gegevens (Thematic Mapper beelden en airborne geofysische gegevens) en de integratie van databestanden ten behoeve van regionale exploratie naar graniet-gerelateerde mineralisatie in centraal west Spanje. In het calibratie-gebied bevindt zich de wolfraam skarn-verertsing van Los Santos, gelegen aan het noord-westelijke contact van de Hercynische Systeem Centraal Batholiet.

De granaat-pyroxeen-scheeliet skarn van Los Santos (1.5 miljoen ton, 079% WO_3) is gevormd door vervanging van Cambische kalksteen. De ligging van de skarn valt samen met de plaats waar het contact aureool anomaal breed is. De aangrenzende graniet-intrusie is sterk gezoneerd, varierend van biotiet-houdende granodioriet in de kern tot muscoviet en cordieriet-houdende monzograniet aan het contact bij Los Santos.

De REE variaties binnen deze peralumineuze, ilmeniet houdende batoliet wijzen op In Situ kristal fractionatie binnen één magma als het belangrijkste genetische proces. De regionale zonering van de intrusie kan voor een groot deel verklaard worden door graduële segregatie van intercumulus smelt gedurende de kristallisatie. Variaties in biotiet compositie geven aanwijzingen dat gedurende dit differentiatieproces de smelt in toenemende mate peralumineus, reducerend en verrijkt met vluchtige stoffen werd. Het meest gefractioneerde en "volaatle" aangerijkte deel van de monzograniet grenst aan de Los Santos verertsing.

Plaatselijke zijn spore-element patronen, typisch voor fractionele kristallisatie (met name die van Ba en Sr), sterk verstoord door contaminatie van het magma. Verhoogde gehalten aan Ba en Sr, en verarming van Rb in de monzogranieten nabij Los Santos, in combinatie met systematische Rb aanraking in de aangrenzende contact metamorfe gesteentes, wijzen op uitwisseling van magmatische vloeistoffen met het sedimentaire nevengesteente. Mogelijk is dit direct gerelateerd aan het verertsings-proces.

De meeste verertsingen in dit gebied bevinden zich binnen het contactmetamorfe aureool, hetgeen als diagnostisch beschouwd kan worden. Er bestaat een significante correlatie tussen de mate van contact metamorfose en gerelateerde gesteente eigenschappen (de mineralogie, het gehalte aan vluchtige stoffen en de $\text{Fe}^{++}/\text{Fe}_{\text{totaal}}$ ratio) enerzijds, en de chemische en mineralogische eigenschappen van de bovenliggende bodems anderzijds. Bodems gevormd op de contactmetamorfe gesteenten zijn meestal

beter ontwikkeld dan die op de omringende graniëten en regionaal metamorfe gesteenten. Zij bevatten meer kaoliniet en goethiet.

Dit heeft op zijn beurt weer een intenser en diverser landgebruik binnen het contact aureool tot gevolg. Het zijn met name deze fenomenen die gerelateerd kunnen worden aan spectrale en texturele variaties in het satelliet beeld. Hierdoor is het mogelijk contactmetamorf gesteente te karteren op basis van satellietgegevens.

Diverse granaat-types en sedimentaire gesteenten kunnen onderscheiden worden op basis van verschillen in radioactieve eigenschappen (thorium-, uranium-, kaliumgehalte en de totale straling). Gebruik makend van "airborne" radiometrische gegevens kunnen dientengevolge de verschillende gesteentetypes geclassificeerd worden. Dit houdt in, dat het granietcontact gekarteerd kan worden vanuit de lucht.

De magnetische eigenschappen van het contact metamorfe gesteente zijn verschillend ten opzichte van de regionaal metamorfe gesteenten, als gevolg van verhitting en rekristallizatie van het gesteente tijdens de granaat-intrusie. Daardoor kunnen regionaalmetamorfe gesteenten die contactmetamorfe veranderingen hebben ondergaan, geïdentificeerd worden op basis van "airborne" magnetische gegevens.

De resultaten van Remote Sensing en data-integratie technieken zijn regelmatig teleurstellend. Hiervoor is een aantal oorzaken aan te wijzen:

- 1) De fundamentele relatie tussen de geologie en de originele data is vaak vertroebeld door ingewikkelde statistische manipulatie van gegevens. Dit staat een goed begrip van het uiteindelijke product in de weg.
- 2) Er is een aanzienlijk risico aanwezig dat gedurende de interpretatie van de gegevens potentieel belangrijke informatie verloren raakt.
- 3) De criteria op basis waarvan geoordeeld wordt over de juistheid van classificatie en interpretatie zijn vaak arbitrair en getalmatig meestal slecht weer te geven.
- 4) Schatting van fouten en kwaliteit is vaak subjectief, en daardoor slecht te reproduceren onder andere omstandigheden.

Het antwoord op deze problemen zal verschillen per situatie, en is daarbij afhankelijk van de aard van de beschikbare gegevens. Hoewel het dus niet goed mogelijk is een pasklare oplossing voor deze moeilijkheden te bieden, kunnen er wel enige vuistregels gegeven worden, die het makkelijker maken met deze problemen om te gaan.

Met betrekking tot het eerste probleem is het van groot belang om de relatie tussen gegevens, interpretatie en geologie zo helder mogelijk te houden, en name te baseren op de ervaring verkregen in het calibratiegebied. Het is van groot belang dat de datamanipulatie direct gericht is op het herkennen van fenomenen, waarvan bekend is dat zij diagnostisch zijn voor de omgeving waarin de verertsing verwacht kan worden.

De geobserveerde relatie bijvoorbeeld tussen metamorfose graad, bodemsamenstelling en spectrale eigenschappen is zeer geschikt om, met een minimum aan statistische manipulatie, zeer doelgericht te zoeken naar contactmetamorfe gebieden.

Mogelijkerwijs is het tweede probleem wel het lastigste te verhelpen. Dit is vooral het geval, wanneer een groot gebied, waar weinig over bekend is, onderzocht wordt. Iedere stap in de dataverwerking (bijv. filteren, classificatie, etc.), houdt automatisch verlies van informatie in. Het belangrijkste is in feite, om controle te hebben over de mate, waarin gegevens verloren raken. De beste manier om dit te bereiken is door elke stap te kwantificeren, zodat het interpretatie proces reproduceerbaar wordt, en dus vergelijkbaar met alternatieve interpretatie methodes.

Het derde probleem is grotendeels te ondervangen door de eigenschappen van omringende "pixels" van een geïdentificeerde pixel, te betrekken bij de beslissing aangaande de juistheid van een classificatie/interpretatie. Voor een pixel die bijvoorbeeld als "kaolinitisch" geïdentificeerd wordt in een TM- beeld, zou de concentratie van soortgelijke pixels in zijn directe omgeving maat kunnen zijn voor de juistheid van de identificatie: Een geïsoleerde "kaoliniet"-pixel die dicht bij meerdere soortgenoten in de buurt ligt, heeft meer kans om correct geklassificeerd te zijn dan één die daar ver van af ligt.

In het geval van gesteente-classificatie op basis van radiometrische data kan bijvoorbeeld het oppervlak van het geklassificeerde gebied als beslissings criterium gebruikt worden: Hoe groter het oppervlak van het gebied, des te groter de kans dat de klassificatie correct is.

Om het vierde probleem te ondervangen kan men gewichten toeekennen aan de mate van onzekerheid binnen een interpretatie. Hierbij is de rol van het calibratiegebied van essentieel belang. Bijvoorbeeld: pixels die als "kaoliniet" geklassificeerd zijn zijn niet uniek voor het contactaureole; erbuiten worden ze ook aangetroffen, om wat voor reden dan ook. Zij zijn echter veel talrijker binnen het contact aureool dan erbuiten. Contouren van het geïdentificeerde beeld levert een concentratiekaart. Vervolgens kan men aan verschillende concentratieklassen gewichten toegekennen, wat in dit geval inhoudt, dat het toegekende gewicht hoger wordt, naarmate de concentratie hoger is.

Als op deze wijze aan elke interpretatie gewichten zijn toegekend, worden ze geïntegreerd tot een kaart die voor elke locatie de waarschijnlijkheid uitdrukt dat mineralisatie aanwezig is. Deze stap is belangrijk om dat het resultaat ervan is, dat pixels die (om wat voor reden dan ook) onjuist geïdentificeerd zijn in een dataset, niet bevestigd worden door andere gegevens. Deze zullen dus met lage waarschijnlijkheden eindigen in een geïntegreerde kaart.

Het uiteindelijke doel van dit onderzoek was een data-integratiemethode te ontwikkelen die als een betrouwbaar hulpmiddel kan dienen tijdens de regionale fase van een exploratie programma. De methodologie, die ontwikkeld is voor het calibratie gebied, is daarom getest op regionale schaal (ongeveer 200*150Km). Het doel hiervan was drieledig:

- 1) Te bepalen welke complicaties men kan verwachten als een dergelijke methodologie wordt toegepast op een groot gebied waar weinig over bekend is;

- 2) Te testen, of de locatie van bekende ertsafzettingen voorspeld hadden kunnen worden op basis van de ontwikkelde methode en;
- 3) Nieuwe locaties te identificeren waar mogelijkerwijs mineralisatie is opgetreden.

Afgezien van het feit dat wij slechts beschikten over een regionaal-geologische kaart op schaal 1:200.000 (hetgeen alleen al de interpretatie van de gegevens aanzienlijk bemoeilijkte), deden zich een aantal nieuwe problemen voor:

- 1) Informatie die, op calibratie-schaal redelijk diagnostisch was voor het contactaureool, bleek op regionale schaal vaak veel minder diagnostisch te zijn. De spectrale reflectie-karakteristieken van het Tertiair bleken bijvoorbeeld erg te lijken op die van de kaoliniet-rijke bodems aangetroffen op contact metamorf gesteente;
- 2) De kwaliteit van de satellietbeeld-interpretatie bleken erg sterk af te hangen van de opname datum van het TM beeld;
- 3) Er deden zich situaties voor, die niet voorkwamen op calibratie-schaal. Bepaalde granaat types bleken bijvoorbeeld radiometrisch sterk te lijken op delen van het Tertiair;
- 4) De kwaliteit van de Airborne-survey was niet al te best. Er zijn bijvoorbeeld aanwijzingen dat het coördinaten systeem van deze data set niet correct is. Mogelijk is de dataset meer dan 2Km naar het noorden verschoven.

De resultaten van deze test geven echter aan, dat de ontwikkelde methodologie voldoende flexibel is om dergelijke complicaties het hoofd te bieden, aangezien de grotere bekende vererstingen samenvallen met zones die, in het onderhavige onderzoek, als gunstig geclassificeerd werden.

Tevens kwam als resultaat van deze test een aantal prospectieve gebieden naar voren, waar nog geen mineralisatie bekend is. Voor deze zones zou extra veldwerk aan te bevelen zijn.

Concluderend kunnen wij stellen dat deze studie laat zien dat Remote Sensing en data-integratie technieken geschikte hulpmiddelen zijn bij de identificatie van doelen in mineraal-exploratie, mits een goed fundamenteel begrip aanwezig is met betrekking tot de variaties die verwacht kunnen worden in Remote Sensing datasets in relatie tot de diagnostische fenomenen, waar men naar op zoek is.

CONTENTS

CHAPTER I: INTRODUCTION

1.1	Synopsis	1
1.2	Definition of the problem	1
1.3	Regional exploration for granite related mineralization	2
1.4	The procedure	3

CHAPTER II: REE-TRENDS IN A PERALUMINOUS, ILMENITE BEARING GRANITOID;

PETROGENETIC MODELS FOR THE HERCYNIAN GRANODIORITE-MONZOGRANITE SEQUENCE OF LOS SANTOS, WESTERN SPAIN.

2.1	Abstract	5
2.2	Introduction	5
2.3	Sampling and analyses	8
2.4	Petrology	9
2.5	Geochemical results	10
2.6	Discussion	16
	Fractionation modelling	18
	Origin of the granitic magma	22
2.7	Conclusions	26
2.8	References	27

CHAPTER III: THE RELATION BETWEEN BIOTITE COMPOSITION AND MAGMATIC DIFFERENTIATION IN THE PERALUMINOUS GRANODIORITE-MONZOGRANITE SEQUENCE OF LOS SANTOS, WESTERN SPAIN.

3.1	Abstract	31
3.2	Introduction	31
3.3	Sampling and analyses	34
3.4	Geochemical and petrological results	34
3.5	Results of mineral analyses	39
3.6	Discussion	42
	Whole rock chemistry	42
	The micas	45
	Conditions of biotite crystallization	50
	Sensor function	53
3.7	Conclusions	55
3.8	References	55

CHAPTER IV: UNRAVELLING OF CRYSTAL FRACTIONATION AND CONTAMINATION USING Ba, Sr, Rb AND Zr MODELLING AND COMPOSITIONS OF ZONED MINERALS

4.1	Abstract	59
4.2	Introduction	59
4.3	Sampling and analyses	61
4.4	Petrology and major element chemistry	61
	Major elements	64
	Feldspars	65
	Micas	66
	Cordierite	67
	Accessories	67
4.5	Trace elements	68
	Trace element modelling	70
	Modelling for contamination	72
4.6	Possible sources of enrichment for Sr and Ba	76
	Petrological evidence for contamination	76
4.7	Conclusions	80
4.8	References	81

CHAPTER V: SPECTRAL DISCRIMINATION OF CONTACT METAMORPHIC ZONES AND ITS POTENTIAL FOR EXPLORATION FOR GRANITE RELATED MINERALIZATION

5.1	Abstract	83
5.2	Introduction	83
5.3	Data collection	85
5.4	Sedimentary rocks	86
	Petrography	86
	Geochemistry	86
5.5	Soils	89
	Field description	89
	Chemistry	91
	Clay mineralogy	92
5.6	Land use	94
5.7	Spectral variation	95
5.8	Classification of the TM image	99
5.9	Conclusions	103
5.10	References	104

CHAPTER VI: INTEGRATION OF LANDSAT TM, AIRBORNE MAGNETIC AND RADIOMETRIC DATA AS AN EXPLORATION TOOL FOR GRANITE RELATED MINERALIZATION

6.1	Abstract	107
6.2	Introduction	107
6.3	Geological background	108
	The tungsten skarn of Los Santos	108
	The granitic rocks	110
	Contact metamorphic rocks	110
6.4	Interpretation of remote sensing data	111
	Landsat Thematic Mapper data	112
	Airborne geophysical data	112
6.5	Further data processing	119
6.6	Integration of the results	122
6.7	Discussion	123
6.8	Summary and conclusions	124
6.9	References	124

CHAPTER VII: A BLIND TEST OF THE DATA INTEGRATION METHODOLOGY

7.1	Abstract	127
7.2	Introduction	127
7.3	Procedure	128
7.4	Thematic Mapper data	130
	Mapping of kaolinitic soils	130
	Land use mapping	142
7.5	Airborne geophysical data	143
	Radiometric data	143
	Magnetic data	144
7.6	Data integration	145
7.7	Discussions and conclusions	147
7.8	References	148

CHAPTER V has been accepted for publication in *Remote Sensing of Environment*.
Co-author: Salomon B.Kroonenberg

CHAPTER VI has been accepted for publication by *Non Renewable Resources*.

CHAPTER 1

INTRODUCTION

1.1 SYNOPSIS

Ground based metal exploration is labour intensive and thus very expensive. Remote sensing and image processing seems to offer a cheaper and attractive strategy to replace some of this effort, notably in the screening phase of a new project. However, realizing this promise requires considerable more than an image processing system and some satellite data. This thesis studies the interpretation of remote sensing data and data integration in regional exploration for granite related mineralization in Central Western Spain.

1.2 DEFINITION OF THE PROBLEM

An inevitable part of mineral exploration programs is the decision making as to whether certain areas are prospective or not. The ability to make the right decisions, which is crucial to success, depends, apart from the human skills, on three main factors: I the availability of information; II the interpretation of the data and: III the amount of money that can be invested.

I. Fast development of data acquisition methods (routine multi element chemical analyses, airborne and satellite data acquisition, digital mapping systems) in the last decades have led to an exponential increase of the amount of information. This has improved the ability to understand the processes that have resulted in mineralization, as well as the capacity to recognize specific anomalies and expressions that are related to mineral deposition.

II. The often overwhelming quantities of information, such as derived from remote sensing platforms, require very sophisticated ways of data management. Adequate interpretation of the data is often very complex. The results can be disappointing, as it is often very difficult to separate relevant and less relevant information.

III. At present metal prices are extremely low, as a result of which exploration budgets are very tight. Cost cutting does not so much affect the data acquisition, since this is a relatively cheap part of the exploration program, as it does affect the expenses related to data compilation and interpretation.

With the development of geographical information systems in the 1970's, it became technically possible to deal efficiently with large amounts of information, in a cost effective manner. Geographic information systems (GIS) have become a valuable tool in many geo-oriented activities. Initially developed as a digital database for maps, the ability of GIS to manipulate spatial data sets has strongly increased, which

made it an indispensable tool in many decision-making and predicting studies. The possibility to combine raster and vector data of many different kinds, using digital image processing techniques, offers great potential in the analysis of spatial data. The analysis of combined data sets can reveal more information than a combination of interpretations of separate data sets. During the last two decades, a considerable amount of work has been done to test the applicability of digital image processing and data integration techniques in mineral exploration. A main task in these studies was to define how procedures of feature recognition and digital data integration should be applied in order to extract the most relevant information from multiple data sets.

While geographical information systems are, in many different professional fields, successfully applied to support decision making, it is surprising to observe that, in spite of all the effort, data integration techniques are still not incorporated as a standard procedure in regional exploration programs.

The aims of the study presented here are: I) to define the nature of the problems that seem to hamper a more widespread use of data integration in metal exploration, and II) to develop a data integration methodology that, in spite of these problems, can effectively support the decision making as to whether, at a certain location, mineralization can be expected or not.

1.3 REGIONAL EXPLORATION FOR GRANITE RELATED MINERALIZATION

This study was carried out in central western Spain. Mineralization of tungsten, tin, lead, zinc, copper, gold and uranium is associated with Hercynian granitic intrusions.

Identification of individual mineral deposits during a regional exploration survey is a very difficult task because of the strong diversity in style of mineralization, size of the deposits, and, most important for exploration, the anomalies that are a result of the mineralizing processes. For example, some of the small sulphidic vein systems are associated with strong iron staining of the overlying soils, others are accompanied by minor greisenization, while the largest deposit in the region, the tungsten skarn of Los Santos, which partly crops out at surface, has hardly any visible surface expression. Although some small scale exploitation of tungsten is reported from 40-50 years back (Garcia Sanchez pers. comm.), the full significance of the deposit was discovered in 1980, during a survey in the contact metamorphic zone, using a UV lamp. In addition, also the scale at which data are collected during a regional survey makes it rather difficult to detect individual deposits. For example, the resolution of Thematic Mapper data is 30*30m. Although theoretically it should be possible to detect surface anomalies related to one single deposit, the information is usually not sufficiently detailed to distinguish individual mineral deposits. Regional airborne magnetic and radiometric surveys usually have a line spacing of more than 1km. Smaller deposits are thus easily missed.

In a regional survey, it is therefore not very sensible to search for individual mineral deposits. It is much

more effective to look for features diagnostic of the setting in which a specific type of deposit is most likely to occur. For granite related mineralization this setting is often the margin of the intrusion and the contact metamorphic aureole. Once favourable zones are delineated in a regional investigation, it can be decided where follow up exploration and detailed fieldwork should be carried out. This is, in fact, very well demonstrated by the way the Los Santos deposit was discovered.

1.4 THE PROCEDURE

The data that are used for the integration part of this study exclusively comprise remotely sensed data: airborne magnetic and radiometric data and Thematic Mapper data. These data were used for two reasons: a) They provide a good starting point for a regional exploration survey in areas where little or no ground data are available and; b) They provide the best opportunity to study the difficulties related with data integration, as the interpretation of remote sensing data is much more subject to uncertainties than any type of ground data.

Anyone who wants to use remote sensing, digital image processing and data integration techniques for purposes of mineral exploration, has to be aware of the fact that for successful application of these methods, understanding of the features diagnostic of the geological setting of the mineralization, and the processes that resulted in the formation of the mineral deposits, is an absolute prerequisite. This is why we started with a very detailed ground study in a calibration area (20*20km) with known significant mineralization. CHAPTERS 2,3 and 4 report on the study of the processes that actually resulted in mineral deposition: the emplacement of granitic magma, using geochemical methods.

For this calibration area it was subsequently determined how the effects of the mineralizing processes can be recognized in remotely sensed data, and how image processing and data integration techniques should be applied to map potentially mineralized rocks (CHAPTERS 5 and 6).

With the knowledge obtained from the calibration area, remote sensing data were used to map the mineral potential of a much larger area (200*150km, CHAPTER 7). As the only ground reference for this area was a 1:200.000 regional geological map, it was to be expected that additional difficulties would be encountered during the interpretation of the data. These difficulties were identified and suggestions for future work are given.

REE-TRENDS IN A PERALUMINOUS, ILMENITE BEARING GRANITOID; PETROGENETIC MODELS FOR THE HERCYNIAN GRANODIORITE-MONZOGRANITE SERIES OF LOS SANTOS, WESTERN CENTRAL SPAIN.

2.1 ABSTRACT

The biotite-rich granodiorites, muscovite and cordierite-bearing monzogranites and the aplitic dikes of the granitoid of Los Santos, in the western part of the Hercynian Spanish Sistema Central are cogenetic. Tonalitic xenoliths, which are widespread in the entire batholith, are probably early derivatives of the same magma. The position of the xenoliths in trace-element variation diagrams rules out mixing between mantle-derived melt and crustal anatexic material as a major reason for the geochemical variations in the granodiorite. REE modelling demonstrates that a 60% In Situ crystal fractionation in a parent magma that has the same composition as the average intrusion, yields a residual melt that corresponds with the average composition of the monzogranites. Although the main REE variations in the batholith are compatible with In Situ crystal fractionation of plagioclase, K-feldspar, apatite, zircon and monazite, gradual segregation of part of the intercumulus melt is responsible for the regional geochemical zoning of the batholith, from intercumulus depleted granodiorites to intercumulus enriched monzogranites. The monzogranitic, intercumulus enriched melt locally developed cryptic intrusive contacts with the granodioritic rocks. Regional low grade metamorphic sediments of the Complejo Esquisto Grauvaquico, and gneisses, abundant as xenoliths in the batholith, were examined as potential source rocks. A granitic melt with the composition equal to that of the average intrusion can be derived better from gneisses than from the low grade metasedimentary rocks. 30% partial batch melting of a gneiss source rock with 0.011wt% monazite produces a melt composition identical to that of the average intrusion.

2.2 INTRODUCTION

The majority of the geochemical information on Spanish Hercynian granitic intrusions consists of conventional major- and trace element analyses (e.g. Barr and Areias 1980; Aparicio et al. 1983; Guijarro et al. 1984; Neiva et al. 1987; Bea et al. 1988; Garcia et al. 1989). Rare Earth Element data are relatively scarce (Albuquerque 1987; Neiva et al. 1987; Carracedo et al. 1989; Rottura et al. 1989) although these highly immobile trace elements are in general very effective for modelling magmatic processes and for determination of potential source rock, due to their specific partitioning behaviour during magma generation (McCarthy and Cable 1978) and its successive crystallization (Gromet and Silver 1983). In this study, whole rock chemistry and in particular REE-data are presented for the granodiorite-monzogranite-aplite sequence south of Los Santos (Fig. 1a), part of the Spanish Central System Batholith (CSB, Rottura et al. 1989), and the surrounding metasedimentary rocks (Fig. 1b).

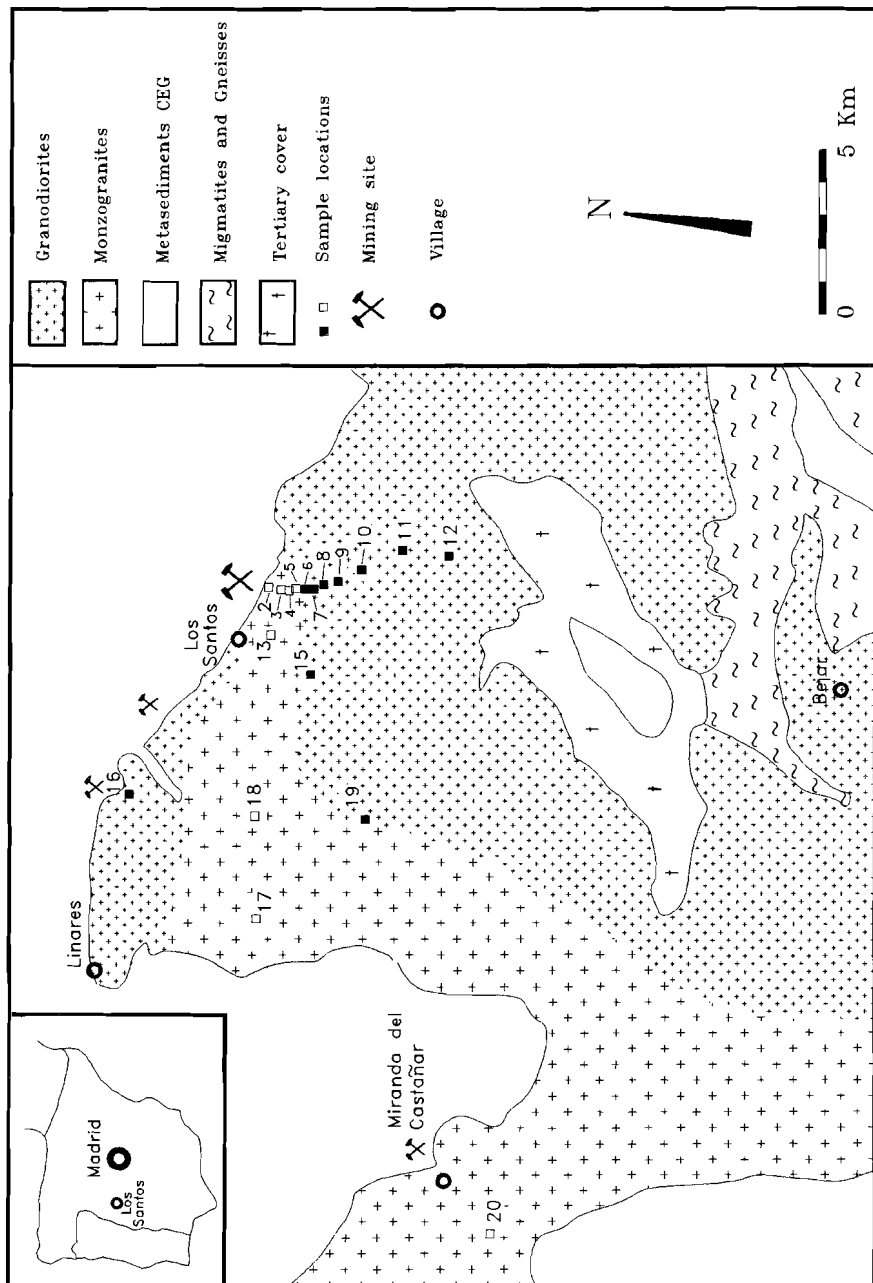


Fig.1a. Simplified geological map, showing the distribution of granodiorites and monzogranites of the intrusion of Los Santos. The sample locations are indicated with solid squares (granodiorites) and open squares (monzogranites).

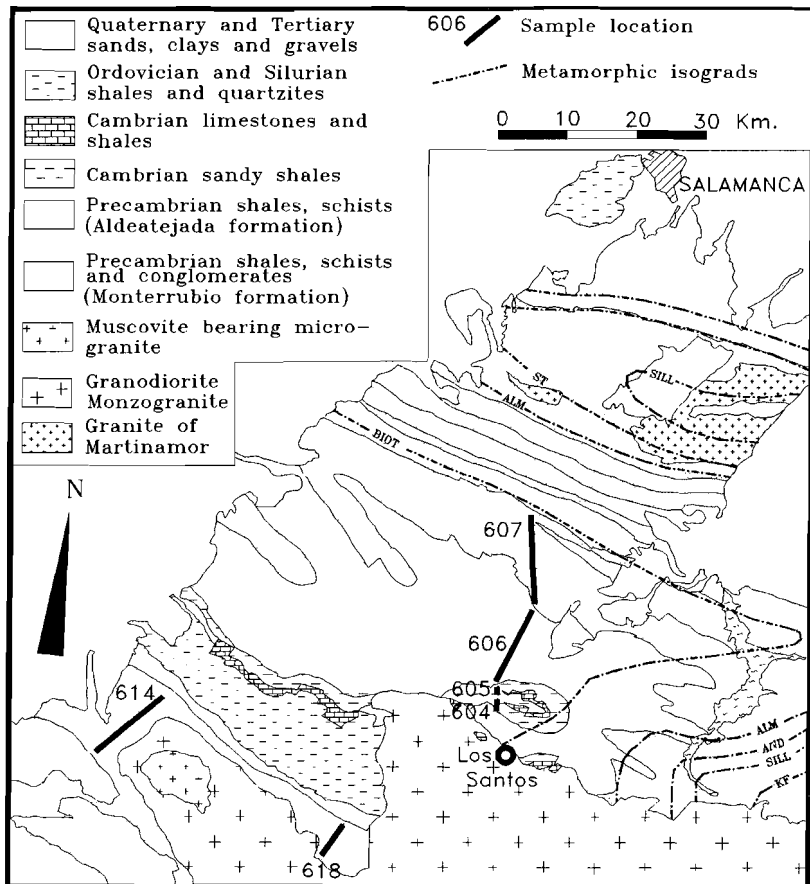


Fig.1b. Regional geological map of the metasedimentary rocks of the Complejo Esquisto Grauvaquico (after simplified after Diez Balda 1982). Metamorphic isograds: Biotite (BIOT), Almandine (ALM), Staurolite (ST), Andalusite (AND), Sillimanite (SILL) and K-feldspar (KF). Samples of regional metamorphic rocks, analized for REE are indicated on the map.

The CSB crops out over an area of approximately 13000 km² in the southern part of the Central Zone of the Iberian Massif (Julivert et al. 1974) and consists mainly of biotite-rich granodiorites and cordierite and muscovite bearing granites. The CSB-granitoids were emplaced during late Hercynian tectonic events (Rottura et al. 1989). The investigated granitoids near Los Santos form the northwestern part of the CSB. They intruded low-grade Precambrian greenschist facies rocks of the Complejo Esquisto Grauvaquico CEG. The intrusion is chemically and mineralogically zoned, and ranges gradually from

biotite-rich granodiorites in the core to muscovite +/- cordierite monzogranites and leucogranitic aplites near the margin (Fig.1a). A small area of granodiorites is present in the NW-corner of the intrusion, near the village of Linares, separated from the main granodiorite mass by the monzogranites. Our field observations indicate that granodiorites and monzogranites cover a surface at a ratio of approximately 6:4. The aplites are volumetrically insignificant, except in vicinity of the Los Santos skarn. The most felsic monzogranites occur adjacent to this large tungsten skarn, together with fine-grained tourmaline-bearing aplitic dikes. Rounded xenoliths with a diameter normally less than 30 cm. occur dispersed throughout the entire batholith. The majority consists of magmatic textured, biotite-rich xenoliths of varying grainsize, but gneissose xenoliths are also abundant. Metasedimentary hornfels xenoliths are most frequent in the monzogranites near the margin of the intrusion. The granitic intrusion is surrounded by a well developed contact aureole. Near the village of Bejar, the granitic rocks grade into anatetic migmatites and gneisses (Ugidos 1974, 1985). Based on the abundance of magmatic xenoliths Rottura et al.(1989) propose a magma mixing model to explain the geochemical variations in granodiorites and monzogranites. Ugidos and Bea (1976) suggest a crustal anatetic origin for the monzogranitic rocks and propose a mixing model between this crustal melt material and deep seated calc-alcaline magma to explain for compositional variations within the granodioritic rocks. However, Bea and Moreno (1985) claim that all intrusive rocks can be explained by means of crustal anatexis.

The purpose of this paper is to explain the geochemical variations in the intrusive sequence, to compare fractional crystallization models with magma mixing, to examine the differentiation of the monzogranites from the granodiorites by mainly In Situ crystallization and to model partial melting, in order to evaluate the surrounding crustal materials as potential source rocks.

2.3 SAMPLING AND ANALYSES

Out of an initial set of 83 samples, ten granodioritic and eight monzogranitic samples were selected for detailed investigation (Fig.1a). Eleven of these were collected along a cross section from the core of the intrusion towards the Los Santos deposit in order to obtain optimal information about the transition from the most mafic granodiorites to the most felsic monzogranites. Five samples (A1 to A5) were collected from aplitic dikes near Los Santos. Sample A5 is from a dike that intruded into the granodiorite, near sample 15, A3 from a dike that intruded the monzogranite, near sample 13 and A1, A2 and A4 are from dikes intruding the contact with the metasediments, near sample 2. Six representative samples were collected from mafic xenoliths. Two of them (X5,X6) were sampled in the granodiorites, near sample 12 and four (X1 to X4) in the monzogranites, near sample 13. In addition, a gneiss xenolith (X7) and a hornfels xenolith (X8) were sampled in the monzogranites, near sample 13. Forty metasediment samples were collected and analyzed for major and trace elements. Eleven of these were selected for REE-analysis. Five (CLS1 to 5) were collected within the contact metamorphic aureole near Los Santos, at respective distances of 50m, 200 m, 500 m, 850 m and 1200 m perpendicular to the contact. The other

six samples are representative for the major lithologic units that crop out between the city of Salamanca and the granite intrusion (Fig.1b).

Granitic and contact metamorphic samples consisted each of approximately 1 Kg of small chips, collected on a surface of at least two square metres. The regional metamorphic rocks were chip sampled over the entire width of each lithologic unit. In quarries rocks were collected containing one or more xenoliths. The sampled xenoliths were usually less than 20 cm. in diameter, which precluded the possibility of taking large samples. In the laboratory, small fragments of a few cubic centimetres were separated from the cores of the xenoliths using a diamond saw, in order to avoid contamination with the surrounding granite material.

All samples were analyzed for major-, trace- and rare earth element composition and thin sections were studied. Whole rock major element composition was determined in lithium metaborate glass beads and whole rock trace element composition in pressed powders with a Philips PW-1400 XRF. The precision is better than 5% for Na_2O , K_2O and MnO analyses, better than 2% for the other major elements and better than 5% for the trace elements. The FeO -content has been determined following Pratt's method (Pratt 1894), with better than 5% precision. REE compositions were determined by Instrumental Neutron Activation Analyses, with 1% analytical error. The neutron activation analyses were carried out in five batches. Two of these have yielded very poor quality results for Nd (23% too high) and Yb (13% too low). The precision for these elements is better than 7% in the other three batches. For La, Sm, Eu Tb and Lu the precision is better than 5% in all batches.

2.4 PETROLOGY

The granodiorites consist of a medium-grained crystal mush of biotites and strongly zoned plagioclase (An_{58-15}), with variable amounts of interstitial quartz, plagioclase and perthitic K-feldspar. Biotite coexists with ilmenite, apatite, zircon and minor monazite in all samples. No muscovite was observed.

The monzogranites additionally contain euhedral quartz and abundant K-feldspar megacrysts. The plagioclases in the monzogranites are occasionally strongly zoned ($\text{An}_{49}-\text{An}_6$). Primary as well as secondary muscovite is present in the monzogranites (Rottura et al. 1989). The amount of cordierite is usually less than 2 vol%. Although a xenocrystic origin for cordierite is inferred by Ugidos (1983, 1985), available textural and chemical data favour a magmatic origin (Bea 1982, Rottura et al. 1989). K-feldspar megacrysts are predominant in the monzogranites. Their abundance increases towards the aplite rich contacts, where they occasionally develop a cumulate character. In the monzogranites they are frequently oriented, locally in circular patterns.

The aplites are rather fine grained rocks consisting of anhedral perthitic K-feldspar, quartz, muscovite and minor plagioclase and biotite. The plagioclase is usually unzoned. In addition, A1 and A2 contain biotite and A4 tourmaline. Zircon and apatite are accessories.

The xenoliths X1-X6 consist of a fine grained groundmass of plagioclase, quartz and biotite with some

large quartz grains and idiomorphic zoned plagioclase crystals, and contain little K-feldspar. The plagioclases in the xenoliths sampled in the monzogranite (X1-X4) are more albited than those sampled in the granodiorite (X5,X6). Biotite occurs both as euhedral grains of variable size and as small flakes with irregular edges. Zircon usually appears as clusters of tiny grains, both within the biotites and in the ground mass. Apatite typically is needle-shaped. Sample X7 is a fine-grained gneiss enclave, whose texture and mineralogy is rather similar to that of the groundmass of X1-X6. Needle-shaped apatites are absent. K-feldspar is very abundant in this sample. Sample X8 is a hornfels xenolith, with abundant quartz, muscovite, cordierite, andalusite, sillimanite, ilmenite, chalcopyrite and enveloped by a tourmaline-rich rim. The low grade metasedimentary rocks outside of the contact aureole are predominantly fine-grained green slates with a chlorite, chloritoid, sericite and quartz association (Diez Balda 1982). Sedimentary rocks of higher metamorphic grade are mapped further away from our study area (Fig.1b, from Diez Balda 1982). Contact metamorphism is notified by the successive development of biotite and cordierite isograds.

2.5 GEOCHEMICAL RESULTS.

The whole rock compositions of the plutonic rocks, and the averages of the tonalitic xenoliths, granodiorites, monzogranites and aplites are listed in table 1a. In these four rock types, from the most mafic to the most felsic, the average contents of TiO_2 , Fe_2O_3 , MnO, MgO and CaO decrease while SiO_2 and K_2O increase.

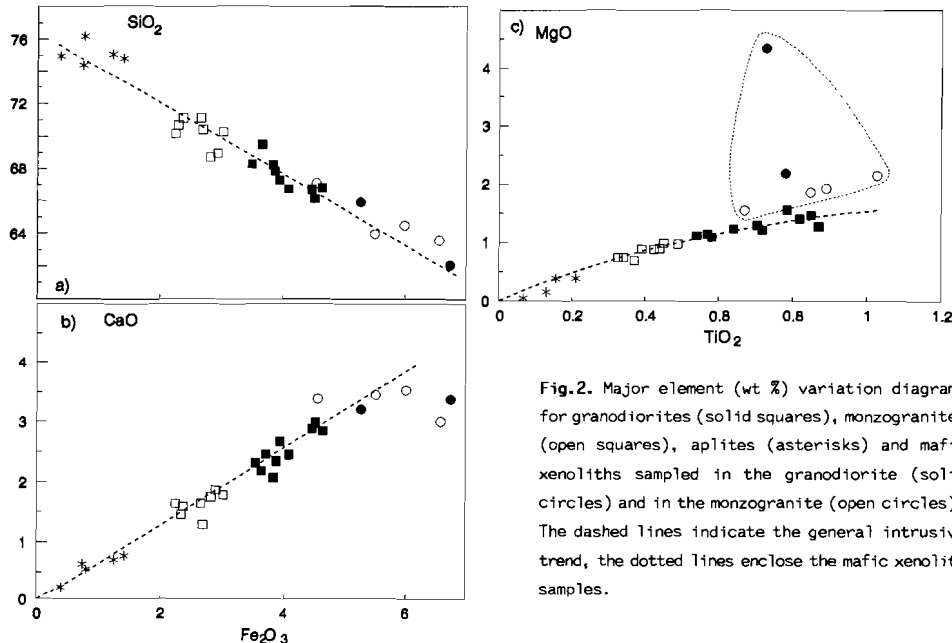


Fig.2. Major element (wt %) variation diagrams for granodiorites (solid squares), monzogranites (open squares), aplites (asterisks) and mafic xenoliths sampled in the granodiorite (solid circles) and in the monzogranite (open circles). The dashed lines indicate the general intrusive trend, the dotted lines enclose the mafic xenolith samples.

Table 1a. Major- and trace element compositions of magmatic xenoliths, granodiorites, monzogranites and aplites.

Nr	GRANODIORITES										MONZOGRANITES									
	10	12	11	7	19	9	8	6	16	15	3	13	18	2	17	5	4	20		
SiO ₂	64.6	65.4	66.0	66.0	67.5	67.8	68.2	68.3	68.7	69.5	68.3	68.8	70.1	70.1	70.3	70.4	70.7	70.7	70.7	
TiO ₂	0.82	0.79	0.87	0.72	0.57	0.85	0.64	0.71	0.54	0.58	0.43	0.45	0.39	0.34	0.49	0.37	0.33	0.44		
Al ₂ O ₃	15.4	15.5	15.5	15.8	15.2	15.3	15.4	16.0	16.1	15.1	16.0	16.0	14.9	15.9	15.3	15.0	15.2	15.6		
Fe ₂ O ₃	4.41	4.37	3.87	4.04	3.73	4.64	3.85	3.87	3.55	3.64	2.81	2.88	2.6	2.25	3.03	2.34	2.31	2.68		
MnO	0.07	0.08	0.06	0.07	0.06	0.07	0.06	0.06	0.07	0.07	0.06	0.06	0.06	0.05	0.07	0.06	0.06	0.06	0.06	
MgO	1.44	1.58	1.3	1.23	1.15	1.49	1.24	1.30	1.14	1.15	0.91	0.98	0.9	0.75	1	0.71	0.76	0.93		
CaO	2.93	2.83	2.61	2.44	2.18	2.89	2.37	2.1	2.34	2.21	1.77	1.89	1.62	1.64	1.8	1.55	1.47	1.29		
Na ₂ O	3.33	3.36	3.26	3.05	3.55	3.59	3.26	3.19	3.57	3.24	3.25	3.49	3.52	4.13	3.46	3.49	3.58	3.28		
K ₂ O	4.27	3.82	4.46	5.31	4.12	3.53	4.3	4.85	4.45	4.24	5.65	5.0	4.26	4.84	4.19	4.83	4.75	5.13		
P ₂ O ₅	0.26	0.24	0.25	0.28	0.21	0.25	0.25	0.28	0.21	0.21	0.22	0.24	0.25	0.29	0.27	0.22	0.24	0.33		
total	97.5	98.0	98.0	98.9	98.3	100.3	99.6	100.7	100.6	99.91	99.5	99.9	98.6	100.1	99.8	99.0	99.6	100.5		
Fe*	0.91	0.78	0.99	0.91	n.d.	0.93	0.85	0.81	n.d.	n.d.	0.92	0.80	n.d.	n.d.	n.d.	0.88	n.d.	n.d.		
Zr	223	218	213	186	180	210	192	190	182	183	151	144	130	116	152	115	115	137		
La	49.7	44.4	42.5	38.8	34	40.3	34.9	37.6	37.2	33.7	29.8	26.7	28.3	21.6	31.5	25.1	23.1	30.2		
Ce	99.1	90.9	90.0	84	75.1	81.6	73.4	78.5	79.4	77.5	66.1	60	64.3	52	67.5	47.6	52	61.7		
Nd	51.9	51.2	42.0	49.4	39.5	49.4	41.2	45.7	36.3	32.8	33.3	29	25.	22	30.3	26.6	26	37.3		
Sm	8.75	8.09	7.7	7.45	6.17	7.77	6.63	7.52	6.66	6.17	5.84	5.3	5.3	4.13	6.06	4.39	4.7	5.47		
Eu	1.4	1.22	1.2	1.34	1.07	1.17	1.00	1.16	1.28	1.12	1.05	0.89	0.92	0.8	1.03	0.78	0.72	0.80		
Tb	0.95	1.13	0.86	1.0	0.77	0.88	0.83	0.85	0.77	0.77	0.63	0.68	0.68	0.53	0.70	0.53	0.51	0.51		
Yb	2.18	2.19	2.32	1.9	2.45	2.48	2.18	1.97	2.34	2.34	2.06	1.6	2	1.22	1.97	1.42	1.38	1.23		
Lu	0.37	0.34	0.35	0.35	0.34	0.41	0.32	0.35	0.32	0.34	0.31	0.26	0.30	0.18	0.29	0.23	0.21	0.17		
Hf	8.26	5.84	6.5	5.5	5.93	7.11	5.81	5.3	6.52	5.9	4.21	4.41	4.41	4.06	5.5	3.98	3.14	3.9		
Th	20.4	19.8	18.1	17.1	15.3	16.6	15.6	16.2	13.9	14.8	15.1	13.4	13.2	10.6	15.2	11.5	11.9	13.8		
Eu/Eu*	0.52	0.47	0.5	0.56	0.55	0.49	0.48	0.5	0.62	0.58	0.59	0.53	0.55	0.61	0.55	0.57	0.50	0.53		
La/Yb	13.9	12.3	11.1	12.3	8.4	9.8	9.7	11.6	9.6	8.7	8.7	10.11	8.57	10.7	9.69	10.74	10.14	14.9		
ΣREE	215	200	186	184	159	184	160	174	164	155	149	124	127	108	139	109	108	137		
APLITES											XENOLITHS									
a2 ¹⁾	a3 ¹⁾	a1 ¹⁾	a4 ²⁾	a5 ³⁾	X6 ⁵⁾	X1 ⁴⁾	X2 ⁴⁾	X4 ⁴⁾	X5 ⁵⁾	X3 ⁴⁾	Xeno- litths	GD	MG	Ap1	Intrusion ⁶⁾					
SiO ₂	74.4	74.4	74.7	75.0	75.0	62.1	63.6	64.0	64.6	65.9	67.1	64.5	67.1	70.0	74.7	68.3				
TiO ₂	0.16	0.13	0.21	0.07	0.07	0.73	1.03	0.85	0.89	0.78	0.67	0.83	0.72	0.41	0.13	0.59				
Al ₂ O ₃	13.7	14.7	14.0	14.6	13.4	16.6	16.9	17.7	16.5	15.9	16.8	16.7	15.6	15.5	14.1	15.6				
Fe ₂ O ₃	1.23	1.75	1.42	0.79	0.39	6.74	6.57	5.51	6.00	5.28	4.56	5.77	4.03	2.61	0.92	3.46				
MnO	0.04	0.06	0.04	0.01	0.02	0.10	0.09	0.08	0.09	0.07	0.07	0.08	0.07	0.06	0.03	0.06				
MgO	0.39	0.17	0.4	0.06	0.03	4.36	2.16	1.87	1.93	2.20	1.56	2.35	1.32	0.86	0.21	1.14				
CaO	0.7	0.64	0.78	0.23	0.56	3.39	3.00	3.47	3.52	3.21	3.41	3.33	2.52	1.62	0.58	2.16				
Na ₂ O	3.8	3.7	3.76	3.7	3.45	2.91	3.79	4.58	4.11	3.27	4.24	3.81	3.31	3.53	3.68	3.40				
K ₂ O	4.45	4.93	4.1	5.53	5.09	3.58	2.71	2.33	2.32	3.57	1.94	2.74	4.36	4.83	4.82	4.55				
P ₂ O ₅	0.12	0.19	0.17	0.3	0.03	0.17	0.31	0.30	0.26	0.29	0.24	0.26	0.26	0.24	0.16	0.25				
total	99.0	99.7	99.7	99.8	98.5	100.8	100.2	100.7	100.3	100.5	100.6									
Fe*	n.d.	n.d.																		
Zr	68	40	68	32	37	162	167	226	234	196	181	194	198	133	49	172				
La	9.8	6.2	11.8	2.2	7.5	20.6	32.1	33.7	37.1	44.5	30.8	33.1	39.3	27.0	7.5	34.4				
Ce	24.4	12.5	28.6	3.9	15.7	42.7	72	72	82	93.9	69	71.9	83.1	58.4	17.0	73.2				
Nd	11	<9	15	<9	21	32	34	36	46	33	33	33.7	43.9	28.8	-	37.8				
Sm	2.63	1.24	3.13	0.49	1.85	4.36	7.68	6.73	7.5	7.8	6.1	6.7	7.29	5.14	1.86	6.4				
Eu	0.3	0.32	0.29	0.06	0.21	0.81	0.8	0.73	0.55	1.15	0.93	0.82	1.19	0.87	0.24	1.06				
Tb	0.44	0.24	0.39	0.12	0.51	0.67	1.12	0.88	0.78	0.89	0.8	0.85	0.88	0.59	0.34	0.76				
Yb	1.61	1.33	1.78	0.48	2.25	1.95	2.83	2.44	2.49	1.98	1.94	2.27	2.23	1.61	1.49	1.98				
Lu	0.27	0.19	0.28	0.08	0.35	0.26	0.43	0.36	0.37	0.33	0.3	0.34	0.31	0.22	0.23	0.27	0.27			
Hf	2.33	1.5	2.49	1.27	1.96	4.37	5.5	6.6	6.4	6.1	5.4	5.59	6.27	4.20	1.91	5.44				
Th	7.44	3.3	8.63	1.4	5.4	6.9	12.5	10.4	16.2	15.7	14.0	12.6	16.8	13.1	5.23	15.3				
Eu/Eu*	0.34	0.74	0.29	0.33	0.29	0.56	0.32	0.34	0.24	0.47	0.48	0.41	0.53	0.55	0.40	0.54				
La/Yb	3.7	2.8	4.0	2.8	2.0	6.4	6.87	8.37	9.03	13.6	9.62	9	11.5	10.1	3.8	10.9				
ΣREE	50	22	61	7	28	92	148	151	166	196	152	151	178	123	34	156				

1) biotite-muscovite aplites; 2) biotite aplite; 3) biotite-tourmaline aplite;

4) magmatic tonalitic xenoliths in monzogranite; 5) magmatic tonalitic xenoliths in the granodiorite; 6) average composition of the intrusion GD₂MG-6:4; Major elements are in weight %, trace elements are in parts per million. Fe : Fe⁺⁺/Fe_{total}.

Table 1b. Major- and trace element composition of sedimentary rocks

SEDIMENTARY ROCKS																
contact metamorphic					low grade metamorphic					Xenoliths			Averages			
CLS1	CLS2	CLS3	CLS4	CLS5	604	605	606	607	614	618	x7	x8	a	b	c	
SiO ₂	60.7	62.9	64.2	75.0	64.1	77	75	66.7	67.1	63.8	64.8	58.9	53.3	65.4	69.0	64.4
TiO ₂	0.81	0.82	0.87	0.4	0.79	0.48	0.46	0.79	0.69	0.82	0.8	1.00	1.24	0.73	1.12	0.78
Al ₂ O ₃	20.3	19.7	19.3	12.4	18.6	11.8	8.5	19.2	17.2	20.5	19.1	19.9	26.8	18.1	16.0	19.2
Fe ₂ O ₃	8.63	8.16	7.04	3.14	7.29	6.8	1.8	6.6	6.1	6.5	6.4	4.98	6.62	6.85	5.7	7.0
MnO	0.11	0.12	0.04	0.04	0.1	0.05	0.06	0.07	0.06	0.08	0.08	0.07	0.20	0.08	0.07	0.09
MgO	3.37	3.15	3.72	1.43	2.82	0.93	4.08	2.24	2.6	2.28	2.64	1.54	2.21	2.89	2.46	2.74
CaO	0.61	0.72	0.21	0.22	0.79	0.0	7.7	0.14	0.25	0.27	0.41	0.98	1.57	0.51	1.46	0.63
Na ₂ O	1.2	1.38	1.09	1.48	2.26	0.22	0.2	1.62	1.63	1.30	2.34	3.11	3.95	1.48	1.22	1.43
K ₂ O	4.01	4.17	4.08	5.4	3.64	2.89	2.41	3.55	4.09	3.93	3.71	9.46	4.47	4.26	3.38	3.87
P ₂ O ₅	0.15	0.17	0.14	0.13	0.15	0.2	0.11	0.16	0.17	0.16	0.16	0.13	0.18	0.15	0.16	0.15
total	99.9	101.3	100.8	99.7	100.6	100.4	100.3	101.6	99.9	99.6	100.4	100	100.7			
Fe [*]	0.82	0.78	0.86	0.74	0.63	0.57	0.53	0.65	n.d	n.d	n.d	n.d	n.d	n.d	n.d	
Zr	114	145	151	137	152	148	269	167	167	190	159	291	281	140	183	161
La	24.3	41.2	43.9	43.3	45	34.6	43	36	31.3	44.3	38.3	54.7	67	39.5	39.7	38.6
Ce	51	85	91.6	88	91	62.9	60.3	67	56	84	81	110	162	81.32	68.5	74.3
Nd	21	37	39	39	44	27	29.8	32	24	42	36	53	73	36	31.8	33.7
Sm	3.86	6.91	7.2	7.2	7.4	5.7	5.4	6.4	5.85	7.4	6.9	8.9	12.3	6.5	6.27	6.4
Eu	0.83	1.45	1.47	1.47	1.43	1.24	1.02	1.21	1.15	1.6	1.6	1.26	2.22	1.33	1.30	1.32
Tb	0.58	0.9	0.75	1.03	0.9	0.65	0.6	0.73	0.81	0.99	0.96	0.82	1.45	0.83	0.79	0.81
Yb	1.58	2.52	2.66	2.51	2.51	2.18	1.59	2.50	2.1	3.17	3.12	1.99	4.73	2.35	2.40	2.40
Lu	0.25	0.39	0.47	0.4	0.41	0.36	0.23	0.39	0.33	0.53	0.53	0.33	0.75	0.38	0.33	0.39
Hf	3.22	4.13	4.1	3.82	4.2	4.12	8.94	4.35	4.85	4.95	4.74	10.7	9.32	3.9	5.32	4.67
Eu/Eu [*]	0.65	0.66	0.67	0.63	0.62	0.70	0.61	0.61	0.61	0.67	0.72	0.47	0.57	0.65	0.65	0.65
La/Yb	15.3	16.3	16.5	17.3	17.9	15.8	27.0	14.4	14.9	13.9	12.27	16.6	8.6	16.7	17.0	16.0
ΣREE	103	175	187	183	193	134	142	146	122	184	168	230	323	168	149	15

X7: Gneiss xenolith; X8: Sillimanite-andalusite bearing hornfels
xenolith. Average of five contact metamorphic sediments (a); of six low grade metamorphic sediments (b); of total sediment dataset (c) (40 major element and 11 REE analyses);

Figure 2a,b and c illustrate the linear relations of Fe₂O₃ with CaO, Fe₂O₃ with SiO₂, and TiO₂ with MgO respectively. The relation between TiO₂ and MgO is curved for the granodiorite-monzogranite-aplite sequence. The xenoliths have much higher MgO content compared to the granodiorites with similar TiO₂ content. The trace elements Zr, Hf and Th also decrease from granodiorites to aplites (Fig.3). However, the xenoliths have an average content of Zr, Hf and Th equal to or lower than that of the granodiorites, and form a separate cluster (Fig.3). As opposed to the straight trends for Zr and Hf with Fe₂O₃ as differentiation index, the trend for Th is curved.

ΣREE ranges from 215 to 155 ppm in the granodiorites, from 149 to 48 ppm in the monzogranites, from 61 to 7 ppm in the aplites and in the xenoliths from 196 to 92 (Table 1a). The Eu-anomalies, defined as Eu/Eu^{*} by Henderson (1984) are in the same range for the granodiorites (0.47 to 0.62) and the monzogranites (0.50 to 0.61), whereas aplites have large Eu-anomalies (0.29 to 0.34). The xenoliths have Eu-anomalies ranging from 0.24 to 0.56. The xenoliths sampled in the monzogranite (X1-X4) display larger Eu-anomalies than those sampled in the granodiorite (X5,X6).

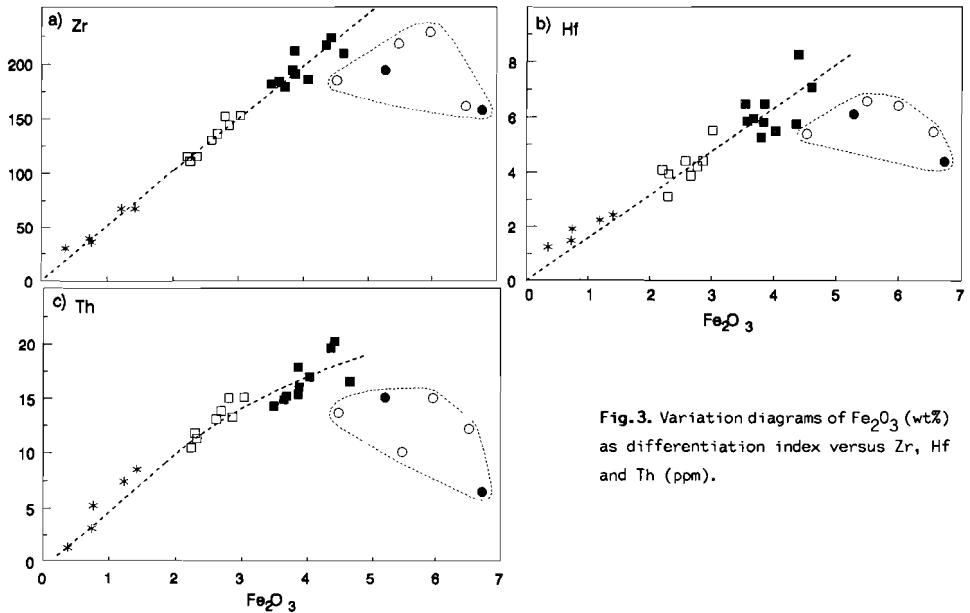


Fig.3. Variation diagrams of Fe_2O_3 (wt%) as differentiation index versus Zr, Hf and Th (ppm).

The chondrite normalized REE abundances (Haskin et al. 1968) display parallel patterns for all granodiorites ($\text{La/Yb}=9.7$ to 13.4) and monzogranites (8.7 to 10.7), and illustrate a gradual decrease (Fig.4a). The chondrite normalized patterns of the tonalitic xenoliths obviously display parallel trends too (Fig.5a), and the average xenolith pattern is almost identical to the average pattern of the granodiorites and monzogranites (Fig.5b). The patterns of the aplites (Fig.4b) demonstrate more variation in REE abundance as well as in slope.

When plotted against Fe_2O_3 , the chondrite normalized REE reveal linear trends for the granodiorite-aplite sequence, which are notably curved for Sm, Eu and Lu, but not for La (Fig.6). The xenoliths plot in a separate cluster for La, Sm and Eu, below the granitic trend. The Lu abundances in aplites are higher than expected on the basis of their Fe_2O_3 content, whereas that of the xenoliths practically fit the curved trend.

Eleven representative major element and REE-analyses of rocks of the surrounding CEG are given in table 1b. The ΣREE of the contact metamorphic rocks ranges from 103 to 193 ppm (average 168 ppm), and from 122 to 184 ppm (average 149 ppm) in the regional metamorphic rocks, whereas the gneiss and hornfels xenoliths have relatively high REE abundances (ΣREE 230 and 323 ppm respectively). The Eu-anomaly of all sedimentary samples ranges from 0.61 to 0.72.

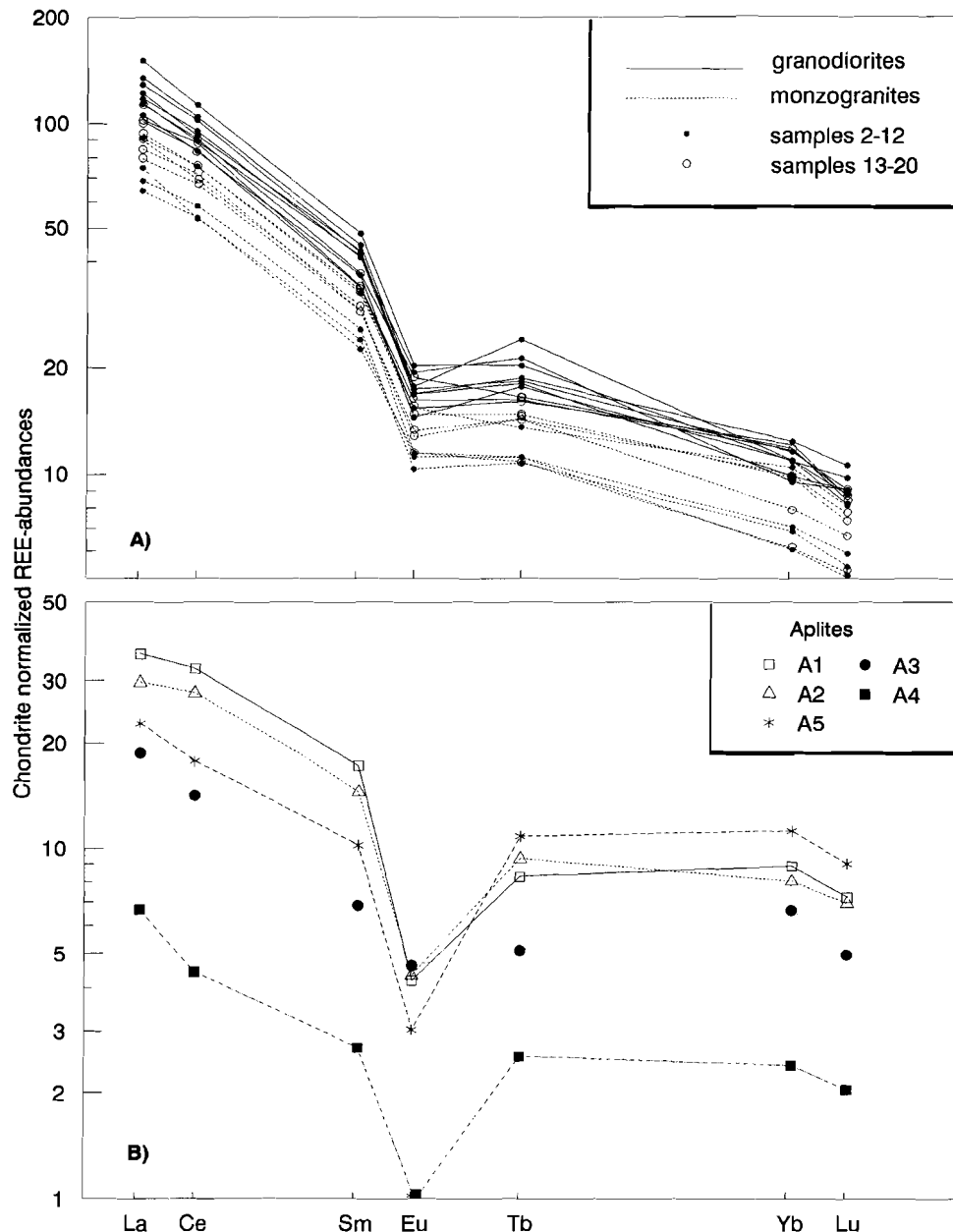


Fig.4. Chondrite normalized REE patterns for granodiorites and monzogranites (a) and for aplites (b).

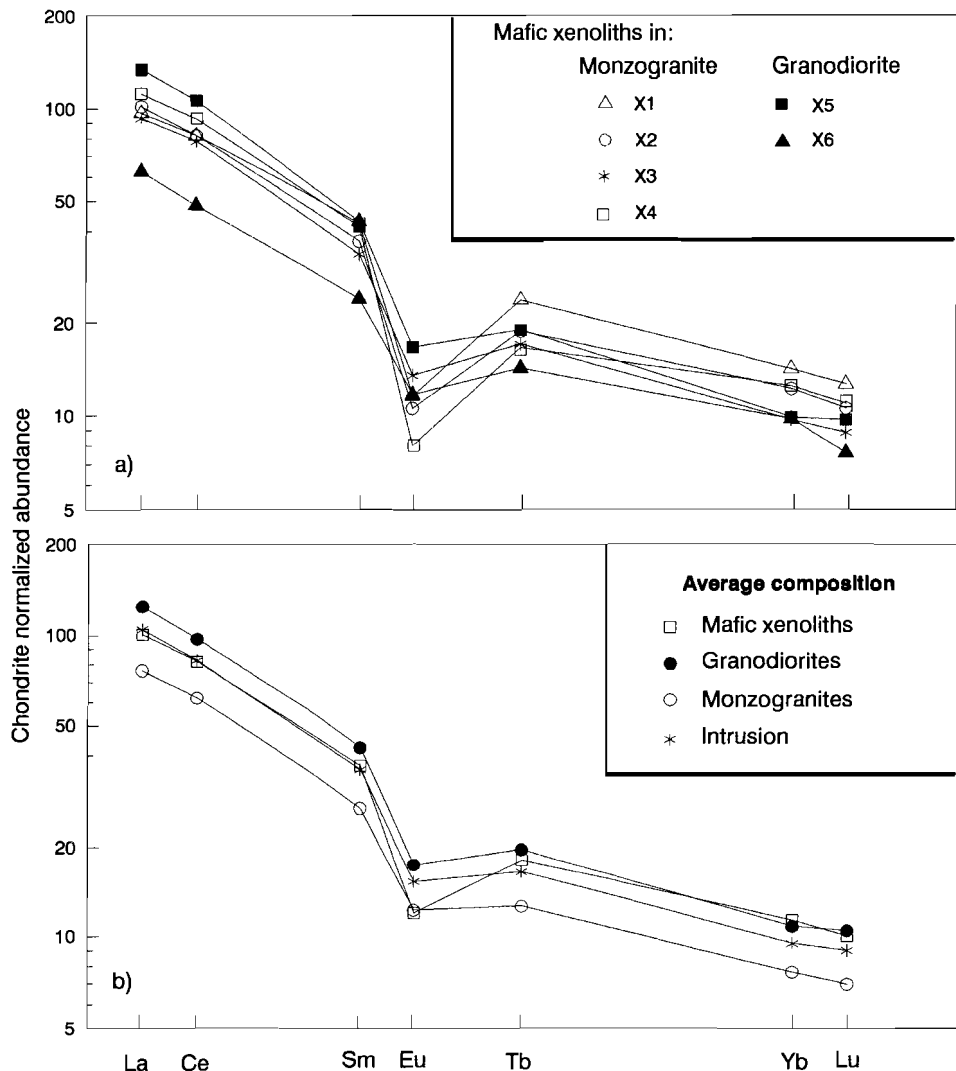


Fig.5. Chondrite normalized REE patterns of mafic xenoliths (a) and average chondrite normalized REE patterns of mafic xenoliths, granodiorites, monzogranites and of the entire intrusion (b).

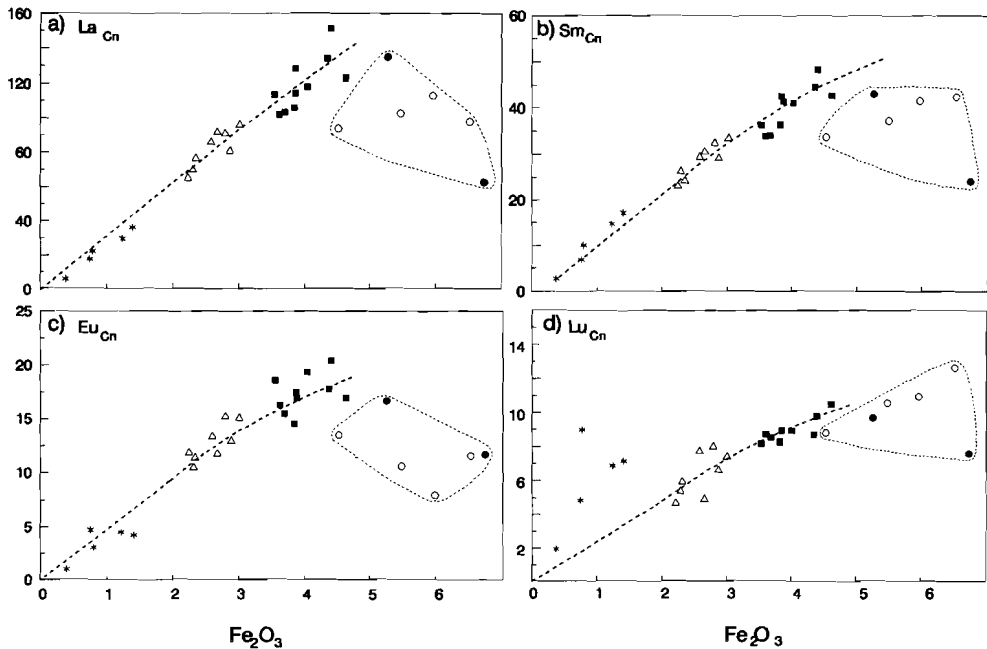


Fig.6. Trace element variation diagrams for chondrite normalized La, Sm, Eu and Lu versus Fe_2O_3 as differentiation index. Symbols are the same as used in Fig.2.

2.6 DISCUSSION.

The perfect linear relation between Fe_2O_3 and SiO_2 (Fig.2a) suggests that the magmatic xenoliths, the granodiorites, monzogranites and aplites belong to one genetic trend, which could be explained with mixing as well as magmatic differentiation. The linear relation of Fe_2O_3 with CaO (Fig.2b) passes through the origin of the plot, which implies that magma mixing is at most of minor importance to the geochemical variation. The common occurrence of magmatic mafic, microgranular xenoliths in the granodiorites was interpreted as evidence for mixing processes between anatetic crustal melt (monzogranites) and possibly mantle derived magmas of different composition (Rottura et al. 1989). In that case it is expected that the granodiorites would have intermediate compositions between the mafic xenoliths and the felsic monzogranites. The diagrams of TiO_2 with MgO (Fig.2c) and Fe_2O_3 with Zr , Hf and Th (Fig.3), and with REE (Fig.6) demonstrate that the granodiorites cannot be regarded as a mixing product, as they do not occupy the intermediate compositional field.

The curved relations of TiO_2 with MgO and of Fe_2O_3 with Th (Fig.3c), Sm_{Cn} , Eu_{Cn} and Lu_{Cn} (Fig.6b,c and d) are irreconcilable with magma mixing, which is marked by straight trends (Fourcade and Allegre 1981; Neiva et al. 1987). They rather favour magma fractionation for the granodiorite-aplite sequence. As crystallization proceeds, the phases which are solid solutions, e.g plagioclase, should change composition systematically, resulting in curved trends on variation diagrams (Price 1983).

The discussion above also forms an argument against the alternative possibility that the mafic xenoliths are a result of assimilation of pre-existing tonalitic rock.

The chondrite normalized REE-patterns of the magmatic xenoliths (Fig.5a,b) are practically identical in shape to those of granodiorites and monzogranites (Fig.4a, 5b), suggesting that these rocktypes are part of one fractionation sequence, in spite of the relatively low ΣREE of the xenoliths. The Eu content in the xenoliths from the monzogranites is similar to the Eu content of the monzogranites, and therefore the large Eu anomaly for these xenoliths is probably due to loss of Eu, resulting from reequilibration with the surrounding monzogranitic melt. Metasomatism in the xenoliths is evidenced by the albitisation of the zoned plagioclases. The hornfels xenoliths indicate stoping during the ascent of the granitic melt rather than assimilation of metasedimentary material, as reported for Portuguese monzogranites (Neiva 1981) as elements like Al_2O_3 , Fe_2O_3 and MgO , whose concentrations are high in the metasediments, do not exhibit any enrichment in the monzogranitic rocks (Table 1a,b).

Fractionation by crystal settling normally leads to changes in Eu-anomalies and La/Lu-ratios (Frey 1978, Henderson 1984). Only the aplites do display these changes, and as they are spatially related to cumulates like K-feldspar rich monzogranites, they may represent segregated residual products of fractionation by crystal settling in the latest crystallization phase of the monzogranites. The parallel shapes of the REE patterns in granodiorites and monzogranites are however irreconcilable with crystal settling and can be explained better with In Situ crystal fractionation,

The REE patterns of the samples 2 to 12, represented by closed circles in Fig.4a, reveal a compositional gap between granodiorites (solid lines) and monzogranites (dashed lines) along the profile, since granodiorite sample 6 and monzogranite sample 5 are located very close to each other. As the tungsten deposit of Los Santos is nearby, this gap could be related to a front of hydrothermal leaching. However, leaching cannot have been very important, as the monzogranitic samples near the deposit geochemically perfectly fall on the trends between granodiorites and intrusive aplites. Because rocks with those intermediate compositions are present, a few kilometres west of the profile (samples 13 to 20, open symbols), it is more likely that the compositional gap along the profile represents a local cryptic intrusive contact of segregated monzogranitic melt with the granodiorites.

Fractionation modelling

In Situ crystal fractionation is supported by the relative scarcity of both evolved and cumulate rocks, as continuous separation of crystals and liquids would have produced a highly zoned pluton, composed of early crystallized cumulates and later crystallized evolved rocks, with generally unzoned crystals (Michael 1984). The common occurrence of strongly zoned plagioclase, even in the most evolved monzogranites additionally supports In Situ crystal fractionation.

On the other hand, if the magma would entirely have crystallized In Situ, the intrusion itself should have been practically unzoned. The observed continuous range of geochemical and mineralogical compositions, in combination with their spatial distribution requires that during the predominantly In Situ crystallization, part of the intercumulus melt segregated dispersedly, and migrated very gradually towards the roof and the northwestern margin of the intrusion, locally developing rocks of monzogranitic composition.

In order to examine whether the monzogranites can represent mainly intercumulus melt, produced during In Situ crystallization of the granodiorites, the REE variations in the intrusion are modelled. The parental magma is assumed to be represented by the average composition of the intrusion, consisting of granodiorites and monzogranites at a ratio of 6:4. The xenoliths and aplites were not involved in the model because of their extreme compositions and their relatively small volume.

Usually the accessory phases like monazite, allanite, zircon and apatite host more than 95% of all REE (Gromet and Silver 1983). Kd-values for the REE in these minerals depend on melt composition (Mahood and Hildreth 1983, Nagasawa 1970). They are larger in acidic magmas than in mafic magmas (Nagasawa and Schnetzler 1971, Watson and Green 1981).

As the cooling of an intrusive magma is normally extremely slow, it is expected that the In Situ crystallizing phases will be in total equilibrium with the surrounding melt (Arth 1976), in which case application of the formula for equilibrium fractionation is most appropriate: $C_1/C_i = 1/[F + D_s(1-F)]$. The symbols are explained in table 2. The compositional zoning of the plagioclases however, argues for surface equilibrium between melt and solid, so that the trace element behaviour during crystallization should be described with the formula $C_1/C_0 = F^{(D_s-1)}$, applied to Raleigh fractionation.

The composition of the theoretical residual melt (C_1) is calculated for 60% crystallization, as this is the surface proportion of the granodiorites. The melt/solid distribution coefficients for each element are given in table 3. The mineralogical composition of the crystallizing material is assumed to correspond with the average normative composition of the granodiorites (Table 4).

Table 2. Symbols used in the equations for partial melting and fractional crystallization.

C_1	: composition of the residual melt
C_i	: composition of the initial melt
C_o	: composition of the source rocks
F'	: weight fraction of melt remaining
F	: fraction of melting
D_s	: bulk solid distribution coefficient $\sum_i^n X_i Kd_i$
X_i	: weight fraction of mineral i in the solid
Kd_i	: distribution coefficient of element n between mineral i and melt.
D_o	: bulk solid distribution coefficient for a given trace element based on the mineral composition of the parent at the onset of melting
P	: bulk distribution coefficient $\sum_i^n p_i Kd_i$ of the minerals that make up the melt
p_i	: normative fraction of mineral i in the melt

Table 3. Solid/melt distribution coefficients used for modelling of fractional crystallization and partial melting.

	Zircon	Apatite	Monazite	Plagioclase	K-feldspar	Garnet
La	-	-	10^4	-	-	0.39
Ce	0.31	29.6	10^4	0.35	0.044	0.62
Nd	0.55	57.1	$8 \cdot 10^3$	0.29	0.025	0.63
Sm	3.24	84.8	$3 \cdot 10^3$	0.15	0.018	2.2
Eu	1.57	9.22	$1 \cdot 10^3$	2.81	1.13	0.7
Tb	-	-	$1 \cdot 10^3$	-	-	-
Yb	890	232	200	0.07	0.012	43
Lu	1230	199	200	0.06	0.006	38

Kd-values for zircon and apatite are from Nagasawa (1970), for plagioclase and K-feldspar from Arth (1976), for monazite in granitic rocks from Condie (1978) and for garnet in dacitic rocks from Henderson (1984). Kd_{Nd} for monazite is a hypothetical value.

Table 4. Normative compositions and aluminosity of the granitic rocks, gneiss xenolith and low-grade metamorphic sediments.

Nr		Biot	An	Or	Ab	Q	Apat	Zircon	A/CNK
12	GD	16.3	14.1	13.1	28.4	27.3	0.61	0.044	1.05
9	GD	16.5	14.3	10.2	30.3	29.3	0.56	0.042	1.03
10	GD	15.8	14.5	16.0	28.1	24.6	0.58	0.045	1.01
7	GD	14.1	12.1	23.1	26.5	24.1	0.58	0.037	1.03
11	GD	14.0	12.9	18.2	27.6	26.2	0.65	0.043	1.04
6	GD	14.0	10.4	17.6	26.9	30.4	0.65	0.038	1.12
8	GD	13.7	11.8	17.4	27.6	29.5	0.58	0.039	1.08
19	GD	13.1	10.8	16.7	30.3	27.8	0.49	0.036	1.07
15	GD	12.9	10.9	17.5	27.4	31.4	0.49	0.037	1.08
16	GD	12.6	11.6	18.9	30.2	27.5	0.49	0.037	1.07
17	MG	10.9	8.9	18.3	29.2	31.6	0.63	0.031	1.13
3	MG	10.0	8.8	27.6	27.5	25.3	0.51	0.030	1.09
13	MG	10.0	9.4	23.4	29.5	26.7	0.56	0.030	1.10
18	MG	9.5	8.0	19.6	29.7	31.1	0.58	0.026	1.11
4	MG	8.3	7.3	23.3	30.3	29.6	0.68	0.023	1.11
2	MG	8.1	8.1	21.8	34.9	26.6	0.51	0.023	1.09
5	MG	8.1	7.7	23.8	29.4	29.4	0.56	0.023	1.09
20	MG	6.1	6.4	26.6	27.7	31.3	0.77	0.027	1.17
a1	aplite	4.8	3.9	21.4	31.8	36.1	0.40	0.014	1.16
a2	aplite	4.3	3.5	23.8	32.1	34.3	0.28	0.014	1.13
a3	aplite	2.4	3.2	27.7	31.3	32.9	0.45	0.008	1.17
a4	aplite	1.9	1.1	28.9	31.3	33.7	0.70	0.006	1.17
a5	aplite	1.0	2.8	32.1	29.2	32.7	0.07	0.007	1.20
X7	Gneiss	15.4	4.8	46.7	26.2	7.3	0.30	0.060	1.16
AVERAGES OF									
GRANITIC ROCKS		12.0	10.6	19.0	28.9	28.5	0.58	0.035	
GRANODIORITE		14.4	12.5	16.9	28.1	27.8	0.61	0.039	
SEDIMENTS		21.8	3.12	10.28	12.0	42.64	0.35	0.032	

Weight normative contents of biotite, anorthite, K-feldspar, albite, quartz, apatite and zircon for granodiorites (GD), monzogranites (MG), aplites and gneiss xenolith. A/CNK: molar ratio of $\text{Al}_2\text{O}_3/\text{CaO}+\text{Na}_2\text{O}+\text{K}_2\text{O}$. The average normative compositions of the granitic rocks, granodiorites, sediments and the gneiss composition are used for crystallization and partial melting modelling.

Model

Due to the difficulty to make correct estimates of the modal amount of monazite, in first instance the residual melt composition (C_1) was calculated assuming that no monazite crystallized, using both equilibrium and Raleigh fractionation models (Fig.7). For equilibrium crystallization C_1 for Eu, Yb and Lu agree reasonably well with their average abundance in the monzogranites (see solid line 4, Fig.7). The calculated concentrations of Ce, Nd and Sm are much too high. La abundance could not be modelled since Kd values for the minerals used are not available. The Raleigh fractionation model yields C_1 values which totally disagree with the actual monzogranite pattern (see dashed line 4, Fig.7).

Monazite has very large Kd's for La and Ce (10.000), for Sm (3000) and Eu (1.000) while its Kd for Yb and Lu is low (200 Condie 1978). For the equilibrium model it is calculated that less than 0.016 wt% of monazite is sufficient to compensate for the difference for Ce between the calculated and the real

concentrations in the monzogranites. The modelling is repeated with 0.016 wt% monazite, which leads to considerably improved results for the LREE and EU (see solid line 5, Fig.7). In the Raleigh fractionation model addition of monazite does not improve the results (Fig.7, dashed line 5). The similarity between predicted intercumulus melt (C_1) for 60% equilibrium crystallization, and average monzogranite composition demonstrates that, with the assumptions made, the monzogranites could be considered as intercumulus melt. The results of equilibrium fractionation model, especially for the HREE, which are independent of monazite addition, are much more in agreement with the analytical data than those of the Raleigh fractionation model. This is additional evidence that In Situ fractionation dominated the crystallization process for the accessory minerals.

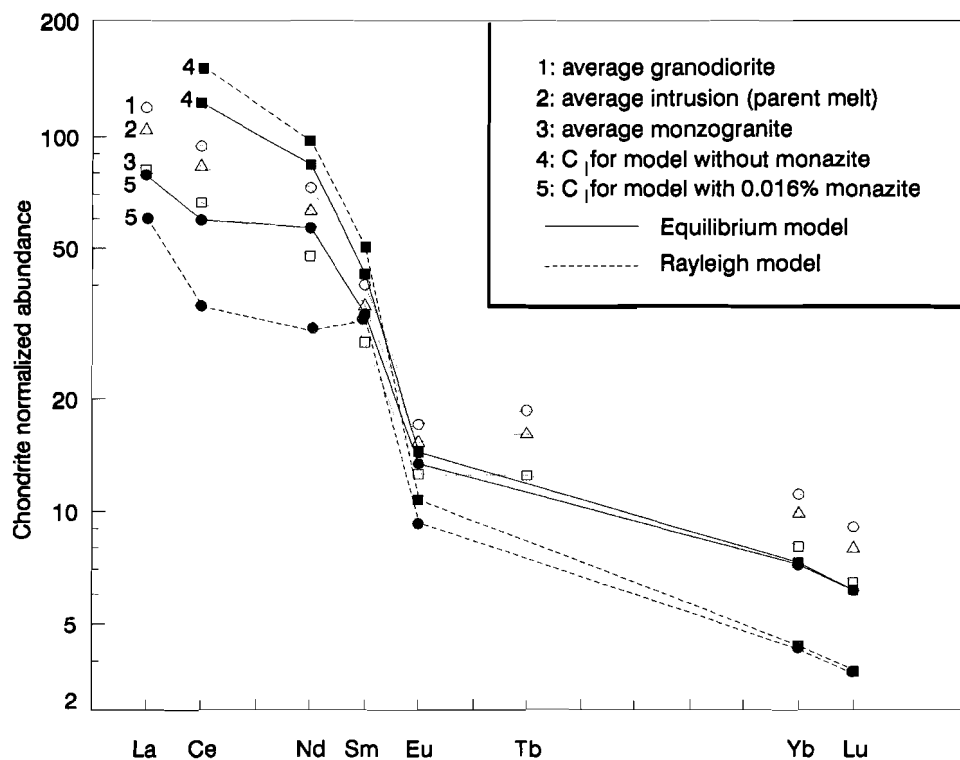


Fig.7. Chondrite normalized results of crystal fractionation modelling for Equilibrium model (solid lines and Rayleigh model (dashed lines) without monazite (lines 4) and with 0.016 wt% monazite (lines 5) in the crystallized solid.

Origin of the granitic magma

The REE patterns of this pluton are similar to those of other Iberian granodioritic and monzogranitic rocks (e.g. Neiva et al 1987) and are explained with partial melting of sedimentary source rock (de Albuquerque, 1978).

Two potential source rocks for the granodioritic magma, low grade metamorphic sediments and gneisses can be examined (Fig.1; Lorenc and Saavedra 1985, Ugidos 1985). Gneiss fragments are common as xenoliths. The REE-patterns of low grade and contact metamorphic sedimentary rocks, a hornfels and a gneiss xenolith are presented in figure 8a. The average sediment composition (Table 5, column a) is similar to that of a mixture of shales and greywackes at a ratio 1:2 (Wedepohl, 1969, Table 5 column c,d,e). The average REE-content resembles that of the North American Shale Composite (Haskin et al. 1968, Table 5, column b). The increase in REE content from low grade to contact metamorphic rock and hornfels xenolith suggests enrichment of REE during heating, perhaps as a result of removal of other elements.

Table 5. Average sediment compositions.

	<u>average</u>	<u>Haskin</u>	<u>Wedepohl</u>			
	a	b	c	d	e	
SiO ₂	64.4		50.7	66.7	58.7	61.4
TiO ₂	0.78		0.78	0.6	0.69	0.66
Al ₂ O ₃	19.2		15.1	13.5	14.3	14.0
Fe ₂ O ₃	7.0		6.7	5.5	6.1	5.9
MnO	0.09		0.08	0.1	0.09	0.1
MgO	2.74		3.3	2.1	2.7	2.5
CaO	0.63		7.2	2.5	4.8	4.06
Na ₂ O	1.43		0.8	2.9	1.9	2.2
K ₂ O	3.87		3.5	2.0	2.75	2.5
P ₂ O ₅	0.15		0.10	0.20	0.15	0.17
Zr	161		-	-		
La	38.6	32	-	-		
Ce	74.3	73	-	-		
Nd	33.7	33	-	-		
Sm	6.4	5.7	-	-		
Eu	1.32	1.24	-	-		
Tb	0.81	0.85	-	-		
Yb	2.4	3.1	-	-		
Lu	0.39	0.48	-	-		
Hf	4.67		-	-		

This study (a); North American Shale Composite (Haskin et al. 1968)(b); compositions of platform shales (c) and greywackes (d) (Wedepohl 1969) and mixtures of these schists and greywackes at ratio 1:1 (e) and 1:2 (f).

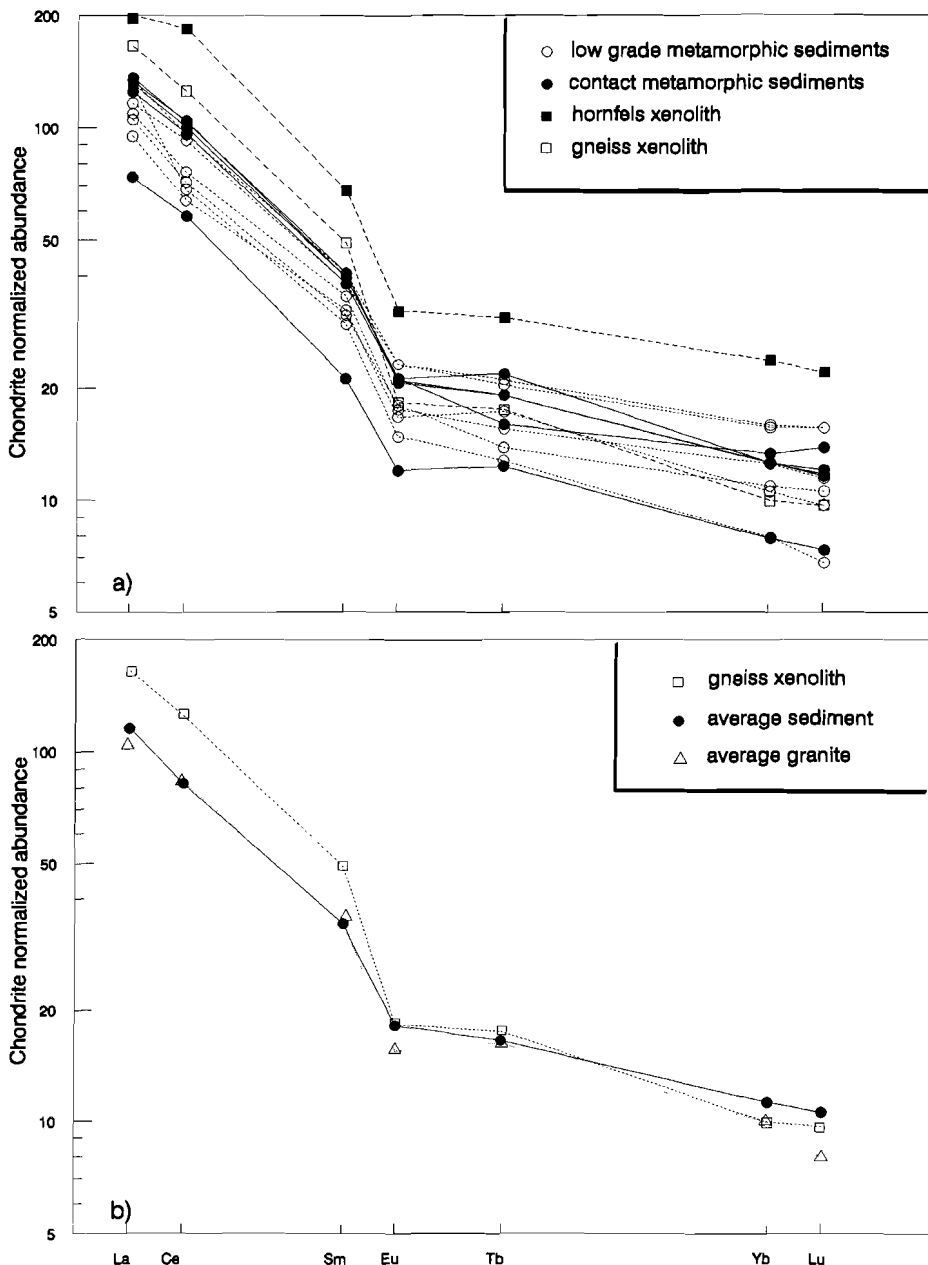


Fig.8. a: Chondrite normalized REE patterns of low grade metamorphic sediments (open circles), contact metamorphic samples (solid circles), hornfels xenolith (solid squares) and gneiss xenolith (open squares). b: Average chondrite normalized pattern of all meta samples, average pattern of the total intrusion, and pattern of the gneiss xenolith.

The average REE-patterns of the granodiorites and monzogranites and the sedimentary rocks are almost identical (Fig.8b), which is a reason to suppose that the intrusion is derived from the metasediments. The fact that the Eu-anomaly of the granitic intrusion is slightly larger than that of the sediments implies feldspar in the residual rock.

Compston and Chappel (1979) argue that 15-25% melting is an appropriate range for the generation of granitoid magmas. At more than 15% partial melting the melt is sufficiently mobile to move upwards away from its source region (van der Molen and Paterson 1979; Price 1983). The sedimentary rocks contain only 0.63 wt% CaO, which implies that partial melting of at most 30% is possible, if the liquid composition corresponds with the average of the intrusion. Therefore 15% and 30% partial melting is modelled.

The chemical composition of the residue at 15% and 30% melting of sedimentary source rocks is calculated (Table 6). At low pressure conditions this composition will produce a mineralogy consisting of quartz, K-feldspar + plagioclase, biotite, cordierite and andalusite /sillimanite. Along the southern boundary of the intrusion, granitic rocks grade into low pressure anatetic migmatites and gneisses that indeed consist of this mineralogy (Ugidos 1974, 1985). Apart from feldspar all these residual rockforming minerals have Kd-values for the REE much below unity (Henderson 1984; Arth 1976), which means that accessory phosphate-minerals and zircon determine the REE-distribution between melt and residual solid.

Table 6. Major element composition of residual solid after removal of 15% and 30% melt respectively.

	parent	melt	residue	
			15%	30%
SiO ₂	64.4	68.3	63.5	62.8
TiO ₂	0.78	0.59	0.81	0.86
Al ₂ O ₃	19.2	15.6	19.5	20.7
Fe ₂ O ₃	7.0	3.46	7.6	8.5
MnO	0.09	0.06	0.09	0.08
MgO	2.74	1.14	3.0	3.4
CaO	0.63	2.16	0.35	0.0
Na ₂ O	1.43	3.40	1.08	0.58
K ₂ O	3.87	4.55	3.69	3.56
P ₂ O ₅	0.15	0.25	0.13	0.11
Zr(ppm)	161	172	158	156
A'	0.113		0.138	0.146
F	0.025		0.033	0.028
M	0.069		0.085	0.075

The composition of the parent rocks is the average of the forty representative sediment samples. The melt composition is equal to the weighed average of the granodiorites and monzogranites. The composition of the residue after 15% and 30% melting are normalized to 100%. A'=Al₂O₃-(K₂O+Na₂O+CaO), F=FeO-(Fe₂O₃+TiO₂), M=MgO (Winkler 1979) and Fe⁺⁺/Fe_{tot}=0.6

Compared to crystal fractionation, modelling of partial melting is complicated by an additional number of uncertainties:

- 1) It is unknown which phosphate minerals were present in the sediment at the event of melting.
- 2) The dissolution kinetics for phosphate minerals and zircon and the behaviour of REE during anatexis are complex (Harrison and Watson 1984, Weber et al 1985, Rapp and Watson 1986)
- 3) During partial melting the partition coefficients for the REE may vary considerably (McCarthy and Kable, 1978);
- 4) The conditions under which partial melting occurred, the timing of separation of the melt from the residue and whether there was melt-solid equilibrium are not known.

With these uncertainties in mind an effort is made to relate the REE abundances of metasediments and granitic rocks. Therefore three main assumptions are made:

- I: All REE in the source rocks are hosted by plagioclase, K-feldspar, apatite, zircon and perhaps monazite.
- II: The Kd's are constant during the partial melting and are the same as used for fractional crystallization.
- III: Modelling is done for 15% and 30% equilibrium melting respectively and batch removal only took place after 15% or 30% melting.

In the batch melting model the trace elements in the melt and in the solid residue are in equilibrium until enough of the lower density melt accumulates so that it separates from the residual solids (Hanson 1978). The formula used for modelling equilibrium melting is: $C_1/C_o = 1/[(D_o \cdot PF) + F]$ (Hanson 1978). For explanation of the symbols see table 2. The theoretical melt composition C_1 , at 15% respectively 30% melting is listed in table 7. When monazite is assumed to be absent in the source rock, all REE abundances in the calculated melt are higher than those in the average granitic composition. It can be calculated that at most 0.0076 wt% of monazite would be needed in addition to the modal minerals, to match the computed Ce-concentration in the melt with that of the average granite. Modelling with 0.0076 wt% monazite yields correct results for La, Nd and Sm. However, calculated Eu, Yb and Lu concentrations are still too high. Assuming more monazite in the source rocks would not improve the results for the HREE, and neither would higher or lower degrees of partial melting. Consequently, under the assumed limiting conditions it will be hard to explain the granitic REE compositions with partial melting of the low grade metasedimentary rocks.

This remains surprising, just considering the strong similarity between the sedimentary REE patterns and that of the average intrusion. Perhaps melting conditions or the mineral assemblage were different than supposed in the partial melting model. Partial melting may have occurred at greater pressures, as garnet bearing metasediments occur further to the east along the contact (Fig.1b). Modelling with 1% garnet in the source rock improves the results for Tb and Lu, but still not for Eu (Table 7), which is probably related to the relatively low feldspar contents in the sedimentary source rock.

Gneiss xenoliths are much more abundant throughout the intrusion than metasedimentary xenoliths, which are mostly confined to the monzogranite, and therefore the gneiss may be a more suitable source

rock. Unfortunately only one gneiss xenolith was sampled. Assuming that this xenolith is representative for the gneiss source rock, partial melting was modelled in the same way as was done for the metasediments. 30wt% partial melting of a source rock without monazite yields good results for Eu, Yb and Lu, whereas calculated concentrations of Ce, Nd and Sm are much too high. However, at most 0.011wt% monazite in the source rocks would be needed to match the calculated melt composition with the average REE abundances in the granite intrusion. These results indicate that gneisses are more suitable as source rock for the granitic intrusion than the schists and greywackes of the Complejo Esquisto Grauvaquiquo.

Table 7. Calculated melt composition derived from low grade sedimentary and gneiss source rocks, by different degrees of partial melting and with varying proportions of monazite and garnet in the source rock.

LOW GRADE METASEDIMENTS				GNEISS XENOLITH				AVERAGE GRANITE COMPOSITION		
X_M	0	0.000076	0	0.00011						
X_G	0	0	0.0099	0	0	0	0			
%melt	15%	30%	15%	30%	15%	30%	15%	30%		
La	-	-	42.4	36.4	36.4	-	43.7	39.0	34.4	
Ce	262	182	71.2	63.6	63.2	320	234	76.2	70.1	73.2
Nd	104	82.4	36.1	33.1	32.9	148	120	42.7	40.0	37.8
Sm	16.7	14.1	10.4	9.40	9.16	23.4	19.8	12.9	11.4	6.40
Eu	2.55	2.86	2.20	2.45	2.42	0.91	0.95	0.85	0.88	1.06
Tb	-	-	-	-	-	-	-	-	0.76	
Yb	2.42	2.68	2.39	2.68	1.80	1.71	1.86	1.68	1.83	1.98
Lu	0.37	0.37	0.36	0.36	0.27	0.25	0.25	0.24	0.25	0.27

X_M is the weight fraction of monazite assumed in the source rock, X_G the weight fraction of garnet. %melt is the weight percentage of melting for which is modelled. The normative mineral contents used for modelling are listed in Table 5. The average composition of the intrusion is added for comparison.

2.7 CONCLUSIONS

- 1) The biotite-rich granodiorites, muscovite-bearing monzogranites, aplitic dikes and perhaps also the tonalitic xenoliths of the Western part of the Spanish Sistema Central are cogenetic.
- 2) Major element and REE variation in the granodiorites and monzogranites is more compatible with In Situ fractionation than with magma-mixing or fractionation by means of crystal settling.
- 3) REE-modelling demonstrates that the monzogranites have a composition similar to intercumulus melt

- after In Situ crystallization of approximately 60% of the parental magma.
- 4) Gradual disperse segregation of the intercumulus melt caused geochemical and mineralogical zoning of the intrusion, ranging from intercumulus depleted granodiorites in the core to intercumulus enriched monzogranites near the margins. Migration of the segregated melt caused local development of cryptic intrusive contacts with the granodiorites.
- 5) The REE-behaviour was mainly controlled by equilibrium crystallization of plagioclase, K-feldspar, apatite, zircon and monazite.
- 6) Petrogenetic modelling based on the abundance of the HREE yields more reliable results than on the basis of the LREE since the LREE preferentially fractionate into traces of monazite, of which the abundance cannot be determined accurately.
- 7) Modelling of partial melting demonstrates that gneiss, present as xenoliths in the intrusion, is a more suitable source rock than the metasediments of the Complejo Esquisto Grauvaquico.

2.8 REFERENCES

- Albuquerque de CAR (1978) Rare Earth Elements in Younger granites, Northern Portugal. *Lithos* 11; 219-229
- Aparicio Yagüe A, Bellido Mulas F, Brandle Matesanz JL, García Cacho L, Santos Serrano V (1983) Caracterización de los granitoides Hercinicos del sector centrooriental del Sistema Central Español. *Estud.Geol.* 39; 271-306
- Arth JG (1976) Behaviour of trace elements during magmatic processes- a summary of theoretical models and their applications. *J.Res.U.S.Geol.Survey* 4; 41-47
- Barr SM, Areias L (1980) Petrology and geochemistry of granitic intrusions in the Viana do Castelo area, northern Portugal. *Geol.Mijnb.* 59; 273-281
- Bea Barredo F (1982) Sobre el significado de la cordierita en los granitoides del Batolito de Ávila (Sistema Central Español). *Bol.Geol.Min.* 93; 59-67
- Bea Barredo F, Moreno-Ventas Bravo I (1985) Estudio petrologico del area centro-norte de la Sierra de Gredos (Batolito de Ávila; Sistema Central Español). *Stud.Geol.Salaman.* 20; 137-174
- Bea F, Sánchez González de Herrero JG, Serrano Pinto M (1988) Una compilación geoquímica (elementos mayores) para los granitoides del Macizo Hespérico. In: Bea F, Carnicer A, Gonzalo JC, López Plaza M, Rodríguez Alonso MD (eds.). *Geología de los granitoides y rocas asociadas del Macizo Hespérico*; 87-194
- Brandenburger E (1984) Les Granitoides Hercyniens tardifs de la Sierra de Guadarrama (Sistema Central, Espagne) Petrographie et Géochimie. *These 3^e cycle C.R.P.G. Vandoeuvre-lès-Nancy*, 209 pp.
- Burnham CW (1979) Importance of volatile constituents. In: Yoder S (ed.) *The evolution of igneous rocks*; 71-136

- Capdevila R, Corretge G, Floor P (1973) Les granitoïdes varisques de la Meseta Iberique. Bull.Soc.Géol. France 15; 209-228
- Carracedo M, Ortega Cuesta LA, Gil Ibarcuchi JI, Sánchez-Carretero R (1989) Aportación a la geoquímica de tierras raras (REE) en el batolito de Los Pedroches (Córdoba-España). Stud.Geol.Salmant. vol Esp.4; 93-104.
- Cerny P, Fryer BJ, Longstaffe FJ, Tammemagi HY (1987) The Archean Lac du Bonnet batholith: Igneous history, metamorphic effects, and fluid overprinting. Geochim.Cosmochim.Acta 51; 421-438
- Compston W, Chappel BW (1979) Sr-isotope evolution of granitoid source rocks. In: McElhinny MW (ed.) The Earth; its origin, structure and evolution; 377-426
- Condie KC (1978) Geochemistry of proterozoic granitic plutons from New Mexico, U.S.A. Chem.Geol. 21; 131-149
- Diez Balda MA (1982) El Complejo Esquisto-Grauvaquico, las series Paleozoicas y la estructura Hercinica al sur de Salamanca. Tesis Doctoral, Universidad de Salamanca
- Fourcade S, Allegre CJ 1981 Trace elements behaviour in granite genesis: a case study. The calc-alkaline plutonic association from the Querigut complex (Pyrenees, France). Contrib.Mineral.Petrol. 76: 177-195
- Frey AF, Chappel BW, Roy SD (1978) Fractionation of rare-earth elements in the Tuolumne intrusive series, Sierra Nevada batholith, California. Geology 6; 239-242
- Garcia-Casco A, Pascual E, Fenoll Hach-Ali P (1989) Petrogenesis del plutón monzogranítico peraluminoso de Santa Eufemia (Batuolito de Los Pedroches, Córdoba) Estud.Geol. 45; 3-20
- Goossens MA (1991) Integration of remote sensing data and ground data as an aid to exploration for granite related mineralization, Salamanca province, w-Spain. Eighth Thematic Conference on Geologic Remote Sensing, Denver, Colorado, USA.
- Gromet LP, Silver LT (1983) Rare earth distributions among minerals in a granodiorite and their petrogenetic implications. Geochim.Cosmochim.Acta 47; 925-939
- Guijarro J, Moreno A, Astudillo J, Gutiérrez A (1984) Estudio petrologico y geoquímico del plutón de Trujillo (Cáceres, España). Estud.Geol. 40; 3-14
- Hanson GN (1978) The application of trace elements to the petrogenesis of igneous rocks of granitic composition. Earth Planet.Sci.Lett. 38; 26-43
- Harrison TM, Watson EB (1984) The behaviour of apatite during crustal anatexis: Equilibrium and kinetic considerations. Geochim.Cosmochim.Acta 48; 1467-1477
- Haskin LA, Frey FA, Wildeman TR (1968) Relative and absolute terrestrial abundances of the rare earths. In: Ahrens LH (ed.) Origin and distribution of the elements. Int.Ser.Monogr.Earth Sci. 30; 889-912
- Henderson P (1984) General properties and abundances of the Rare Earth Elements. In: Henderson P (ed.), Rare Earth Element Geochemistry. Developments in Geochemistry. Elsevier.
- Julivert M, Fontbote JM, Ribeiro A, Conde L (1974) Mapa tectónico de la Península Ibérica y Baleares. Madrid IGME 113 p.

- Lorenc M, Saavedra J (1985) Estudio geológico ácido-básico y su entorno metamórfico en el área de Guijuelo-Bercimuelle (SE de Salamanca). *Bol.Geol.Min.* 96; 62-73
- Mahood G, Hildreth W (1983) Large partition coefficients for trace elements in high-silica rhyolites. *Geochim.Cosmochim.Acta* 47; 11-30
- McCarthy TS, Kable EJD (1978) On the behaviour of rare-earth elements during partial melting of granitic rock. *Chem.GeoL.* 22; 21-29
- Michael PJ (1984) Chemical differentiation of the Cordillera Paine granite (southern Chile) by in situ fractional crystallization. *Contrib.Mineral.Petrol.* 87; 179-195
- Miller CF, Watson EB, Harrison TM (1988) Perspectives on the source, segregation and transport of granitoid magmas. *Trans.R.Soc.Edinburg: Earth Sciences* 79; 135-156
- Molen I van der, Paterson MS (1979) Experimental deformation of partially melted granite. *Contrib.Mineral.Petrol.* 70; 299-318
- Nagasawa H (1970) Rare earth concentrations in zircons and apatites and their host dacites and granites. *Earth Planet.Sci.Lett.* 9; 359-364
- Nagasawa H, Schnetzler CC (1971) Partitioning of rare earth, alkali and alkaline earth elements between phenocrysts and acidic igneous magma. *Geochim.Cosmochim.Acta* 35; 953-968.
- Neiva AMR (1981) Geochemistry of hybrid granitoid rocks and their biotites from central northern Portugal and their petrogenesis. *Lithos* 14; 149-163
- Neiva AMR, Neiva JMC, Parry S (1987) Geochemistry of the granitic rocks and their minerals from Serra da Estrela, Central Portugal. *Geochim.Cosmochim.Acta* 51; 439-454
- Pratt JH (1894) Am J Sci.; 149
- Price RC (1983) Geochemistry of a peraluminous granitoid suite from North-eastern Victoria, South-eastern Australia. *Cosmochim.Geochim.Acta* 47; 31-42
- Rapp RP, Watson EB (1986) Monazite solubility and dissolution kinetics: implications for the thorium and light rare earth chemistry of felsic magmas. *Contrib.Mineral.Petrol.* 94; 304-316
- Rottura A, Bargossi GM, Caironi V, D'Amico C, Maccarone E (1989) Petrology and Geochemistry of late-hercynian granites from the Western Central System of the Iberian Massif. *Eur.J.Mineral.* 1; 667-683
- Saavedra Alonso J, Garcia Sanchez A (1974) Estudio geoquímico de algunos granitos de la provincia de Salamanca. *Bol.Geol.Min.* 85; 182-192
- Shaw HR (1965) Comments on viscosity, crystal settling and convection in granitic magmas. *Am.J.Sci.* 263; 120-152
- Simmons WB, Lee MT, Brewster RH (1987) Geochemistry and evolution of the South Platte granite-pegmatite system, Jefferson County, Colorado. *Geochim.Cosmochim.Acta* 51; 455-471
- Tindle AG, Pearce JA (1981) Petrogenetic modelling of in situ fractional crystallization in the zoned Loch Doon Pluton, Scotland. *Contrib.Mineral.Petrol.* 78; 196-207
- Ugidos JM (1974) Metasomatismo y granitización en el complejo metamórfico de Bejar-Barco de Avila-Plasencia. Petrogenesis de los granitos de tendencia alcalina. *Studia Geol.* 8; 27-44

- (1983) Sobre el significado de la cordierita en los granitos calcoalcalinos del Batolito de Avila (Sistema Central Español) Bol.Geol.Min. 94; 63-68
 - (1985) Características del metamorfismo de baja presión en zonas centro-occidentales españolas en relación con minerales aluminicos en los granitos. IX Reunao de geología do oeste Peninsular, Porto, Portugal.
- Ugidos JM, Bea F (1976) Análisis comparativo de los granitos del área Bejar-Plasencia con otros granitos "Younger" centro peninsulares; Precisiones sobre la Serie Mixta. Studia Geol. 10; 45-59
- Watson EB, Green TH (1981) Apatite/liquid partition coefficients for the rare earth elements and strontium. Earth Planet.Sci.Lett. 56; 405-421
- Weber C, Barbey P, Cuney M, Martin H (1985) Trace element behaviour during migmatization. Evidence for a complex melt-residuum-fluid interaction in the St.Malo migmatitic dome (France). Contrib.Mineral.Petrol. 90; 52-62
- Wedepohl KH (1969) Composition and abundance of common sedimentary rocks. Handbook of Geochemistry I; 250-271. Springer Verlag, New York
- Winkler HGF 1979 Petrogenesis of metamorphic rocks. Springer verlag, New York. 345pp

CHAPTER 3

THE RELATION BETWEEN BIOTITE COMPOSITION AND MAGMATIC DIFFERENTIATION IN THE PERALUMINOUS GRANODIORITE SEQUENCE OF LOS SANTOS, WESTERN CENTRAL SPAIN.

3.1 ABSTRACT

A Hercynian ilmenite bearing peraluminous granitic intrusion and its biotites are studied. The intrusion is zoned and consists of granodiorites in its centre, to muscovite-cordierite-bearing monzogranites and aplites near the intrusive contact with the metasediments of the Precambrian Complejo Esquisto Grauvaquico. The most felsic rocks occur near the village of Los Santos, adjacent to a large tungsten skarn. The granodiorite-monzogranite-aplite sequence is characterized by gradual changes in whole rock and biotite composition. The entire sequence is cogenetic. With DI increasing from 64 to 93, FeO in biotites decreases from 23 wt% to 19.5 wt%, MgO from 9 wt% to 7 wt%, TiO₂ from 4.1 wt% to 3.2 wt%, while Al₂O₃ increases from 15.5 wt% to 20 wt% and F from 0.25 wt% to 0.9 wt%. The ratio of Al₂O₃/(FeO + MgO + TiO₂) increases from 0.44 to 0.65. Fe²⁺/Fe_{total} in the biotites increases from 0.83 to 0.94 and Fe²⁺/Fe²⁺ + Mg from 0.54 to 0.60. Progressive Al-substitution at the expense of Fe and Mg is characteristic for the biotites of the granodiorite-aplite sequence. The Al-content of the biotites was buffered by the aluminosity of the melt, which increased with the degree of differentiation. The TiO₂-content of the biotites decreases with DI as a result of cooling of the magma during crystallization. During differentiation the temperature of the melt dropped from about 705°C to approximately 665°C while Log(fH₂O/fHF) decreases from 4.35 to 3.83. In the monzogranites and aplites, the biotites and muscovites are not in equilibrium. The biotite compositions in the monzogranites adjacent to the Los Santos skarn were generally unmodified by hydrothermal processes, and therefore the strong whole rock zoning in this part of the intrusion is mainly attributed to magmatic differentiation, and not to hydrothermal alteration during the formation of the skarn. Because the composition of the biotites is a function of the conditions that prevail during crystallization of the magma, the ratio of Al₂O₃/(FeO + MgO + TiO₂) in unaltered biotites is proposed as a differentiation index for peraluminous granitic rocks, in addition to the existing whole rock differentiation indices.

3.2 INTRODUCTION

The peraluminous granodiorite-monzogranite sequence near Los Santos is part of the Spanish Sistema Central (CSB, Rottura et al. 1989), a syn- to late-tectonic (Oen Ing Soen 1970; Priem et al. 1970; Capdevila et al. 1973) Hercynian granite complex which is, like many Iberian granites of the same period, associated with mineralization of tungsten and tin. The skarn of Los Santos is the largest known tungsten deposit related to the CSB, and is located at the intrusive contact (Fig.1) with pelitic metasediments and marbles of the Complejo Esquisto Grauvaquico (CEG). Saavedra et al. (1974) have recognized a regional chemical zoning in the batholith. Rottura et al. (1989) report porphyritic biotite

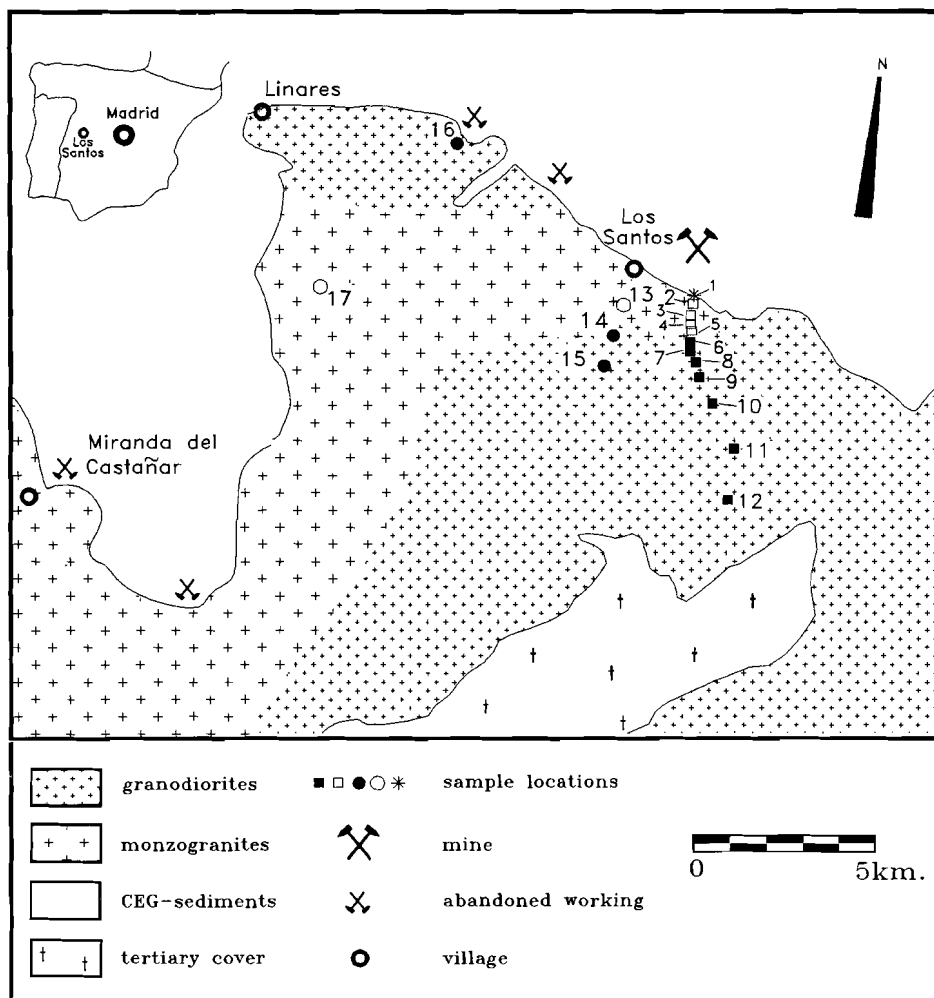


Fig.1. Simplified geological map showing granodiorites and monzogranites. Solid sample markers correspond with granodiorites, open ones with monzogranites. Sample 1 (asterisk) represents aplitic monzogranite (see text). The samples 2 to 12 are indicated with squares, samples 13 to 17 with circles. The large mine symbol corresponds with the Los Santos deposit.

monzogranites-granodiorites (BG) and argue for distinction of muscovite \pm cordierite monzogranites (MCG) in the westernmost part of the intrusion. These authors suggest that the monzogranites cannot be easily interpreted either as differentiates of the dominant granodiorites, or as a result of different

degrees of partial melting of one source, but are more likely to be a result of mixing of two different magmas. Eighty chemical whole rock analyses, part of our own work, reveal a complex zoning, which is illustrated by the distribution of Zr as a representative example (Fig. 2).

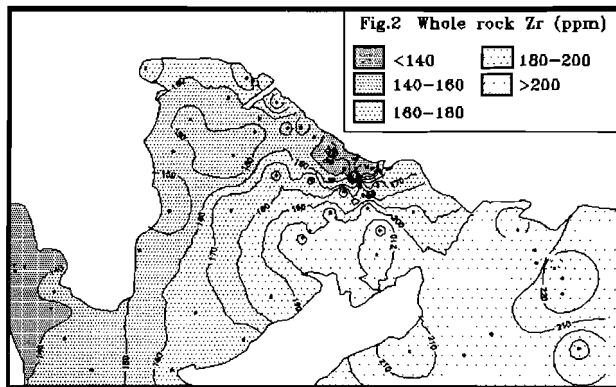


Fig.2. Distribution map of Zr (ppm) in the granitic rocks. Sample locations are indicated with small dots.

A pronounced regional zoning in the granodiorites and a local concentric zoning in the monzogranites around the skarn deposit are observed. Whole-rock major element and REE modelling has demonstrated that the granodiorite-monzogranite-aplite sequence is cogenetic and probably a result of mainly In Situ crystal fractionation (CHAPTER 2). Gradual segregation of intercumulus melt caused the main differentiation between granodiorites and monzogranites. Leaching of the granitic rocks by hydrothermal fluids that formed the tungsten deposit could, however, not be ruled out as an additional cause for the local zoning around the Los Santos deposit. Discrimination between various, often interrelated, magmatic and hydrothermal processes based on whole rock chemistry is complicated, because the minerals that form the granitic rocks are often zoned, and each individual phase will be affected in a different way by magmatic processes, fluid interaction, alteration etc. The composition of micas and particularly that of biotites is very sensitive to magmatic (Speer 1984; Leake 1974; Barriere and Cotten 1979) and hydrothermal (Speer 1984; Konings et al. 1988; Moore and Czamanske 1973; Jacobs and Parry 1979) processes because it is restricted by conditions such as pressure and temperature (Jacobs and Parry 1979; Dymek 1983; Ahlin 1988), melt composition (Puziewicz and Johannes 1988, 1990; De Albuquerque 1973; Mahmood 1983; Rossi and Chevremont 1987), oxygen fugacity (Wones and Eugster 1965; Speer 1984) and composition of the coexisting fluids (Muñoz 1984; Parry and Jacobs 1975; Gunow et al. 1980). This paper focusses on the compositional relationship between the whole rock and its magmatic biotites in order to:) determine more accurately the

magmatic conditions during the In Situ fractionation of the batholith; 2) examine whether the local zoning adjacent to the Los Santos skarn is a result of hydrothermal activity; and 3) to examine the interrelation between whole rock composition and biotite chemistry during magmatic differentiation.

3.3 SAMPLING AND ANALYSES

Seventeen granitic samples out of the original eighty were selected for detailed study of whole rock- and biotite major element composition. Samples 1 to 12 are located along a cross-section from the Los Santos mine towards the south east, perpendicular to the chemical zonation (Fig. 1), in such a way that they provide optimal information about the transition from BG and MCG. Because along the profile the transition from granodiorites to monzogranites turned out to be rather abrupt, samples 13 to 17 were collected away from the profile where the transition is more gradual. All samples represent normal medium grained granitic rock except sample 1, which is a fine grained aplitic monzogranite, located at the direct contact with the metasediments near Los Santos. Samples 87, 86, 67, 78, 32 and 31 are from aplites in vicinity of the Los Santos skarn.

Each sample consists of ten chips of about 100 gram each, that were collected on a surface of at least two square metres. Thin sections were made of one chip of each sample. Whole-rock major element composition was determined in lithium metaborate glass beads with a Philips PW-1400 XRF. The precision is better than 5% for Na_2O , K_2O and MnO analyses and better than 2% for the other major elements. Whole rock lithium concentration was determined with a Perkin Elmer PE-460 atomic absorption spectrometer, with a precision better than 10%. Microprobe analyses of the biotites were made with a JEOL 8600 Superprobe at the department of geochemistry of the University of Utrecht. Biotite concentrates were prepared with a Frantz magnetic separator and purified to >95% under a binocular. The lithium content in biotite concentrates was determined with an ICP-AES ARL-34000. FeO-contents in the whole rock and biotite concentrates were analyzed following the procedure of Pratt (1894), with a precision better than 5%.

3.4 GEOCHEMICAL AND PETROLOGICAL RESULTS.

The intrusive body consists of rocks ranging from biotite-rich granodiorites in the centre to biotite + muscovite + cordierite monzogranites near the northwest contact with the CEG. Within this granitic complex no evident intrusive relationships exist, except for aplitic dikes. Geochemically the variation from granodiorites to aplites is very gradual (Table 1). In this sequence the contents of TiO_2 , Fe_2O_3 , MgO and CaO systematically decrease while SiO_2 increases. The aluminosity, defined as the molar ratio of $\text{Al}_2\text{O}_3/(\text{CaO} + \text{Na}_2\text{O} + \text{K}_2\text{O})$ (Clarke 1981), varies between 1.00 and 1.08 in the granodiorites (except sample 6), between 1.09 and 1.13 in the monzogranites and between 1.11 and 1.21 in the aplites. X_{Mg} , defined as the molar ratio of $\text{Mg}/(\text{Fe}_{\text{total}} + \text{Mg})$ is constant for the entire intrusion. $\text{Fe}^{+++}/\text{Fe}_{\text{total}}$ varies between 0.01 and 0.20. The normative feldspar and quartz composition is calculated after correction for the amount of SiO_2 , K_2O , Na_2O and Al_2O_3 hosted in biotite (Table 2).

Table 1. Major element compositions of granodiorites, monzogranites and aplites.

Nr	GRANODIORITES										MONZOGRANITES							APLITES						
	10	12	11	7	9	8	6	16	14	15	3	13	2	17	5	4	1	31*	32	87*	67*	86*	78	
SiO ₂	64.6	65.4	66.0	66.0	67.8	68.2	68.3	68.7	69.3	69.5	68.3	68.8	70.1	70.3	70.4	70.7	74.9	74.0	74.4	74.4	74.7	75.0		
TiO ₂	0.82	0.79	0.87	0.72	0.85	0.64	0.71	0.54	0.51	0.58	0.43	0.45	0.34	0.49	0.37	0.33	0.2	0.07	0.05	0.16	0.13	0.21	0.07	
Al ₂ O ₃	15.4	15.5	15.5	15.8	15.3	15.4	16.0	16.1	15.6	15.1	16.0	16.0	15.9	15.3	15.0	15.2	14.9	14.29	14.8	13.73	14.74	14.0	14.59	
Fe ₂ O ₃	4.41	4.37	3.87	4.04	4.64	3.85	3.87	3.55	3.17	3.64	2.81	2.88	2.25	3.03	2.34	2.31	1.12	0.5	0.42	1.23	0.75	1.42	0.79	
MnO	0.07	0.08	0.06	0.07	0.07	0.06	0.06	0.07	0.06	0.07	0.06	0.06	0.05	0.07	0.06	0.06	0.04	0.05	0.01	0.04	0.06	0.04	0.01	
MgO	1.44	1.58	1.3	1.23	1.49	1.24	1.30	1.14	1.14	1.15	0.91	0.98	0.75	1.0	0.71	0.76	0.41	0.09	0.14	0.39	0.17	0.4	0.06	
CaO	2.93	2.83	2.61	2.44	2.89	2.37	2.1	2.34	2.16	2.21	1.77	1.89	1.64	1.8	1.55	1.47	1.11	0.47	0.46	0.7	0.64	0.78	0.23	
Na ₂ O	3.33	3.36	3.26	3.05	3.59	3.26	3.19	3.57	3.57	3.24	3.25	3.49	4.13	3.46	3.49	3.58	3.9	3.95	2.79	3.8	3.7	3.76	3.7	
K ₂ O	4.27	3.82	4.46	5.31	3.53	4.3	4.85	4.45	4.54	4.24	5.65	5.0	4.84	4.19	4.83	4.75	4.36	4.75	6.5	4.45	4.93	4.1	5.09	
P ₂ O ₅	0.26	0.24	0.25	0.28	0.25	0.25	0.28	0.21	0.25	0.21	0.22	0.24	0.29	0.27	0.22	0.24	0.17	0.18	0.37	0.12	0.19	0.17	0.3	
Li(ppm)	56	51	72	72	82	85	145	n.a	n.a	n.a	132	115	216	n.a	153	169	133	n.a	n.a	n.a	n.a	n.a	n.a	
total	97.5	98.0	98.0	98.9	100.3	99.6	100.7	100.6	100.3	99.91	99.5	98.6	100.1	99.8	99.0	99.6	101.1	98.4	99.5	99.0	99.7	99.6	99.8	
Fe*	0.09	0.12	0.01	0.09	0.07	0.15	0.19	n.a	n.a	n.a	0.08	0.20	n.a	n.a	0.12	n.a	n.a	n.a	n.a	n.a	n.a	n.a	n.a	
X _{Mg}	0.40	0.44	0.40	0.38	0.40	0.39	0.40	0.39	0.42	0.39	0.39	0.40	0.40	0.41	0.39	0.40	0.44	0.26	0.4	0.39	0.31	0.36	0.13	
A/CNK	1.00	1.05	1.04	1.03	1.03	1.08	1.16	1.07	1.06	1.08	1.09	1.10	1.09	1.13	1.09	1.11	1.13	1.14	1.19	1.11	1.17	1.16	1.21	

Total Fe as Fe₂O₃. Fe*: Fe⁺⁺⁺/Fe_{total}. X_{Mg}: molar ratio of Mg/(Fe+Mg)

A/CNK: molar ratio of Al₂O₃/(CaO+Na₂O+K₂O). n.a.= not analyzed.

All aplites contain muscovite; those marked with * additionally contain biotite.

Table 2. Weight normative compositions of granodiorites, monzogranites and aplites.

Nr	Q	Or	Ab	An	Bi	Mt	An%*	probe max	An% min
GRANODIORITES									
10	23.5	14.7	28.0	12.1	18.3	39.4	30	32.6	31.8
12	25.5	12.4	28.2	13.4	18.6	54.7	32	43.7	31.0
11	24.6	17.2	27.4	12.1	15.7	10.5	31	49.3	31.5
7	23.4	21.5	25.6	10.7	17.8	27.2	29	45.7	22.1
9	27.9	10.6	30.5	12.2	18.2	2.5	30	35.2	31.3
6	26.9	19.7	26.7	10.4	15.6	12.2	28	33.9	21.5
8	28.1	16.5	27.4	11.7	15.5	3.7	30	34.5	32.9
16	25.5	17.7	30.2	11.6	15.0	3.8	28	57.6	12.6
15	30.2	16.5	27.4	10.9	15.0	1.3	28	42.2	20.6
14	26.1	19.8	30.0	10.3	13.6	2.1	26	26.4	17.7
MONZOGRANITES									
3	24.6	26.1	27.1	8.7	12.4	1.1	24	46.9	17.3
13	25.6	22.6	29.2	9.3	12.5	4.3	24	27.3	22.9
2	25.6	20.9	34.7	8.1	9.5	4.2	19	14.6	12.3
17	32.5	15.6	29.2	8.9	13.7	4.1	23	49.3	8.6
5	28.5	22.4	29.2	7.7	10.6	34.1	21	38.9	23.3
4	28.6	22.2	29.9	7.2	10.0	n.d.	19	28.2	6.3
1	32.8	22.6	32.6	5.4	5.0	12.0	14	13.9	12.9
APLITES									
87	34.3	23.8	32.1	3.5	4.3	2.7	9	n.d.	n.d.
86	36.1	21.4	31.7	3.4	4.8	<0.2	10	n.d.	n.d.
67	33.0	27.7	31.3	3.2	2.4	2.4	9	(10.6)	
31	32.1	27.2	33.4	2.3	1.5	4.9	7	(4.3)	
78	33.8	28.9	31.2	1.1	1.9	1.3	4	n.d.	n.d.
32	32.1	37.6	23.6	2.3	1.5	4.4	9	n.d.	n.d.

Biotite contents are the averages of the respective amounts in table 5. Normative compositions of quartz and feldspars are calculated after correcting the whole rock compositions for SiO₂, K₂O and Na₂O hosted by biotite. Magnetite (ppm) is determined by separating as much as possible from the crushed sample using a hand magnet. An* is An/Ab+An *100%. The minimum and maximum An-percentages of zoned plagioclases are calculated on the basis of electron microprobe analyses. For aplites 67 and 31 only one analysis was available. n.d.: not determined. Aplite samples 87, 86, 67 and 31 are muscovite-biotite bearing and 78 and 32 muscovite bearing.

The correction is necessary since in sample 12, for example, 54 wt% of all potassium is hosted by biotites, but in sample 1 only 9.6wt%. Misleading effects caused by non-uniform distribution of biotite are thus eliminated. The normative abundance of biotite is determined, assuming that all TiO₂, MgO and FeO is hosted by the biotites, by calculating [X]_{whole rock}/[X]_{biotite} (Table 7), where [X] is the concentration of TiO₂, MgO and FeO respectively in the whole rock (Table 1) and biotites (Table 5). The amount of magnetite is determined semi-quantitatively, by separating as much as possible of this mineral from the crushed sample with a magnet. Normative feldspar and quartz are considered more accurate than the modal determinations of these minerals (Table 3). This is partly due to the fact that point counting was carried out mainly to determine the amounts of muscovite, biotite, cordierite and chlorite, while determination of K-feldspar and plagioclase was not very accurate, since they look

Table 3. Modal mineral composition of granodiorites, monzogranites and aplites, determined by point counting.

Sample nr	GRANODIORITES						MONZOGRANITES					
	12	11	10	9	8	7	6	14	13	5	4	3
Quartz	15	12	19	31	35	31	32	32	32	29	29	26
Plagioclase	50	45	36	37	32	32	36	36	27	28	28	31
K-feldspar	15	23	26	14	17	17	17	17	28	28	31	26
Muscovite	0	0	0	0	0	0	1.7	1.5	1.3	0.9	1.9	2.1
Biotite	19	17	18	18	15	18	13	12.1	12	9	13	7
Cordierite	0	0	0	0	0	0	0	1	1	1	1.2	0.5
Chlorite	1.2	2.5	0.4	0.2	1	0.3	0.9	0.3	0	0	0.1	0.2
Ilmenite	a	a	a	a	a	a	a	a	a	a	a	a
Apatite	a	a	a	a	a	a	a	a	a	a	a	a
Zircon	a	a	a	a	a	a	a	a	a	a	a	a
Monazite	a	a	a	a	a	a	a	a	a	a	a	a
Tourmaline	0	0	0	0	0	0	0	0	0	0	0	0

APLITES						
87	86	78	67	32	31	
Quartz	33	39	32	33	32	33
Plagioclase	18	23	22	19	16	23
K-feldspar	39	31	38	37	40	34
Muscovite	4.4	2.3	1.1	4.7	3.5	6.6
Biotite	3.7	4.1	0	1	0	a
Cordierite	0.7	0.8	0	1.8	0	0.5
Chlorite	1.3	0.8	0	1.7	0	0.8
Ilmenite	a	a	a	a	a	a
Apatite	a	a	a	a	a	a
Zircon	a	a	a	a	a	a
Monazite	a	a	a	a	a	a
Tourmaline	0	0	7.6	0.9	8.3	2.1

For each thin section between 4000 and 5000 points were counted, with a density of 7 counts per mm.
a=accessory mineral

similar under the microscope.

The granodiorites are a crystal mush with variable amounts of biotite and zoned euhedral Ca-rich plagioclase (see Table 2) with interstitial quartz, plagioclase and perthitic K-feldspar. Small euhedral, very early biotites are included in large, zoned plagioclase crystals and the synchronous crystallization of plagioclase and biotite is obvious in the granodiorites. The granodiorites contain between 23.4 and 30.2wt% normative quartz, between 10.6 and 21.5wt% orthoclase, between 25.6 and 30.5wt% albite, between 10.3 and 13.4wt% anorthite and between 13.6 and 18.6wt% biotite. Ilmenite is the dominant oxide mineral in all samples, but small amounts of magnetite (1-55ppm) are also present (Table 2). Some muscovite is observed in samples 14 and 6 (Table 3). The biotites of sample 11 are slightly chloritized. In the other samples chlorite is a very minor constituent (Table 3).

The monzogranite samples contain between: 24.6 and 32.8wt% normative quartz, 15.6 and 26.1wt% orthoclase, 27.1 and 34.6wt% albite, 5.4 and 13.7wt% anorthite, 5.0 and 13.7wt% biotite and 0.9 and 3.4wt% modal muscovite. The plagioclases of the monzogranite contain calcic cores up to An₄₃, but are in general more albitic than in the granodiorites. Zoned K-feldspar phenocrysts with compositions between Or₈₆₋₉₇ Ab₁₄₋₃, are common (Table 4). Their abundance increases towards the contact, where they occasionally display a cumulate texture, locally oriented in small scale circular patterns. Muscovite

is developed as: 1) a euhedral coarse grained magmatic phase , 2) a finer grained hydrothermal phase along cracks in feldspars and 3) a fine grained sericitic generation replacing feldspars (Rottura et al 1989). The amount of cordierite is usually less than 2 vol%. A xenocrystic origin for the cordierites is inferred by Ugidos (1983, 1985), but available textural and chemical data favour a magmatic origin (Rottura et al. 1989; Bea 1982). The majority of the cordierite is altered into green prisms of chlorite-pennine intergrowths. The monzogranites are dominantly ilmenite bearing, with even smaller amounts of magnetite (34-1.1ppm) than the granodiorites.

The aplites are divided in biotite+ muscovite (samples 87, 86, 67 and 31) and muscovite bearing (samples 78 and 32) rocks. Cordierite is common in most aplites. In some aplites tourmaline is a major constituent. Magnetite is a trace constituent. Sericitisation and kaolinitisation of feldspars is subordinate in granodiorites and monzogranites, but more substantial in the aplites.

Table 4. Representative electron microprobe analyses of minerals that coexist with biotites in the granodiorites, monzogranites and aplites.

	Plagioclase				K-feldspar			Muscovite	
	(1 ^c)	(2 ^r)	(3 ^c)	(4 ^r)	(5)	(6)	(7)	(8)	(9)
SiO ₂	56.11	60.32	57.64	61.46	64.43	63.84	45.03	46.17	45.63
TiO ₂	0.00	0.00	0.00	0.00	0.04	0.00	0.18	0.65	1.3
Al ₂ O ₃	27.58	25.14	26.37	23.63	19.01	18.61	32.52	35.98	35.71
FeO	0.00	0.16	0.00	0.15	0.00	0.00	3.06	1.20	1.43
MnO	0.00	0.00	0.00	0.00	0.00	0.00	0.00	0.00	0.00
MgO	0.00	0.00	0.00	0.00	0.00	0.00	2.09	0.91	0.78
CaO	9.23	6.57	8.33	5.01	0.00	0.00	0.11	0.13	0.00
BaO	0.00	0.00	0.00	0.00	0.31	0.37	0.00	0.07	0.00
K ₂ O	0.16	0.28	0.23	0.24	16.46	14.56	10.84	10.52	10.55
Na ₂ O	6.41	8.01	7.23	9.12	0.34	1.60	0.20	0.42	0.55
P ₂ O ₅	0.00	0.00	0.00	0.00	0.00	0.00	0.00	0.00	0.00
Cl	0.00	0.00	0.00	0.00	0.00	0.00	0.04	0.00	0.00
F	0.00	0.00	0.00	0.00	0.00	0.00	0.33	0.00	0.23
Total	99.49	100.5	100.0	99.62	99.82	99.01	94.43	96.05	95.86
X _{Mg}							0.55	0.57	0.50
X _{Na}					0.03	0.14	0.03	0.06	0.07
	Muscovite	Cord	Apatite		Ilmenite		Tourmaline		
	(10)	(11)	(12)	(13)	(14)	(15)	(16)	(17)	(18)
SiO ₂	46.17	46.49	46.00	46.39	0.19	0	0.37	0.34	34.76
TiO ₂	0.63	0.92	0.00	0.00	0.34	0.01	51.52	52.1	0.67
Al ₂ O ₃	35.14	34.77	35.71	31.57	0.38	0.12	0.00	0.01	34.24
FeO	0.98	1.42	1.35	8.51	0.56	0.45	36.89	19.18	19.29
MnO	0.00	0.00	0.00	0.57	0.38	0.27	8.17	28.3	0.49
MgO	0.48	0.70	1.09	6.87	0.00	0.00	0.19	0.01	2.32
CaO	0.15	0.00	0.00	0.01	55.9	54.9	0.00	0.01	0.29
BaO	0.10	0.07	0.00	0.00	0.00	0.00	0.37	0.29	0.02
K ₂ O	10.89	10.56	9.58	0.02	0.00	0.00	0.09	0.01	1.87
Na ₂ O	0.62	0.54	0.44	1.21	0.00	0.12	0.12	0.01	0.01
P ₂ O ₅	0.00	0.00	0.00	0.00	38.9	42.0	0.00	0.00	0.00
Cl	0.00	0.01	0.00	0.00	0.02	0.07	0.00	0.01	0.00
F	0.15	0.00	0.00	0.00	4.20	3.96	0.00	0.07	0.41
Total	95.31	95.53	94.44	95.14	100.6	101.9	97.73	100.2	88.34
X _{Mg}	0.47	0.47	0.59	0.59				0.82	0.59
X _{Na}	0.08	0.07	0.07						

Plagioclase (1,2 core, rim) from sample 12, (3,4 core, rim) from sample 5. K-feldspar (5,6) from sample 13. Magmatic looking muscovite (see text, 10,11,12), replacement muscovite (7,8,9). Cordierite (13) from sample 13. Apatite (14,15) from samples 13 and 12. Ilmenite (16,17) from samples 5 and 31. Tourmaline (18,19) from samples 78 and 67. X_{Mg} = molar MgO/(MgO+FeO); X_{Na} = molar Na₂O/(Na₂O+K₂O).

3.5 RESULTS OF MINERAL ANALYSES

Representative analytical data for minerals coexisting with biotite are presented in Table 4. Tourmalines are Mg-rich. Ilmenite is MnO-rich, in particular in the aplites. Apatite is mostly F-saturated in all samples. Cordierite is Na₂O-rich. Similar sodium contents in cordierites from the Piedmont granites, USA, formed an argument for Speer (1981) to classify them as magmatic. Sodium values in metamorphic cordierites are generally less than 0.5wt% Na₂O (Leake 1960). Three representative analyses of secondary muscovites, replacing other minerals (7,8,9), and three of large euhedral primary looking muscovite grains (10,11,12) are presented in Table 4. These data demonstrate large chemical variation and compositional overlap for both muscovite types. The average biotite compositions are listed in Table 5. For each granodiorite and monzogranite sample two representative analyses are added. The formula proportions are calculated on the basis of 24(O,OH,F). The average composition of biotites in granodiorites, monzogranites and aplites changes systematically, as is illustrated by the relation with whole rock DI (Or + Ab + Q, Thornton and Tuttle 1960) in Figure 3.

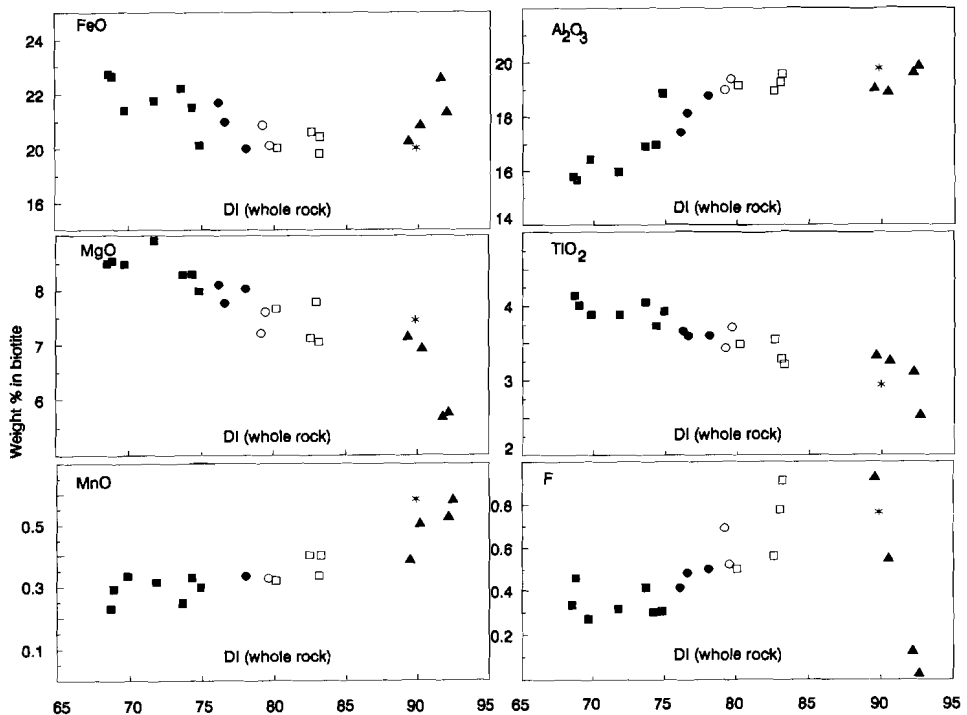


Fig.3. Average biotite composition (wt%) of each sample plotted against the whole rock Differentiation Index (Q+Or+Ab). Symbols are the same as in Fig.1. Solid triangles are biotite+muscovite aplites, open triangles are muscovite aplites.

Table 5. Representative electron microprobe analyses of biotites and average biotite compositions for each sample.
Cation compositions are based on 24(O+H+F). n.d.=not determined; d.l.=below detection limit

	MONZOGANITES																				
nr of analyses	sample 1		mean	sample 2		mean	sample 3		mean	sample 4		mean	sample 5		mean	sample 13		mean	sample 17		
	21	21	45	45	46	46	61	61	61	61	61	10	10	9	9	17	19	19			
SiO ₂	35.88	35.75	35.77	35.24	35.75	35.43	35.03	35.79	35.35	36.84	35.36	35.61	35.44	35.01	35.07	35.36	35.58	35.44	35.02	35.62	35.21
TiO ₂	3.24	3.17	2.96	3.55	3.35	3.21	3.97	3.23	3.50	3.49	3.74	3.27	3.63	3.54	3.55	3.77	3.7	3.70	3.34	3.67	3.44
Al _{2*} ₃	20.03	19.93	19.8	19.63	19.41	19.55	19.18	19.5	19.18	18.4	19.67	19.28	19.49	18.89	18.99	19.67	19.9	19.38	19.27	18.97	19.01
FeO	19.67	21.29	20.04	21.15	20.11	20.42	20.58	20.35	20.08	18.2	20.25	19.87	20.54	19.71	20.67	20.04	20.01	20.17	21.55	20.52	20.91
MnO	0.70	0.68	0.59	0.45	0.39	0.40	d.1	d.1	0.31	0.30	0.35	0.34	0.38	0.35	0.40	0.35	0.28	0.33	n.d.	n.d.	n.d.
MgO	6.96	7.61	7.49	7.61	6.65	7.05	7.65	7.91	7.69	7.41	7.96	7.80	7.25	7.39	7.13	7.69	7.91	7.62	7.40	7.28	7.24
Li	n.d.	n.d.	1773	n.d.	n.d.	1644	n.d.	n.d.	852	n.d.	n.d.	1183	n.d.	n.d.	n.d.	n.d.	n.d.	n.d.	n.d.	n.d.	n.d.
CaO	d.1	0.13	0.03	0.17	d.1	0.116	d.1	d.1	0.14	0.32	d.1	0.07	0.13	d.1	0.06	0.17	0.15	0.09	d.1	d.1	0.01
Na ₂ O	0.18	0.16	0.14	0.24	0.16	0.13	0.20	0.27	0.17	0.23	0.19	0.18	0.18	0.11	0.16	0.18	0.19	0.19	0.13	0.19	0.16
K ₂ O	9.67	9.64	9.69	9.30	9.73	9.61	9.57	9.41	9.73	8.97	9.61	9.64	9.84	9.69	9.66	10.24	9.81	9.85	9.93	9.68	9.67
F	0.89	0.76	0.76	0.88	1.10	0.91	0.65	0.67	0.50	0.88	0.86	0.78	0.59	0.53	0.56	0.46	0.68	0.52	0.94	0.78	0.69
C1	0.11	0.12	0.12	0.12	0.16	0.14	0.06	0.07	0.06	0.10	0.10	0.09	0.08	0.06	0.16	0.06	0.05	0.06	0.01	0.04	0.04
Total	97.33	99.24	97.37	98.34	97.31	96.98	97.18	97.50	96.7	95.53	97.82	96.96	97.55	95.28	96.41	97.99	97.43	97.43	97.19	96.61	96.45
Fe ⁺⁺⁺ /Fe _{tot}	0.09		0.11		0.06		0.08		0.07		0.07		0.07		n.d.						
Si ^{IV}	5.41	5.33	5.40	5.29	5.45	5.39	5.32	5.39	5.37	5.62	5.31	5.40	5.34	5.38	5.37	5.31	5.31	5.35	5.33	5.41	5.39
Al ^{IV}	2.59	2.67	2.60	2.71	2.55	2.61	2.68	2.61	2.63	2.38	2.69	2.60	2.66	2.62	2.63	2.69	2.69	2.65	2.67	2.59	2.61
Al ^{VI}	0.98	0.83	0.93	0.77	0.94	0.90	0.75	0.86	0.8	0.92	0.79	0.85	0.79	0.80	0.80	0.78	0.82	0.80	0.78	0.81	0.81
Ti ^{VI}	0.37	0.36	0.33	0.40	0.38	0.37	0.45	0.37	0.4	0.40	0.42	0.37	0.41	0.41	0.41	0.43	0.42	0.42	0.38	0.42	0.40
Fe	2.48	2.65	2.53	2.66	2.56	2.60	2.61	2.56	2.55	2.32	2.54	2.52	2.65	2.6	2.65	2.51	2.50	2.55	2.74	2.61	2.68
Mn	0.09	0.09	0.07	0.06	0.06	0.05	-	-	0.04	0.04	0.04	0.04	0.05	0.05	0.05	0.04	0.04	0.04	-	-	-
Mg	1.57	1.69	1.69	1.7	1.51	1.60	1.73	1.78	1.74	1.68	1.78	1.76	1.63	1.69	1.63	1.72	1.76	1.71	1.68	1.65	1.65
Li	-	-	0.23	-	-	0.21	-	-	0.11	-	-	0.13	-	-	-	-	-	-	-	-	-
Ca	-	0.02	-	0.03	-	0.02	-	-	0.02	0.05	-	-	0.02	-	-	0.03	0.02	-	-	-	-
Na	0.05	0.05	0.04	0.07	0.05	0.04	0.06	0.08	0.05	0.07	0.06	0.05	0.05	0.03	0.05	0.05	0.06	0.05	0.04	0.06	0.05
K	1.86	1.83	1.87	1.78	1.89	1.87	1.85	1.81	1.88	1.75	1.84	1.87	1.89	1.90	1.89	1.96	1.87	1.90	1.93	1.88	1.89
OH	3.55	3.61	3.58	3.55	3.55	3.52	3.67	3.66	3.74	3.55	3.57	3.60	3.70	3.73	3.69	3.77	3.67	3.74	3.55	3.61	3.66
F	0.42	0.36	0.36	0.42	0.42	0.44	0.31	0.32	0.24	0.42	0.41	0.37	0.28	0.26	0.27	0.22	0.32	0.25	0.45	0.37	0.33
C1	0.03	0.03	0.03	0.03	0.03	0.04	0.02	0.02	0.02	0.03	0.03	0.02	0.02	0.02	0.04	0.02	0.01	0.02	0.0	0.01	0.01
ΣCations	15.40	15.52	15.70	15.47	15.39	15.66	15.45	15.46	15.59	15.23	15.47	15.60	15.50	15.50	15.48	15.51	15.49	15.47	15.55	15.43	15.48
X _{Mg}	0.39	0.39	0.40	0.39	0.37	0.38	0.40	0.41	0.41	0.42	0.41	0.41	0.38	0.39	0.38	0.41	0.41	0.40	0.38	0.39	0.39

Table 5 continued

GRANODIORITES

	sample 6	mean	sample 7	mean	sample 8	mean	sample 9	mean	sample 10	mean	sample 11	mean	sample 12	mean							
	22		10		13		16		16		23		10								
SiO ₂	35.53	35.43	35.40	35.67	34.70	35.12	35.47	35.43	35.02	36.67	35.53	35.69	34.91	35.29	35.48	35.60	36.60	35.92	35.78	35.94	34.97
TiO ₂	4.05	4.00	3.93	4.13	4.09	4.06	3.92	3.94	3.73	4.05	4.12	3.88	4.23	3.85	4.12	4.05	3.90	3.89	4.25	4.17	4.02
Al ₂ O ₃	18.72	19.27	18.9	16.76	16.96	16.94	16.55	16.85	17.04	16.72	16.78	16.46	15.52	15.61	15.80	15.91	16.08	16.01	15.73	15.67	15.70
FeO	20.11	19.27	20.12	21.33	22.65	22.27	21.95	20.91	21.55	21.25	20.79	21.43	22.06	21.75	22.75	22.19	21.12	21.82	22.11	22.71	22.67
MnO	0.25	0.32	0.29	0.25	0.26	0.25	0.31	0.34	0.32	0.32	0.34	0.34	0.22	0.21	0.23	0.35	0.27	0.31	0.30	0.30	0.29
MgO	8.52	7.76	7.99	8.26	8.32	8.30	8.72	8.46	8.31	8.49	8.77	8.49	8.53	8.81	8.55	8.94	8.85	8.94	8.51	8.72	8.55
Li	n.d.	n.d.	450	n.d.	n.d.	n.d.	n.d.	n.d.	n.d.	n.d.	362	n.d.	n.d.	n.d.	n.d.	n.d.	334	n.d.	n.d.	n.d.	n.d.
CaO	0.25	d.1	0.08	d.1	d.1	d.1	d.1	d.1	0.08	0.14	0.28	0.07	d.1	d.1	d.1	0.22	0.13	0.13	d.1	0.08	d.1
Na ₂ O	0.34	0.30	0.28	0.16	0.17	0.19	0.19	0.20	0.20	0.18	0.22	0.20	0.18	0.07	0.11	0.15	0.08	0.11	0.13	0.16	0.13
K ₂ O	9.32	9.59	9.58	9.42	9.21	9.51	9.52	9.42	9.47	9.44	9.52	9.60	9.07	9.88	9.62	9.30	9.65	9.46	9.60	9.50	9.49
F	0.26	0.35	0.31	0.54	0.40	0.42	0.26	0.27	0.30	0.30	0.27	0.24	0.51	0.33	0.29	0.36	0.32	0.46	0.36	0.46	0.46
C1	0.09	0.09	0.1	0.14	0.10	0.13	0.09	0.11	0.10	0.15	0.10	0.13	0.15	0.11	0.11	0.08	0.12	0.08	0.09	0.12	0.12
Total	97.44	96.38	96.98	97.23	97.05	97.39	97.11	96.16	96.04	97.84	96.99	96.67	95.21	96.09	97.1	97.08	97.47	96.99	96.96	97.73	96.56
Fe ⁺⁺⁺ /Fe _{tot}	0.04		0.15		0.1		0.08		0.08		0.17		0.15		0.17		0.15		0.17		
Si ^{IV}	5.33	5.36	5.35	5.44	5.32	5.38	5.42	5.44	5.40	5.52	5.42	5.47	5.45	5.47	5.45	5.44	5.55	5.48	5.49	5.48	5.42
Al ^{IV}	2.67	2.64	2.65	2.56	2.68	2.62	2.58	2.56	2.60	2.48	2.58	2.53	2.55	2.53	2.55	2.56	2.45	2.52	2.51	2.52	2.58
Al ^{VI}	0.65	0.80	0.72	0.46	0.38	0.43	0.40	0.49	0.49	0.49	0.43	0.44	0.30	0.33	0.31	0.31	0.43	0.36	0.33	0.29	0.29
Ti ^{VI}	0.46	0.46	0.45	0.47	0.47	0.47	0.45	0.46	0.43	0.46	0.47	0.45	0.49	0.45	0.48	0.47	0.44	0.45	0.49	0.48	0.47
Fe	2.52	2.44	2.54	2.73	2.91	2.85	2.8	2.69	2.78	2.68	2.65	2.75	2.88	2.82	2.92	2.84	2.68	2.79	2.84	2.89	2.94
Mn	0.03	0.04	0.04	0.03	0.03	0.03	0.04	0.04	0.04	0.04	0.04	0.04	0.03	0.03	0.05	0.03	0.03	0.04	0.04	0.04	0.04
Mg	1.91	1.75	1.8	1.88	1.9	1.89	1.99	1.94	1.91	1.91	1.99	1.94	1.99	2.04	1.96	2.04	2.00	2.03	1.95	1.98	1.98
Li	-	-	0.05	-	-	-	-	-	0.05	-	-	-	-	-	-	-	0.05	-	-	-	
Ca	0.04	-	0.01	-	-	-	-	-	0.01	0.02	0.05	0.01	-	-	-	0.04	0.02	0.02	-	0.01	-
Na	0.10	0.09	0.08	0.05	0.05	0.06	0.06	0.06	0.05	0.07	0.06	0.05	0.05	0.02	0.03	0.04	0.02	0.03	0.04	0.05	0.04
K	1.79	1.85	1.85	1.83	1.8	1.86	1.86	1.85	1.86	1.81	1.85	1.88	1.8	1.95	1.88	1.81	1.87	1.84	1.87	1.84	1.88
OH	3.85	3.81	3.83	3.70	3.78	3.77	3.85	3.84	3.83	3.82	3.83	3.84	3.84	3.74	3.81	3.84	3.80	3.82	3.75	3.80	3.75
F	0.12	0.17	0.15	0.26	0.19	0.20	0.13	0.13	0.14	0.14	0.14	0.13	0.12	0.25	0.16	0.14	0.17	0.15	0.22	0.17	0.22
C1	0.02	0.02	0.03	0.04	0.03	0.03	0.02	0.03	0.03	0.04	0.03	0.03	0.04	0.03	0.03	0.02	0.03	0.02	0.02	0.03	0.03
ΣCations	15.50	15.43	15.54	15.45	15.54	15.59	15.60	15.53	15.63	15.46	15.55	15.62	15.54	15.64	15.61	15.60	15.49	15.61	15.56	15.58	15.68
X _{Mg}	0.43	0.42	0.41	0.41	0.40	0.40	0.42	0.42	0.41	0.42	0.43	0.42	0.41	0.42	0.40	0.42	0.43	0.42	0.41	0.41	0.40

Table 5 continued

GRANODIORITES

APLITES

	sample 14	mean 32	sample 15	mean 12	sample 16	mean 17	87 18	86 17	67 5	31 2			
SiO ₂	35.96	35.00	35.39	36.07	36.11	35.88	35.51	36.45	35.71	35.20	35.39	35.03	35.28
TiO ₂	3.54	3.46	3.59	3.87	3.42	3.66	3.94	3.4	3.60	3.28	3.33	3.12	2.53
Al ₂ O ₃	19.21	18.47	18.81	17.14	17.72	17.46	17.78	18.48	18.19	19.09	19.21	19.69	19.89
FeO ^{#3}	20.73	19.75	20.03	21.41	22.14	21.65	21.00	21.01	21.00	20.84	20.30	22.52	21.13
MnO	0.79	0.56	0.34	n.d.	n.d.	n.d.	n.d.	n.d.	n.d.	0.49	0.38	0.53	0.58
MgO	6.61	8.69	8.05	8.26	7.93	8.10	7.56	7.54	7.78	6.93	7.12	5.68	5.69
Li	n.d.	n.d.	n.d.	n.d.	n.d.	n.d.	n.d.	n.d.	n.d.	n.d.	n.d.	n.d.	n.d.
CaO	d.1	0.14	d.1	d.1	0.13	d.1	d.1	0.13	0.07	0.05	0.06	0.05	0.06
Na ₂ O	0.08	0.21	0.18	0.19	0.13	0.14	0.12	0.12	0.13	0.15	0.13	0.10	0.06
K ₂ O ⁵	9.25	9.50	9.51	9.44	9.37	9.68	9.77	9.75	9.70	9.14	9.26	9.22	9.06
F	0.67	0.61	0.49	0.55	0.49	0.41	0.56	0.47	0.48	0.56	0.92	0.12	0.01
C1	0.08	0.03	0.04	0.07	d.1	0.08	0.05	0.07	0.06	0.08	0.10	0.07	0.13
Total	96.92	96.42	96.43	96.75	97.25	97.06	97.5	96.61	96.82	99.24	99.27	99.95	98.34
Fe ⁺⁺⁺ /Fe _{tot}		n.d.		n.d.		n.d.		n.d.					
Si ^{IV}	5.45	5.34	5.38	5.48	5.47	5.46	5.44	5.49	5.44	5.40	5.42	5.38	5.46
Al ^{IV}	2.55	2.66	2.62	2.52	2.53	2.54	2.56	2.51	2.56	2.60	2.58	2.62	2.54
Al ^{VI}	0.89	0.66	0.75	0.56	0.63	0.59	0.65	0.77	0.70	0.86	0.88	0.94	1.09
Ti ^{VI}	0.40	0.40	0.41	0.44	0.39	0.42	0.45	0.39	0.41	0.38	0.38	0.36	0.29
Fe	2.63	2.52	2.55	2.72	2.80	2.75	2.69	2.65	2.67	2.68	2.60	2.89	2.74
Mn	0.10	0.07	0.04	-	-	-	-	-	-	0.06	0.05	0.07	0.08
Mg	1.49	1.98	1.82	1.87	1.79	1.84	1.73	1.69	1.77	1.59	1.62	1.30	1.31
Li	-	-	-	-	-	-	-	-	-	-	-	-	-
Ca	-	0.02	-	-	0.02	-	-	0.02	0.01	0.01	0.01	0.01	0.01
Na	0.02	0.06	0.05	0.06	0.04	0.04	0.04	0.04	0.04	0.05	0.04	0.03	0.02
K	1.79	1.85	1.84	1.83	1.81	1.88	1.91	1.87	1.88	1.79	1.81	1.80	1.79
OH	3.66	3.70	3.75	3.72	3.77	3.78	3.72	3.76	3.75	3.71	3.53	3.92	3.96
F	0.32	0.29	0.24	0.26	0.23	0.20	0.27	0.22	0.23	0.27	0.45	0.06	0.00
C1	0.02	0.01	0.01	0.02	-	0.02	0.01	0.02	0.02	0.02	0.03	0.02	0.03
ΣCations	15.32	15.56	15.41	15.48	15.48	15.52	15.47	15.43	15.48	15.42	15.39	15.40	15.33
X _{Mg}	0.36	0.44	0.42	0.41	0.39	0.40	0.39	0.39	0.40	0.37	0.38	0.31	0.32

Within individual biotite crystals compositional variation exists, as is illustrated for single grains in samples 17, 16, 15, 4 and 2 in Table 6. At the scale of the present study, systematic variation between cores and rims is seldomly observed, and the zoning of the biotite may be rather complex.

3.6 DISCUSSION

Whole Rock chemistry

The reduced, ilmenite dominant and peraluminous nature and the relatively high K₂O and Na₂O content are similar to properties found to be characteristic for S-type granites (White and Chappel 1983). Chemically, the intrusive rocks are similar to other Iberian Hercynian granitoids considered to be of crustal origin (De Albuquerque 1973; Barr and Areias 1980; Aparicio Yague et al. 1983; Bea and Morena-Ventas 1985; Neiva et al. 1987). The least evolved granodiorites, which resemble plagioclase and biotite rich crystal mushes, have an A/CNK-ratio just over one, whereas the most evolved

intercumulus enriched monzogranites have an A/CNK-ratio of 1.13, and the aplites an A/CNK-ratio between 1.11 and 1.21. Feldspars have an A/CNK ratio of 1, while biotites are variably peraluminous. Therefore, the aluminosity of the melt can only increase with differentiation if the original magma was more peraluminous than the crystallizing granodiorites.

Table 6. Compositional variations within single biotite grains in samples 16, 15, 17, 4 and 2.

Sample	SiO ₂	TiO ₂	Al ₂ O ₃	MgO	FeO	Na ₂ O	K ₂ O	C1	F	Total
16	35.6	3.9	17.33	7.44	20.76	0.13	9.47	0.1	0.42	95.81
Grano	35.24	3.72	17.55	7.16	20.75	0.12	9.71	0.08	0.44	95.09
diorite	35.34	3.55	18.04	8.19	21.18	0.16	9.59	0	0.41	96.81
	34.91	3.67	18.04	7.35	20.88	0.15	9.37	0.07	0.37	95.1
	35.98	3.82	18.14	7.51	20.58	0.18	9.94	0.07	0.57	97.19
	36.28	3.89	18.18	7.68	20.47	0.13	9.59	0.06	0.54	97.19
	36.45	3.4	18.48	7.54	21.01	0.12	9.75	0.07	0.47	97.88
	35.47	3.65	18.54	7.66	21.33	0.11	9.89	0.06	0.51	97.47
15	36.5	3.8	16.95	8.27	21.2	0.22	9.81	0.1	0.54	97.5
Grano	36.07	3.87	17.14	8.26	21.41	0.19	9.44	0.07	0.55	97.45
diorite	35.51	3.87	17.16	8.11	21.41	0.19	9.64	0.08	0.44	96.71
	35.96	3.8	17.16	7.91	21.84	0.12	9.82	0.09	0.42	97.38
	35.09	3.65	17.19	8.61	22.17	0.11	9.61	0.09	0.51	97.43
	35.96	3.9	17.23	8.11	21.75	0.19	9.7	0.1	0.37	97.72
	35.77	3.79	17.67	8.06	22.23	0.19	9.78	0.07	0.56	98.23
	35.53	3.97	17.95	8.24	21.27	0.07	9.81	0.07	0	97.03
17	34.89	3.49	18.91	7.08	20.84	0.15	9.81	0.03	0.5	95.7
Monzo	35.62	3.67	18.97	7.28	20.52	0.19	9.68	0.04	0.78	96.95
granite	34.68	3.6	19.07	7.61	20.44	0.15	9.68	0.05	0.57	95.96
	35.36	3.44	19.16	6.98	20.62	0.18	9.75	0.03	0.67	96.19
	34.87	3.49	19.18	6.85	20.61	0.16	9.55	0.04	0.65	95.41
	35.04	3.14	19.42	7.35	20.38	0.16	9.5	0.04	0.6	95.81
	34.64	3.42	19.5	7.03	21.64	0.2	9.66	0.03	0.6	96.72
	35.94	3.37	19.67	7.2	20.87	0.19	9.53	0.04	0.56	97.37
	35.86	3.52	19.71	7.23	21.11	0.19	9.44	0.05	0.76	97.87
4	32.95	2.84	16.55	5.5	21.03	0.12	8.28	0.09	0.4	88.15
Monzo	32.65	3.24	17.55	6.86	21.18	0.13	9.46	0.09	0.88	92.35
granite	34.57	3.49	18.18	7.48	20.06	0.2	9.61	0.09	0.75	94.84
	34.49	3.77	18.67	7.53	20.37	0.22	9.13	0.09	1.03	95.75
	34.59	3.45	18.86	7.44	19.88	0.22	9.61	0.1	0.71	95.34
	36.01	3.39	19.67	8.03	20.19	0.2	9.5	0.09	0.92	98.5
	37.14	3.55	20.14	8.14	19.98	0.19	9.83	0.07	0.81	100.12
2	35.45	3.85	18.44	6.85	20.15	0.13	9.62	0.13	0.77	95.75
Monzo	35.51	3.00	18.91	6.81	21.79	0.08	9.95	0.14	0.94	97.5
granite	35.53	3.24	18.99	6.75	21.68	0.09	9.83	0.12	0.78	97.29
	35.28	3.14	19.1	6.96	20.79	0.12	9.71	0.13	0.45	96.03
	35.49	3.52	19.16	6.86	21.38	0.18	9.64	0.14	0.71	97.45
	35.00	3.30	19.29	7.06	21.34	0.03	9.84	0.13	0.77	97.22
	35.68	3.52	19.33	7.21	21.60	0.15	9.75	0.13	0.74	98.42
	35.71	3.74	19.41	6.9	20.93	0.16	9.91	0.13	0.73	97.92
	35.51	3.59	19.61	6.86	20.85	0.08	9.66	0.15	1.03	97.77
	35.58	2.94	19.67	7.06	20.94	0.08	9.84	0.12	0.91	97.62
	36.05	3.05	19.86	7.23	19.86	0.12	9.97	0.16	0.81	97.6
	35.13	3.20	19.95	6.73	20.57	0.11	9.76	0.12	0.77	96.82

The crystallization sequence is illustrated by the position of the samples in the normative ternary feldspar diagram (Fig.4). Arbitrarily assuming that the magma was water-saturated and that $P_{\text{tot}} = P_{\text{H}_2\text{O}}$ \approx 5 Kbar, the samples are projected on the corresponding solidus surface (Winkler, 1979). The granodiorite samples follow a curved trend, almost perpendicular to the An-Ab axis. The granodiorite crystallization would have occurred between 705°C and 680°C. This is a relatively small temperature range, compatible with In Situ crystallization. The monzogranite samples do not show a trend, but plot in a cluster near the cotectic line. We have no direct explanation for the amount of scatter in the monzogranites nor for the fact that they plot above the cotectic line. A possible explanation might be a rising F-activity in the melt during differentiation as the average fluorine content of the biotites increases from 0.27 wt% in the granodiorites (Fig.3) to 0.91 wt% in the monzogranites. Manning (1981) has demonstrated that an increase in the amount of fluorine in the system Qz+Ab+Or causes a shift of the eutectic point towards the albite apex. The aplites plot on a trend on the opposite side of the cotectic line, suggesting mainly K-feldspar fractionation.

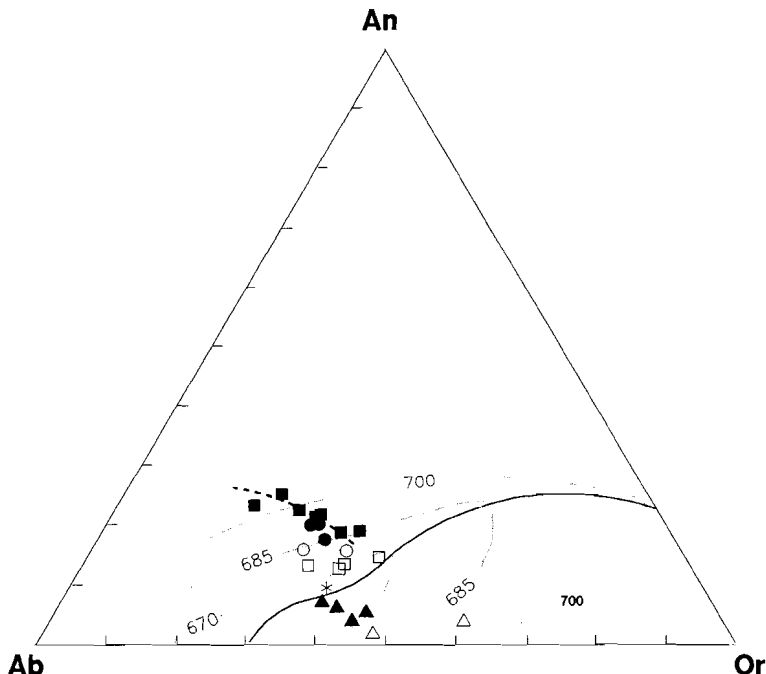


Fig.4. Weight normative feldspar composition of the granitic rocks, projected on the solidus surface at $P_{\text{tot}} = P_{\text{H}_2\text{O}} = 5 \text{ Kbar}$ (Winkler 1979). The symbols are the same as in Fig.3. The dashed line indicates the trend for the granodiorites

The micas

Compositions of magmatic muscovites and biotites are easily altered during hydrothermal events, and therefore we have examined the micas in order to determine whether the rocks near Los Santos have undergone hydrothermal overprint.

Textural differences amongst muscovites suggest the presence of both magmatic and hydrothermal phases. However, the lack of correlation between texture and chemistry (Table 4) indicates that the muscovites cannot simply be identified as magmatic and hydrothermal minerals on the basis of texture. The secondary muscovite grains (7,8,9, Table 4) all replace feldspar. Additionally, (7 and 8) are intergrown, and microscopically identical. Nevertheless the chemical variation is large. Muscovites 8 and 9 have high TiO_2 -content, which is often an important argument for the recognition of igneous muscovite (Miller 1981; Speer 1984). On the other hand, one of the primary looking muscovites (12) contains no TiO_2 , suggesting that it is secondary.

All available muscovite analyses from monzogranites and aplites are plotted in a ternary Fe_2O_3 - MgO - TiO_2 diagram (Fig.5a,b).

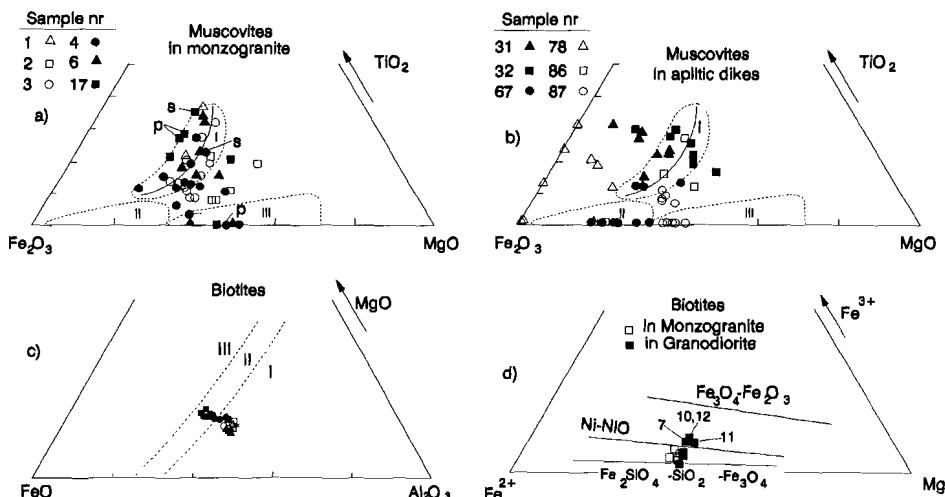


Fig.5. a,b: Ternary diagrams with muscovite compositions (wt%) in monzogranites (a), in aplites (b): Fields I, II and III represent the compositional fields typical for magmatic, late magmatic and hydrothermal muscovites (Monier et al. 1984). P and S indicate the primary and secondary muscovites presented in Table 4. **c:** average biotite compositions; I, II and III are the compositional fields of igneous biotites associated with muscovite, no other mafic mineral, and with hornblende, pyroxene or olivine (Nockolds 1947) respectively. **d:** average biotite compositions in relation with the Magnetite-Hematite, Ni-NiO and Quartz-Magnetite-Fayalite buffers. Symbols in c and d are the same as in Fig.3.

This diagram is used to distinguish between magmatic, late magmatic and post-magmatic hydrothermal muscovite (Monier et al. 1984). The primary and secondary muscovites presented in Table 4 are marked. The majority of the muscovites from the monzogranite plot in the magmatic field. The muscovites that plot below the magmatic but above the post magmatic fields, could be primary muscovites that have undergone hydrothermal reequilibration. The muscovites from the different aplites form separate clusters (Fig. 5b). On the basis of this plot, muscovites from sample 87 are mainly hydrothermal, those from sample 67 mainly late magmatic. The muscovites of the remaining samples should mainly be magmatic. The low MgO content of all muscovites of sample 78, and some of samples 31 and 32 may be an effect of partitioning of Mg into tourmaline.

Granitic textures of biotites are often preserved during hydrothermal reequilibration, while their original chemistry is modified. Jacobs and Parry (1979) report a progressive increase of X_{Mg} and SiO_2 with a simultaneous decrease of TiO_2 and Al_2O_3 in biotites from granodiorite porphyries during sequential potassic, argillic, phyllitic and prophyllitic alteration. Moore and Czamanske (1973) report significantly higher X_{Mg} and lower TiO_2 in hydrothermally altered biotites from monzogranites relative to unaltered magmatic biotites from the same rocks.

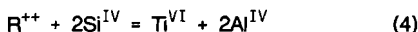
The linear relation between biotite composition and DI (Fig. 3) suggests that the biotites in all rocks are primary magmatic. If the biotites near Los Santos would have been affected hydrothermally they would not form such a continuous compositional trend with those further away from the skarn. The primary nature of the biotites is supported by their relatively high TiO_2 content (3 to 4 wt%), their low Fe^{+++} -content and their low X_{Mg} (0.41).

The analyzed biotites showed no microscopic indication for alteration to muscovite or chlorite. However, this type of alteration can form submicroscopic solid solutions, resulting not only in increasing Al and Si contents and decreasing Mg, Fe and Ti contents but also in deficient octahedral or interlayer occupancy (Σ cations < 15, Konings et al 1988). However, Σ cations is high for all biotites (15.4-15.7, Table 5), proving that no substantial alteration to muscovite took place. In addition, the relatively large compositional variation in individual biotite grains (Table 6) indicates that pervasive hydrothermal re-equilibration did not occur, since this would have resulted in a much more uniform composition within single grains.

Apparently, the systematic variation in biotite chemistry is not caused by alteration, which implies that the local chemical zoning in the monzogranitic part of the complex near the tungsten skarn is not an effect of a late-post magmatic hydrothermal overprint.

In order to understand the changes in biotite chemistry, the major substitution schemes are examined. The cation compositions of the biotites differ from the theoretical range of the phlogopite-annite series by low magnesium plus iron (Table 5). Mg and Fe are substituted by Al, Ti or Li and vacancies.

Most relevant substitutions involve replacement of Mg and Fe⁺⁺ by Al and Ti on the octahedral site, of Si by Al on the tetrahedral site (after Dymek 1983 and Guidotti 1984) and by Li on the octahedral site (Konings et al. 1988):



Substitution of Fe⁺⁺⁺ is not taken into account as Fe⁺⁺⁺/Fe_{tot} ratios in the biotites are low. The contribution of these five substitution reactions to the substitution of octahedral (Fe,Mg) was calculated, departing from the theoretical phlogopite-annite composition, for those biotites in which Li was determined. The results (Fig. 6) demonstrate that with DI increasing from 68 to 88, the substitution of (Fe,Mg) increases from 1.2 to 1.87 cations. In the biotites of the granodiorites and monzogranites most of the Al^{VI} and Ti^{VI} is substituted according to reactions (1), and (5). Substitution of Ti^{VI} according to reaction (4) occurs only in the granodiorites. Substitution of Al^{VI} following reactions (2) and (3) only occurs in the monzogranites.

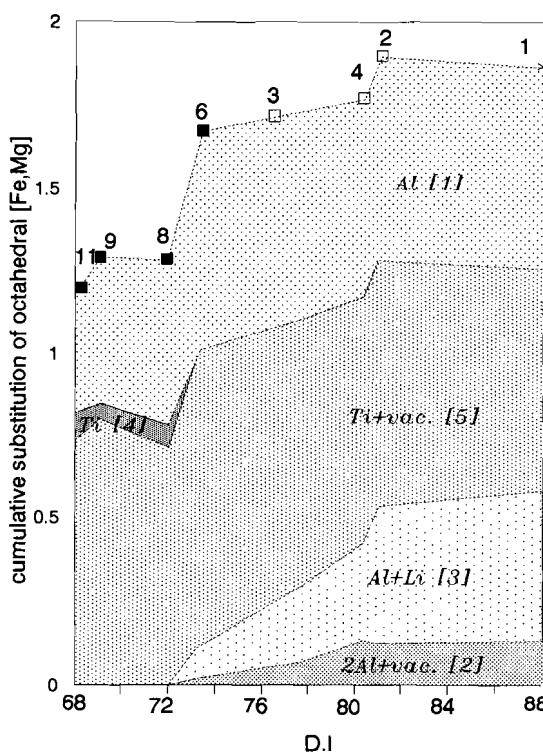


Fig.6. Amount of (Fe,Mg)VI-cations substituted by Al, Ti, Li and vacancies, following substitution reactions 1 to 5 (see text), as a function of the whole rock Differentiation Index (Q+Or+AB), for samples 1 (aplitic monzogranite, asterisk), 2-4 (monzogranites, open squares) and 6,8,9,11 (granodiorites, closed squares).

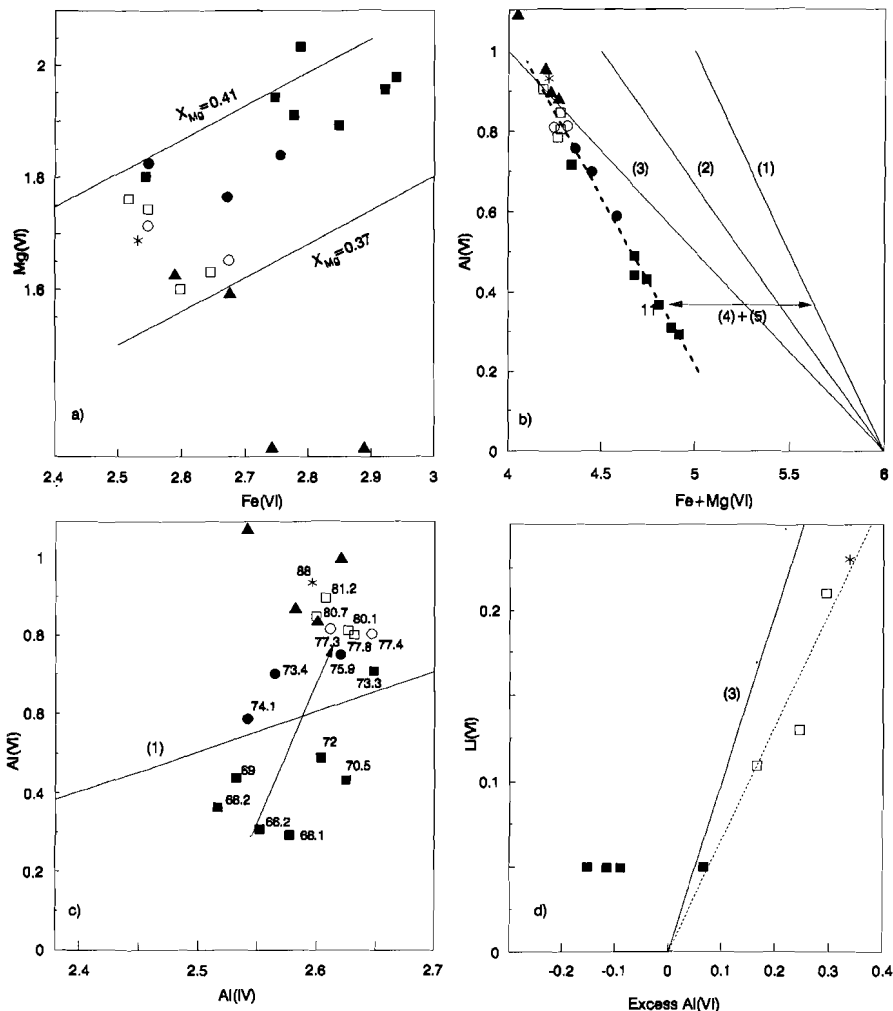


Fig. 7. a) Relation between Mg^{VI} and Fe^{VI} for average biotite compositions. Lines represent compositions with constant X_{Mg} ; b) Relation between Al^{VI} and $(Fe+Mg)^{VI}$. For meaning of lines and arrows see text; c) Relation between Al^{VI} and Al^{IV} . The numbers represent the DI of the corresponding whole rock sample; d) Relation between excess Al^{VI} (see text) and Li^{VI} . Meaning of lines and arrows is explained in the text. The symbols are the same as in Fig.3.

Apparently Fe and Mg are substituted in equal proportions for the granodiorites and most monzogranites, as the X_{Mg} remains fairly constant 0.39 ± 0.02 (Fig. 7a). The biotites of some monzogranites and the aplites tend to prefer Mg-replacement, as these biotites have lower X_{Mg} . This may be due to preferential partitioning of Mg (Puziewicz et al. 1990) into muscovite ($X_{Mg} = 0.48$, Table 4), cordierite ($X_{Mg} = 0.59$) and tourmaline ($X_{Mg} = 0.59$ to 0.82), while at the same time X_{Mg} in the whole rock remains (Table 1).

The substitution Fe and Mg by Al^{VI} follows a clear trend for the entire intrusive sequence (Fig. 7b). The trend is almost parallel to the line that represents substitution (1), and is offset from line (1) due to substitution by Ti^{VI} in reactions (4) and (5), as the length of the arrow corresponds with 0.79 cations, the amount of [Ti + coupled vacancies] in sample 11 (Fig. 6).

The relation between Al^{IV} and Al^{VI} is presented in Fig. 7c. Line (1) represents the composition of the biotites according to substitution scheme (1). The vertical distance of a sample to line (1) can be regarded as the amount of excess Al^{VI} , the amount of Al^{VI} that is not compensated with substituted Al^{IV} , which is negative for the samples below the line and positive above the line. The arrow indicates the general trend, showing that excess Al^{VI} increases with the differentiation index. The relation between excess Al^{VI} and Li is displayed in Fig. 7d. If all excess Al^{VI} is coupled with Li, the samples would plot on line (3). They plot on the dashed line, which corresponds with $2/3(\text{reaction 3}) + 1/3(\text{reaction 2})$, suggesting that excess Al^{VI} is coupled for only two-thirds with Li, and for one-third with vacancies.

Table 7. Biotite concentrations (weight% and modal%) in aplites, monzogranites and granodiorites

	Sample	MgO	FeO	Normative TiO_2	Modal TiO_2
Aplites	31	1.6	2.1	2.8	<1
	67	3.0	3.0	4.1	1
	86	5.6	6.2	6.3	4
	87	6.8	5.3	4.8	4
Monzo granite	1	5.5	5.1	6.5	3
	4	9.8	10.4	10.7	9
	5	9.9	10.1	10.4	12
	2	10.6	9.9	10.6	7
	3	11.8	12.6	12.2	13
	13	12.8	12.8	12.7	12
	17	13.8	13.0	14.2	n.d
Grano diorite	14	14.1	14.2	14.2	12
	15	14.2	15.1	15.8	n.d
	11	14.3	15.6	16.8	17
	16	14.7	15.2	15.0	n.d
	7	14.8	17.3	19.7	18
	8	14.8	16.1	16.2	15
	6	16.3	17.3	15.8	13
	10	16.3	17.8	21.0	18
	9	17.6	19.0	18.0	18
	12	18.5	17.3	19.7	19

Normative biotite concentrations were calculated using MgO-, FeO-, TiO_2 -contents (in wt%) and modal biotite concentrations were determined by point counting (in vol%).
n.d.=not determined.

Conditions of biotite crystallization

The biotite compositional differences are not a result of post magmatic alteration, and they therefore could either be a result from changes in melt conditions, such as melt and fluid composition, temperature, pressure and fO_2 during magma differentiation, or from coexistence in different AFM mineral assemblages. The AFM mineralogy changes from biotite in the granodiorites to biotite + muscovite + cordierite in the monzogranites and aplites, which is an indication for crystallization pressures between 3 and 5 Kbar (Speer 1984). The composition of the samples in the ternary plot of Fe-Mg-Al (Fig 5c), with respect to the different fields of igneous biotites associated with muscovite (I), unaccompanied by other mafic minerals (II) and associated with hornblende, pyroxene or olivine (after Nockolds 1947), plots on a range which corresponds with the expected position on the basis of the mineralogy of the granodiorites, monzogranites and aplites. Were the biotite compositions controlled by equilibria in the AFM mineral assemblage, one would expect two clusters of biotite compositions, one for the biotite assemblage (granodiorites) and one for the biotite-muscovite-cordierite assemblage (monzogranites and aplites). However, the compositional range (Fig. 5c) and the almost linear continuous decrease of FeO, MgO and TiO₂ and the increase of Al₂O₃, MnO, F and Li with DI (Fig. 3) indicate that the biotite composition in the granodiorites, monzogranites and aplites changed as a result of gradually changing conditions in the melt during magmatic differentiation.

The most important changes in the biotite composition with increasing DI are a decrease of Ti and an increase of Al at the expense of Fe+Mg. Various authors (e.g. Ahlin 1988; Fershtater 1973) report a positive correlation between the TiO₂-content of biotites, that coexist with other titaniferous phases, and temperature of equilibration. As the biotites in this study coexist with ilmenite, the decrease of TiO₂ in the biotites suggests decreasing equilibrium temperatures during crystallization of the magma. This was already argued on the basis of the feldspar composition (Fig. 4).

Al₂O₃ in the biotites does not correlate with Al₂O₃ in the whole rock (Fig. 8a), while a clear correlation exists with the A/CNK-ratio (Fig. 8b), indicating that the Al₂O₃-content of the biotites is buffered by the aluminium activity in the melt.

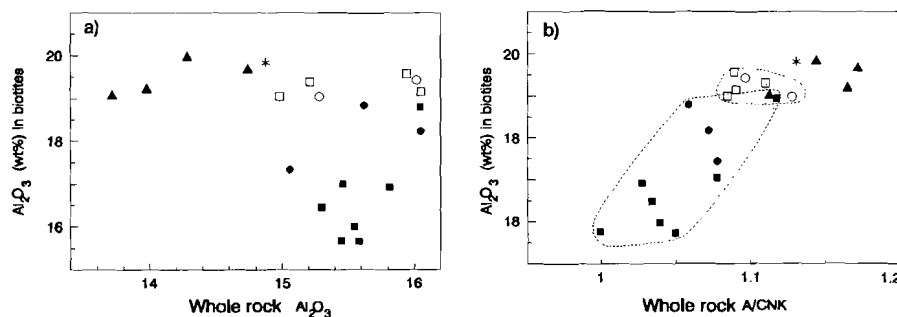


Fig.8. Average Al₂O₃ (wt%) content in biotites plotted against whole rock Al₂O₃ (wt%) and molar Al₂O₃/CaO+Na₂O+K₂O. symbols are as in Fig. 3.

This is in accordance with the findings of De Albuquerque (1973), who suggested that the increasing Al^{VI} in biotites reflects the increasing aluminium activity in the magma during crystallization, and of Puziewicz and Johannes (1988) who argued that, under conditions where biotite and cordierite are stable (2-5 Kbar, 710-880 °C), an increasing Al-activity (the molar ratio A/CNK) in granitic melts leads to higher Al_2O_3 and lower ($\text{FeO} + \text{MgO}$) and contents in the biotites.

Oxygen fugacity

An approximation of the oxygen fugacity of the granitic rocks during differentiation can be made from estimates of the composition of biotite solid solutions in the ternary system $\text{Mg} - \text{Fe}^{2+} - \text{Fe}^{3+}$ (Eugster and Wones, 1965). The compositions of the biotites are plotted in the ternary system with magnetite-hematite, Ni-NiO, and fayalite-quartz-magnetite buffers (Fig. 5d). The granodiorite samples 10, 12, 11 and 7 plot just above the Ni-NiO buffer, while all other samples plot below the Ni-NiO buffer. All samples plot above the fayalite-quartz-magnetite buffer. This implies that magnetite must have been present in addition to ilmenite, as true ilmenite-series granitoids plot on or below the QFM-buffer (Albuquerque 1973; Burkhard 1992). It is shown in Table 2 that small amounts of magnetite are present indeed, and that the samples above the Ni-NiO buffer contain higher amounts of magnetite than those below this buffer. The $\text{Fe}^{3+}/\text{Fe}^{2+}$ ratio in biotites (Fig. 5d) and the amount of magnetite (Table 2) in the rocks decreases from granodiorites to aplites, implying that the oxygen fugacity decreased during magma differentiation. Perhaps magnetite was a relatively early crystallizing phase compared to ilmenite, so that the oxygen fugacity was increasingly buffered by ilmenite during the differentiation. The ratio of $\text{Fe}^{2+}/(\text{Fe}^{2+} + \text{Mg})$ in the biotites ranges from 0.54 in the granodiorites to 0.60 in the monzogranites. This implies that the decrease in temperature must have been relatively small during crystallization (Speer 1984). On the basis of the feldspar assemblage (Fig. 4), it was already suggested that the entire intrusion crystallized over a rather limited temperature range of 30-40°C.

Fluorine fugacity

Unlike the apatites, which are fluorine saturated in all rocktypes, the biotites in the granitic rocks adjacent to the Los Santos skarn contain significantly higher amounts of fluorine than those in the rocks further away from the deposit. The association of tungsten deposits with fluorine enrichment is reported by many authors (Boissavy-Vinau and Roger 1980; Munoz 1984; Kooiman et al. 1986; Baker and Hellingwerf 1988). Fluorine is predominantly hosted in the micas, where it replaces the hydroxyl. The most important factors that govern the extent of halogen replacement are: 1) the activity of the halogen ion or acid during crystallization; 2) the cation population of the octahedral sheet; 3) the temperature at the moment of hydroxyl-halogen exchange; and 4) the effects of post crystallization leaching or enrichment by hydrothermal fluids (Munoz 1984). The systematic increase of fluorine in the biotites (Table 5) can either be explained with increasing activity of F in the melt during progressive differentiation of the magma (Bailey 1977; Keith et al. 1989), or with subsolidus re-equilibration (Parry and Jacobs 1975; Barriere and Cotten 1979; Gunow et al. 1980). In the case of magmatic differentiation, the volatiles, H_2O , F and Cl are controlling factors in the partitioning behaviour of ore forming elements

between crystals, melt and associated magmatic fluids and therefore can be important in the formation of magmatic hydrothermal ore deposits (Manning 1984; Candela 1989).

The biotites become enriched in F with increasing DI (Fig. 3), in contrast to Cl, which does not show a systematic variation (Table 5). Fluorine partitions into the melt, and therefore may be retained in the melt portion of the magma until an advanced stage of crystallization is reached , as opposed to Cl, which partitions in the exsolved aqueous fluids (Bailey 1977; Kwak 1987).

In order to determine whether the F-enrichment is related to the magmatic differentiation process, intercept values (IV(F)) for biotites and muscovites are calculated and plotted against the DI (Fig. 9).

The formulas for calculation of IV(F) are from Munoz (1984):

$$IV(F)_{\text{biotite}} = 1.52X_{\text{Mg}} + 0.42X_{\text{An}} + 0.20X_{\text{Sid}} - \log(X_F/X_{\text{OH}});$$

$$IV(F)_{\text{muscovite}} = 1.52X_{\text{Mg}} + 0.42X_{\text{Fe}} - 0.11X_{\text{Al}} - \log(X_F/X_{\text{OH}});$$

$$X_{\text{Sid}} = [(3-\text{Si}/\text{Al})/1.75][1-X_{\text{Mg}}] \text{ and } X_{\text{An}} = 1-(X_{\text{Mg}} + X_{\text{Sid}})$$

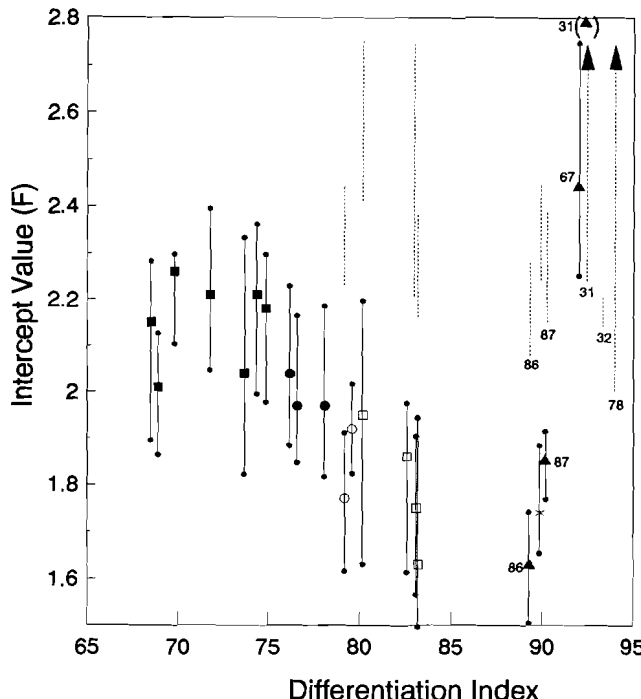


Fig. 9. Averages and ranges for fluorine Intercept Values in biotites (solid lines) and muscovites (dashed lines) as a function of DI (Q+Or+Ab). Aplite samples are indicated with their numbers. The biotite samples of samples 31 are between brackets because they have an IV of 3.4. Arrows indicate that the range continues upwards.

For the biotites average IV(F) values are plotted as well as the ranges, which are indicated by the solid vertical lines. Analyses from the aplites are indicated with the corresponding sample number. For the muscovites only ranges are indicated (dashed vertical lines), since many muscovites, in particular in the monzogranites, had F-contents below the detection limit. The average IV(F) in biotites decreases gradually from about 2.2 in the granodiorites, to about 1.6 in the monzogranites. As smaller IV(F) mean higher degrees of F-enrichment, these data suggest that the granitic melt became enriched in F during differentiation. The biotites in the aplites 86 and 87, which have lower DI (89 to 90.2) also have low intercept values, and therefore high fluorine activities. The biotites in the most felsic aplites, 67 and 31 however demonstrate a strong increase in IV(F), which may indicate that during the latest magmatic stages, F has escaped from the crystallizing aplitic melt. All muscovites yield higher IV(F) than the biotites from the same sample. Using the relation $\text{Log}[\text{f}(\text{H}_2\text{O})/\text{f}(\text{HF})] = 2100/T + \text{IV(F)}$ (Munoz 1984) at crystallization temperatures for granodiorites and monzogranites obtained from the feldspar mineralogy feldspar (approximately 705°C-665°C), the variation in $\text{Log}[\text{f}(\text{H}_2\text{O})/\text{f}(\text{HF})]$ can be estimated. For biotites this ratio decreases from 4.35 to 3.83. Assuming a crystallization temperature of 660°C for the muscovites, $\text{Log}[\text{f}(\text{H}_2\text{O})/\text{f}(\text{HF})]$ must have been 4.5 or higher. Consequently the muscovites were in disequilibrium with the biotites and therefore they either crystallized later than the biotites or suffered post magmatic leaching. Disequilibrium for the micas is supported by the different X_{Mg} values for biotites (0.39+2) and muscovites (0.47-0.59). In the case of leaching, it obviously did not affect the biotites, since otherwise these minerals would have yielded intercept values similar to the muscovites, or the ranges should at least overlap.

Sensor function

Usually the concentrations of major (or trace) elements are proposed as an index for fractionation e.g.: Fe_2O_3 (Neiva et al. 1987), SiO_2 (Pearce et al. 1984), normative Q + Ab + Or (Hudson and Arth 1983). The disadvantage of this type of indices is that it is based on whole rock composition, which can be very much altered by late stage magmatic fluids and additional postmagmatic alteration processes.

Leaching may cause significant variations in CaO - and Fe_2O_3 - content while silicification and quartz veining may mask the magmatic SiO_2 signature. The feldspar composition can be affected by processes like albitisation, k-feldspatization, kaolinitisation, muscovitisation etc. Additionally, inhomogeneous distribution of the various minerals are responsible for considerable variation in whole rock chemistry. The additional availability of a mineralogical differentiation index, like the biotite composition may provide a possibility to distinguish magmatic differentiation from other processes more adequately. The magmatic processes can be defined more accurately if the investigation is focused on the composition of magmatic biotite instead of the whole rock (e.g. Nockolds 1947; Heathcote and McCormick 1989). Biotite is a very useful tool in this study of magmatic differentiation processes because: 1) it crystallized as the major mafic mineral throughout the entire magmatic sequence; 2) petrologically and chemically all biotites are unaltered; 3) any late hydrothermal alteration can, if present, easily be detected in the chemical composition of the biotites and visibly altered biotites are excluded from electron microprobe analyses; 5) the mafic elements strongly concentrate into the biotite

and: 6) the relative variation of these elements in the biotites is larger than in the whole rock. In this study the variation in Al_2O_3 , FeO , MgO and TiO_2 in biotites reflects the changes in magma composition during differentiation. Because of the negative correlation of Al_2O_3 with FeO , MgO and TiO_2 , the ratio wt% $\text{Al}_2\text{O}_3/(\text{FeO} + \text{MgO} + \text{TiO}_2)$ may serve as a fractionation index. Even if biotite is present in very small amounts this index may be applicable. In order to compare the validity of this index it is plotted against the indices Fe_2O_3 , SiO_2 and $\text{Or} + \text{Ab} + \text{Q}$ (Fig. 10).

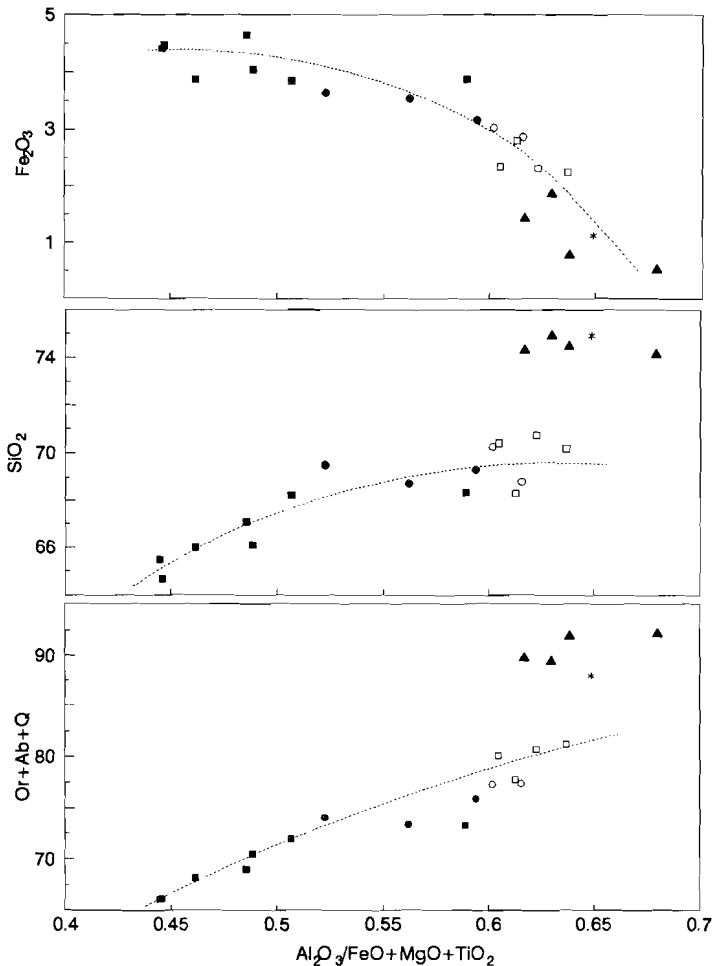


Fig. 10. Average $\text{Al}_2\text{O}_3/\text{FeO} + \text{MgO} + \text{TiO}_2$ (wt%) in biotites plotted against some conventional whole rock differentiation indices, Fe_2O_3 , SiO_2 and $\text{Q} + \text{Or} + \text{Ab}$ (wt%).

For the granodiorites the biotite index is more discriminative than Fe_2O_3 , SiO_2 and $\text{Or} + \text{Ab} + \text{Q}$, as there is less compositional overlap. For the monzogranites Fe_2O_3 and $\text{Or} + \text{Ab} + \text{Q}$ are as discriminative as the biotite index, while SiO_2 is less indicative due to the overlap with the more felsic granodiorites. For the aplites the results correspond less well with the quartz content and the DI of the whole rock. This is due to the fact that the aplites are enriched in quartz and K-feldspar. On the basis of these results it seems that this ratio is applicable as an additional, mineralogical differentiation index. Its wider application requires however additional study of the effects of biotite alteration on this ratio, and comparison with biotites from other granitic intrusions.

3.7 CONCLUSIONS

- 1) The composition of the rocks in the granodiorite-monzogranite sequence near Los Santos changes systematically from the centre of the intrusion towards the margin.
- 2) Systematic variations in whole rock composition and biotite composition indicate that the granodiorites and monzogranites are produced during differentiation of one single magma.
- 3) The biotite composition correlates with the Differentiation Index of the surrounding rock. With increasing DI the contents of FeO , MgO , and TiO_2 decrease while Al_2O_3 , Li, F and K_2O increase.
- 4) The biotites of the granodiorites are Al-undersaturated whereas those of the monzogranites contain Al^{VI} in excess of Al^{IV} . Progressive Al-substitution is characteristic for the entire sequence. A normal Tschermark Al-substitution is dominant in the biotites of the granodiorites whereas in the biotites of the monzogranites Al^{VI} -substitution additionally takes place coupled with Li and vacancies.
- 5) The concentration of FeO , MgO , TiO_2 and Al_2O_3 in biotites depends on aluminosity, temperature, oxygen fugacity and volatile content of the melt. The aluminosity of the melt increased during fractional crystallization, causing Al_2O_3 in the biotites to rise at the expense of $(\text{FeO} + \text{MGO})$ contents. The entire sequence may have crystallized between 705°C and 665°C .
During differentiation the oxygen fugacity of the melt decreased, while the fluorine fugacity increased. The fluorine enrichment is most notable in the rocks near the tungsten skarn of Los Santos.
- 6) Biotite compositions indicate that the zoning in the granitic rocks near the skarn of Los Santos is a result of magmatic differentiation and not of hydrothermal interaction.
- 7) The ratio of $\text{Al}_2\text{O}_3 / (\text{FeO} + \text{MgO} + \text{TiO}_2)$ in biotites is proposed as a useful mineralogical sensor for magmatic fractionation, in addition to the existing indices based on whole rock chemistry.

3.8 REFERENCES

- Ahlin S (1988) Interpretation of biotite-garnet partitioning data from two Svecokarelian metamorphic rock units. *Lithos* 22:25-29
- Albuquerque CAR de (1973) Geochemistry of biotites from granitic rocks, Northern Portugal. *Geochim.Cosmochim.Acta* 37:1779-1802

- Aparicio Yagüe A, Bellido Mulas F, Brandle Matesanz JL, García Cacho L, Santos Serrano V (1983) Caracterización de los granitos hercínicos del sector Centro-oriental del Sistema Central Espanol. *Estud.Geol.*39:271-306
- Bailey JC (1977) Fluorine in granitic rocks and melts; a review. *Chem.Geol.* 19;1-42
- Baker JH, Hellingwerf RH (1988) The geochemistry of tungsten-molybdenum-bearing granites and skarns from western Bergslagen, central Sweden. *Proc. 7th Quadrennial Symposium. Schweizerbart'sche Verlagsbuchhandlung, Stuttgart;* 327-338
- Barr SM, Areias L (1980) Petrology and Geochemistry of the granitic intrusions in the Viana do Castelo area, northern Portugal. *Geol.Mijnbouw* 59:273-282
- Barriere M, Cotten J (1979) Biotites and associated minerals as markers of magmatic fractionation and deuterium equilibration in granites. *Contrib.Mineral.Petrol* 70:183-192
- Bea F (1982) Sobre el significado de la cordierita en los granitoides del batolito de Ávila (Sistema Central Español). *Bol.Geol.Min.Esp.*93:59-67
- Bea F, Morena-Ventas I (1985) Diferentes series de rocas con afinidad granodioríticas en la Sierra de Gredos (Batalito de Ávila, Sistema Central Español). Criterios sobre su identificación. *Stud.Geol.Salam.*20;175-203.
- Bea F, Sánchez González de Herrero JG, Serrano Pinto M (1988) Una compilación geoquímica (elementos mayores) para los granitoides del Macizo Hespérico. In: Bea F (ed) *Geología de los granitoides y rocas asociadas del Macizo Hespérico.* 87-193
- Boissavy-Vineau M, Roger G (1980) The TiO₂/Ta ratio as an indicator of the degree of differentiation of tin granites. *Min.Dep.*15;231-236
- Burkhard 1991 the cooling history of granitic intrusions. *Proc. 1st Dutch conference on earthsciences*
- Candela PA (1989) Felsic magmas, volatiles, and metallogenesis. In: Whitney JA and Naldrett AJ (ed.) *Rev.Econ.Geol; Ore deposits associated with magmas;* 223-233
- Capdevila R, Corretgé G, Floor P (1973) Les Granitoides varisques de la Meseta Iberique. *Bol.Soc.Geo.France* 7,XV;209-228.
- Clarke DB (1981) The mineralogy of peraluminous granites: a review. *Can.Mineral* 19:3-17
- Dymek RF (1983) Titanium, aluminium and interlayer cation substitutions in biotite from high-grade gneisses, West Greenland. *Am.Mineral.*68:880-899
- Ferstahter GB (1973) Distribution of titanium and sodium between minerals of granitoids as a geological thermometer. *Geochem. Int.*110:57-65
- Guidotti CV (1984) Micas in metamorphic rocks. In: Bailey SW (ed) *Rev.in mineral.*13, Micas, 357-468
- Gunow AJ, Ludington S, Munoz JL (1980) Fluorine in micas from the Henderson Molybdenite Deposit, Colorado. *Econ.Geol.*75:1127-1137
- Heathcote RC, McCormick GR (1989) Major cation substitution in phlogopite and evolution of carbonatite in the Potash Sulphur Springs complex, Garland County, Arkansas. *Am.Miner.*74;141-150
- Hudson T, Arth JG (1983) Tin granites of the Seward Peninsula, Alaska. *Bull.Geol.Soc.Am.*94:768-790

- Jacobs DC, Parry WT (1979) Geochemistry of biotite in the Santa Rita Porphyry Copper Deposit, New Mexico. *Econ.Geol.*74:860-887
- Keith JD, Middelaar W van, Clark AH, Hodgson CJ (1989) Granitoid textures, compositions, and volatile fugacities associated with the formation of tungsten-dominated skarn deposits. In: Whitney JA and Naldrett AJ (ed.) *Rev.Econ.Geol; Ore deposits associated with magmas;* 223-233
- Konings RJM, Boland JN, Vriend SP, Jansen JBH (1988) Chemistry of biotites and muscovites in the Abas Granite, northern Portugal. *Am.Mineral.* 73:754-765
- Kooiman GJA, McLeod MJ, Sinclair WD (1986) Porhyry tungsten-molybdenum orebodies, polymetallic veins and replacement bodies, and tin-bearing greisen zones in the Fire Tower zone, Mount Pleasant, New Brunswick. *Econ.Geol.*81:1356-1373
- Kwak TAP (1987) W-Sn Skarn deposits and related metamorphic skarns and granitoids. Elsevier, Amsterdam 451pp.
- Leake BE (1960) Compilation of chemical analyses and physical constants of natural cordierites. *Am.Miner.*45:282-298
- Leake BE (1974) The crystallization history and mechanism of emplacement of the western part of the Galway Granite, Connemara, western Ireland. *Mineral.Mag.*39:498-513
- Mahmood A (1983) Geochemistry of biotites from a zoned granitic pluton in Morocco. *Mineral.Mag.*47:365-369
- Manning DAC (1981) The effect of fluorine on liquidus phase relationships in the system Qz-Ab-Or with excess water at 1 kb. *Contrib.Mineral.Petrol.*76:206-215
- Miller CF, Stoddard EF, Bradfish LJ, Dollase WA (1981) Composition of plutonic muscovite: genetic implications. *Can.Miner.*19:25-34
- Monier G, Mergoil-Daniel J, Labernadière H (1984) Générations successives de muscovites et feldspaths potassiques dans les leucogranites du Massif de Millevaches (Massif Central français). *Bull.Miner.*107:55-68.
- Moore WJ, Czamanske GK (1973) Compositions of biotites from unaltered and altered monzonitic rocks in the Bingham mining district, Utah. *Econ.Geol.*68:269-280
- Munoz JL (1984) F-OH and Cl-OH exchange in micas with applications to hydrothermal deposits. In: Bailey SW (ed) *Reviews in Mineralogy* 13, Micas, 469-544
- Neiva AMR, Neiva JMC, Parry SJ (1987) Geochemistry of the granitic rocks and their minerals from Serra da Estrela, Central Portugal. *Geochim.Cosmochim.Acta* 51: 439-454
- Nockolds (1947) The relation between chemical composition and paragenesis in the biotite micas of igneous rocks. *Am.J.Sci.*245:401-420
- Oen Ing Soen (1970) Granite intrusion, folding and metamorphism in Central Northern Portugal. *Bol.Geol.Min.Esp.*131:217-298.
- Parry WT, Jacobs DC (1975) Fluorine and Chlorine in biotite from Basin and Range Plutons. *Econ.Geol.*70:554-558
- Pearce JA, Harris NBW, Tindle AG (1984) Trace element discrimination diagrams for the tectonic interpretation of granitic rocks. *Journ.Petrol.*25:956-983

- Pratt (1894) Am.J.Sci.149
- Priem HNA, Boelrijk NAIM, Verschure RH, Hebeda EH (1970) Dating events of acid plutonism on granitic rocks in northern Portugal. *Geol.&Mijnb.*46:369-373.
- Puziewicz J, Johannes W (1988) Phase equilibria and compositions of Fe-Mg-Al minerals and melts in water-saturated peraluminous granitic systems. *Contrib.Mineral.Petrol.*100:156-168
- Puziewicz J, Johannes W (1990) Experimental study of a biotite- bearing granitic system under water-saturated and water- undersaturated conditions. *Contrib.Mineral.Petrol.*104:397-406
- Rossi P, Chevremont P (1987) Classification des associations magmatiques granitoides. Application a la cartographie des granitoides dans le cadre de la carte géologique au 1/50000 de la France. *Géochronique* 21:14-18
- Rottura A, Bargossi GM, Ciarconi V, D'Amico C, Maccarone E (1989) Petrology and geochemistry of late-Hercynian granites from the Western Central System of the Iberian Massif. *Eur.J.Mineral.* 1:667-683
- Saavedra Alonso J, Garcia Sanchez A (1974) Estudio geoquímico de algunos granitos de la provincia de Salamanca. *Bol.Geol.Min.*135;182-192.
- Speer JS (1981) Petrology of cordierite and almandine-bearing granitoid plutons of the southern Appalachian Piedmont, USA. *Can.Miner.*19;35-46
- Speer JS (1984) Micas in igneous rocks. In: Bailey SW (ed) *Reviews in Mineralogy* 13, Micas, 299-356
- Thornton CP Tuttle OF (1960) Chemistry of igneous rocks I. Differentiation Index. *Am.J.Sci.*258;664-684
- Ugidos JM (1983) Sobre el significado de la cordierita en los granitoides del batolito de Avila (Sistema Central Espanol). *Bol.Geol.Min.*94: 63-68
- Ugidos JM (1985) Cordierita, andalucita, sillimanita y topacio en las rocas graníticas. Fases magmáticas o residuales? IX reunaio de Geología do Oeste Peninsular. Fac Ciencias, Porto, Portugal, 30/IX-4X, 1985
- White AJR, Chappel BW (1983) Granitoid types and their distribution in the Lachlan Fold Belt, southeastern Australia. *Geol.Soc.Am. Mem.*159:21-34
- Winkler HGF (1979) Anatexis, formation of migmatites and origin of granitic magmas. In: Winkler HGF *Petrogenesis of metamorphic rocks.* 283-339
- Wones DR, Eugster HP (1965) Stability of biotite: experiment, theory and applications. *Am.Mineral.*50:1228-1272

CHAPTER 4

UNRAVELLING OF CRYSTAL FRACTIONATION AND CONTAMINATION, USING Ba, Sr, Rb AND Zr MODELLING AND COMPOSITIONS OF ZONED MINERALS.

4.1 ABSTRACT

The Hercynian granitic complex between Bejar, Linares and Miranda del Castañar (Salamanca, Spain) is geochemically and mineralogically zoned in a complex manner. A combination of detailed geochemical mapping, major and trace element modelling and electron microprobe analyses of zoned minerals demonstrates that the complex zoning is probably a result of interaction of crystal fractionation and possibly four different types of contamination processes. Original Ba, Sr, Rb relationships characteristic for crystal fractionation were locally destroyed by addition of more than 100 ppm Sr and up to 300 ppm Ba due to: 1) early contamination with CaO, Sr and Ba derived from Cambrian limestones and Precambrian schists and greywackes; 2) contamination with Ba along intrusive contacts with pelitic metasediments; 3) contamination with Ba along faults and; 4) interaction of late magmatic hydrothermal fluids with metasedimentary rocks. This occurred in the most felsic part of the monzogranites, and is probably related to significant mineralization of tin, tungsten, lead, copper and uranium. Fluid loss into the nearby sedimentary rocks may additionally have depleted these monzogranites in Rb and Zr.

4.2 INTRODUCTION

The granitic rocks in the study area (Fig 1.) are zoned and range in composition from granodiorites in the core to muscovite + cordierite bearing monzogranites and aplites near the north western intrusive margin (see CHAPTERS 2 and 3). Ugidos and Bea (1976) and Rottura et al. (1989) suggest a crustal anatetic origin for the monzogranitic rocks and propose a mixing model between this crustal material and deep-seated calc-alkaline magma to explain compositional variations within the granodioritic rocks. According to Bea (1985) all granitic rocks can be explained by means of crustal anatexis. Our work has demonstrated that there is no convincing evidence for magma mixing, and that the most significant geochemical and mineralogical variations in this part of the batholith can be explained with In Situ crystal fractionation of a single magma (CHAPTERS 2,3).

As a result of this geochemical study it can be concluded that the zoning of the intrusion is most likely the result of more processes than magma fractionation alone. Good understanding of the processes that caused the zoning is particularly important, as most mineralization in the area is spatially related to the

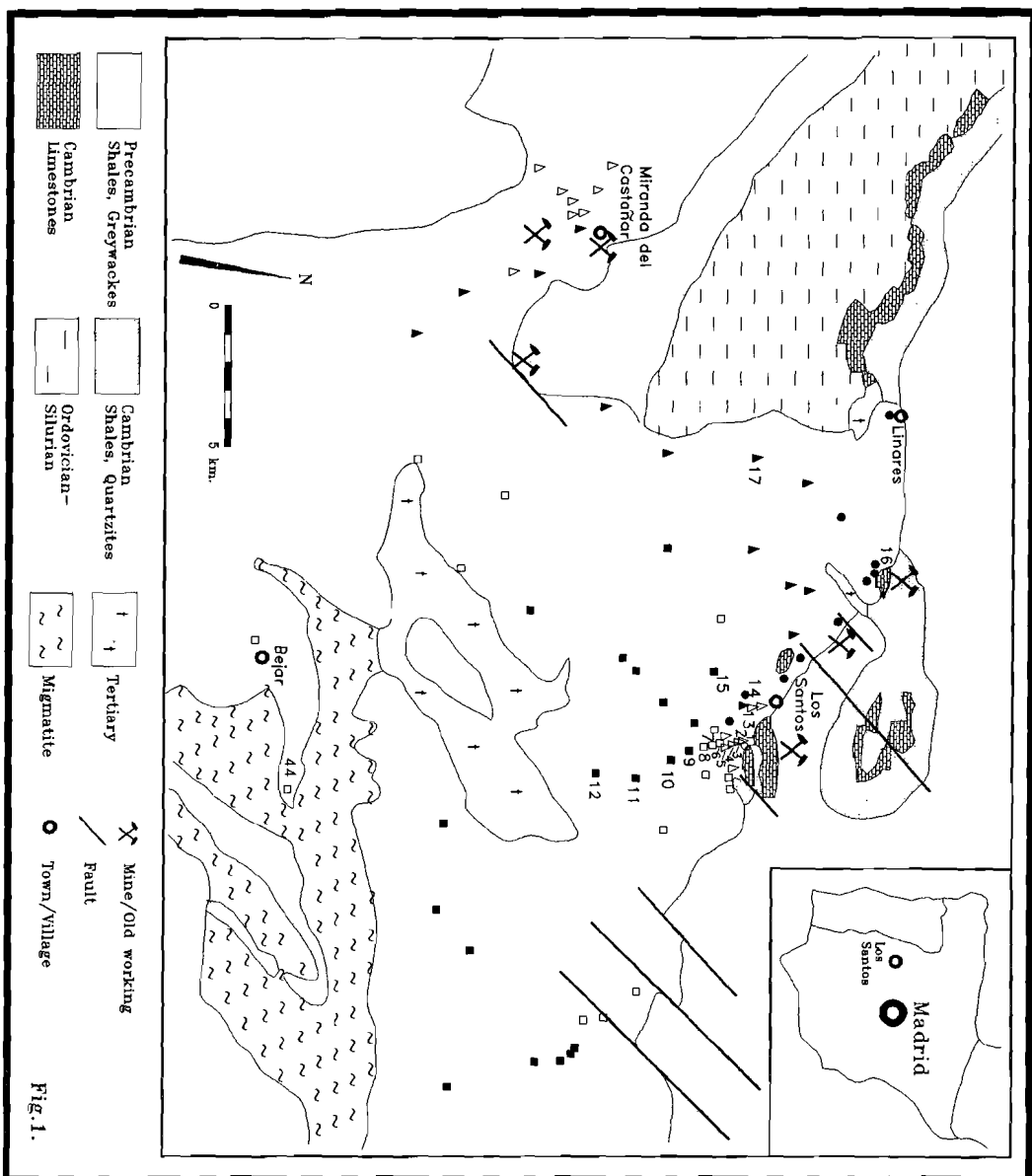


Fig.1. Simplified geological map of the study area with sample locations. Closed squares: uncontaminated main granodiorite; Open squares: contaminated main granodiorite (see section on contamination modelling); Closed circles: Linares granodiorites; Closed triangles: monzogranites; Open triangles: contaminated monzogranite; Open circle: two-mica microgranite. Aplites (asterisks in the following plots) are not plotted on the map, but are all from the vicinity of the skarn. The samples with numbers 1 to 17 are used for microprobe analysis.

parts of the intrusion where the zoning is most strongly developed. In vicinity of the Los Santos tungsten skarn, the intrusion changes from granodiorite to granite composition within a few kilometres distance, and the most felsic part is situated adjacent to the tungsten skarn (Goossens, 1991).

Petrogenetic processes in granitic intrusions can be studied well, using trace elements. The use of trace elements on behalf of modelling magma differentiation processes is extensively documented, and often it seems quite well possible to assess the role of various magmatic processes in the petrogenesis of an intrusive complex. Much more difficult is it however to deal with processes like magma contamination. Contamination processes usually occur randomly and cannot easily be described by petrogenetic modelling. In addition it is usually very difficult to determine the source of the contamination and its composition. In the previous chapters a petrogenetic model is proposed on the basis of a selected number of samples, located in a strongly zoned part of the intrusion.

The aim of this study is: 1) to map the geochemical variations in entire study area in detail; 2) to estimate the influence of crystal fractionation and contamination on the basis of our geochemical data; 3) to propose a realistic petrogenetic model for the zoned intrusion based on trace element modelling and zoned mineral chemistry.

4.3 SAMPLING AND ANALYSES

Rock samples were collected during three successive fieldwork campaigns, in order to optimize the precision of the documentation on the chemical zoning. Each sample consisted of chips of about 100 gram, with a total weight of at least one Kg. Wherever possible, samples were collected in quarries. Samples were subsequently crushed, split and analyzed for major and trace elements. Whole rock major elements were determined in Lithium metaborate glass beads, and trace elements in pressed powder tablets, with a Philips PW-1400 XRF. The precision is better than 5% for Na_2O , K_2O and MnO , better than 2% for the other major elements and better than 5% for the trace elements. Microprobe analyses of feldspars, micas and cordierites in selected samples were made with a JEOL 8600 Superprobe at the department of Geochemistry of the University of Utrecht.

4.4 PETROLOGY AND MAJOR ELEMENT GEOCHEMISTRY

The granitic area studied covers a surface of approximately 600 Km² (Fig.1). The squares represent granodiorites, and the triangles represent monzogranites. Granodioritic rocks are also found near Linares (closed circles). These rocks are separated from the main granodiorite body by a monzogranite zone. The transition between granodiorites and monzogranites is gradual without any mutual intrusive relationship. In addition to these rock types, a two-mica microgranite with strong aplitic affinities is developed near the contact with the Los Santos skarn (Fig.1, open circle). Aplites are locally abundant near the contact, in particular near Los Santos. Centimetre to decimetre-sized microgranular enclaves of tonalitic-dioritic material are abundant throughout the intrusion (Aparicio et al. 1983; Rottura et al. 1989).

The granodiorites show clear cumulus-intercumulus relationships of biotites and zoned Ca-rich plagioclases

with interstitial quartz, plagioclase and perthitic K-feldspar. The monzogranites additionally contain euhedral quartz and variable amounts of large K-feldspar phenocrysts, muscovite and cordierite and cumulus textures are developed less clearly. Apatite, zircon, monazite and ilmenite occur as accessory minerals in all rock types. Very minor amounts of magnetite are present in all samples (CHAPTER 3).

The whole-rock major element and normative composition of representative samples is listed in Table 1.

Table 1. Chemical and weight-normative composition of representative samples.
The samples with numbers 1 to 17 are the ones analysed microprobe
and are indicated on the sample map (Fig.1). The symbol indications
refer to those used in most figures.

Nº	Granodiorites							Monzogranites							Aplites				
	10 solid squares	12 solid squares	11 solid squares	9 solid squares	15 solid squares	8 open squares	6 open squares	7 solid circles	16 solid circles	14 solid circles	17 solid triangles	3 open triangles	13 open triangles	2 open triangles	5 open triangles	4 open triangles	1 open circles	asterisks	
SiO ₂	64.6	65.4	66.4	67.0	69.5	68.2	68.3	66.4	68.7	69.3	70.2	70.2	68.3	68.8	70.1	70.4	70.7	74.9	74.7 74.0
TiO ₂	0.7	0.69	0.62	0.7	0.58	0.58	0.62	0.63	0.54	0.51	0.49	0.47	0.43	0.47	0.34	0.34	0.35	0.2	0.21 0.07
Al ₂ O ₃	15.4	15.5	15.5	15.3	15.0	15.4	16.0	15.8	16.0	15.6	15.2	15.8	16.0	16.0	15.9	15.0	15.2	14.9	14.0 14.2
Fe ₂ O ₃	4.41	4.37	3.87	4.34	3.64	3.85	3.87	4.04	3.55	3.17	3.03	2.85	2.81	2.88	2.24	2.34	2.31	1.12	1.42 0.5
MnO	0.07	0.08	0.06	0.07	0.07	0.06	0.06	0.07	0.07	0.06	0.07	0.07	0.06	0.06	0.05	0.06	0.06	0.04	0.04 0.05
MgO	1.44	1.58	1.3	1.49	1.15	1.24	1.3	1.23	1.14	1.14	1.0	1.01	0.91	0.98	0.75	0.71	0.76	0.41	0.4 0.09
CaO	2.93	2.83	2.61	2.89	2.21	2.37	2.1	2.44	2.34	2.16	1.8	1.63	1.71	1.89	1.64	1.55	1.47	1.11	0.78 0.47
Na ₂ O	3.33	3.36	3.26	3.59	3.24	3.26	3.19	3.13	3.57	3.57	3.46	3.36	3.25	3.49	4.13	3.49	3.58	3.9	3.76 3.95
K ₂ O	4.27	3.82	4.46	3.35	4.24	4.3	4.36	5.31	4.45	4.54	4.19	4.7	5.65	5.0	4.48	4.83	4.75	4.36	4.1 4.75
P ₂ O ₅	0.26	0.24	0.25	0.25	0.21	0.28	0.28	0.21	0.25	0.27	0.29	0.22	0.24	0.29	0.22	0.24	0.17	0.17	0.17 0.18
Tot	97.5	98.0	98.0	99.3	99.9	99.6	100.1	99.0	100.6	100.1	99.8	100.3	99.4	99.8	100.0	98.9	99.4	101.1	99.6 98.38
Bi(wt%)	15.8	16.2	14.0	16.4	12.9	13.6	14.0	14.1	12.6	11.7	10.9	10.5	10.0	10.5	8.0	8.1	8.2	4.2	4.8 1.4
KV(wt%)	16.0	13.0	18.1	10.1	17.5	17.4	17.5	23.1	18.9	19.9	18.3	21.6	27.5	23.4	21.7	23.8	23.2	23.3	21.4 27.2
Ab(wt%)	28.1	28.3	27.5	30.3	27.3	27.5	26.9	26.4	30.1	30.1	29.2	28.3	27.4	29.4	34.9	29.4	30.2	32.9	31.7 33.3
An(wt%)	14.5	14.0	12.9	14.3	10.9	11.7	10.4	12.1	11.6	10.7	8.9	8.0	8.7	9.3	8.1	7.6	7.2	5.5	3.8 2.3
Q(wt%)	24.6	27.3	26.1	29.2	31.3	29.5	30.3	24.1	27.5	28.0	31.6	30.5	25.2	26.6	26.5	29.3	29.6	33.7	36.1 32.0
DI	68.7	68.7	71.8	69.8	76.2	74.4	74.9	73.7	76.6	78.1	79.2	80.5	80.2	79.6	83.2	82.6	83.1	89.9	89.3 92.6
Nb	15	14	15	16	13	13	14	13	11	12	12	13	11	11	14	11	11	11	10 6
Zr	223	218	213	210	183	192	190	186	182	155	152	146	151	144	116	115	115	68	68 47
Y	30	33	33	34	31	33	34	31	29	30	29	28	25	24	26	25	15	25	16
Sr	186	182	185	160	134	156	177	178	215	207	156	145	196	182	163	166	149	114	82 59
Rb	168	182	161	181	193	191	222	191	177	216	246	276	261	216	267	258	252	221	236 253
Th	13	17	18	12	16	15	14	13	14	15	15	16	14	16	12	10	10	7	8 6
Pb	22	29	22	21	24	28	28	26	27	28	24	24	37	30	33	27	29	28	32 32
Zn	68	51	63	67	58	63	66	60	56	59	94	54	61	53	35	53	41	21	37 22
La	22	37	37	29	26	22	20	22	23	20	25	24	23	20	10	13	14	7	1 7
Ba	621	686	557	396	461	603	712	882	637	522	370	396	826	644	713	586	408	319	173 181
Ti	4934	4196	4731	5121	3441	3848	4459	4343	3089	2836	2916	2706	2580	2740	2101	2275	1992	1000	868 251
P	1571	1209	1496	1344	973	1163	1343	1467	1009	1311	1299	1338	1278	1145	1039	1051	1074	699	795 986
Cs	8	8	10	12	18	12	12	9	18	22	28	29	12	15	22	16	24	19	11 13

For calculation of the weight-norms the average biotite composition for this part of the intrusion (CHAPTER 3), $K_2(FeMgTi)_6(Si_2Al_2)O_{20}(OH)_4$ is used. The normative data are plotted in a Q'-ANOR diagram (Fig.2), proposed by Streckeisen and Le Maitre (1979) for conversion of normative data to the modal QAPF-nomenclature. The figure shows that the rocks range from granodiorites (squares and closed circles) to granites (asterisks). Four granodiorite samples plot in the monzogranite field. These samples have essentially granodioritic characteristics, but are relatively intercumulus rich.

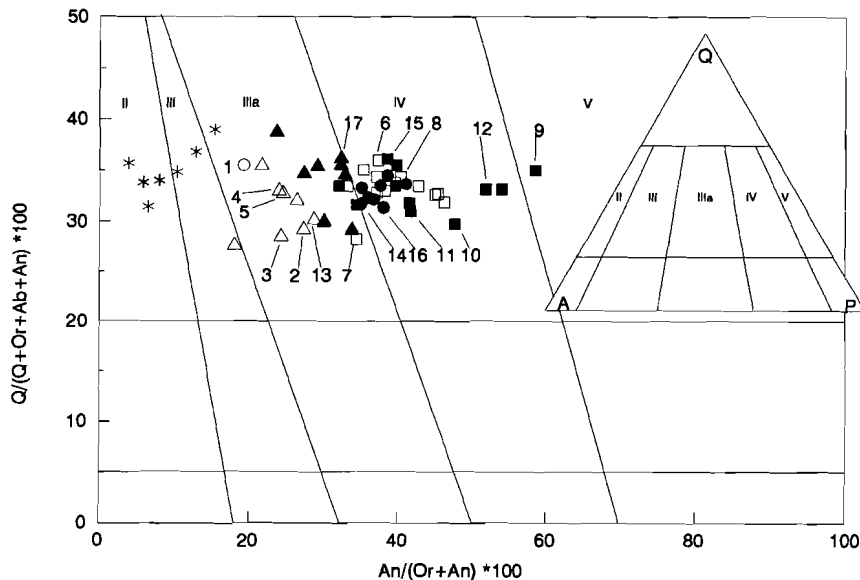


Fig.2. Chemical classification of the intrusive rocks (after Streckeisen and Le Maitre 1979) The symbols and the numbers correspond with those in Fig.1. The Roman numerals correspond with those in the conventional QAPF-diagram.

The normative minerals are plotted against a Differentiation Index ($Q + Or + Ab$, Thornton and Tuttle 1960) in figure 3. Biotite (Fig.3a) and anorthite (Fig.3b), and to a lesser extent K-feldspar (Fig.3c) correlate well with DI. Biotite forms one trend. For anorthite two trends appear, one (I) for the main granodiorite (squares) and another (II), with slightly enhanced An-content, for the Linares granodiorites (circles), monzogranites (triangles) and aplites (open circle and asterisks). The variation of albite is more complex (Fig.3d). Sample 44, which has a deviate composition (Table 4), is collected near a migmatite contact (Fig.1). It contains abundant cordierite, sillimanite and andalusite and is therefore expected to be strongly contaminated with metasedimentary material.

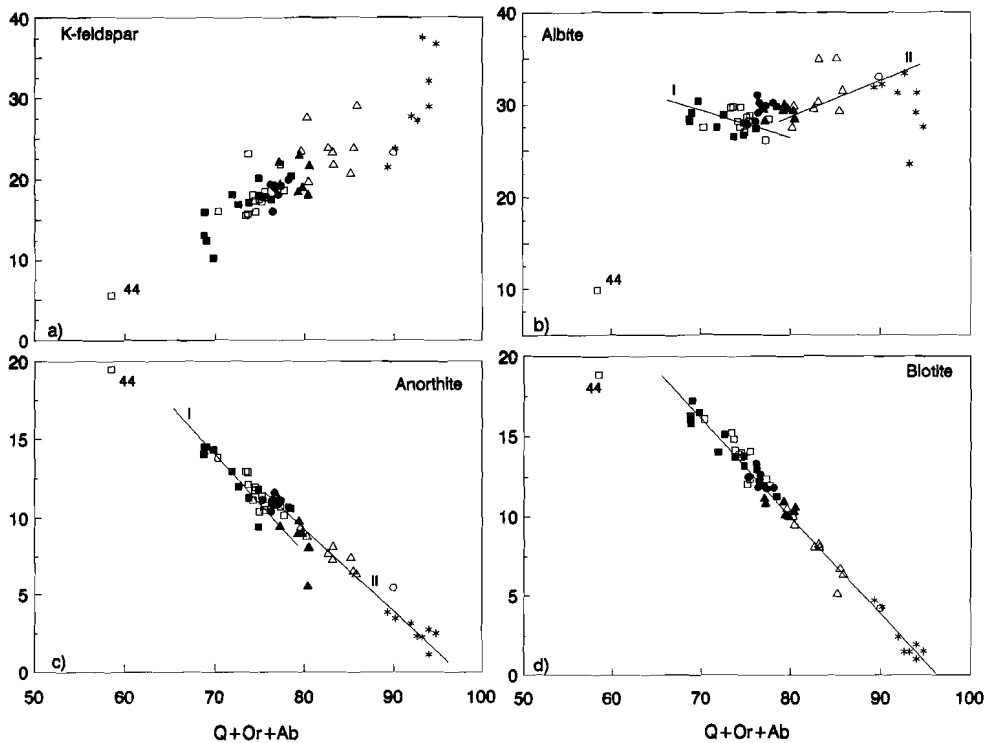


Fig.3. Normative composition of the rocks plotted against the Differentiation Index (Q+Or+Ab, Thornton and Tuttle 1968). The solid lines indicate the directions of the normative trends. For symbols see Fig.1.

Major elements

The samples are plotted in a diagram (Fig.4) proposed by Debon and Le Fort (1983) to classify magmatic associations. They defined the term "association" to describe a group of samples showing a community of characteristics and originating from the same igneous body or from a related set of bodies. They distinguished aluminous (I), alumino-cafemic (II) and cafemic (III) associations. The compositional fields for the three types of associations are indicated. Cafemic associations may proceed either from an exclusively mantle source, or from a mixed crustal and mantle source with prevailing mantle component. The alumino cafemic associations probably also have a mixed origin, with either predominantly crustal or mantle contribution. The aluminous associations are mainly or totally derived from the anatexis of sialic material (Debon and Le Fort 1983). The arrows represent a number of different plutonic associations from Hercynian terrains: Pyrenees (PY, domain III), Corsica (BS, domain II), Massif Central (AU, GU, domain I). All samples are peraluminous ($A > 0$). All monzogranites and the majority of the granodiorites plot within the aluminous domain (I). The remaining granodiorites plot either within the aluminoCAFEMIC domain (II) or in the overlap between I and II.

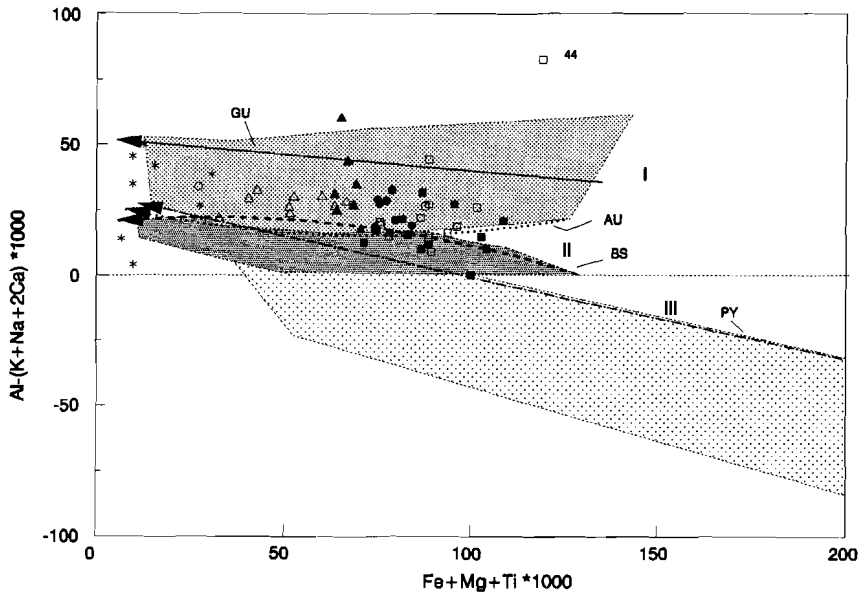


Fig.4. A-B diagram (after Debon and Lefort 1983) to identify magmatic associations. Meaning of the fields I, II, and III and the four arrows (GU, AU, BS, PY) is explained in the text. For symbols see Fig.1.

Most samples seem to be part of one magmatic association. Whether this is an aluminous or aluminocafemic association is not clear, but because of its relatively high aluminosity, it can be expected that the magma was formed predominantly by melting of crustal material. This would confirm earlier conclusions made on the basis of REE-modelling (CHAPTER 2).

Feldspars

The texture, chemistry and abundance of the plagioclase is very variable in all rocktypes. The anorthite percentage of zoned crystals in the granodiorites ranges from 55% (cores) to 20% (rims) (CHAPTER 3). In the monzogranites, plagioclase crystals are generally less euhedral. Individual grains may have calcic cores, with up to 50% anorthite. The rims generally have An-contents between 10% and 20%. The occasional high anorthite content indicates that the cores of some of the plagioclases in the monzogranites are relatively old in the magmatic evolution.

While the whole rock anorthite content decreases from 15 wt% in the granodiorites to 6 wt% in the monzogranites, the average An content in plagioclase drops from 37 wt% to less than 20% (Fig.5). However, samples 16, 3 and 5 have rather enhanced average An contents compared to the rest of the samples, and the compositional ranges of samples 16 and 17 and 3 are relatively large (Fig.5). This will be discussed in a later section.

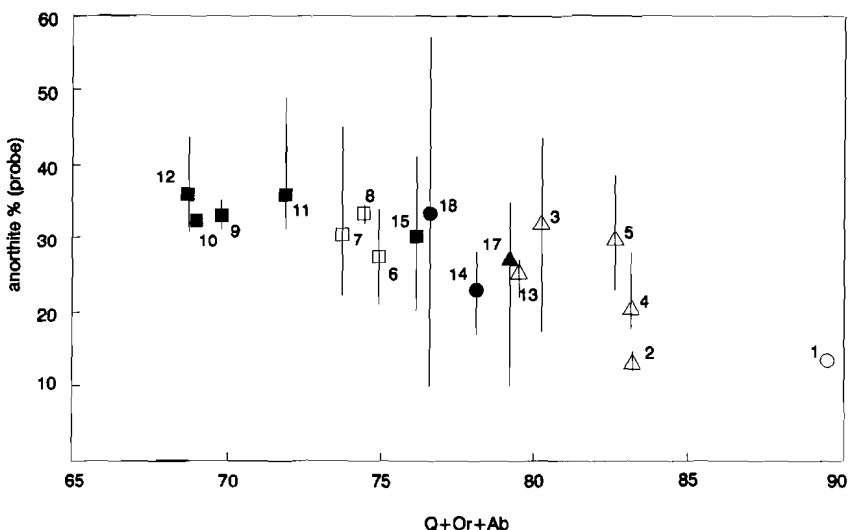


Fig.5. Anorthite content of plagioclases (electron microprobe analyses) as a function of the Differentiation Index of the corresponding sample. Vertical lines represent the compositional range in each sample and the symbols mark the average composition. The symbols and numbers correspond with those in Fig.1.

K-feldspar is developed both as intercumulus perthitic mineral and as large euhedral phenocrysts up to 10 cm. in size. The intercumulus perthitic feldspar occurs in all granitic rocks, representing, together with quartz, a later crystallization stage. The normative amount of K-feldspar generally increases with DI of the rock (Fig.3c). Euhedral phenocrysts are particularly abundant in the MCG. Their abundance in the monzogranites is in the order of 100 to 200 crystals per m² outcrop and may locally reach cumulus like amounts, while the granodiorites contain usually less than 60 phenocrysts per m² outcrop. In the monzogranite, the phenocrysts are mostly oriented, more or less parallel to the intrusive contact with the metasedimentary country rocks. On a small scale, they occasionally show a whirly circular orientation, presumably indicating magma flow. The phenocrysts are compositionally zoned, which is emphasized by bands of small biotite inclusions parallel to the crystal planes. This typical zoning is attributed to a pulsed growth (Aparicio et al. 1983). The chemical composition of the feldspars will be discussed in a later section.

Micas

Biotite is the main mafic mineral in all granitic rocks. The normative amount varies between 20% and 15% in the granodiorites, and between 12% and 3% in the monzogranites (CHAPTER 3). There is an excellent negative linear correlation between the normative amount of biotite and the DI (Fig. 3a).

The biotites of ten granodiorite, six monzogranite, and one microgranite samples were analyzed with electron microprobe. The main compositional variation in the biotites is related to changes in magma composition during differentiation (CHAPTER 3).

Muscovite exclusively occurs in the monzogranites (Rottura et al. 1989), and is developed as : 1) a magmatic looking coarse grained phase, in cases coexisting with biotite; 2) a fine grained hydrothermal phase along cracks in feldspars and; 3) a fine grained sericitic generation replacing plagioclase. The wide compositional range of the magmatic muscovites (CHAPTER 3) indicates that the crystallisation of primary muscovite may have started at the magmatic stage, but continued in the postmagmatic stage. The magmatic origin of part of the muscovite implies that the granite is peraluminous by itself and therefore that the crystallization of muscovite does not automatically imply addition of aluminium due to contamination.

Cordierite

The occurrence of cordierite is restricted to the monzogranites and aplites, where it constitutes between 1 and 5 modal %. It occurs as prismatic crystals of about one cm. in size, and is normally totally altered to greenish chloritic-muscovitic aggregates. Fresh cordierites are rare. The ideas about the origin of the cordierite are controversial. According to Ugidos (1974) the cordierites represent xenocrystic, residual minerals from assimilated pelitic material, implying strong contamination with metasedimentary material. According to Bea (1982) it is of orthomagmatic origin, and crystallized relatively late in the magmatic process. Our study reveals a number of features that support the orthomagmatic theory. 1) Electron microprobe analyses of fresh cordierites reveal high Na_2O contents (between 0.99 and 1.58, Table 2). Similar sodium contents in cordierites from the Piedmont granites, USA, formed an argument for Speer (1981) to classify them as magmatic. Sodium values in metamorphic cordierites are generally less than 0.5 wt% (Leake 1960). 2) Comparison with analyses of cordierites from sedimentary hornfels xenoliths in the monzogranite reveals very clear differences between the two types of cordierite (Table 2). The cordierites in the monzogranite have lower SiO_2 , Al_2O_3 and totals, and significantly higher Na_2O than those from the xenolith. Would the cordierites in the monzogranite represent residual minerals from assimilated metasedimentary material, the compositions of the two types would be expected to be more similar, unless the granitic cordierite has reequilibrated while the xenolithic cordierite has not. The absence of zoning within a single crystal however precludes reequilibration.

3) Cordierite is abundant in many aplites, and reaches a crystal size of more than 10 cm. in pegmatitic dikes.

Table 2. Average composition of cordierites from monzogranite and hornfels xenolith.

	granites		xenolith	
	avg	stdev	avg	stdev
SiO_2	46.5	0.3	47.8	0.24
TiO_2	0.0	0.0	0.0	0.0
Al_2O_3	31.8	0.15	32.9	0.13
FeO	8.9	0.49	9.0	0.24
MnO	0.5	0.08	0.6	0.02
MgO	6.3	0.29	6.3	0.16
CaO	0.0	0.00	0.0	0.00
K_2O	0.012	0.010	0.03	0.03
Na_2O	1.22	0.17	0.89	0.07
tot	95.4	0.29	97.7	0.44

Accessories

The accessory minerals in all granitic rocks are ilmenite, apatite, zircon, monazite and magnetite. These minerals are all closely associated with and often enclosed by biotite. Ilmenite composition is highly variable with respect to its MnO content (CHAPTER 3). Apatite occurs as both rounded and elongated hexagonal crystals, and is always rich in fluor. Zircon occurs as small rounded grains and as larger idiomorphic crystals, which are often zoned. Tourmaline is exclusively encountered in the monzogranite and aplites.

4.5 TRACE ELEMENTS

Representative whole rock trace element analyses are listed in Table 1. Since trace element patterns usually give a better insight in magmatic processes, more samples were analyzed for trace elements than for major elements. In order to correlate the variation of the trace elements with magmatic differentiation an alternative Differentiation Index is required. As the DI and Zr (Fig.6a) correlate strongly, Zr is used in this section as DI.

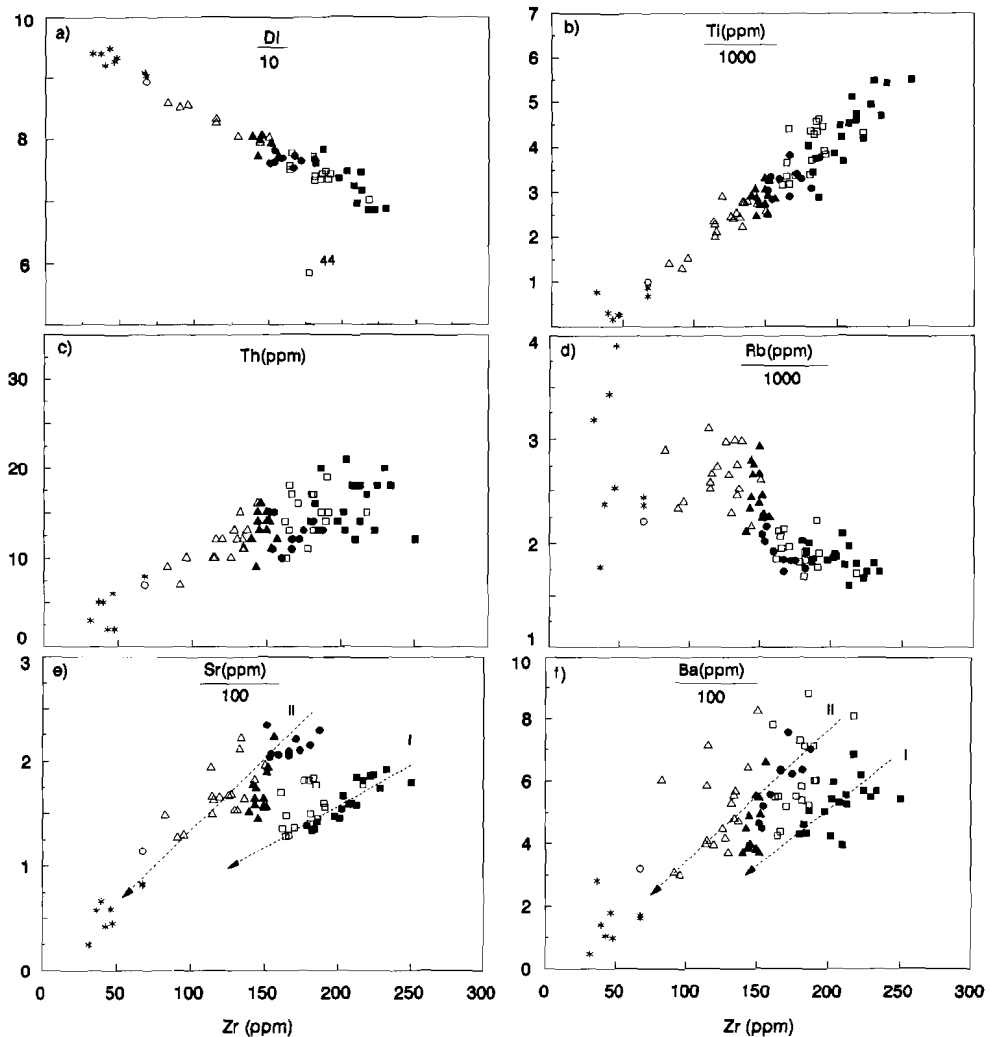


Fig.6a-f. Relation between Zr and DI ($Q+Or+Ab$), and relation between Zr, used as DI and Ti, Th, Rb, Sr and Ba. Dashed arrows represent inferred compositional trends (I and II) for Sr and Ba. For symbols see Fig.1.

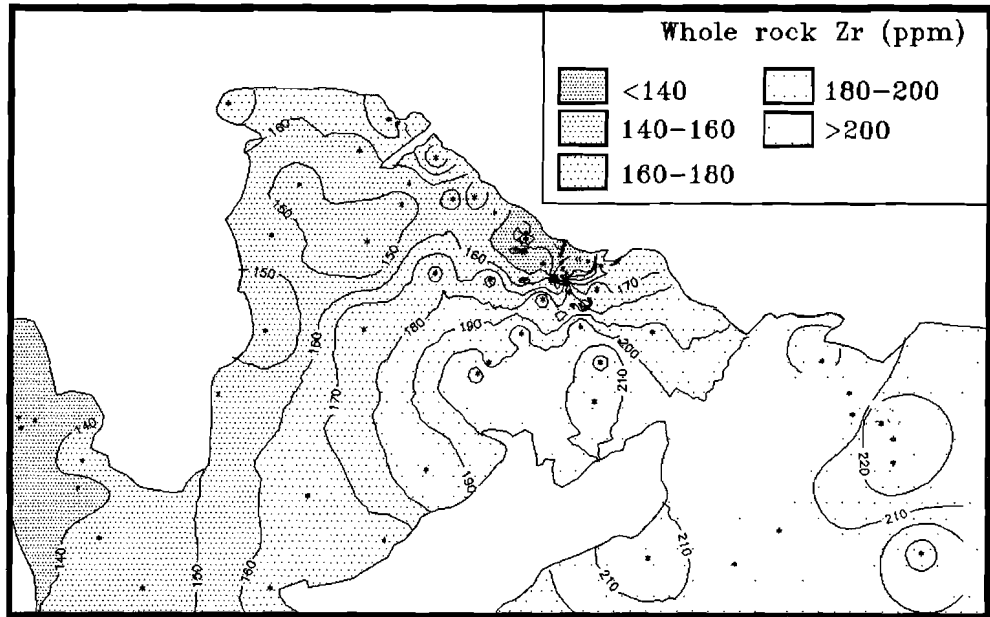


Fig.7. Zoning of the intrusive complex, illustrated by a contour map of Zr in ppm. Small asterisks indicate the sample locations. For contour map of Zr/Rb ratio see CHAPTER 6.

The spacial distribution of Zr (Fig.7) demonstrates the complex zonal pattern of the intrusion. In addition to a general decrease in Zr from east to west, it drops strongly in vicinity of the Los Santos tungsten skarn. The zonal pattern is confirmed by the results of an airborne radiometric survey (CHAPTER 6). Two types of element associations can be distinguished on the basis of the correlation with Zr: elements like Ti, Y, Th and La (Fig.6b,c) that correlate well, and elements that show a more complex relation with Zr: Rb, Sr and Ba (Fig.6d-f). In contrast to Rb, which shows a curved but continuous trend, Ba and in particular Sr display two very distinct trends. Trend I, with relatively low Sr and Ba is formed exclusively by the Main granodiorites (squares). Trend II, with high Sr and Ba includes the Linares granodiorites (solid circles), monzogranites (triangles), microgranite (open circle) and aplites (asterisks). A few Main granodiorites (trend I) have relatively elevated Ba- and Sr content (open squares). The granodiorites of trend II are more felsic than many samples of trend I (Figs.2,4,6a-e). The behaviour of Sr and Ba was an important reason for Rottura et al. (1989) to propose two different magmas for the granodiorites and the monzogranites. However, as the data presented in CHAPTERS 2 and 3 strongly argue for one magma, alternative explanations, like magmatic contamination and hydrothermal alteration, have to be considered to explain the deviate behaviour of Sr and Ba.

Trace element modelling

The elements Sr, Ba and Rb are normally pre-eminently suitable for fractionation modelling and process identification, because of their well known partitioning behaviour between the rock forming minerals plagioclase, K-feldspar and biotite (Tindle and Pearce 1981, Michael 1984). Modelling is one way to assess the influence of crystallization, magma mixing and contamination.

For trace element modelling of granite fractionation a number of assumptions must be made concerning initial melt composition, solid/melt distribution coefficients, mineralogy of the crystallizing solid, physical and chemical crystallization conditions and the type of fractionation. The complications related to these factors are extensively discussed by many authors (e.g. Arth 1976, McCarthy and Hasty 1976, Allegre and Minster 1978, see CHAPTER 2). Obviously the complexity of the fractionation process, combined with the high degree of uncertainty concerning the above factors usually forces one to model qualitatively rather than quantitatively.

Our model will be based on a number of assumptions, thus simplifying the extremely complicated process of crystal fractionation.

- 1) The type of crystallization lies somewhere between the extremes of equilibrium and perfect Rayleigh crystallization, as high viscosities in granitic melts usually prohibit efficient separation of solid from melt (Tindle and Pearce 1981).
- 2) The formula used for modelling is that for Rayleigh fractionation (Hanson 1978) : $C_1/C_o = F^{(D-1)}$, where C_1 is the residual melt composition, C_o the original melt composition, F the fraction of melt left and D the bulk distribution coefficient for the crystals settling out of the melt.
- 3) Mineral/melt distribution coefficients are constant. The distribution coefficients used for Rb, Ba and Sr in plagioclase (Table 3) and K-feldspar are from McCarthy and Hasty (1976) and in biotite from Hanson (1978).

Table 3. Distribution coefficients, ¹⁾ from McCarthy and Hasty (1976), ²⁾ from Hanson (1978), used for trace element modelling.

	Plagioclase ¹⁾	K-feldspar ¹⁾	biotite ²⁾
Ba	0.4	6	6.36
Rb	0.04	0.8	3.26
Sr	3.35	3.6	0.12

- 4) The starting composition for the melt is chosen at: Ba=520ppm, Sr=150ppm, Rb=200ppm and Zr=205ppm, which is approximately the average composition of the uncontaminated granodiorite (Table 4). Changing this starting composition would not affect the directions of the melt and cumulus lines in interelement plots, but only shift their starting points.
- 5) The normative compositions encountered in the granitic intrusion change from granodiorite to granite (Table 1). In order to assess the influence of this changing mineralogy on the positions of cumulus and melt composition lines, they are calculated on the basis of both constant mineralogy and changing mineralogy.

The changing mineralogy is based on the average data presented in Table 4.

Table 4. Average composition of various granite types and sedimentary rocks.

	avg1	avg2	avg3	avg4	avg5	avg6	44	lime	sed i
SiO ₂	67.1	67.9	68.7	69.4	70.3	74.6	66.6	na	64.4
TiO ₂	0.65	0.59	0.51	0.45	0.34	0.11	0.72	na	0.78
Al ₂ O ₃	15.4	15.6	15.7	15.4	15.4	14.2	16.3	na	19.2
Fe ₂ O ₃	4.04	3.81	3.37	2.91	2.22	0.79	5.19	2.68	7.00
MnO	0.07	0.06	0.07	0.07	0.05	0.03	0.08	0.14	0.09
MgO	1.32	1.26	1.14	0.97	0.75	0.19	1.81	na	2.74
CaO	2.49	2.33	2.21	1.78	1.56	0.61	3.93	53.3	0.63
Na ₂ O	3.34	3.32	3.48	3.44	3.64	3.59	1.17	na	1.43
K ₂ O	4.20	4.40	4.35	4.45	4.80	5.12	2.81	na	3.87
P ₂ O ₅	0.24	0.24	0.23	0.25	0.24	0.19	0.12	0.17	0.15
Tot _{Si}	98.7	99.6	99.9	99.2	99.4	99.4	98.8	-	97.5
Bi(wt%)	14.5	13.7	12.2	10.5	8.07	2.57	18.9	-	-
Kf(wt%)	15.4	18.0	18.6	20.2	23.7	28.8	5.58	-	-
Ab(wt%)	28.3	28.1	29.4	29.1	30.8	30.3	9.88	-	-
An(wt%)	12.4	11.6	10.9	8.86	7.73	3.01	19.5	-	-
Q(wt%)	28.0	28.5	28.6	29.8	28.4	33.1	43.0	-	-
Nb	14	13	11	12	12	9	15	6	13
Zr	209	179	167	148	122	50	178	54	169
Y	34	32	31	29	27	20	35	9	32
Sr	152	158	214	163	177	63	182	272	104
Rb	193	193	191	248	264	268	183	<6	143
Th	16	15	13	13	11	5	11	7	14
Pb	23	26	30	26	28	30	27	9	19
Zn	67	63	62	59	56	25	94	99	99
La	31	26	21	20	14	2	35	na	na
Ba	525	619	598	450	500	167	553	0	757
Cs	11	11	16	25	22	18	11	0	8

Av1:main granodiorite, uncontaminated (solid squares); Avg2:main granodiorite, contaminated (open squares); Avg3:Linares granodiorite (solid circles); Avg4:monzogranite (solid triangles); Avg5:monzogranite, contaminated (open triangles); Avg6:applites (open circle and asterisks); 44:contaminated granodiorite near Bejar; Lime: limestone near Los Santos; Sedi: average of 42 schist- and greywacke samples.
na:not analyzed.

As their bulk distribution coefficient is greater than 1, Ba and Sr contents in the residual melt usually decrease during magmatic differentiation processes. For Rb usually the opposite is the case. Therefore Ba and Sr are plotted against Rb (Fig.8a,c). The solid arrows represent cumulus and melt composition lines for progressive Rayleigh fractionation during crystallization of a solid with constant average granodiorite composition. Most of the main granodiorites (squares) fall between those compositional limits, indicating crystal fractionation indeed. The scatter in the main granodiorite can be attributed to variations in the proportions of cumulus and intercumulus (McCarthy and Robb 1978). Some of the main granodiorite samples plot above the melt line, particularly for Ba, implying enrichment of Ba and Sr.

The Linares granodiorite samples (closed circles) and the monzogranites (triangles) plot outside of the granodiorite fractionation field. They also plot outside of the cumulus-melt lines that are calculated on the basis of a changing mineralogy during crystallization (Fig.8b,d). Therefore the deviation from the main granodiorite trend cannot be explained with just a change in mineralogy. These samples all contain too much Sr and Ba. If we would assume a different magma for these rocks, and repeat the modelling with a different starting position of the melt (dashed arrows), we observe that only a small part of the monzogranite samples (mostly the solid triangles) can be fitted between the cumulus-melt composition lines for

crystallization of monzogranite material. The rest of the monzogranite samples display considerable scatter. It is important to note that, in particular for Sr, the Linares granodiorites (solid circles) cannot be fitted in a fractionation trend, since they follow a nearly horizontal direction. Either Ba and Sr, or Rb, or both must have been added from outside to the melt.

The aplites plot on the extension of the main granodiorite trend, which suggests that they represent very late residual melts that are expelled from the main granodiorite body.

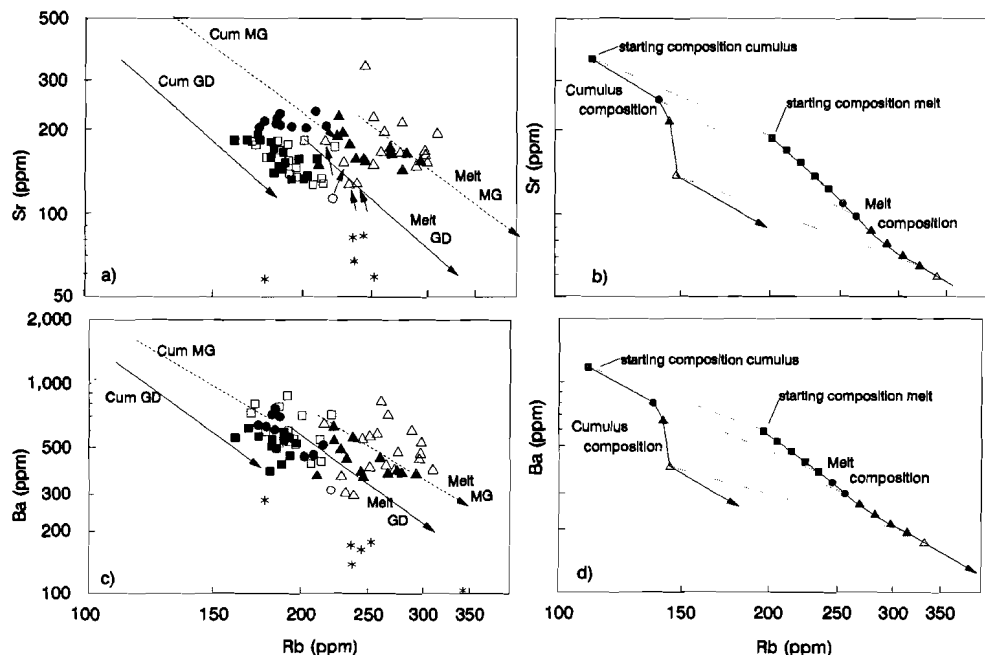


Fig.8a-d. Logarithmic Sr-Rb (a,b) and Ba-Rb (c,d) diagrams. For symbols see Fig.1. The solid and dashed arrows in a and c represent calculated melt-cumulus relationships using average granodiorite (GD) and monzogranite (MG) mineralogy respectively. Parental melt compositions are hypothetical (see text). The curved lines in b and d represent melt-cumulus relationships based on gradually changing mineralogy during fractionation. The symbols (b,d) indicate the mineralogical composition of the solid used for the calculation (see Table 4) at successive steps of 10% crystallisation. The dotted tie-lines connect melt composition with corresponding cumulus composition. Some asterisks are not plotted as they have low Ba and Sr content. Small arrows mark a number of monzogranites that may be depleted in Rb (see Fig.9).

Modelling for contamination

Although it is fairly clear that some elements have been introduced into the magma from an outside source, the relationships observed above do not indicate whether the addition concerns only Sr and Ba, or also Rb. An attempt to define the nature of the contamination more accurately, is made by modelling Ba, Sr and Rb separately, using Zr as an independent fractionation index.

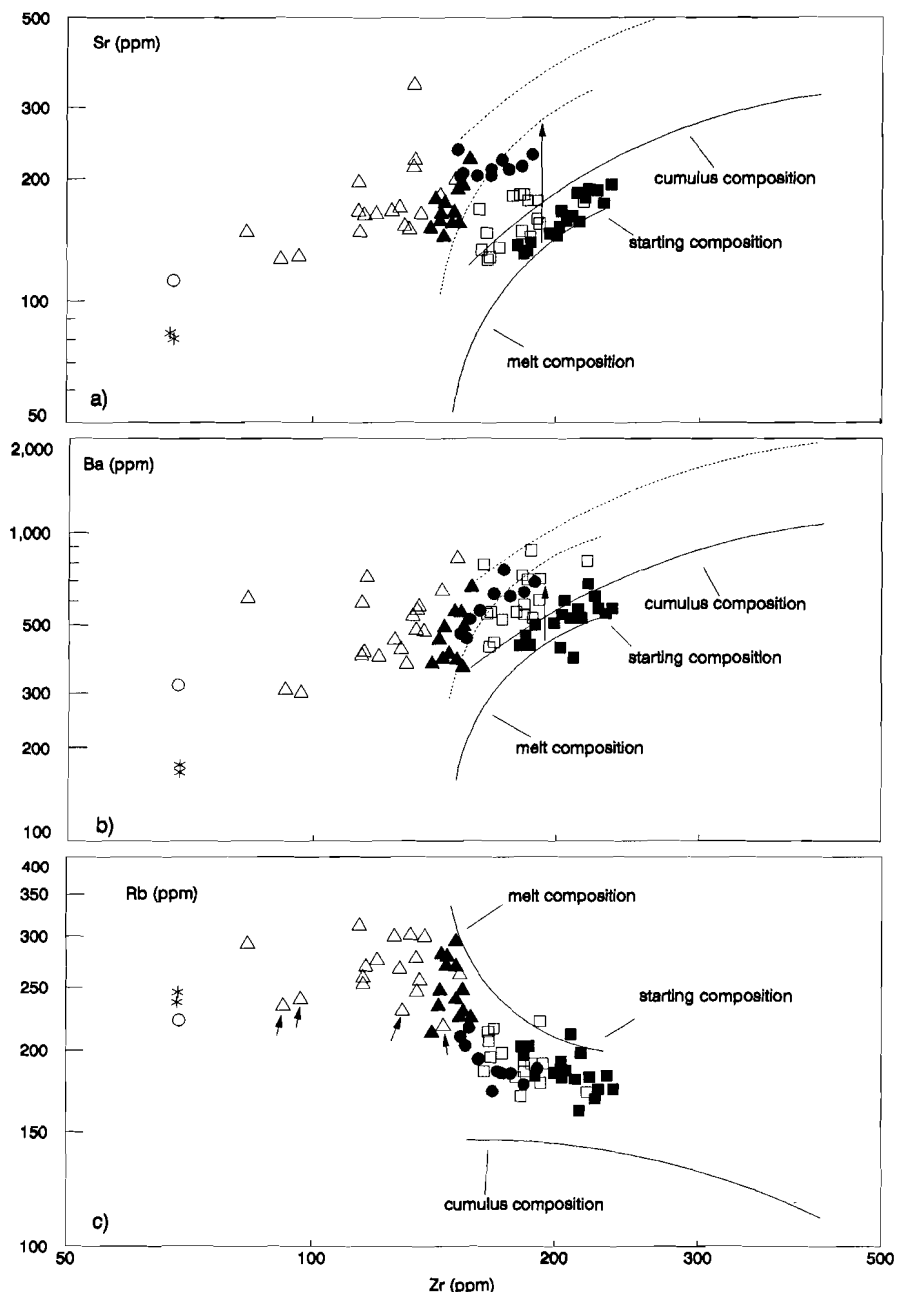


Fig. 9a-c. Logarithmic diagrams of Sr-Zr(a), Ba-Zr(b) and Rb-Zr(c) contents, compared with theoretical melt-cumulus relations (solid lines) in a model with changing mineralogy during fractionation. The dashed lines also represent the theoretical melt-cumulus relations, but for enhanced Sr- and Ba contents (vertical arrows). For symbols see Fig. 7. Aplites with less than 50 ppm Zr are not plotted. Marked triangles (small arrows) are monzogranites that are probably depleted in Rb.

The results of course have to be interpreted with caution, since Zr generates its own mineral: zircon. This causes uncertainties in the use of the solid/melt distribution coefficient (D_{Zr}). But the results may serve our purpose, which is to test whether Rb, Ba and Sr are likely to have suffered from contamination. Since we found that the Main granodiorite trend (Fig.8) represents fractionation, not influenced by contamination, we determined D_{Zr} by fitting the melt- and cumulus lines along trend I, resulting in a D_{Zr} of 4000. This value seems realistic as the calculated $D_{Zr} = [Zr_{(solid)}]/[Zr_{(melt)}]$ (Haskin 1984), lies between 5000 and 2500 for the monzogranites and granodiorites. The melt lines and associated cumulus lines are again based on observed changes in mineralogy. The results show that as far as Rb (Fig.9c) is concerned, the general trend is parallel to the calculated liquidus trend, implying that the enrichment in Rb can be a result of magmatic differentiation, and that it is not necessary to assume Rb contamination. For Sr (Fig.9a) most Main granodiorite samples plot between the melt-cumulus lines. For Ba (Fig.9b) a part of these samples plot however above the cumulus line. These samples have been distinguished by open squares, as they probably were contaminated with Ba, and to a smaller extent also with Sr. All Linares granodiorite and all monzogranite samples plot above the calculated cumulus line and must therefore have been enriched in Sr and Ba. Would these rocks represent a second magma, enriched in Ba and Sr, but for the rest nicely fractionated, it should be possible to fit their compositions between the melt-cumulus lines by shifting the lines in vertical direction (arrows). As this is not possible (Figs.9a,b), we must conclude that contamination of Sr and Ba interfered with fractionation indeed.

When we look more carefully at this contaminated group of samples, we may be able to separate the effects of contamination and fractionation.

The Linares granodiorite (solid circles) shows a small compositional trend that, in particular for Sr, crosses the melt composition line. Such a trend probably indicates that the magma was progressively contaminated during crystallization of the Linares granodiorite, and more strongly so for Sr than for Ba.

The monzogranites (triangles) can be divided empirically into two groups, on the basis of their Ba content (Fig.9b). Those that seem to plot within the calculated melt-solid compositional range (black triangles), are distinguished from those that have too high Ba (and Sr) to fit the fractionation trend (open triangles). The black triangles, which are the least felsic of the monzogranites (Fig.2), are the same as those that also fit between the melt-solid lines in figures 8a,c. Therefore the compositional variation of this group is compatible with fractionation of a melt that was already enriched in Sr and Ba: e.g. the Linares granodiorite. The open triangles represent more felsic monzogranites (Fig.2). They are enriched in Ba as well as Sr, compared to the black triangles. For this group, crystal fractionation trends are obscured by the addition of Ba and Sr. The high degree of scatter within this group indicates however that the process that caused the enrichment was irregular. Additionally, it might be that some of these rocks are depleted in Rb. We refer in particular to the four open triangles that plot below the dashed cumulus line in Figure 8a, which correspond with the four marked triangles in Figure 9c. Loss of Rb-enriched fluids would be compatible with the observation, that the contact metamorphic metasediments near Los Santos show a systematic enrichment in Rb (CHAPTER 5). In addition, the data (Fig.9) indicate depletion of Zr in the most fractionated monzogranites (open triangles) and aprites (asterisks). These rocks may have been affected by late stage volatile-rich phases, which have the capacity of mobilizing or removing relatively immobile elements (Hanson 1978).

It is probably very confusing to distinguish the effects of all the processes described above (fractionation, contamination, depletion), as they all interact to some degree.

Therefore we summarize the effects of the these processes in Figure 10. A: crystal fractionation (Main granodiorites); B: Sr and Ba contamination (some Main granodiorites and the Linares granodiorite); C: Sr and Ba contamination and some fractionation (Linares granodiorite); D: fractionation of contaminated magma (least fractionated monzogranites); E: contamination with Sr and Ba, fractionation and loss of Zr (most fractionated monzogranites and aplites); F: loss of Rb in addition to E.

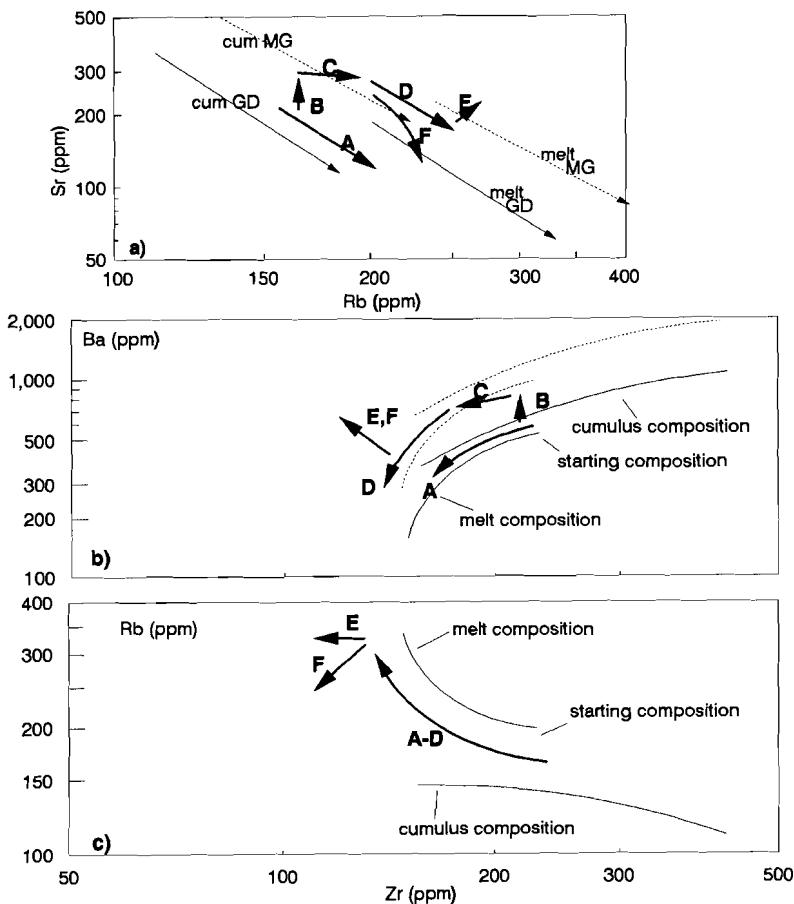


Fig.10a-c. Summary of the effects that various combinations of fractionation, contamination and depletion have on the magma composition during the various stages of its evolution (see section on contamination modelling).

4.6 POSSIBLE SOURCES OF ENRICHMENT FOR Sr AND Ba

The origin of the contamination can either be magmatic (e.g. magmatic fluids), hydrothermal (e.g. along fault zones) or sedimentary (e.g. along the intrusive contact). In addition, sedimentary contamination may have been selective for certain elements only. In order to have more clues on the origin of the Ba and Sr, we have looked at the spatial distribution of the various granitic groups (Fig. 1).

The uncontaminated Main granodiorites (solid squares) are located in the central part of the intrusion. A number of contaminated granodiorite samples (open squares) is clearly related with faults. Another group of open squares is located near the tungsten skarn of Los Santos. Two open squares, near Bejar, are near to the contact with the migmatites.

The Linares granodiorite (solid circles) is exclusively found along the northern contact, west of Los Santos, exactly where the intrusion intersects with the Cambrian limestone formation. The presence of both giant skarnoid limestone blocks and metasedimentary xenoliths within the granite prove that stoping took place (Saavedra 1978), and as large parts of the limestone formation between Los Santos and Linares have disappeared, there is little doubt that reaction with the magma took place. One available analysis of a limestone (Table 4) indicates that the Sr content of these rocks is sufficiently high to cause contamination. It may not be responsible for the enrichment of Ba however, as the Ba content of this sample is very low. Alternatively, Ba could be that from the schists and greywackes, as these rocks have high average Ba content (Table 4). Individual samples may even contain up to 1300 ppm Ba.

The monzogranites represented by solid triangles form a zone directly adjacent to the Linares granodiorites. The results of trace element modelling indicate that Ba and Sr variation in these samples could represent a fractionation sequence, but that they are derived from a readily contaminated source magma. Their position adjacent to the contaminated Linares granodiorites therefore indicates that these granodiorites and monzogranites originate from the same melt, that was contaminated early, during the crystallization of the Linares granodiorites, but before crystallization of the monzogranites.

The monzogranites represented by open triangles are more felsic compared to the other monzogranites (black triangles), and as they are located in zones contiguous to the zone of solid triangles, we suggest that they belong to the same fractionation series as the contaminated Linares granodiorites and the derived monzogranites (CHAPTER 2).

Results of trace element modelling however strongly suggest considerable, but very variable contamination and as the location of both of these open triangles coincides with mineralization of tungsten and tin, near Los Santos and Miranda del Castañar, we conclude that these monzogranites are additionally contaminated very late in the crystallization history, due to fluid interaction with the metasediments during the mineralizing event. It was already demonstrated in CHAPTER 3, that fluids played a more important role in the magma adjacent to Los Santos than in the rest of the intrusion.

Petrological evidence for contamination

If the contamination occurred locally during the magmatic stage, it is expected that the composition of zoned feldspars and biotites provide additional evidence, since these minerals are the main hosts for those

elements and may have recorded changes in chemical composition of the melt. Therefore the major element composition as well as the Sr and Ba content of a number of zoned plagioclases, K-feldspar phenocrysts, biotites and also late interstitial K-feldspar from samples representative for trend I: Main granodiorites (closed squares, samples 9,10,11,12,15, and open squares, samples 6,7,8) and trend II: Linares granodiorite (closed circles samples 14, 16), and associated monzogranites (closed triangles, sample 17, and open triangles, samples 2,3,4,5) were investigated in detail, using electron microprobe analysis.

Sr turned out to be below the detection limit in most analyses, but a parallel behaviour to that of Ba is expected on the basis of the similar variations of whole rock Ba and Sr. The Ba content in the K-feldspars is plotted against $\text{Na}_2\text{O}/\text{K}_2\text{O}$ (wt%) (Fig. 11a). Analyses of a phenocryst from sample 6 are marked "f". All other analyses are from interstitial K-feldspar. The symbols are the same as in the previous figures. The phenocryst has higher Ba content than most of the interstitial feldspar. The Ba content in the interstitial feldspar is generally below 0.25%, except for two analyses from sample 16, with very high Ba-contents, and one from sample 2. The phenocryst analyses were made on a profile from core to rim. The Ba content is presented as a function of the distance to the core (Fig. 11b). The drastic rise of the Ba content near the rim provides evidence that the magma indeed was contaminated with Ba, perhaps towards the final stage of crystallization.

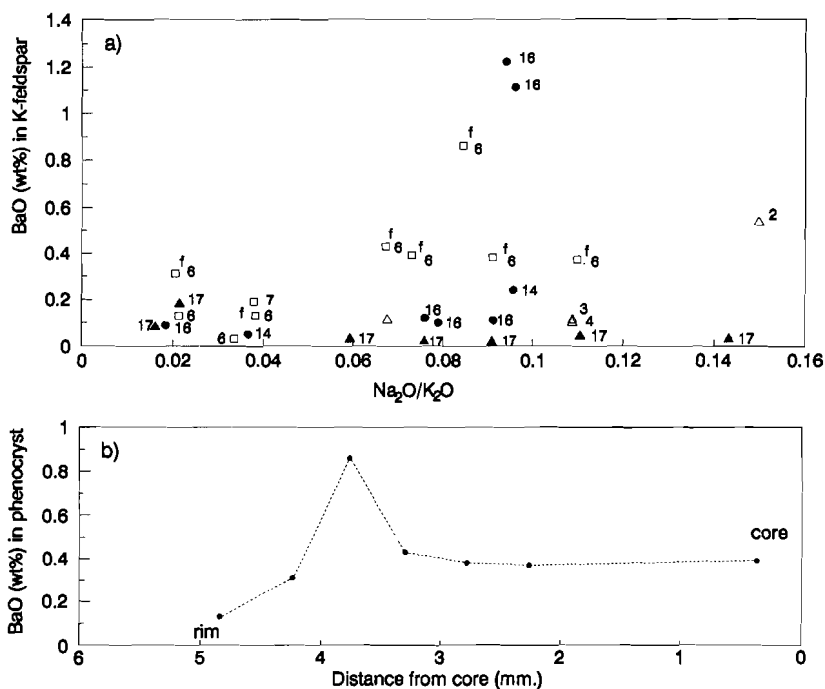


Fig.11a,b. Ba content (electron microprobe analyses) of K-feldspars plotted versus the $\text{Na}_2\text{O}/\text{K}_2\text{O}$ ratio. Symbols are the same as used in Fig.1. The numbers represent the sample numbers (see Fig.1). The analyses marked by an "f" are from a profile through one K-feldspar phenocryst, which is presented separately in Fig.11b.

The Ba content of the plagioclases is presented (Fig.12) in a similar way as their An content in (Fig.5). This demonstrates the large contrast between the Ba content of samples 16 and 17 (0 to 0.11 %) and that of all others (0%).

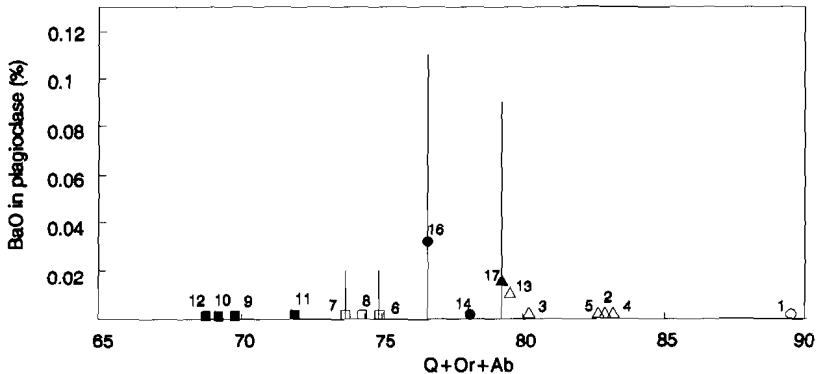


Fig.12. BaO content of plagioclases as a function of the Differentiation Index ($Q+Or+Ab$) of the corresponding sample. Ranges of each sample are represented by vertical lines. Average are indicated with symbols. For symbols and numbers, see Fig.1.

Various profiles across zoned plagioclases were analyzed, and representative examples demonstrate a large compositional contrast between the plagioclases representative of the main granodiorite trend (Fig.13a) and the others (Figs.13b-e). In the plagioclases of the main granodiorite trend (samples 7, 11 and 15; Fig.13a), Ba was below the detection limit, while in the plagioclases of samples 16 and 17, Ba is very variable. Also the anorthite content of the plagioclases in sample 17 (Fig.13b,c) and 16 (Fig.13d,e) is different to that of the main granodiorite trend (Fig.13a). The An content for is more irregular and much higher in the cores, but at the same time much lower in the rims, compared to the plagioclases of the main trend. The compositional range from core to rim in samples 16 and 17 is much wider (58% to 15%) than in the plagioclases of the main trend (45% to 25%). This is a curious situation, if we consider that, in many respects (see also CHAPTERS 2,3), the Linares granodiorites are more felsic than the Main granodiorites, but less felsic compared to the monzogranites. This suggests a large amount of Ca that was suddenly added to this magma, was rapidly buffered by crystallization of An-richer plagioclases. The high BaO and relatively high CaO values in the cores of the plagioclases of samples 16 and 17 indicate that the magma must have been enriched in these elements in a very early stage, and the high Ba contents in the rims of the plagioclase indicate that the magma was rich in Ba at least until most of the plagioclase crystallized. The high degree of variation in Ba and An in the plagioclases of these samples indicates pulsewise contamination of the magma during its crystallization. The plagioclases of the contaminated monzogranites (samples 2-5 and 13, open triangles) have a low Ba content, but the interstitial feldspar of sample 2 is rather high, which may support relatively late magmatic. We realize however than many more K-feldspar analyses should be

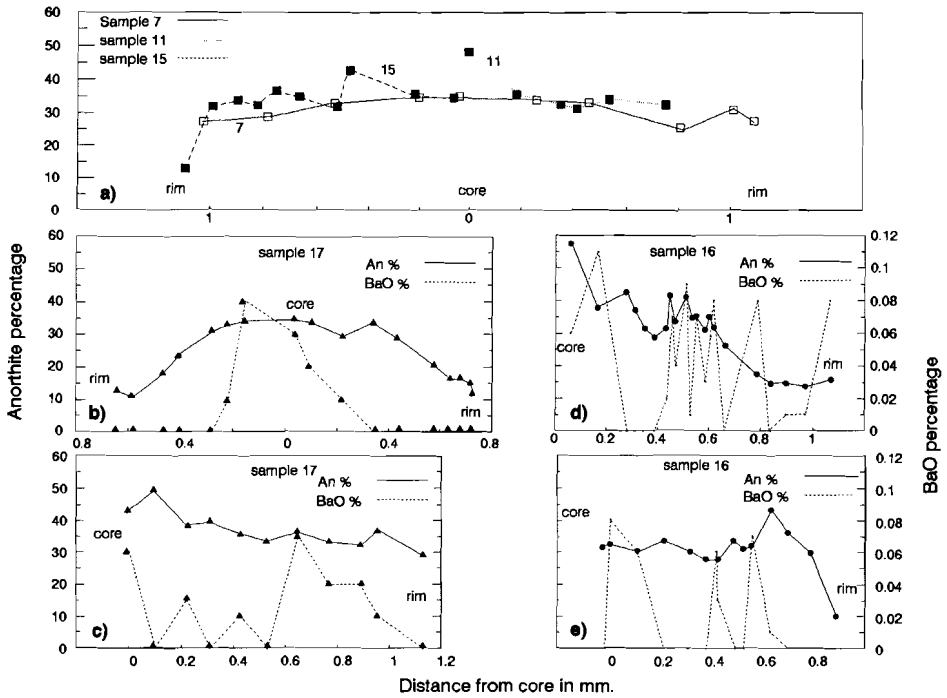


Fig. 13a-e. BaO and An percentage along profiles through zoned plagioclases as a function of the distance to the core. Fig.13a: samples 7,11,15 (BaO was below detection limit in these samples); Fig.13b,c: Sample 17; Fig.13d,e: Sample 16.

carried out before this conclusion can be drawn with certainty.

Many of the biotites are chemically zoned (CHAPTER 3). The zoning is however difficult to interpret in terms of timing of crystallization since, unlike for plagioclase, there is no way to tell petrographically which part of a biotite is early and which is relatively late. The results indicate anyway that often the core of a biotite is not the earliest crystallized part. Therefore we only present the compositional range and the average composition of the biotites (Fig.14a,b). Most biotites have a wide range of Ba values, up to 0.3 wt% BaO, but the average Ba content is fairly constant, slightly decreasing towards the more fractionated rocks. Again sample 16 distinguishes from the others, with a large compositional range (0 to 0.53 wt%), and a high average value (0.29 wt%). Ba is the only element by which the biotites of sample 16 distinguish from those of the other samples. For all other elements analyzed sample 16 nicely fits the chemical trend, as is exemplified by Al_2O_3 (Fig.14b, see CHAPTER 3). In this figure only the biotites of sample 6 have a higher Al_2O_3 content than expected on the basis of its DI.

In samples 16 and 17 late carbonate veins are present. Electron microprobe analysis reveals that these are

pure calcite, not containing any detectable Sr or Ba. This indicates that post magmatic Sr and Ba contamination may not be of much importance.

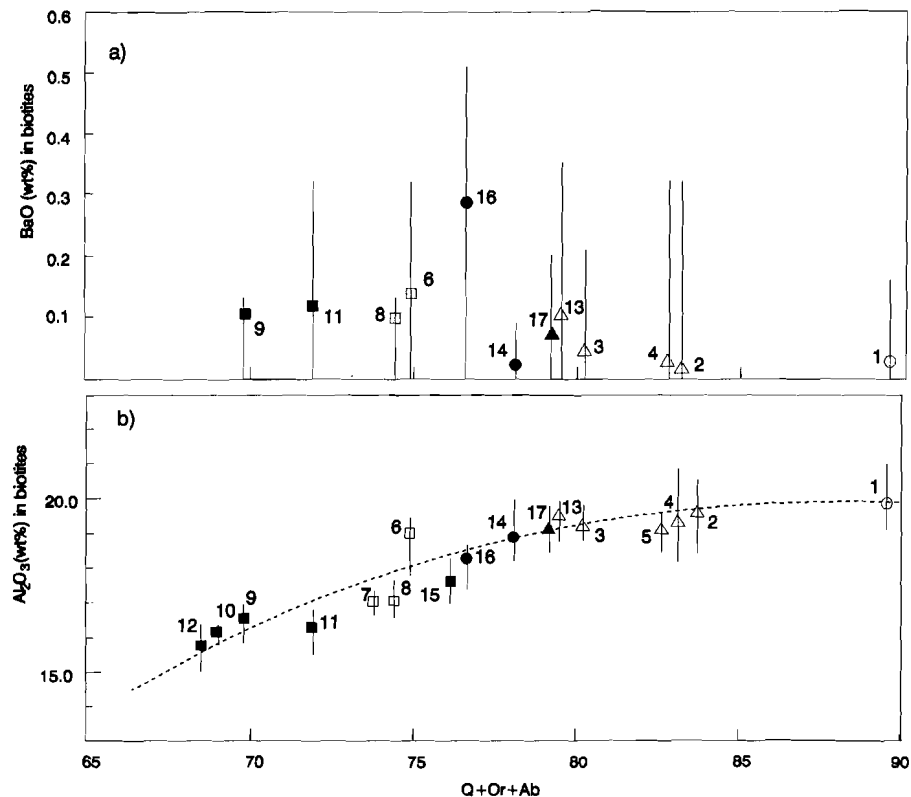


Fig. 14a,b. Compositional range (vertical lines) and averages (symbols) for BaO and Al₂O₃ in biotites, as a function of the Differentiation Index (Q+Or+Ab) of the corresponding samples. For symbols and numbers see Fig. 1. The dashed line in Fig. 14b indicates the inferred relation between DI and Al₂O₃ content in biotite.

4.7 CONCLUSIONS

- 1) Based on the Ba and Sr content, the rocks of the intrusion south of Los Santos can be divided into populations: Low Ba and Sr Main granodiorites and high Ba and Sr Linares granodiorites and associated monzogranites, suggesting two different magmas. Previous studies (CHAPTERS 2 AND 3) have however demonstrated that all rocks are likely to be part of one single magma fractionation sequence.
- 2) Trace element modelling with Ba, Sr, Rb and Zr, in combination with information derived from the chemistry of zoned minerals enables recognition of complex interference of contamination processes with crystal fractionation in one single magma.

- 3) Trace element modelling shows that the Main granodiorites are part of one fractionation sequence (trend I), and that the variation of Ba and Sr in the Linares granodiorites and associated monzogranites (trend II), cannot be explained satisfactorily with fractionation.
- 4) The rocks of trend II represent a magma that was derived from the main intrusive body (CHAPTER 2). This magma became contaminated with Ba, Sr and Ca derived from metasedimentary rocks.
- 5) Although crystal fractionation continued in the contaminated magma, the expected trace element patterns were additionally obscured by late, local hydrothermal contamination near faults and mineralization channels.
- 6) Combining geochemical, petrological and cartographic evidence, a relatively simple mechanism emerges to explain the observed variations:
- A: In first instance a granodioritic magma was crystallizing In Situ. Only locally, near faults and intrusive contacts, this magma was contaminated with Ba, and to a lesser extent with Sr.
- B: Part of the intercumulus melt segregated from the main intrusive body and formed an intrusion by itself, west of the Main granodiorite (see CHAPTER 2).
- C: The removed melt reacted with carbonate rocks and became enriched in Ca, Sr and Ba. Subsequently crystal fractionation started again, evolving southward and eastward
- D: During the last crystallization stages hydrothermal interaction with metasedimentary rocks, probably related to mineral deposition near Los Santos and Miranda del Castañar, again caused enrichment of Ba and Sr and probably depletion of Rb and Zr.

4.8 REFERENCES

- Allegre CJ, Minster JF 1978. Quantitative models of trace element behaviour in magmatic processes. Earth Planet. Sci. Lett. 38;1-25.
- Aparicio Yague A, Bellido Mulas F, Brandle Matessanz JL, Garcia Cacho L, Santos Serrano V 1983. Caracterizacion de los granitoides hercinos del Sector centrooccidental del Sistema Central Espanol. Estudios Geol.39: 271-306.
- Arth JG 1976. Behaviour of trace elements during magmatic processes- a summary of theoretical models and their applications. J. Res. U.S. Geol. Surv. 4; 41-47.
- Bea F 1982. Sobre el significado de la Cordierita en los granitoides del batolito de Avila (Sistema Central Espanol) Bol. Geol. Min. 93 59-67.
- Bea F 1985. Los granitos de la mitad occidental del batolito de Avila (sector de Gredos). Aproximacion mediante el concepto de superficies. Rev. Real. Acad. Ciencias Exactas Fis. y Nat. LXXXIX-4,549-572.
- Debon F, Le Fort P 1983. A chemical-mineralogical classification of common plutonic rocks and associations. Trans. Roy. Soc. Edinburgh. 73; 135-149.
- Goossens MA 1991. Integration of remote sensing data and ground data as an aid to exploration for granite related mineralization, Salamanca province, w-Spain. Proceedings VIII Thematic conference of Geologic Remote Sensing, Denver, Colorado; 393-406.

- Hanson GN 1978. The application of trace elements to the petrogenesis of igneous rocks of granitic composition. *Earth Planet.Sci.Lett.* 38;26-43.
- Haskin LA 1984. Petrogenetic modelling-use of rare earth elements. In: Henderson P. (ed.) *Developments in geochemistry 2: Rare earth element geochemistry*; 115-152.
- Leake BE 1960. Compilation of chemical analyses and physical constants of natural cordierites. *Am. Miner.* 45; 282-298.
- McCarthy TS, Hasty RA 1976. Trace element distribution patterns and their relationship to the crystallization of granitic melts. *Geochim. Cosmochim. Acta* 40; 1351-1358.
- McCarthy TS, Robb LJ, 1978. On the relationship between cumulus mineralogy and trace and alkali element chemistry in an Archean granite from the Barberton region, South Africa. *Geochim. Cosmochim. Acta* 42; 21-26.
- Michael PJ 1984. Chemical differentiation of the Cordillera Paine granite (southern Chile) by in situ fractional crystallization. *Contrib. Mineral. Petrol.* 87; 179-195.
- Rottura A, Bargossi GM, Caironi V, D'amico C, Maccarone E 1989. Petrology and geochemistry of the late Hercynian granites from the western Central System of the Iberian Massif. *Eur. J. Mineral.* 1; 667-683.
- Saavedra J 1978. Consideraciones sobre el area granitica comprendida entre Bejar y Linares de Riofrio (Salamanca). *An.Cent.Edif.Biol.Apl.Salamanca* 4;305-317.
- Speer JA 1981. Petrology of cordierite and almandine-bearing granitoid plutons of the southern appalachian Piedmont, USA. *Can.Miner.* 19; 35-46.
- Streckeisen A, Le Maître RW 1979. A chemical approximation to the modal QAPF classification of the igneous rocks. *N.Jb.Miner.Abh.* 136; 169-206.
- Thornton CP, Tuttle OF 1960. Chemistry of igneous rocks I. Differentiation Index. *Am.J.Sci.* 258; 664-684.
- Tindle AG, Pearce JA 1981. Petrogenetic modelling in the zoned Loch Doon pluton, Scotland. *Contrib. Mineral. Petrol.* 78;196-207.
- Ugidos Meana JM 1974. Los granitos biotíticos + cordierita de Bejar y areas adyacentes. *Bol. Geol. Min.* 85; 214-222.
- Ugidos Meana JM, Bea F 1976. Análisis comparativo de los graniotos de area Bejar-Plasencia con otros granitos "younger" centro peninsulares; precisiones sobre la serie mixta. *Stud. Geol.*10; 45-59.

CHAPTER 5

SPECTRAL DISCRIMINATION OF CONTACT METAMORPHIC ZONES AND ITS POTENTIAL FOR EXPLORATION FOR GRANITE RELATED MINERALIZATION.

5.1 ABSTRACT

A procedure is presented that successfully distinguishes soils overlying contact metamorphic rocks, using Thematic Mapper Imagery. Detection of contact metamorphic soils is based on expected spectral variation due to differences in clay mineralogy. In the mineralized contact aureole of Los Santos, Spain, contact metamorphic grade and clay mineralogy in soils correlate systematically. From the exocontact towards the granite intrusion the proportions of kaolinite, illite and free iron in soils increase, while the proportions of chlorite and smectite decrease. Laboratory reflectance spectra of soil samples demonstrate that with the increase of the proportion of kaolinite, illite and free iron and the decrease of chlorite, ratios of band2/band3, band2/band5 and band2/band7 decrease while ratios of band3/band4, band4/band7 and band5/band7 increase. Soil reflectance is significantly affected if more than 1.5% organic carbon is present. In the TM image, pixels that correspond with kaolinitic soils are identified by elimination of other pixels during a process of stepwise masking various band ratio images. The first step was to eliminate the effect of vegetation and organic material, by masking high values of the ratio of $(\text{band4} * \text{band5}) / (\text{band3} * \text{band7})$. The second step was to eliminate chloritic soils by masking the ratio of band2/band7. The third step was to isolate the most kaolinitic and limonitic soils using the ratio of band3/band4. Finally a maximum likelihood classification was performed on original band ratio images, using the result of the masking as training set, in order to optimize the classification results.

5.2 INTRODUCTION

Since the introduction of digital satellite data, much work has been done on the understanding and interpretation of spectral reflectance data. With the help of advanced digital processing techniques exploration geologists have started using the data to identify areas of potential interest for mineralization (e.g. Agterberg et al. 1972). Mapping of these areas is often performed using supervised classification methods, based on thorough studies of a specific pilot area. As a consequence it is often difficult to apply the training data in other regions, where geological, geomorphological and climatic conditions may be entirely different. In this study an effort is made to develop a classification technique that is not supervised, but based on expected spectral variations as a result of differences in soil mineralogy, in order to discriminate contact metamorphic zones. The detection of areas underlain by granite bodies, by means of classification of contact metamorphic zones may help to locate potentially mineralized areas (e.g. Rowan et al. 1987, Antón Pacheco 1989). Many ore deposits are genetically related to granite

intrusion. The granitic rocks of the western part of the Spanish Central System Batholith are associated with (sub)economic mineralization of base metals, uranium and gold. Most mineralization occurs close to the granite contact, usually within the contact metamorphic zone. The granite contact between Linares and Guijuelo (Fig.1) is of special interest, because of the occurrence of the large (15.000t WO_3) tungsten skarn of Los Santos. The width of the contact aureole at the surface is variable and ranges from 700m. to 2200m.

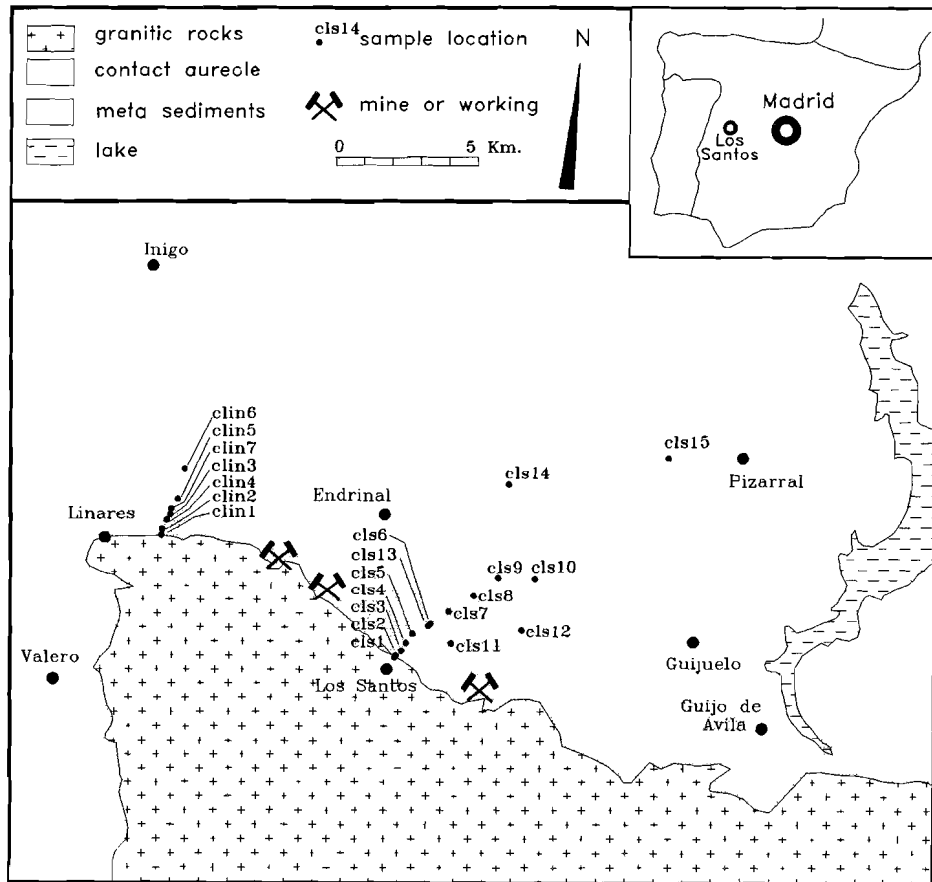


Fig.1. Simplified geological map showing the granitic, contact metamorphic and regional metamorphic terrain, the location of mineralization and the sample locations.

The area is geochemically (CHAPTERS 2-4) and geologically (Diez Balda 1982, Billiton International Metals 1980-1986) well-documented and provides a good opportunity to study the relation between contact metamorphic rocks and spectral response from TM imagery.

The contact metamorphic terrain is marked by a zone of bright white and bluish green colours on a colour composite image of TM134 (plate 1). Initial fieldwork, combined with interpretation of aerial photographs and TM images showed that a strong correlation exists between rock type, soil composition, degree of weathering and land use.

The aims of this work are to: 1) document the relation between contact metamorphism, soil type and land use; 2) study the relation between variations in soil mineralogy and reflectance spectra; 3) demonstrate how soils underlain by contact metamorphic rocks can be detected in a TM-image, on the basis of expected spectral variations due to differences in soil composition.

5.3 DATA COLLECTION

In order to study the relation between the degree of contact metamorphism, the composition of the corresponding soils and their spectral reflectance, rocks and overlying soils were sampled along two lines perpendicular to the granite contact (Fig.1). The width of the contact aureole is very variable, and mineralization seems to be related to the wider parts of the aureole. Therefore one sample line (Clin) transverses the narrow part of the contact aureole, near Linares, while the second line (Cls) is located in the broadest part of the aureole, near Los Santos. In addition to the samples along the profiles, three samples (Cls11, Cls12, Cls13) were taken of anomalously red soil, which predominantly occurs within the contact zone, formed by deep weathering of hornfelses. Soil samples were taken from the surface, where possible in ploughed fields, in order to enable correlation of laboratory spectra with TM-data.

Major and trace elements in the rocks were analyzed with XRF (Philips PW-1400) in glass beads and pressed powder tablets respectively. Major and trace elements in the soil fractions < 0.5mm. were analyzed with ICP after digestion with HF. Thin sections of the rock samples were prepared for petrographical description. Clay mineralogy, organic carbon, free iron and moisture content of the soils were determined at the Department of Soil Science and Geology, Agricultural University of Wageningen. Laboratory reflectance spectra of soils were determined at the German Aerospace Institute, Oberpfaffenhofen, using an IRIS IV spectrometer. The percentage reflectance was calculated using a polytetrafluoroethylene (Halon) reference standard.

5.4 SEDIMENTARY ROCKS

Petrography

The rocks outside the contact aureole predominantly consist of very fine grained low grade metamorphic green chloritic schists. The mineralogy of these rocks mainly comprises chlorite, chloritoid, white mica and quartz (Diez Balda 1982, Lieftink 1991). The first sign of contact metamorphism is the occurrence of microscopic biotite blasts, at a distance of 3500 m from the contact in the Los Santos profile and at 1200 m in the Linares profile. The cordierite isograde is the first macroscopic sign for contact metamorphism at a distance of 2200 m in the Los Santos profile and at 700 m in the Linares profile. In the direction of the contact muscovite, biotite and cordierite increase in abundance. The endocontact opaque mineralogy consists of ilmenite, pyrrhotite and chalcopyrite while the exocontact opaque mineralogy comprises anatase and minor amounts of ilmenite.

Geochemistry

Major and trace element compositions of the rock samples are listed in Table 1. The distance of the samples along the two traverses (Cl1 and Clin) towards the contact is given in meters. Approaching the contact, systematic variation is observed for a number of chemical components: the volatile content (Fig.2b) decreases and $\text{Fe}^{++}/\text{Fe}_{\text{total}}$ (Fig.2a), Co and MnO increase. Close to the contact the value for the $\text{Fe}^{++}/\text{Fe}_{\text{total}}$ ratio is similar to that in the granitic rocks (0.85, CHAPTER 3). Additionally, in the Los Santos profile there is enrichment of Rb and Cs (Fig.2c,d) towards the contact. For the remaining elements no relation with the distance to the contact is observed and their rather large standard deviation in regional metamorphic rocks (Table 1) points to primary variation in sediment composition, rather than variation as a result of contact metamorphism. Studies that have examined the variation of whole-rock composition with grade in contact aureoles indeed show that there is generally little chemical variation with grade, apart from loss of volatiles (Pattison and Tracy, 1991). Pelitic rocks in contact aureoles are commonly depleted in volatiles relative to their protoliths (Labotka 1991), because the formation of biotite and cordierite in originally low grade chlorite-muscovite bearing pelites implies dehydration and loss of H_2O (Guidotti 1984). The contact metamorphic rocks studied here typically lack chlorite and contain biotite and cordierite, and the decreasing volatile content (Fig.2b) therefore can be explained by progressive dehydration as a result of increasing grade of contact metamorphism. The systematic change of the $\text{Fe}^{++}/\text{Fe}_{\text{total}}$ ratio towards the intrusive contact suggests that originally trivalent iron, present in chlorite and oxide minerals in the pelites is reduced to divalent iron as a result of increasing temperature. Sedimentary rocks normally contain organic matter, which recrystallizes to graphite upon increasing metamorphism. The oxygen fugacity in a pelitic environment containing graphite and H_2O is buffered by iron minerals (Labotka 1991). From temperature- $f\text{O}_2$ phase diagrams presented by this author it can be concluded that the $\text{Fe}^{++}/\text{Fe}_{\text{total}}$ ratio will increase with temperature in the presence of graphite in order to maintain equilibrium in oxygen fugacity. Therefore the increasing Fe^{++} content

No	c1s1	c1s2	c1s3	c1s4	c1s5	c1s7	c1s8	c1s9	c1s10	c1s12	c1s13	c1s14	clin1	clin2	clin3	clin5	clin6	clin7	AVG ¹	STD ¹
Distance	100	200	500	850	1200	2700	3700	4800	6000		1850	8000	10	200	700	1500	3000	1000		
SiO ₂	72.53	61.39	62.12	59.84	62.39	58.68	62.49	59.77	59.86	58.9	57.76	56.74	58.78	62.78	57.65	55.98	57.24	59.4	62.8	5.35
TiO ₂	0.39	0.8	0.84	0.8	0.76	0.8	0.69	0.77	0.89	0.84	0.74	0.79	0.8	0.69	0.87	0.9	0.75	0.76	0.73	0.15
Al ₂ O ₃	12.06	19.26	18.74	20.01	18.12	19.57	18.18	19.22	19.82	20.6	20.54	21.33	20.9	19.42	20.08	20.96	20.26	19.23	17.61	3.79
Fe ₂ O ₃	3.04	7.96	6.81	8.5	7.09	8.02	6.49	7.73	7.34	8.1	7.73	8.03	7.96	7.12	7.58	8.5	8.01	7.5	6.2	1.54
MnO	0.04	0.12	0.04	0.11	0.1	0.09	0.09	0.11	0.08	0.12	0.09	0.08	0.12	0.09	0.11	0.08	0.07	0.09	0.08	0.03
MgO	1.38	3.07	3.59	3.32	2.74	3.24	2.58	2.98	2.81	3.07	3.02	3.21	3.09	2.83	2.78	3.31	3.25	2.91	2.4	0.71
CaO	0.21	0.7	0.2	0.6	0.77	0.46	0.51	0.44	0.16	0.48	0.32	0.17	1.11	0.82	0.36	0.04	0.12	0.75	0.6	1.55
Na ₂ O	1.43	1.34	1.06	1.18	2.19	1.89	2.26	1.27	1.46	1.42	1.14	1.04	2.04	2.05	1.48	1.21	0.81	2.24	1.2	0.53
K ₂ O	5.22	4.07	3.95	3.95	3.54	3.21	3.82	4.33	3.54	3.76	4.49	3.74	4	3.47	4.01	3.83	3.93	3.15	3.43	0.67
P ₂ O ₅	0.13	0.17	0.14	0.14	0.15	0.15	0.15	0.14	0.14	0.17	0.17	0.14	0.17	0.15	0.17	0.11	0.14	0.15	0.14	0.02
10 _i	1.5	2.49	3.3	3.3	2.81	4.52	3.16	4.42	5	2.97	4.28	5.42	1.66	1.28	4.61	5.27	5.38	4.06	4.97	1.65
total ₁	97.9	101.37	100.79	101.7	100.66	100.63	100.42	101.18	101.1	100.25	100.28	100.69	100.63	100.7	99.7	100.19	99.96	100.24	100.3	0.62
Fe [*]	0.82	0.77	0.86	0.79	0.73	0.61	0.56	0.54	0.55	0.72	0.76	0.65	0.76	0.84	0.56	0.59	0.68	0.64		
Nb	8.59	15.81	15.04	14.75	14.83	14.14	14.06	14.07	15.83	15.7	14.65	15.07	15.73	13.77	15.03	15.5	14.4	13.3	13.1	2.82
Zr	114	145	151	137	152	140	152	170	179	143	136	135	145	131	157	157	140	138	188.6	72.44
Y	23	33	33	33	32	30	22	29	34	32	33	32	31	27	34	43	30	29	33.5	10.16
Sr	115	100	75	138	161	129	130	75	106	127	130	95	185	169	114	82	55	161	88.9	20.95
Rb	199	164	183	157	145	131	151	143	141	144	177	151	152	125	165	158	148	130	129	37.09
Zn	48	115	111	132	108	122	95	97	107	120	114	117	123	103	114	120	134	115	91.2	27.64
Ni	26	53	51	54	50	56	47	46	43	58	48	50	54	49	56	61	49	52	39.9	13.37
Co	109	49	30	36	37	29	16	21	23	44	23	34	54	64	24	27	20	27	25.7	10.18
Ba	928	654	732	715	648	525	776	953	659	704	729	668	628	727	742	679	659	538	771.6	196.4
Cs	11	20	20	8	13	6	8	6	6	6	11	8	8	7	10	8	8	9	5.92	3.19

Table 1. Whole rock major and trace element composition of sedimentary rocks.
 $Fe^* = Fe^{++}/Fe_{total}$. AVG¹ average composition and STD¹ standard deviation of 18 representative regional metamorphic schist and greywacke samples.

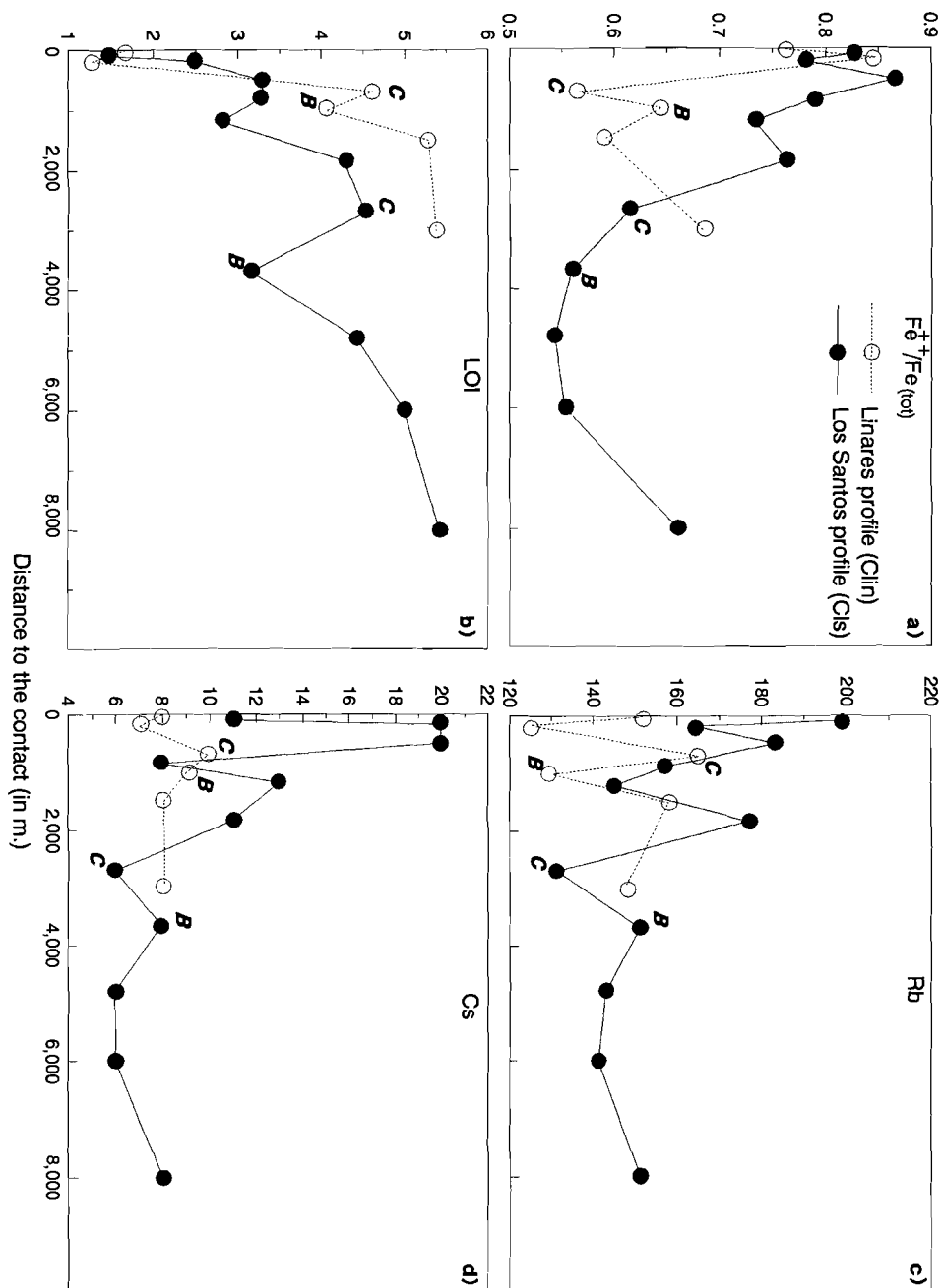


Fig.2. Variation in $\text{Fe}'^+/\text{Fe}_{\text{total}}$ (a), LOI(b), Rb(c) and Cs(d) in the sedimentary rock samples, as a function of the distance to the contact, along two traverses perpendicular to the contact. The position of the biotite and cordierite isograd are indicated with B respectively C.

towards the contact will correlate with grade of metamorphism. The increase of Rb, Cs, Co and MnO towards the contact suggests that these elements were essentially supplied by fluids probably derived from the granitic intrusion. Relatively high contents for these elements (up to 275ppm, 26ppm, 200ppm and 2.5% resp) in the tungsten skarn of Los Santos suggest hydrothermal enrichment. The contact rocks near Los Santos are enriched in Rb and Cs while those near Linares are not, which can be explained by the fact that the granitic rocks near Los Santos are more evolved and richer in Rb and Cs than those near Linares (CHAPTER 4). Whereas the increase of Rb, Cs, Co and MnO towards the contact has probably to do with metasomatic processes due to external supply of fluids and not directly with the temperature effect, the systematic changes in volatile- and Fe⁺⁺-content are a direct consequence of the contact metamorphic heating. These changes are obviously reflecting diagnostic differences in mineral assemblages: disappearance of chlorite and appearance of biotite, cordierite and ilmenite. This is illustrated by the position of the biotite-in and cordierite-in isograds (Fig.2). Therefore the relative volatile content and Fe⁺⁺/Fe_{total}-ratio should be useful as indicators for the degree of contact metamorphism.

5.5 SOILS

Field description

The soil cover on top of the chlorite schist is usually poorly developed, with a depth normally less than 10 cm. although locally deeper soils are observed (Table 2). These greyish-green soils are often very stoney, with a rather low clay content. In contrast, the contact metamorphic soils are deeper, clay-richer and usually have a patchy red to yellow-red colour. The most common soil colour in this zone is 7.5 YR to 10 YR on the Munsell colour scale. Locally intense red patches, up to 2.5 YR, are developed.

	7 A	10 A	10-14 A	14 A	colour	depth	rock
c1s1	67	33	0	0	7.5 YR 3/2	20	Hornfels
c1s2	60	32	5	3	10 YR 5/4	20	Hornfels
c1s3	57	36	5	2	5 YR 4/4	—	Hornfels
c1s4	53	29	0	18	7.5 YR 4/4	20	Hornfels
c1s5	68	23	5	4	7.5 YR 4/4	10	Hornfels
c1s13	73	18	3	6	7.5 YR 4/6	10	Hornfels
c1s6	47	35	6	12	10 YR 3/6	10	Spotted slate
c1s7	35	45	6	14	10 YR 4/4	20	Spotted slate
c1s8	37	48	5	10	10 YR 4/6	20	Spotted slate
c1s9	36	45	0	19	10 YR 5/4	10	Schist
c1s10	39	31	0	30	10 YR 5/6	5	Schist
c1s14	45	30	0	25	2.5 Y 5/4	2	Schist
c1s11	72	23	5	0	2.5 YR 4/6	20	Hornfels
c1s12	76	10	5	9	2.5 YR 4/8	25	Hornfels
C1s15	29	33	0	38	10 YR 5/4	20	Schist
clin1	59	25	8	8	10 YR 4/4	20	Hornfels
clin2	54	23	12	11	10 YR 3/4	30	Hornfels
clin4	51	25	12	12	10 YR 4/4	>40	Hornfels
clin3	54	28	3	15	7.5 YR 5/4	10	Spotted slate
clin5	42	21	2	35	10 YR 5/6	5	Schist
clin6	49	27	0	24	N.D	5	Schist

Table 2: Relative peak height of clay minerals, Munsell colour, distance of surface to saprolite (in cm.) and underlying rocktype for soil samples .

	c1s1	c1s2	c1s3	c1s4	c1s5	c1s6	c1s7	c1s8	c1s9	c1s10	c1s13	c1s14	c1s15	c1s11	c1s12	c1in1	c1in2	c1in3	c1in4	c1in5	c1in6
Dist	100	200	500	850	1200	1900	2700	3700	4800	6000	1850	8000				10	200	700	450	1500	3000
Al ₂ O ₃	11.2	11.4	13.6	16.7	15.5	14.7	14.2	11.3	10.4	13.6	18.3	16.8	10.7	19.7	21.7	14.4	13.1	16.4	15.8	23.9	15.1
TiO ₂	0.46	0.61	0.81	0.96	0.91	1.13	0.96	0.75	0.61	1.43	0.91	1.08	1.11	0.85	0.85	0.63	1.15	0.95	0.83	1.18	0.78
Fe ₂ O ₃	2.55	3.54	4.81	7.18	7.32	5.44	5.35	4.36	3.24	5.76	8.09	7.11	3.44	7.41	10.7	3.47	5.54	7.09	5.36	9.72	5.19
MnO	0.07	0.07	0.07	0.12	0.07	0.14	0.12	0.10	0.05	0.12	0.06	0.10	0.07	0.08	0.05	0.10	0.15	0.29	0.13	0.10	0.21
MgO	0.58	0.68	1.13	1.63	1.71	1.29	1.58	1.18	1.05	1.78	1.13	2.31	1.01	1.30	1.53	0.86	1.66	1.55	1.03	3.26	1.03
CaO	1.4	0.43	0.15	0.21	0.15	0.18	0.32	0.18	0.12	0.25	0.15	0.09	0.15	0.15	0.08	0.40	0.43	0.33	0.29	0.14	0.22
Na ₂ O	0.45	0.51	0.30	0.37	0.30	0.48	0.87	0.79	1.29	1.15	0.32	0.51	1.35	0.35	0.22	0.78	0.37	0.39	0.45	0.55	0.39
K ₂ O	3.08	3.01	3.39	3.37	2.91	2.96	2.90	2.60	2.21	2.51	2.98	3.07	1.94	3.22	2.37	6.01	2.54	2.94	2.71	4.01	3.38
P ₂ O ₅	0.21	0.14	0.11	0.16	0.09	0.14	0.13	0.10	0.09	0.14	0.13	0.18	0.10	0.11	0.11	0.26	0.28	0.26	0.17	0.14	0.17
Fe*	0.39	0.48	0.36	0.39	0.41	0.37	0.27	0.33	0.26	0.20	0.60	0.16		0.46	0.63	0.28	0.39	0.40	0.48	0.20	0.25
O	4	3.1	0.9	1.8	0.6	1.5	2	1.3	1.1	2.2	0.8	3.5		0.5	0.2	2	1.4	6.9	4.9	0.8	10.7
M	1.5	1.3	0.6	1.4	1.3	0.4	1.4	0.8	0.5	0.9	1.3	1.2		1	0.9	1.1	1.4	2.6	2.6	2	3.2
Sr	52	43	24	47	30	37	57	46	46	73	33	54	85	26	25	83	58	51	49	72	42
Ce	72	80	101	96	105	125	80	75	53	87	108	69	69	103	82	89	78	104	98	158	94
Co	5	12	17	31	20	23	17	15	11	21	15	18	81	20	22	8	15	25	15	26	20
Ba	568	580	580	724	523	532	524	482	532	483	588	518	453	643	536	659	461	594	502	723	546
Zn	76	64	145	142	203	145	174	85	169	201	217	152	79	273	144	85	212	141	116	153	199
Cu	17	19	51	43	45	31	28	24	20	35	48	35	18	45	54	13	40	41	29	45	30
Li	33	42	58	94	58	45	47	38	28	43	54	55		70	74	72	45	66	60	66	70
Zr	105	129	132	116	121	114	109	135	95	121	127	119	142	114	120	186	112	115	126	142	117
Ni	20	21	34	53	52	43	39	33	25	41	50	47	53	62	58	16	42	65	40	65	44
Cr	35	44	68	86	91	71	66	43	37	65	90	81	42	103	66	33	63	80	71	98	64

Table 3. Major (%) and trace (ppm) element analyses of soil samples (fraction <0.5mm.). Distance to contact in m.

*: organic carbon, M: moisture content, Fe : Fe_{free}/Fe_{total}

Chemistry

The chemical analyses of fractions <0.5mm. of the soil samples are presented in Table 3. Most major elements are slightly depleted in the soils with respect to the underlying rocks. Al, Ti, Fe, Mg and Na tend to be slightly more depleted in soils overlying the contact metamorphic rocks. The only real significant variation, related to the distance from the contact is found for the ratio $\text{Fe}_{\text{free}}/\text{Fe}_{\text{total}}$ (Fig.3a).

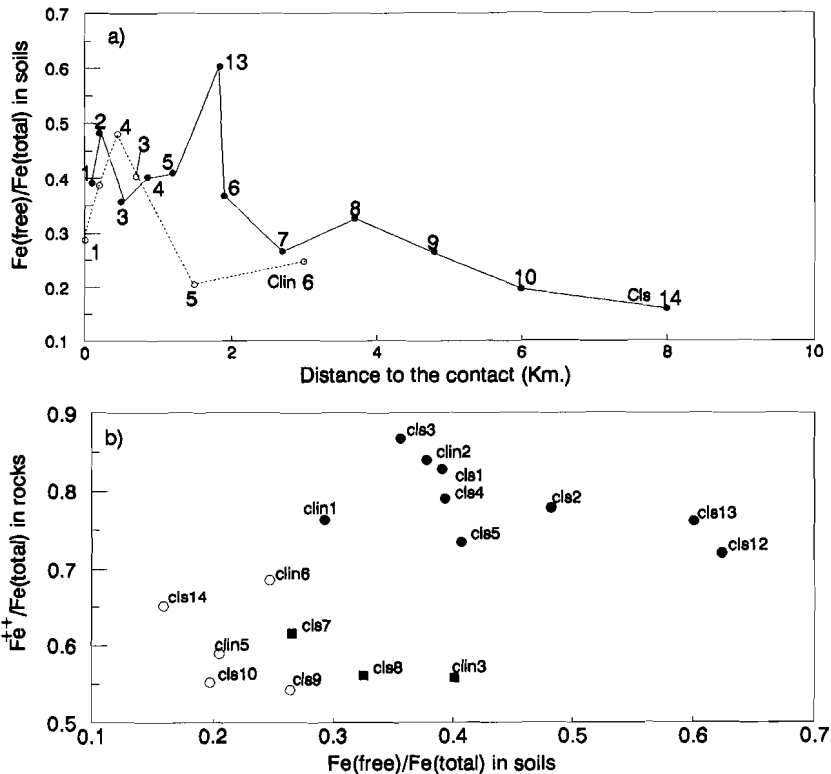


Fig.3. a: $\text{Fe}_{\text{free}}/\text{Fe}_{\text{total}}$ in soils overlying the rock samples presented in Fig.2. b: the relation between $\text{Fe}^{++}/\text{Fe}_{\text{total}}$ (rocks) and $\text{Fe}_{\text{free}}/\text{Fe}_{\text{total}}$ (overlying soils); Closed circles: hornfelses and overlying soils; closed squares: spotted slates and overlying soils; open circles: chlorite schists and overlying soils. The numbers correspond with the sample numbers (Fig.1.)

This ratio was found to be a particularly sensitive indicator of relative soil development, reflecting the degree of primary mineral alteration and the amount of clay formed (Rebertus and Buol 1984). The increasing $\text{Fe}_{\text{free}}/\text{Fe}_{\text{total}}$ value towards the granite contact indicates an increasing degree of soil development in the contact metamorphic zone. The ratio of $\text{Fe}_{\text{free}}/\text{Fe}_{\text{total}}$ in soils is plotted against

$\text{Fe}^{++}/\text{Fe}_{\text{total}}$ in the rocks (Fig. 3b), in order to illustrate the relation between the degree of metamorphism and weathering. The endocontact samples except Cls7, Cls8 and Clin3, plot in a cluster with high values for both $\text{Fe}^{++}/\text{Fe}_{\text{total}}$ in rocks and $\text{Fe}_{\text{free}}/\text{Fe}_{\text{total}}$ in soils and can clearly be distinguished from the exocontact samples. This implies that soil develops better on top of contact metamorphic rocks.

The samples Cls7, Cls8 and Clin3 have relatively low Fe^{++} -content for contact metamorphic rocks. This may be explained by the fact that they are the least metamorphic samples of the contact aureole.

Clay Mineralogy

The relative peak heights in the diffractograms of the clay fractions are listed in Table 2. The peak heights are normalized to the sum of all 7 \AA , 10 \AA , mixed-layer and 14 \AA minerals. Except for Cls1,2,11,12,13 smectite is present in all samples, as the 10 \AA /14 \AA ratio increases after heating to 600°C. Chlorite is present in samples Clin3,5,6 and Cls2,6,7,9,10,14 as in these samples the 14 \AA peak is still present both after treatment with glycerol and heating to 600°C. Kaolinite (7 \AA) and illite (10 \AA) are present in all samples. Mixed layer minerals are present in minor quantities in most samples. The normalized peak heights can be used as an indication for the proportion of each of these minerals in the clay fraction as the diffraction peaks are fairly sharp. The relative peak heights are plotted as a function of distance to the granite contact (Fig.4) for the profiles at Los Santos and Linares.

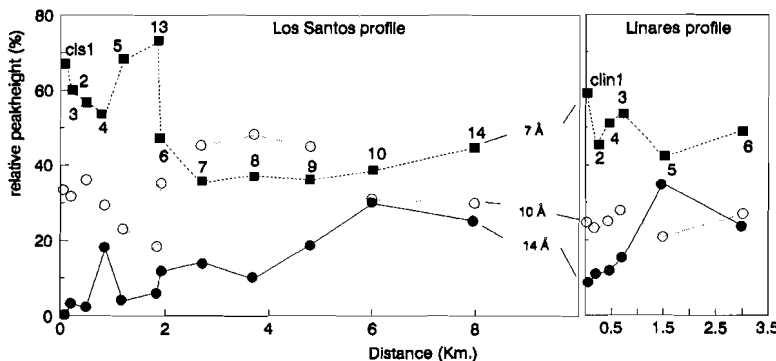


Fig.4. Relative heights of 14 \AA , 10 \AA and 7 \AA peaks in soil samples as a function of the distance to the contact. Sample numbers are added.

The proportion of chlorite + smectite steadily decreases from >25% in the regional metamorphic terrain to 0% near the contact. In the Los Santos profile two populations of contact metamorphic soils are encountered: an inner zone (0-2000m.) with relatively high (>45%) kaolinite proportions, and an outer zone (2000-5000m.) with relatively high (>40%) illite contents. The proportion of mixed-layer minerals

is generally very low and does not vary with the distance to the contact. The Linares profile shows, although on a smaller scale, similar features to the Los Santos profile. The ratio $\text{Fe}_{\text{free}}/\text{Fe}_{\text{total}}$ increases with Kaolinite (Fig.5) and decreasing chlorite + smectite.

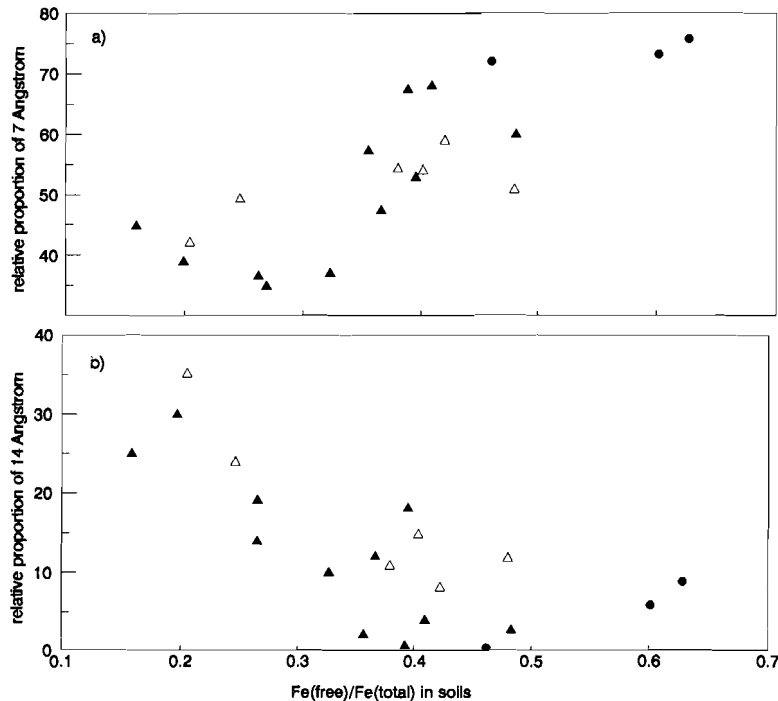


Fig.5. Relation between the proportions of free iron and kaolinite(a, normative height of 7 Å peak), and chlorite+smectite(b, 14 Å) in the soil samples. Open triangles: Linares profile; closed triangles: Los Santos profile; closed circles: anomalously red soils (C1s11, C1s12 and C1s13).

The chlorite content in samples from the Linares profile is generally higher than for the Los Santos profile. The correlation between $\text{Fe}_{\text{free}}/\text{Fe}_{\text{total}}$ ratio in soils and both soil mineralogy and the $\text{Fe}^{++}/\text{Fe}_{\text{total}}$ ratio in the underlying rocks indicates that the degree of weathering and the mineralogical composition of the soils are related to the degree of contact metamorphism of the underlying rocks. Differences in Fe^{++} -content, original mineralogy and texture of the rocks may determine both the ability of the rocks to weather and the weathering products.

The contact metamorphic rocks contain much biotite, cordierite and white mica. During weathering biotite weathers to kaolinite, accompanied by phases like goethite and gibbsite, and minor amounts of

vermiculite (Harris et al. 1985), which explains the correlation between $\text{Fe}_{\text{free}}/\text{Fe}_{\text{total}}$ and kaolinite. X-ray diffractograms of weathered cordierite nodules indicate that cordierite altered to a mixture of quartz, illite and goethite. White mica transforms to illite. Chlorite under similar climatic conditions may weather to chlorite/vermiculite interstratifications, as demonstrated for chlorite rocks in the Massif Central, France (Proust 1982), or ultimately to Fe^{3+} -rich smectite, as demonstrated for chlorite rocks in northwestern Spain (Buurman et al. 1988).

The contrast in kaolinite and illite content between inner and outer contact may find its origin in different ages of the inner contact and outer contact soils (Buurman pers.comm.). The inner contact soils, overlying hornfelses, may be older soils, protected from erosion, while the outer contact soils, overlying spotted slates are more recent. The inner contact soils may have been protected from erosion because the hornfelses show a deep, torwise, chemical weathering, while the (spotted) slates weather much more superficially. The fact that illite is much more abundant in the outer zone suggests that under the present conditions white mica and cordierite in the rocks weather faster than biotite.

5.6 LAND USE

Information on the land use in the study area is available in the form of field data, aerial photography and 1:50000 land-use maps. All data demonstrate very obvious contrasts in land use for regional metamorphic, contact metamorphic and granitic terrains:

- 1) Agricultural fields are concentrated in the contact zone, and are relatively scarce in the chlorite schist terrain. As the soils underlain by contact metamorphic rocks are much better developed than those underlain by chlorite schist, it seems logical to relate the relative abundance of these fields to the type of underlying rocks.
- 2) The contact area has more relief than the regional metamorphic terrain. Consequently the scale of land use in the contact zone is much smaller than that on the chlorite schists. Small valleys are usually occupied by trees, bushes and other green vegetation.
- 3) Due to crop rotation most fields remain fallow for 3 to 5 years before being ploughed and sown. The result of this is a patchwork of small fields with different degrees of vegetation cover.
- 4) The granitic terrain has intermediate topographic relief, due to the presence of many joints and faults. Generally little soil is developed. Abundant granite crops out, but is mostly covered with lichen (Rowan et al. 1987, Ager and Milton 1987). The terrain is mainly used for pasture.

Obviously the geology to a great deal determines the type and scale of land use. Therefore it should be possible to extract information from a TM-image concerning the geology by looking at the vegetation cover. This is illustrated in figure 6, showing the diversity in a TM image of band3/band4. This figure was produced using a 15*15 diversity filter. A diversity filter counts the number of different digital numbers within the direct environment (in this case 15*15 pixels) of the central pixel. The regional metamorphic terrain is obviously rather homogeneous in land use, characterized by low diversity values (0-67). A

greater heterogeneity is found for the granitic terrain, characterized by higher diversity values (up to 103). The highest diversity (up to 140) in land use is found, as expected, in the contact metamorphic terrain.

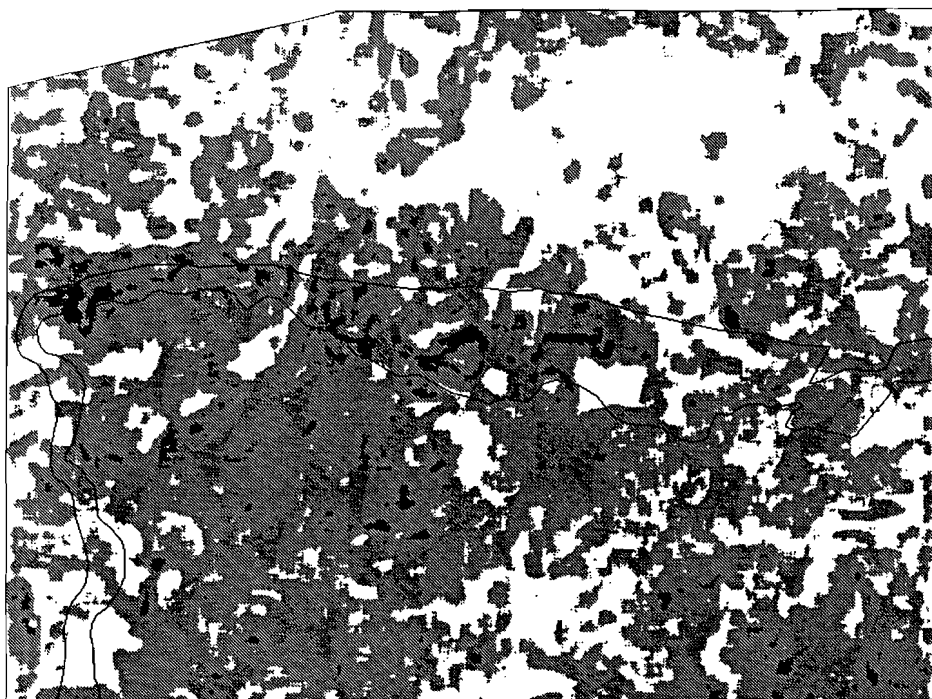


Fig.6. Spectral diversity in the ratio image of TM3/TM4. This is a product of diversity filtering with a 15*15 kernel, and represents the amount of different digital numbers within the 15*15 pixel environment around each pixel. White: diversity 0-67; grey: diversity 68-102; black: diversity 103-140. The boundaries of granite and contact aureole are indicated with solid lines.

5.7 SPECTRAL VARIATION

Laboratory spectra were determined of samples Cls1 to Cls14 and Clin5 and 6. Representative reflectance spectra are shown in Fig.7. Cls5,11,12,13 are kaolinite and goethite rich soils. Cls6,7,8 are illite rich soils and Clin5 is a chlorite rich soil. The absorption band near 900nm in Cls5,11,12,13 is due to the presence of Fe⁺⁺⁺ in the form of limonite, while the Fe-absorption band in clin5 is caused by the presence of Fe⁺⁺⁺ in chlorite. The size of this absorption band in chlorite depends on the amount of Fe⁺⁺⁺ in six-fold coordination (Hunt and Salisbury 1970). All samples show clear hydroxyl absorption peaks at 1400nm, 1900nm and between 2000nm and 2600 nm, typical for the clay minerals involved.

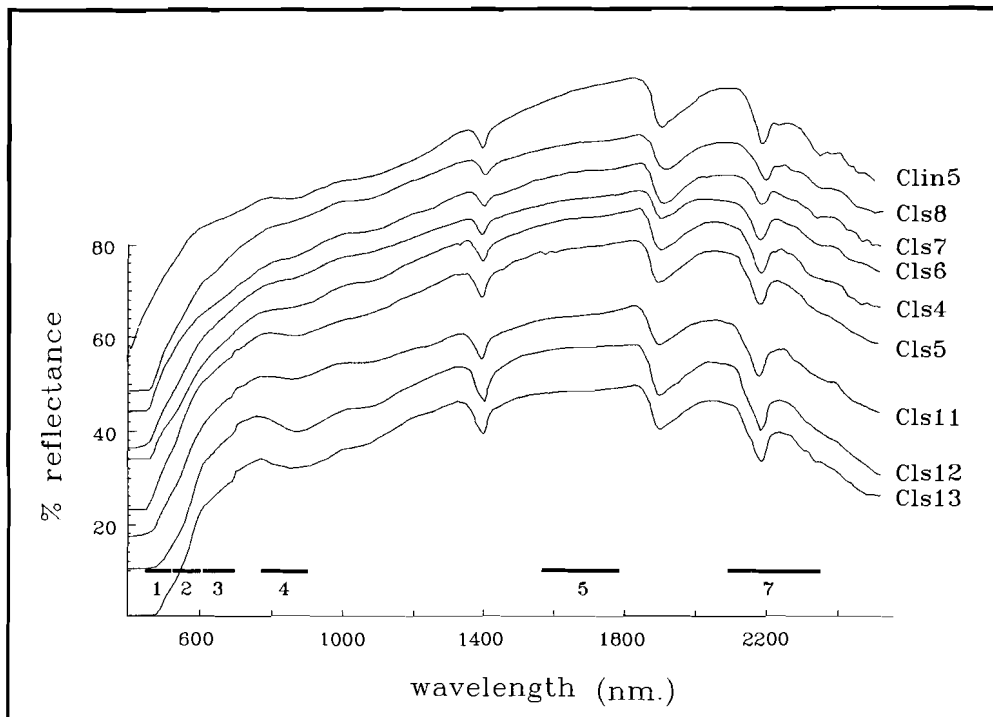


Fig.7. Representative spectral reflectance curves of soil samples obtained from laboratory measurements. The horizontal bars indicate the range of the corresponding TM bands.

It is hardly possible to relate the laboratory spectral curves directly to soil mineralogy, as we did not determine the amount of each mineral phase in the soil samples. In order to interpret the spectral variation in terms of general changes in soil mineralogy, degree of weathering, and indirectly, contact metamorphic grade, band ratios are plotted against the ratio $\text{Fe}_{\text{free}}/\text{Fe}_{\text{total}}$ (Fig.8).

The $\text{Fe}_{\text{free}}/\text{Fe}_{\text{total}}$ ratio increases with the degree of weathering, with the relative amount of kaolinite (7\AA , Fig.5a), with decreasing chlorite+smectite (14\AA , Fig.5b) and with increasing degree of contact metamorphism of the underlying rocks (Fig.3).

Significant differences in kaolinite/illite ratios content occur between inner and outer aureole (Fig.4), and as illite and kaolinite have quite distinct reflectance spectra (Fig.10), it is expected that soil reflectance depends on the ratio of $7\text{\AA}/10\text{\AA}$. Therefore the samples were subdivided into two groups: $7\text{\AA}/10\text{\AA} > 2$ (open symbols), which corresponds with the relatively kaolinite rich soils of the inner aureole, and $7\text{\AA}/10\text{\AA} < 2$ (closed symbols), corresponding with the relatively illite and chlorite rich soils of the outer

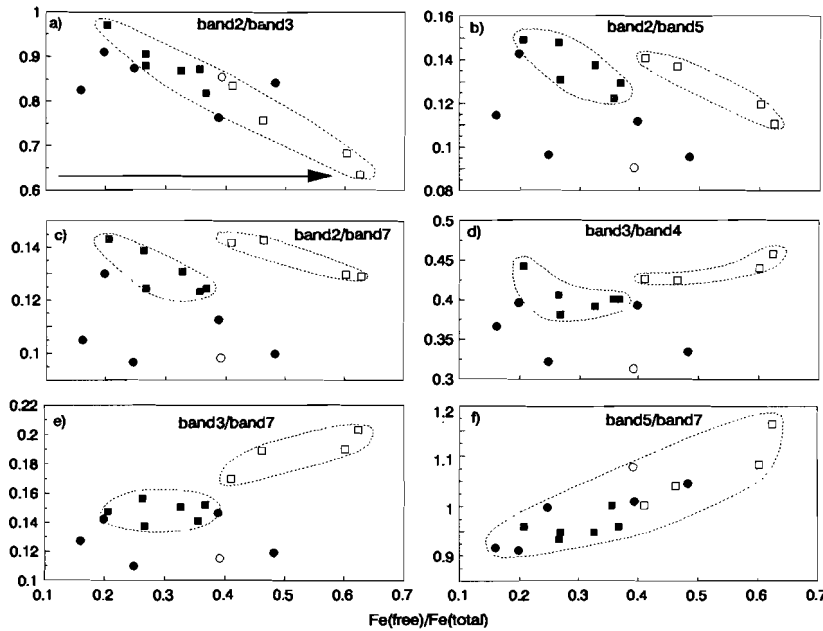


Fig.8. Band ratios, calculated from the laboratory spectra of soil samples, plotted against their proportion of free iron. Circles: samples with more than 1.5% organic carbon; squares: samples with less than 1.5% organic carbon. Open symbols: samples with a ratio of $7\text{\AA}/10\text{\AA} \geq 2$; closed symbols represent those with a ratio < 2 . The direction of the arrow (Fig.8a) indicates the increasing degree of weathering, and grade of contact metamorphism in the underlying rocks.

aureole and the low grade metamorphic terrain. Using band ratios at this stage has the advantage that they can be compared with band ratios from TM-images, since they are not influenced by differences in brightness and illumination angle (Lillesand and Kiefer 1987).

All band ratios are to a certain extent affected by the amount of organic carbon in the soils. The most illustrating examples are presented in figure 9. The reflectance appears to be seriously affected if organic carbon exceeds 1.5 wt%, which is similar to results in other studies (e.g. Stoner and Baumgartner 1981). Therefore two groups of samples were distinguished: with more than 1.5% (circles) and less than 1.5% (squares) organic carbon. The plots in Fig.8 demonstrate that the kaolinite rich samples and the illite rich samples form two discrete groups, and form either two separate trends (Fig 8b,c,d,e) or one continuous trend (Fig.8a,f) with the $\text{Fe}_{\text{free}}/\text{Fe}_{\text{total}}$ ratio. The carbon-rich samples plot in all figures outside the trends indicated by the dotted outlines. The general directions of the trends can be understood if the gross mineralogical changes are compared with laboratory spectra of pure minerals (Fig.10). Ratios of band2/3 and band3/4 mainly represent variations in free iron. The ratio of band3/band4 is high both for chlorite-rich and goethite-rich samples. This is due to the fact that the Fe-dip in band4 is present in both goethite and chlorite. The positive slope for the ratio of band 5/7 is a result of the simultaneous decrease of chlorite and increase of kaolinite + illite. Ratios of band2/7, band 2/5 and band3/7 especially

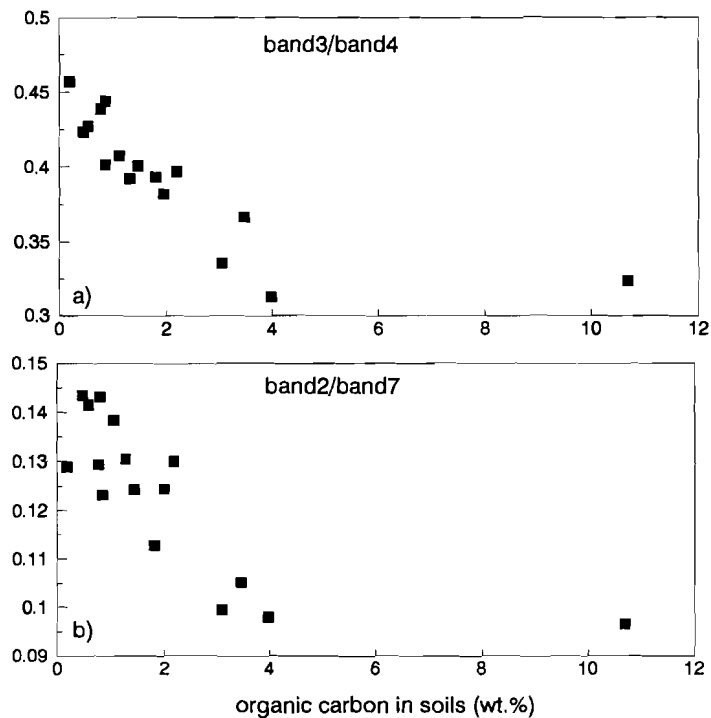


Fig.9. Illustration of the disturbing effect of organic carbon in soils in the spectral reflectance.

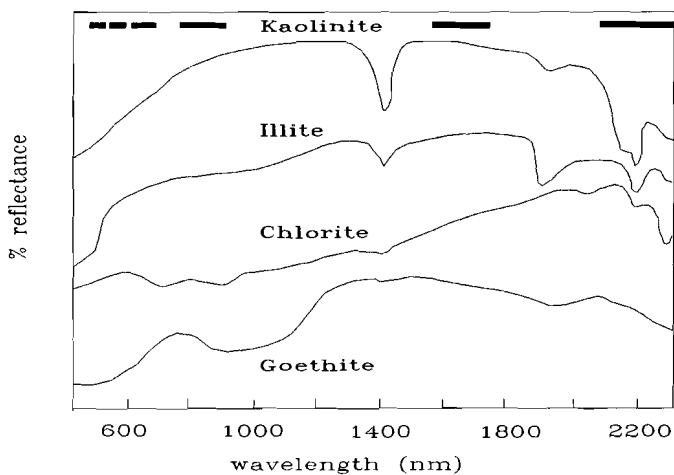


Fig.10. Reflectance spectra of relevant pure minerals. From Hunt and Salisbury (1970) and Antón Pacheco (1989). Horizontal bars indicate the range of the various TM bands.

show the combined effect of increasing free iron, (negative slope), and increasing kaolinite (enhanced ratios for open squares). Kaolinite has a much larger water absorption peak in band7 than the other clay minerals and a negative slope in the band 5. Therefore the dominance of kaolinite in samples Cls5,11,12 and 13 compared with the other samples causes higher values for ratios with band7 and band5.

5.8 CLASSIFICATION OF THE TM IMAGE

The previous section demonstrates that on laboratory scale it is possible to distinguish soils overlying contact metamorphic rocks on the basis of characteristic spectral differences. The next step is to examine whether the observed variations are also present in TM images. If this is the case, digital classification of contact metamorphic areas provides a helpful tool in the exploration for granite related mineralization.

Classification of the TM image was done using an ILWIS image processing system, developed by the International Institute of Aerospace Survey and Earth Sciences, Enschede, the Netherlands. In the first instance a supervised classification, based on field mapping, aerial photograph interpretation, and topographic data was carried out in order to classify contact metamorphic soil. The spectral characteristics of the various classes were however not in agreement with the variations expected on the basis of soil mineralogy and laboratory spectra. Apparently supervised classification does not enable sufficient control over the data. For example the amount of organic carbon in the soils could not be accounted for, neither could the amount of organic litter on top of the soils be estimated. Therefore another approach was developed, using the variations expected on the basis of the trends in Fig.8. Images of selected band ratios were stepwise masked in order to systematically remove all pixels with the least favourable spectral signatures. Before calculating the ratio images, haze was corrected for by subtracting the digital numbers recorded for the lake of Santa Teresa (Fig.1) from the original images. The first step in the procedure was to eliminate the effect of organic carbon, litter and green vegetation. This could be done masking TM3/TM4, but better results were obtained by using a ratio of two band ratios, TM3/TM4 and TM5/TM7 (Fig.11). Both green vegetation and soils with much organic material appear brighter in this ratio image. The result (Fig.12a) gives the locations of bare soil and rock. The next step was to remove pixels that correspond with chlorite rich soils from the resulting image. This was done by masking the pixels with the highest values for TM2/TM7 (Fig.12b). Similar results were obtained using TM2/TM3, but this image contained more noise, presumably due to the strong correlation of these two bands and therefore TM2/TM7 was preferred. Once the chlorite pixels were removed, the pixels corresponding with the most kaolinite and free iron rich soils were obtained by removing the pixels with the lowest TM3/TM4 ratio. The remaining pixels were assigned the value 1. In the resulting image, small amounts of isolated single pixels occurred. It is assumed that, if these single pixels are not located close to other pixels, they are not significant and therefore have to be filtered out. The (binary) filtering was done in three steps. First an eight-neighbour expansion, followed by an eight-neighbour erosion (Fabbri

1984) was carried out in order to connect single pixels that are situated close to each other. Next a "pepper-and-salt filter" was applied to remove isolated pixels. The resulting image (Fig.12c) reveals the locations of the most weathered soils, most of which are inside or very near to the contact aureole, and clearly associated with the wider parts of the contact aureole. Two groups (G and I) of pixels in the regional metamorphic area, classified as "kaolinite" coincide with the location of large villages, Guijuelo and Iñigo resp. Probably the tiles in the roofs of the houses, which are made from clay, look similar to kaolinitic soils.

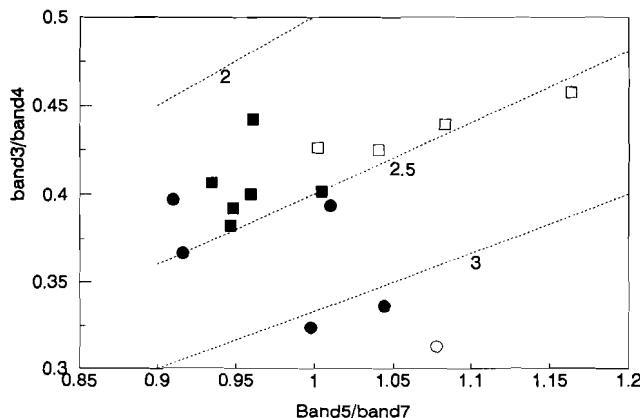


Fig.11. Relation between the band ratios TM3/TM4 and TM5/TM7. The symbols are the same as used in Fig.8. The lines indicate constant values for the ratio of $(\text{TM5}/\text{TM7})/(\text{TM3}/\text{TM4})$, which is used to remove pixels from the TM image that are contaminated by the presence of organic material.

The result shown in figure 12 is one example of the application of the classification method described above. The technique can be carried out using different masking levels and also other sets of band ratios. This implies that numerous combinations of band ratios and masking levels are possible, some of which may yield better results. As it would be extremely time consuming and inefficient to carry out all possible combinations, it is proposed to add an extra step to the classification procedure.

The map in Fig.12c only reveals the most "kaolinitic" and "goethitic" pixels. From this map appropriate pixels are selected and used as training pixels for maximum likelihood classification of the original band ratio images. More band ratio images can be included, and the classification threshold, the Mahalanobis Distance (MD) can be varied. The MD expresses the probability (Mather 1987) that a classified pixel belongs to a certain class. By increasing MD more pixels will be classified but the accuracy of the classification decreases. By increasing the MD, the optimum classification threshold for the test area can be defined. In doing so the results of the classification are quantified and can be compared. This is illustrated by the results in Table 4. The image presented in Fig.12c was used as sample map, and a maximum likelihood classification was carried out with band ratios $\text{TM5}*\text{TM4}/\text{TM3}*\text{TM7}$, $\text{TM3}/\text{TM4}$, $\text{TM2}/\text{TM7}$ and $\text{TM5}/\text{TM7}$. In Table 4 the amount of "kaolinite" pixels in each unit (contact metamorphic,

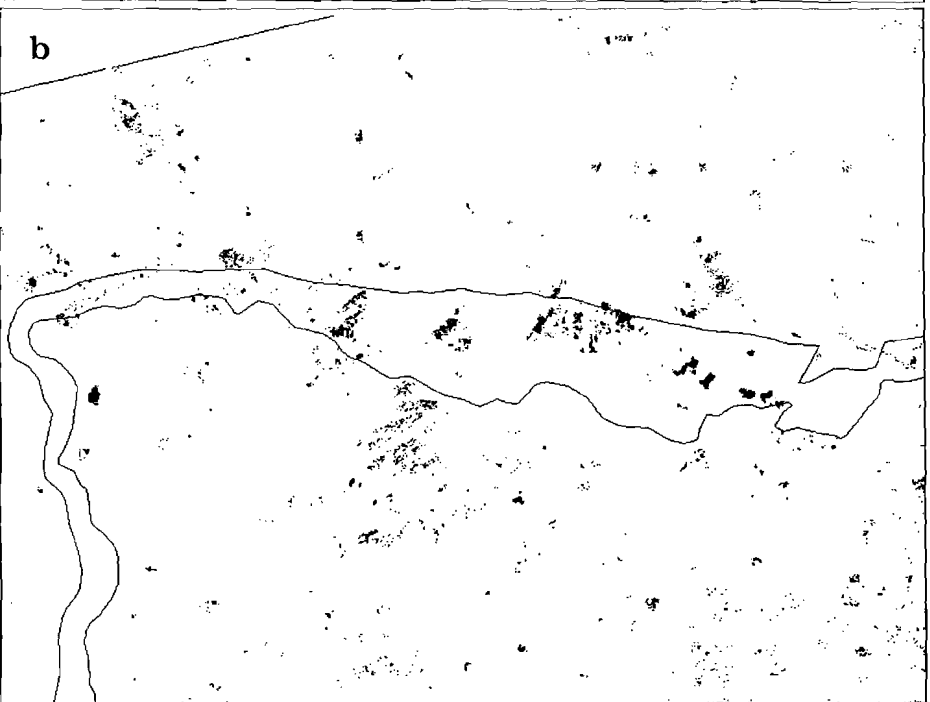
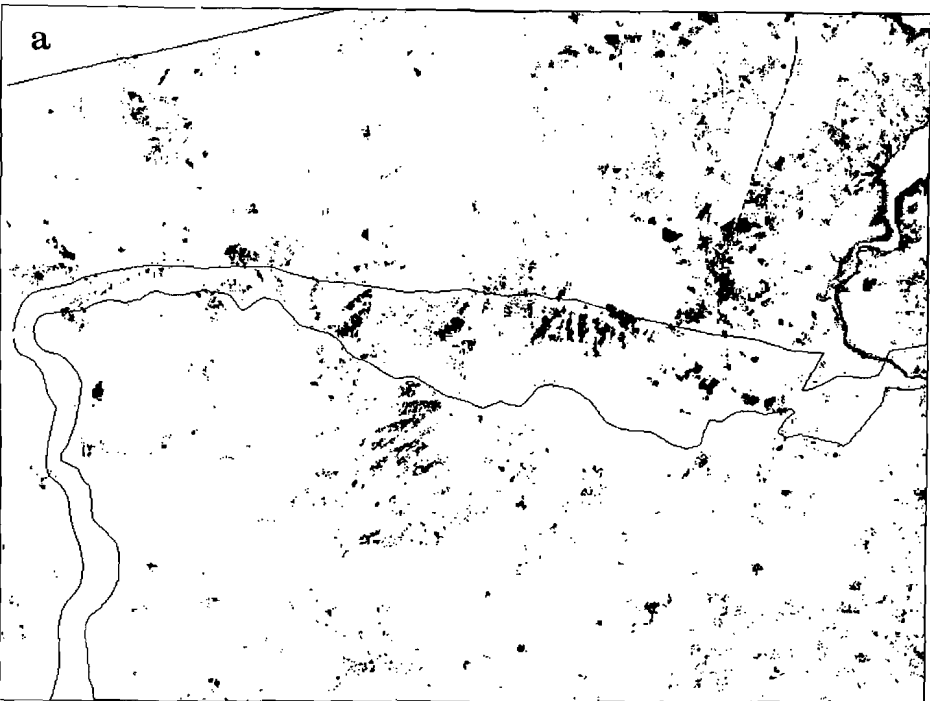
granites and regional metamorphic terrains resp.) is listed for the original (Fig.12c) classification (b3), and for the maximum likelihood classification with Mahalanobis Distances (MD) of 10, 15, 20, 25 and 30, prior to and after filtering out isolated pixels.

	contact		granites		schists		R/W
	pixels	%	pixels	%	pixels	%	
b3	1348	1.50	236	0.050	733	0.165	6.79
b3*	1688	1.88	199	0.042	890	0.200	7.77
MD=10	344	0.38	34	0.007	141	0.031	10
MD=10*	464	0.51	7	0.001	135	0.030	16.5
MD=15	1126	1.25	189	0.040	500	0.112	8.22
MD=15*	1516	1.68	161	0.034	580	0.130	10.2
MD=20	1668	1.85	397	0.085	892	0.201	6.47
MD=20*	2078	2.31	427	0.091	1080	0.244	6.90
MD=25	2003	2.23	622	0.133	1265	0.285	5.33
MD=25*	2478	2.76	702	0.150	1595	0.359	5.42
MD=30	2271	2.53	879	0.188	1699	0.382	4.44
MD=30*	2759	3.07	1024	0.219	2122	0.478	4.40

Table 4. Amount of pixels classified as contact metamorphic in: contact aureole, granitic area and low grade metamorphic area. The % columns give the surface percentage of each area that is classified as contact metamorphic. B3 corresponds with result of the stepwise masking, shown in fig. 12c. MD is the Mahalanobis Distance used for maximum likelihood classification (see text). * represent the results after filtering out isolated pixels (see text). R(right)/W(rong) is the ratio %(contact)/% (granite)+% (schists), which is the percentage of misclassification

The % columns give the percentage of the surface of each unit that is classified as "kaolinite". The column R(right)/W(rong) is the ratio of the columns (% contact)/(% granite + % schists) and is a measure for the degree of misclassification.

With increasing MD the number of classified pixels increases, but the ratio of R/W decreases. Up to MD = 25 the removal of isolated pixels improves the result. The best results are obtained with MD = 10, but the number of pixels classified is low. The original result, b3, is slightly better than a classification with MD = 20. It may be remarked that there are still a fair number of incorrectly classified pixels. In the contact aureole the kaolinite pixels are concentrated in a narrow zone, while in the granites as well as the schists the kaolinite pixels are distributed much more randomly. Furthermore the possibility kaolinitic spots are also present in soils outside the contact aureole must not be excluded.



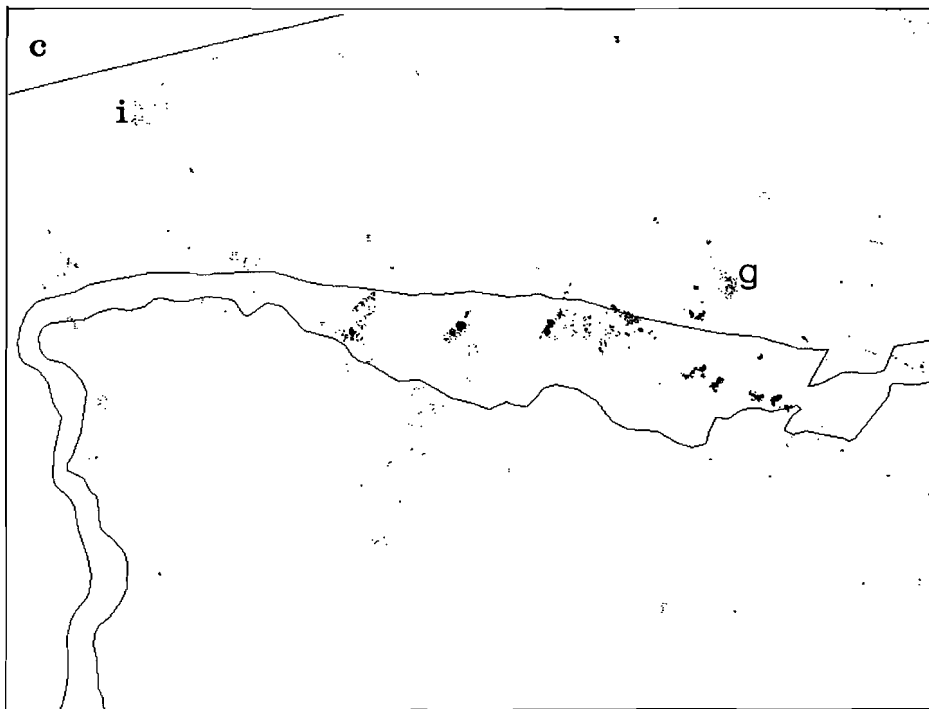


Fig.12. Results of masking. **a:** black pixels represent those that have a value below 118 for $[(\text{TM}5/\text{TM}7)/(\text{TM}3/\text{TM}4)]*50$, displaying the areas with relatively small amounts of organic material; **b:** black pixels represent those that additionally have a value below 86 for $(\text{TM}2/\text{TM}7)*200$; **c:** black pixels represent those pixels that in addition have a value above 177 for $(\text{TM}3/\text{TM}4)*200$. These are most likely to correspond with kaolinitic, goethitic soils. The boundaries of the intrusion and of the contact aureole are indicated with black lines. The clusters of pixels that are indicated with "G" and "I" correspond with the location of the villages of Guijuelo and Iñigo respectively

5.9 CONCLUSIONS

- 1) The chemistry and mineralogy of the rocks correlate with the metamorphic grade of the rocks. From the exocontact towards the intrusion biotite, muscovite and cordierite as well as the $\text{Fe}^{++}/\text{Fe}_{\text{total}}$ ratio of the rocks increase systematically while simultaneously the amount of chlorite and the volatile content decrease.
- 2) The degree of weathering of the soils increases with the metamorphic grade of the underlying rocks.
- 3) The increasing degree of weathering of the soils accompanied by increasing proportions of kaolinite, illite and $\text{Fe}_{\text{free}}/\text{Fe}_{\text{total}}$, and decreasing proportions of chlorite.
- 4) Variations in laboratory spectra of soils show a systematic correlation with the changing mineralogy of the soils.

- 5) Using the systematic correlation between selected band ratios and soil mineralogy, pixels that correspond with kaolinite and free iron rich soils are classified in a TM image, by subsequent masking of various band ratio images.
- 6) This classification technique is based on the understanding of spectral variations due to differences in soil mineralogy, in contrast to supervised classification techniques that depend on the selection of training pixels from a fieldwork area. The results are more reliable and can be interpreted more accurately, and it is expected that the technique will be useful in regions where local conditions may be different and no extensive ground study has been carried out.
- 7) The land use is strongly related to underlying rock type and geomorphology. Agricultural fields are mostly restricted to the contact metamorphic terrain, as a result of the presence of well developed soils. Since the landuse in the contact aureole typically is small scale, the diversity in vegetation is high. This high diversity zone is mapped using an image of TM3/TM4
- 8) Direct search for soils overlying contact metamorphic zones, using the stepwise masking procedure, is useful in the exploration for granite related mineralization, in particular in the case of blind cupolas.

5.10 REFERENCES

- Agterberg FPC, Chung AG, Fabbri AG, Kelly AM, Springer JS 1972. Geomathematical evaluation of copper and zinc potential of the Abitibi Area, Ontario and Quebec. Geol. Surv. Can. Paper 71-41; 55p.
- Ager CM, Milton N, 1987. Spectral reflectance of lichens and their effects on the reflectance of rock substrates. Geophysics 52; 898-906.
- Antón Pacheco C 1989. Cartografía digital de rocas en el área Albuquerque-La Codosera, Extremadura, utilizando imágenes Landsat Thematic Mapper. III reunión científica del grupo de trabajo en teledetección, Madrid;157-168.
- Billiton International Metals 1980-1986. Internal reports Los Santos Tungsten mine.
- Buurman P, Meijer EL, van Wijck JH 1988. Weathering of chlorite and vermiculite in ultramafic rocks of Cabo Ortegal, Northwestern Spain. Clays and Clay Miner. 36; 263-269.
- Diez Balda MA 1982. El Complejo Esquisto-Grauváquico, las series Paleozoicas y la estructura Hercínica al sur de Salamanca. PhD-Thesis. Univ. of Salamanca.
- Fabbri AG 1984. Image processing of geological data. Van Nostrand Reinhold Company, New York. 244p.
- Flood RH, Shaw SE 1975. A cordierite bearing granite suite from the New England batholith,N.S.W. Contrib. Miner. Petr. 52; 157-164.
- Goossens MA 1991. Integration of remote sensing data and ground data as an aid to exploration for granite related mineralization. Proceedings VIII Thematic conference on geologic remote sensing, Denver Colorado;393-406

- Guidotti CV 1984. Micas in metamorphic rocks. In: Bailey SW, Ed. Micas. Rev. Mineral.13;357-468
- Harris WG, Zelany LW, Baker JC, Martens 1985. Biotite kaolinization in Virginia Piedmont soils:I. Extent, profile trends and grain morphological effects. *Soil.Sci.Soc.Am.J.* 49:1290-1297.
- Hunt GR, Salisbury JW 1970. Visible and near infrared spectra of minerals and rocks: I silicate minerals. *Modern Geology* 1;283-300.
- Labotka TC 1991. Chemical and physical properties of fluids. In: Kerrick MD Ed. Contact Metamorphism. Rev. Mineral.26;43-97.
- Lieftink D. 1991 Internal report, Department of Geology, University of Utrecht.
- Lillesand TM, Kiefer RW 1987. Remote sensing and image interpretation. John Wiley & Sons, New York. 721 pp.
- Mather PM 1987. Computer processing of remotely sensed images. John Wiley&Sons, New York. 352pp.
- Pattison DRM, Tracy RJ 1991. Phase equilibria and thermobarometry of metapelites. In: Kerrick MD Ed. Contact Metamorphism. Rev. Mineral. 26;105-182.
- Proust D 1982. Supergene alteration of metamorphic chlorite in an amphibolite from Massif Central, France. *Clay Miner.* 17;159-173.
- Rebertus RA, Buol SW, 1984. Iron distribution in a developmental sequence of soils from mica gneiss and schist. *Soil sci.soc.Am.J.* 49;713-720.
- Rowan LC, Antón-Pacheco C, Brickey DW, Kingston MJ, Payas A, Vergo N, Crowly JK, 1987. Digital classification of contact metamorphic rocks in Extremadura, Spain using Landsat thematic mapper data. *Geophysics* 52;885-897.
- Stoner ER, Baumgartner MF, 1981. Characteristic variations in reflectance of surface soils. *Soil Sci.Soc.Am.J.* 45;1161-1165.

CHAPTER 6

INTEGRATION OF LANDSAT TM, AIRBORNE MAGNETIC AND RADIOMETRIC DATA, AS AN EXPLORATION TOOL FOR GRANITE RELATED MINERALIZATION.

6.1 ABSTRACT

This study demonstrates how remote sensing and data integration techniques can be successfully used as a tool in the exploration for granite related mineralization. A methodology is developed to overcome a number of problems that hamper efficient incorporation of these techniques as a standard routine in exploration for potentially mineralized areas: 1) The basic relation between geology and the original data is often obscured by complex data manipulation, which obstructs the understanding of the final output. 2) The risk of removing potentially important information during the interpretation of the data is normally considerable, and therefore needs to be controlled. 3) The decision criteria with respect to the correctness of classifications are often arbitrary and therefore need to be quantified. 4) Error- and quality assessment is often subjective and therefore not reproducible under different circumstances.

6.2 INTRODUCTION

Since the introduction of relatively cheap, PC-based image processing systems in the 1970's, exploration geologists have been testing the applicability of satellite and airborne remote sensing, data integration and image processing techniques for characterisation and classification of mineralized areas (e.g. Amor et al. 1989, Rheault et al. 1990). A main task in these studies is to define how the procedures of feature recognition (Fabbri 1984) and digital data integration (Bonham-Carter et al. 1990) should be applied in order to extract the most relevant information from available data sets.

At present much effort goes into developing methodologies of combining multiple data sets. Powerful statistical analysis and classification techniques are applied to cluster the information into relevant classes (e.g. Franklin and Gillespie 1990). Red-green-blue and intensity-hue-saturation visualisation methods are commonly used as output to present the final data set (e.g. Harris 1990). These techniques however have disadvantages when used by exploration geologists. The interpretation of the final output, and understanding of its basic relationship with geology is obscured by the high degree of statistical manipulation and by the often complex colour representation of the data. Additionally, when good results are obtained for a specific calibration area, it is often difficult to apply the methodology elsewhere to less well documented areas.

In mineral exploration, after initial survey data have been collected, three steps are involved (Mellinger 1990): 1) Interpretation of each survey; 2) integration of relevant information from several surveys; 3) decision making, concerning the potential presence of mineralization. Mineralization is often

accompanied by anomalies which, although sharing general characteristics, are highly variable and typical only of individual mineral deposits, as is illustrated by the vast amount of literature published on individual mineral occurrences. Therefore, successful application of remote sensing data and data integration techniques in exploration is highly dependent on the flexibility of the predicting procedure. This paper presents a study which investigates, in a calibration area with a diversity of known granite related mineralization:

1) how the variation in airborne magnetic and radiometric data and Landsat Thematic Mapper data relate to geology and mineralization and; 2) how digital image processing and data integration can be used to develop a flexible decision-making tool for the prognostication of granite-related mineralization.

6.3 GEOLOGICAL BACKGROUND

The study area is located in central-western Spain (Fig.1). Granitic rocks of the Hercynian Central System Batholith intruded metasediments of Precambrian to Silurian age. The contact aureole is host to a large tungsten skarn deposit and a number of small vein deposits of tungsten (wolframite and scheelite), tin, lead, zinc, copper, uranium and gold. The vein deposits are located in fracture systems of Hercynian age (Diez Balda 1982) with NE and WNW strike. The area is well documented due to exploration and mining activities by Billiton Española SA and the Junta de Castilla y León, and scientific studies, mainly conducted by the University of Salamanca (e.g. Ugidos 1974, Saavedra and García 1974, Pellitero 1980, Diez Balda 1982, Bea 1982, Lorenc and Saavedra 1985, Rottura et al. 1989)

The tungsten skarn of Los Santos

The situation in the vicinity of the skarn deposit, east of the village of Los Santos, is of particular interest to this study for a number of reasons: 1) it is a large and potentially economic deposit; 2) it is genetically related to the intrusive event (Villadeval et al. 1980); 3) the study of the granitic (CHAPTERS 2-4) and contact metamorphic (CHAPTER 5) aureole has revealed well developed geological and geochemical anomalies in the environment of the skarn; 4) the mineralization is well documented as a result of the development of the deposit, undertaken by Billiton between 1980 and 1985.

The skarn deposit, located at the granite contact near Los Santos, has an estimated reserve of 1.5 million tonnes at a grade of 0.79% WO_3 . It is hosted by Cambrian limestones and its mineralogy mainly comprises garnet and pyroxene and smaller amounts of wollastonite, plagioclase and sulphides. Tungsten occurs almost exclusively as scheelite. It is intersected by a major NE-trending fault-zone, which was active during granite emplacement. This fault-zone probably provided the necessary pathways for mineralizing fluids (Westerhof, pers.comm).

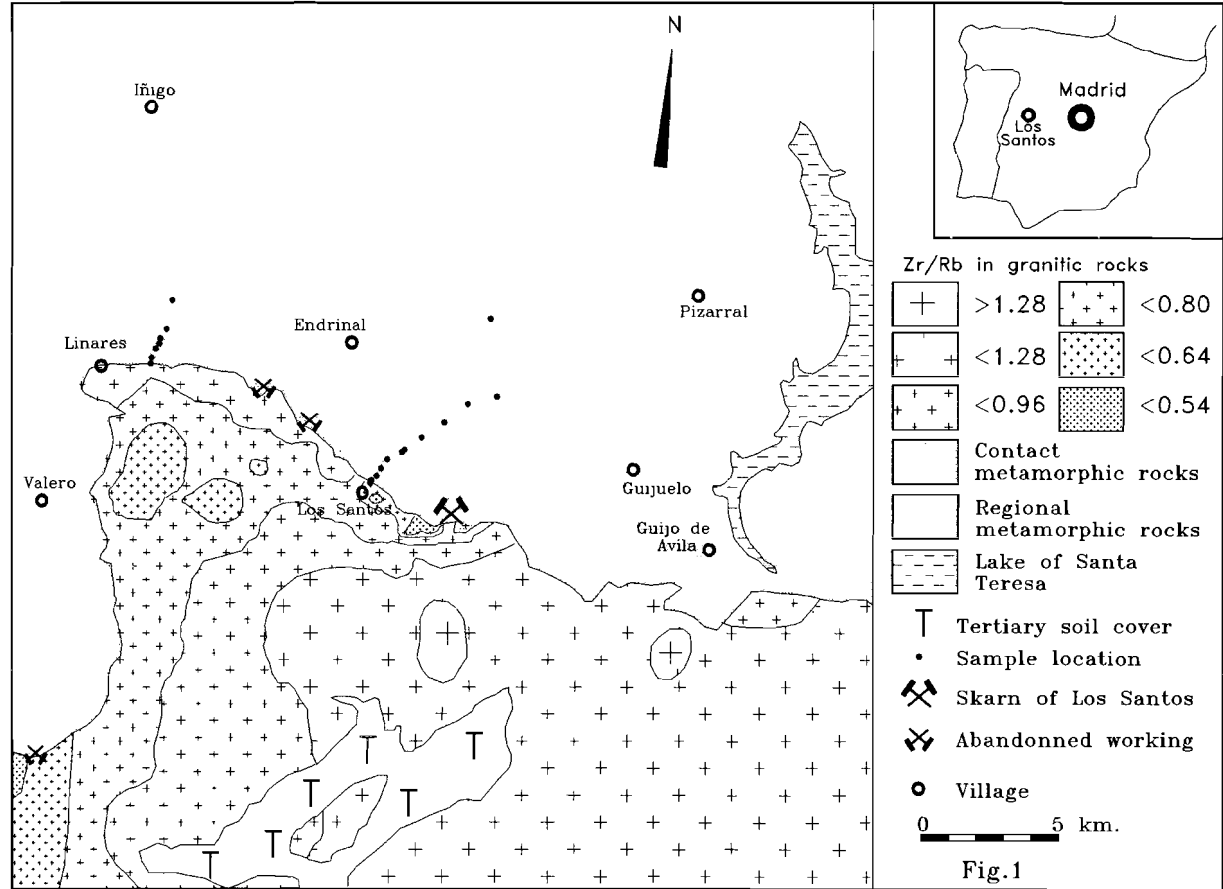


Fig.1. Simplified geological map with the granitic, contact metamorphic and regional metamorphic rocks. The contours of whole rock Zr/Rb illustrate the zoned character of the intrusion. Rocks with $Zr/Rb < 0.8$ correspond with monzogranites, otherwise with granodiorites

The granitic rocks

The intrusion south of Los Santos is geochemically and mineralogically zoned. This is illustrated by the contour map (Fig.1) of the Zr/Rb-ratio, which is based on more than 83 whole rock analyses. The granitic rocks grade from granodiorites in the core of the intrusion to muscovite + cordierite bearing monzogranites at its margin. The most fractionated part of the intrusion occurs adjacent to the tungsten skarn, and is accompanied by numerous aplitic dikes and sills. Ratios of $Zr/Rb > 0.8$ correspond with granodiorites (Fig.2), while ratios < 0.8 correspond with muscovite + cordierite bearing monzogranites.

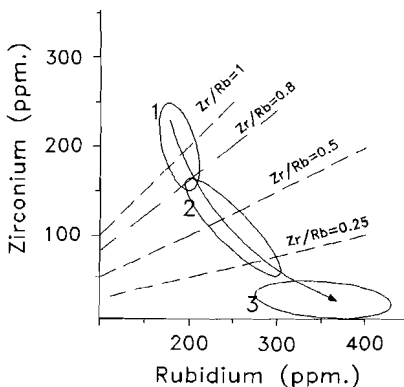


Fig.2. Relation between Zr and Rb in samples from the zoned intrusion. Field 1 corresponds with the compositional field of the granodiorites, field 2 with that of the monzogranites and field 3 with that of the aplitic dikes.

Study of biotite compositions shows that the magma in the vicinity of the skarn was richer in fluorine than in other parts of the intrusion (CHAPTER 3) which is a reason to suspect that the granitic magma provided the fluids that reacted with the limestone. Whether the granite also provided the tungsten is debated. The tungsten was probably derived from volcanogenic formations within the Precambrian sedimentary rocks of the Complejo Esquistoso Grauvaquique (Pellitero 1980, Saavedra 1982, Billiton 1983).

Contact metamorphic rocks

Along the granite contact a clear thermal aureole developed in the greenschist facies metamorphic sediments. Significant variation exists in the surface width of the aureole. In non-mineralized parts the biotite isograd is located at a distance of 700m but in the vicinity of the skarn (Fig.1) the isograd is situated at more than 2000m perpendicular to the contact. The reason for this variation is not yet clear. It may be that the granite contact is shallower near Los Santos than in other parts of the contact, although drillcore data, available down to a depth of 150m, indicate a fairly steep contact. The contact metamorphic rocks, which grade from biotite-bearing spotted slates at the outer boundary to cordierite-biotite hornfelses at the granite contact were sampled along two profiles perpendicular to the contact,

one in the wider part of the aureole and the other in the narrow part (Fig.1). In the direction of the contact, chlorite gradually disappears while biotite, cordierite and muscovite increase in abundance. The changing mineralogy is accompanied by clear geochemical variations (CHAPTER 5), e.g. by increasing $\text{Fe}^{++}/\text{Fe}_{\text{tot}}$ -ratio (Fig.3a) and decreasing LOI-content (Fig.3b). Metasomatic activity in the aureole near Los Santos is evidenced by increasing contents of Rb, Cs, Co and MnO when the contact is approached.

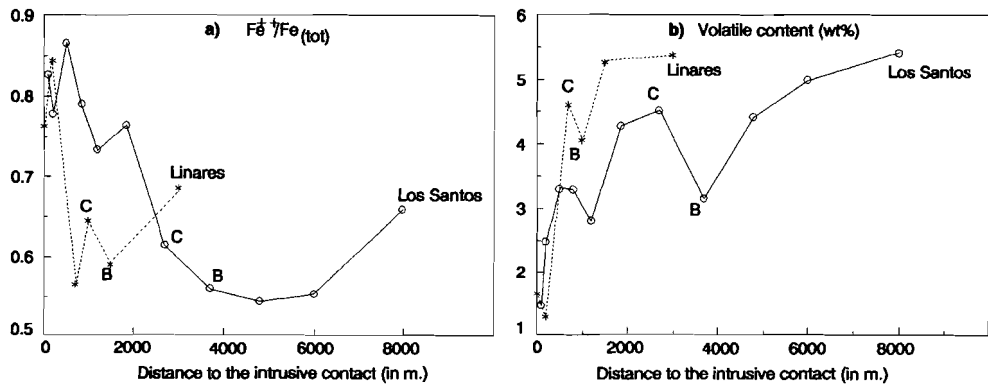


Fig.3. Variation of $\text{Fe}^{++}/\text{Fe}_{\text{total}}$ and LOI in whole rock sedimentary samples as a function of the distance from the intrusion, along two profiles perpendicular to the contact (see Fig.1.) Contact metamorphic biotite and cordierite isograds are indicated in both profiles by B and C respectively.

6.4 INTERPRETATION OF THE REMOTE SENSING DATA

Our objective is to develop a data processing methodology that provides the exploration geologist with the flexibility necessary for the prediction of potentially mineralized areas in poorly known REGIONS. Although ground data provided the basic understanding of the significance of variations in the remote sensing datasets, the procedure is demonstrated using only remote sensing data (TM-imagery and airborne geophysics), without the involvement of ground data for two reasons: 1) in many reconnaissance exploration surveys, detailed ground data are absent; 2) the need for such a methodology is much higher for remotely sensed data than for ground data, since the risk of misinterpretation is much greater for remotely sensed data.

Our primary target is to detect features related to the intrusive contact, such as the contact itself and contact metamorphic rocks, as most of the mineralization in this region is confined to the contact aureole, and gossans or other anomalies specifically related to the mineralization are absent.

First, the significance of variations in the remote sensing data in relation to the geology is explained. All image processing was performed using an Iwvis GIS, developed by the International Institute of Aerospace Survey and Earth Sciences, Enschedé, the Netherlands.

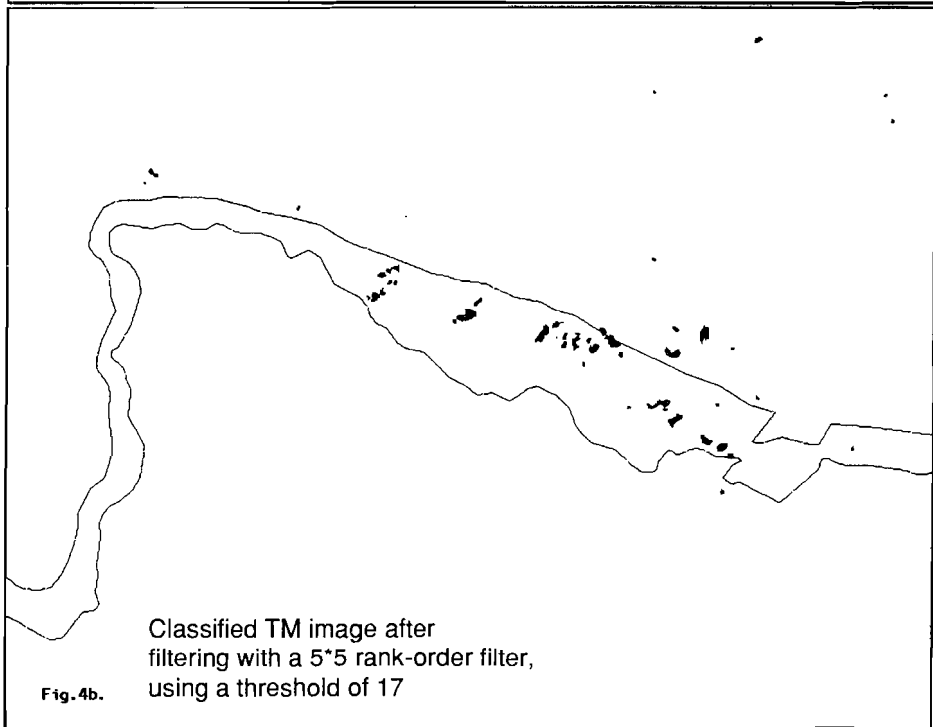
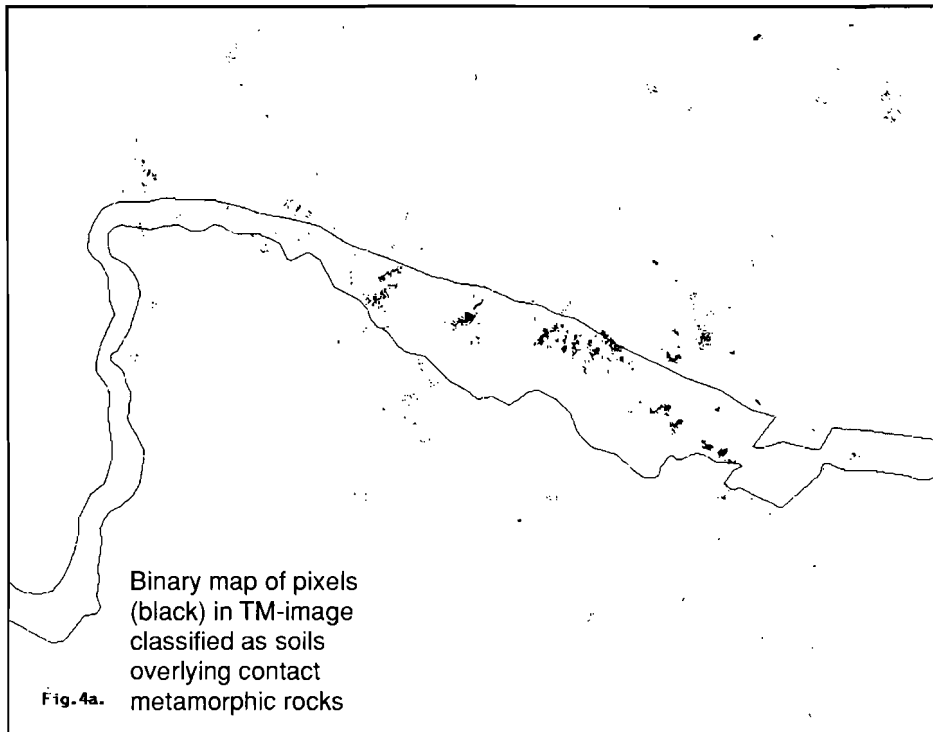
Landsat Thematic mapper data

In the Los Santos area soils overlying the contact metamorphic rocks are distinguished in TM-images (acquisition date 12 Nov.1984) from other soils by means of subsequently masking various band ratio images (CHAPTER 5). This masking procedure is based on the difference in clay mineralogy of soils overlying contact metamorphic rocks and regional metamorphic rocks. Soils overlying the contact rocks are relatively rich in kaolinite, illite and free iron, and poor in chlorite and smectite, WHEN compared to exocontact soils. Laboratory spectra demonstrate that the mineralogical variations are accompanied by well defined changes in ratios of TM2/TM3, TM2/TM5, TM2/TM7, TM3/TM4, TM4/TM7 and TM5/TM7. The systematic relation between clay mineralogy and spectral behaviour is used to identify pixels that are likely to represent contact soil overlying contact metamorphic rocks (Fig.4a).

In addition to the pure spectral information, the TM-data provide very useful textural data, with particular reference to the type and scale of land use (CHAPTER 5). In the Los Santos area the land use is closely related to underlying rock type. The regional metamorphic terrain has low relief, little soil cover, has a rather uniform vegetation cover and is predominantly used for cattle grazing. The granite terrain has intermediate relief, variable soil cover and vegetation and, although locally used for agricultural purposes, it mainly serves for pasture. The contact metamorphic area however has well developed soils, relatively high relief, diverse vegetation cover and is predominantly used for small scale agricultural purposes. This variation in land use and vegetation cover is detectable by passing a diversity filter over an image of TM3/TM4. A diversity filter replaces the central value in a kernel by the total amount of different values that are present within the kernel. For a 15*15 kernel the diversity theoretically can range between 1 and 225. Highest diversity is found for the contact area, with small scale land use, intermediate diversity for the granitic terrain, while low diversity predominates in the low grade metamorphic terrain (Fig.5a)

Airborne geophysical data

The airborne data were acquired during a survey carried out in 1980 for the ENUSA, the Spanish uranium consortium. The survey was flown at a height of 120m above ground level, with a line spacing of 1 km. Gamma ray data were collected using four NaI crystals, each of a size of 4*4*16 inch. A separate crystal of 4*4*10 inch was carried to correct for atmospheric radiation. The magnetic data were collected using a precision proton magnetometer, reading every second with a resolution of 0.25 gammas. Severe levelling problems were encountered for the magnetic data, since tie lines were not flown. For the purpose of this study, contoured maps were digitized and the data were re-gridded using GEOSOFT software, to a pixel size of 30m., in order to be compatible with the TM data. All data were georeferenced to UTM projection zone 30, Hayford ellipsoid, to conform to the projection used in topographic maps published by the Spanish military geographical service.



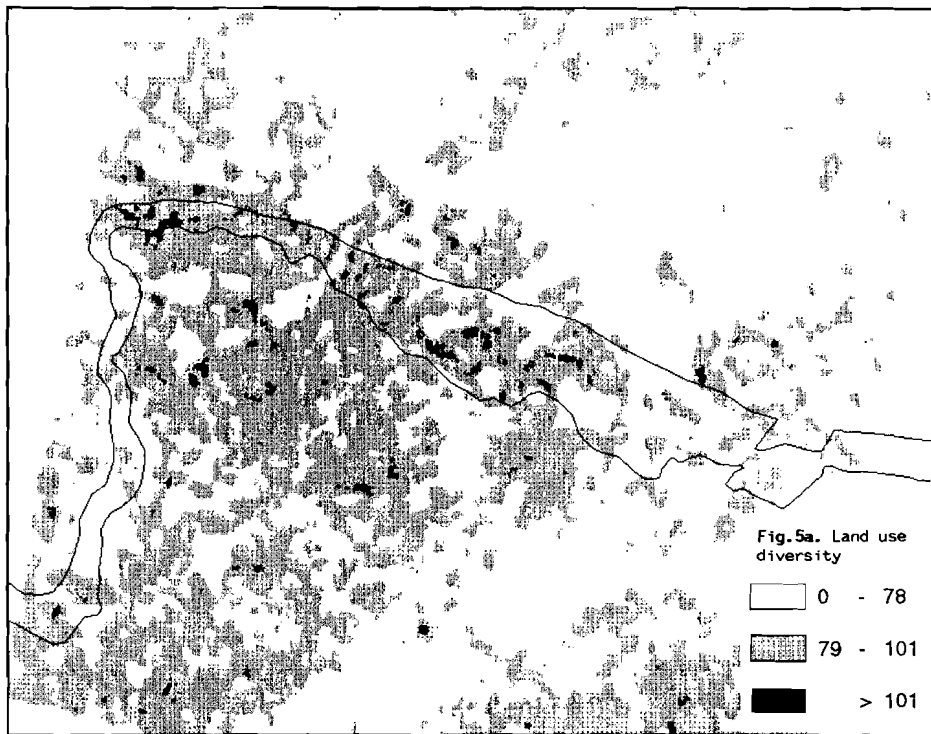
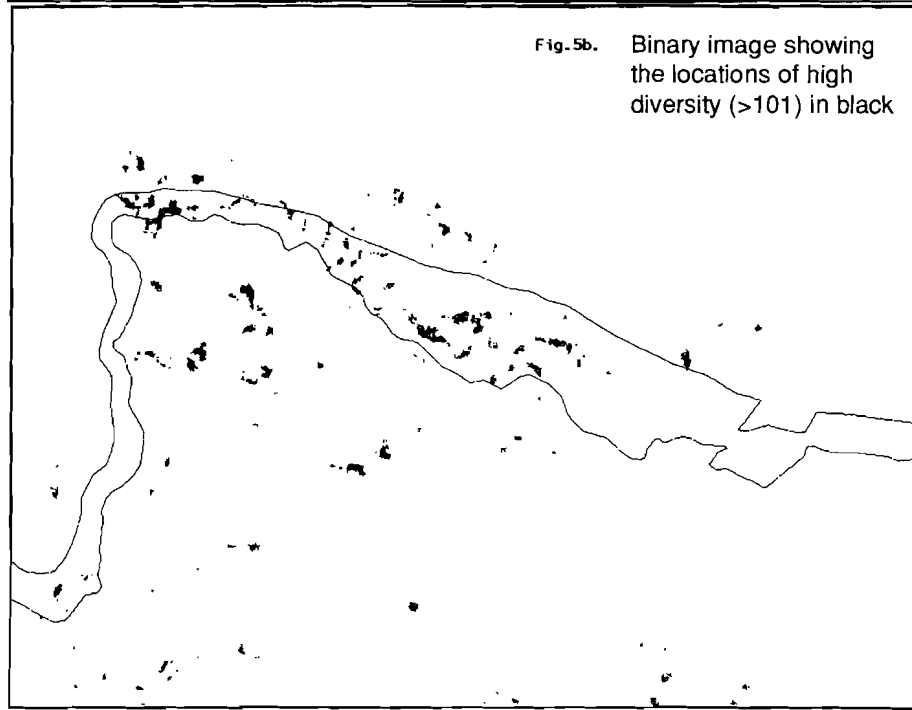


Fig.5b. Binary image showing the locations of high diversity (>101) in black



Radiometric data

Average airborne radiometric values for %K₂O, eU and eTh in the granitic, contact metamorphic and regional sedimentary terrain are listed in Table 1. Whole rock contents for these elements are also listed in this table. These were analyzed using both X-Ray Diffraction and Neutron Activation. For U and Th the quality of the Neutron Activation analyses is better than that of the XRF analyses, but fewer samples were analyzed with Neutron Activation, since these analyses are much more expensive.

Table 1. Average K₂O(wt%), U(ppm) and Th(ppm) content of granitic, contact metamorphic and regional metamorphic terrain.

	K ₂ O	U	Th	n
granite ¹⁾	3.04	4.15	13.74	90736
contact ¹⁾	2.48	3.12	11.57	485079
sediments ¹⁾	2.21	2.78	10.17	429094
granite ²⁾	4.55	4.31	13.9	86
contact ²⁾	3.93	< 4	13.8	16
sediments ²⁾	3.29	< 4	12.7	15
granite ³⁾	4.57	4.46	15.7	13
contact ³⁾	3.97	2.08	12.4	5
sediments ³⁾	3.71	2.52	12.0	6

¹⁾ From gridded airborne radiometric data, ²⁾ Whole rock X-Ray Fluorescence Analyses, ³⁾ Whole rock Neutron Activation Analyses. n represents the number of data used for calculation of averages.

Notwithstanding the fact that the average values for airborne K₂O and Th are lower than those for the whole rock data, there is a good correlation with the ground data. Granites are distinguished from sedimentary rocks by higher average K₂O, U and Th contents. The average data suggest that the granites could be distinguished from metasediments using individual radiometric datasets, however this is not the case, as is illustrated by the Th map (Plate 4a). Low Th values do not exclusively occur in the sedimentary terrain, and high values are not restricted to the granite terrain. This is partly due to the zoned character of the granite intrusion. The contour pattern in the granite area is similar to the element distribution patterns based on whole rock analyses (Fig.1). When the gridded values of eTh in the granitic rocks are plotted against those of whole rock Zr/Rb (Fig.6), two clusters appear. Ninety-five percent of the data plot in cluster (a), with a correlation coefficient of 0.67. High thorium values correspond with granodiorites while the lowest Th values correspond with the fractionated cordierite + muscovite bearing monzogranites. The second cluster (b), with relatively high Th contents, corresponds with an area near known mineralization of Sn, Th and U in the southwestern corner of the image.

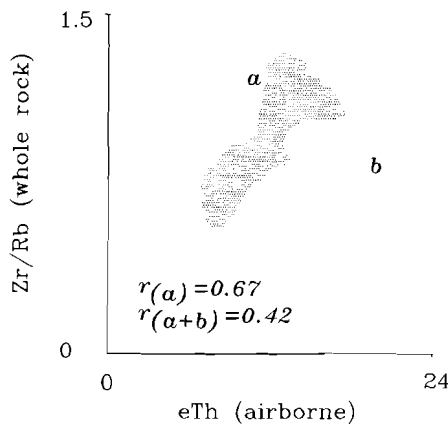


Fig. 6. Relation between gridded airborne eTh in granitic terrain and gridded whole rock Zr/Rb. 95% of the data plot in cluster (a), with a correlation coefficient of 0.67. the correlation of the total data set is 0.42.

As demonstrated, adequate distinction between granites and sediments is not possible on the basis of individual radiometric datasets. However, combined classification of %K, eTh, eU images by means of a maximum likelihood classifier produces useful results. Because the intrusion is geochemically zoned, with a large compositional range for the three radioelements, five different granite training classes were sampled. One additional training class in the metasedimentary terrain was sufficient to allow good discrimination between granites and sediments. The average values and standard deviation for the radioelements in each sampled class are listed in table 2.

	eU(ppm)		eTh(ppm)		K ₂ O(percent)	
	Mean	Stdv	Mean	Stdv	Mean	Stdv
S	3.62	0.23	10.2	0.6	2.03	0.24
G1	4.58	0.44	17.5	0.54	3.26	0.11
G2	4.4	0.28	14.4	0.24	2.9	0.09
G3	3.85	0.21	12.9	0.62	2.75	0.08
G4	3.71	0.16	10.7	0.34	2.97	0.0
G5	3.17	0.11	8.5	0.64	2.45	0.4

Table 2. Average and standard deviation for eU, eTh and K₂O in training sample sets, used for supervised classification of radiometric data. (S) sedimentary rocks and (G1-G5) granitic rocks.

The maximum likelihood classification is carried out with various Mahalanobis Distances (Mather 1987, Richards 1986), in order to define how optimum distinction between the rock types can be obtained. The Mahalanobis Distance (MD) expresses the probability that a classified pixel belongs to a certain class.

As pixel values with high MD are relatively far away from the mean of the training class, as opposed to those with a low MD, increasing the MD has the effect that more pixels will be classified but the accuracy of the results decreases. By varying MD, the optimum classification parameters can be determined. The results of classification with different MD are listed in table 3. With increasing MD the degree of misclassification slightly increases, but the percentage of unclassified pixels decreases significantly. In spite of some misclassification, most useful results are obtained with MD = 100 (Plate 4b).

Table 3. Results of supervised classification with different Mahalanobis distances.

Rocktype: Classified as (in %):		CONTACT METAMORPHIC ROCKS						
		U	S	G1	G2	G3	G4	G5
MD = 20	83.9	10.0	0.6	0.1	3.9	0.9	0.4	
MD = 35	69.0	21.7	1.4	0.2	5.5	1.3	0.6	
MD = 50	55.7	31.8	2.1	0.3	6.9	1.8	1.0	
MD = 70	38.2	45.1	2.9	0.9	8.9	2.2	1.4	
MD = 100	22.0	55.3	5.1	2.9	10.4	2.2	1.7	
median25	21.0	56.7	5.3	3.2	10.0	2.2	1.3	
median127	13.7	69.5	6.1	8.7	1.5	0.2	0	

Rocktype: Classified as (in %):		INTRUSIVE ROCKS						
		U	S	G1	G2	G3	G4	G5
MD = 20	47.2	0.8	11.1	17.3	16.6	3.2	3.4	
MD = 35	25.0	3.0	17.5	23.0	22.3	4.0	4.9	
MD = 50	17.1	4.5	19.6	24.5	23.8	4.4	5.7	
MD = 70	11.7	5.8	21.0	25.2	24.9	4.6	6.4	
MD = 100	7.5	7.7	21.5	25.4	25.8	4.8	6.9	
median25	7.0	7.0	21.4	26.5	26.5	4.6	6.7	
median127	4.2	6.9	22.5	32.5	24.1	5.1	4.4	

Rocktype: Classified as (in %):		LOW GRADE SEDIMENTARY ROCKS						
		U	S	G1	G2	G3	G4	G5
MD = 20	84.5	14.3	0.0	0.0	0.1	0.0	0.8	
MD = 35	67.5	29.5	0.2	0.0	0.2	0.0	2.4	
MD = 50	50.9	43.5	0.5	0.2	0.3	0.1	4.1	
MD = 70	29.2	61.9	0.7	0.7	1.3	0.1	5.7	
MD = 100	11.8	75.6	1.0	1.2	2.8	0.2	7.1	
median25	9.8	79.1	1.2	1.2	2.4	0.1	5.8	
median127	3.4	93.3	2.5	0.0	0.0	0	0.5	

This table shows the surface percentage of each of the mapped rockunits: granites, contact metamorphic and regional metamorphic that is unclassified (U), classified as sediment (S) or as granite (G1-G5, see table 2.), using different Mahalanobis Distances (MD). Median25 and Median127 are the results of passing a 25*25 and 127*127 median filter over the classified image (MD=100).

Apart from a good separation of granites and sediments, the zonal pattern within the intrusion is also retrieved. The contact aureole is predominantly classified as sediment (55.3%), however a considerable part (22%) of the contact remains unclassified. Misclassification of the contact aureole occurs mainly in the southwest corner of the image, and may be due to the facts that: 1) the flight lines end here; 2) there are fairly steep mountain ridges, so effects of topography may be present; 3) mineralization of U and Th is present in this part of the area, causing radiometric anomalies. The main part of the aureole is classified as sediment, which implies that the intrusion of granites did not cause any radiometric anomaly. Of the intrusive rocks 7.5% remains unclassified and 7.7% is misclassified as metasediment. Of the metasediments 11.8% remains unclassified while 12.3% is misclassified as granite. Most of the misclassified sediments are similar to granite type 5, which corresponds with the monzogranitic part of the intrusion (Fig.1), and a part of the monzogranite is classified as metasediments.

Residual aeromagnetic data

The image of the residual airborne magnetic data is presented in Plate 5a. There is a strong contrast in magnetic field over the granites and the sediments. The sediments are more magnetic and exhibit greater magnetic contrast than the granites. The absence of magnetic relief in the granitic area is probably related to the fact that the intrusion is uniformly ilmenite bearing. The linear features in the magnetic image over the sediments suggest the presence of faults. Unfortunately the flight line direction is the same as the dominating fault strike direction (NE). As mentioned before, severe levelling problems were encountered, and although some of the variations may coincide with faults, it was decided that the magnetic data should not be used for structural interpretation. Levelling errors only seem to be present in the metasedimentary area, probably due to the greater magnetic contrasts in these rocks.

More relevant is the fact that the magnetic field over the wider part of the contact aureole is similar to that over the granite intrusion, while the narrower part of the aureole is more similar to the sedimentary rocks. The flat magnetic relief over the contact is presumably a result of resetting of the rock magnetism, due to contact metamorphic heating. The systematic increase of $\text{Fe}^{++}/\text{Fe}_{\text{total}}$ towards the contact (Fig.3a) proves that during heating and recrystallization of the sedimentary rocks, Fe^{+++} was reduced to Fe^{++} (CHAPTER 5). The recrystallization and reduction of ferric iron probably caused resetting of the magnetic field, which resulted in low magnetic values and little magnetic contrast. Resetting of the remanent magnetism in rocks adjacent to intrusive rocks is a well known phenomenon (e.g. Speer 1981, Buchan and Schwartz 1985, Schwartz and Buchan 1989). The distance over which resetting occurred corresponds well with the width of the aureole, as is illustrated by the $\text{Fe}^{++}/\text{Fe}_{\text{total}}$ variation along the two profiles as a function of distance to the contact (Fig.3a).

6.5 FURTHER DATA PROCESSING

In this section it is demonstrated how the data presented above can be used to predict the presence of contact metamorphic rocks. It is not pretended that the results presented here are optimal since the purpose is to demonstrate how information can be handled interactively in a flexible manner, how errors in the interpretation can be estimated, how various decision criteria can be adjusted and what the consequence is for the predictive model. Optimization would not significantly change the methodology, it would only make the data handling more complex. The procedure that was followed is schematically presented in Fig.7.

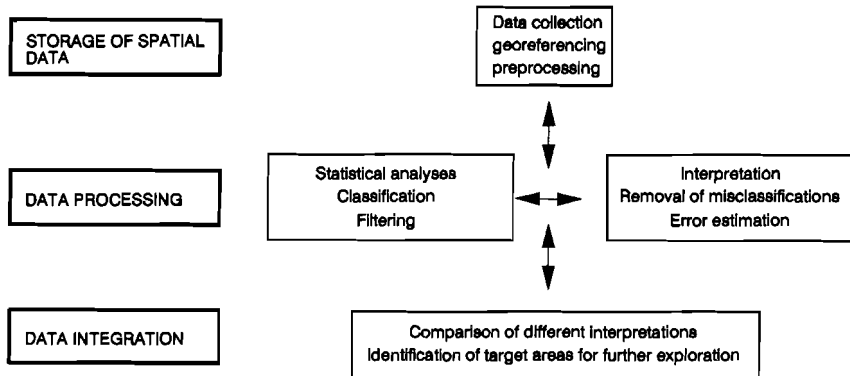


Fig.7. Schematic representation of the different phases of data processing in this study. All arrows are in two directions because most steps are iterative.

The image in Fig.4a shows the location of soils classified in a TM image as overlying contact metamorphic rocks. Most of the black pixels are in clusters that form a zone within the contact aureole. However, they are not unique for the contact aureole, as many, usually smaller, clusters occur in the low grade sedimentary as well as in the granitic terrain. At this point it must be decided which pixels are probably misclassified, and therefore have to be removed. During this step it is inevitable that valuable information is either regarded as misclassified, or unintentionally lost during the subsequent filtering. This can however be obviated by linking a reproducible numerical value to the decision whether a pixel, or a group of pixels is classified correctly or not, so that during a later stage of interpretation the decision can be reconsidered and modified if necessary. In this case the amount of black pixels within a given area is a useful criterion on whether they are classified correctly or not, and also provides such a numerical link. A rank order filter is very appropriate to assess which pixels were misclassified, as is demonstrated by the example of a 5*5 kernel and a threshold of 17 in (Fig.8a). The kernel covers an area of 25 pixels, with values between 1 and 25. When ranked from low to high, the 17th value in this range of numbers is seventeen and therefore the central value in the kernel (16) will be replaced by 17. As the classified image is a binary one, all clusters below a desired size can be removed by passing a

rank order filter over the image, using the proper threshold. For example, using a 5*5 filter and a rank of 17, all clusters consisting of less than 9 black pixels (binary 1) are removed (Fig.8b).

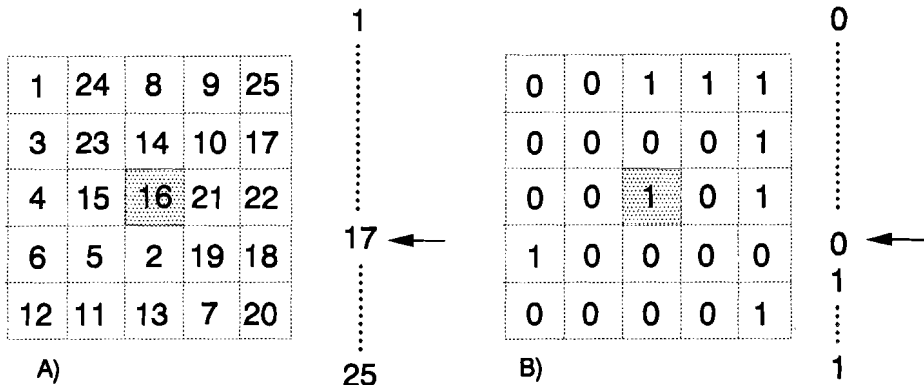


Fig.8. Illustration of a 5*5 rank order filter, using a threshold of 17. a: for a grey scale image; b: for a binary image.

The result of passing this filter over the classified image (Fig.4a) is that most black pixels outside of the contact aureole disappear (Fig.4b). However, although most classified pixels are restricted now to the contact aureole, a large part of the aureole is unclassified. This is mainly due to the relative scarcity of well exposed soils. In order to assess whether the unclassified pixels in between the classified pixels might also be contact metamorphic, the sphere of influence of the classified pixels can be extended. This could be done using binary dilation (Fabbri 1984), but this method has the disadvantage that small clusters "grow" relatively faster, and thus become relatively more important than larger clusters. Rather, the extension of the sphere of influence should be related to the concentration of pixels in an area. The classified image (Fig.4b) is therefore contoured with a 50*50 kernel. The result was subsequently level sliced into three classes (Plate.1c): 1-3 pixels per window (green), 4-18 (blue) and 19-44 (red). The significance of each specific contour value is illustrated in the diagram (Plate 2). The blue line shows the surface percentage of the contact metamorphic aureole (left axis) with a specific contour value (X-axis). The orange line does the same for the granites + metasediments. The purple line gives the ratio (right axis) of the two lines for each contour value, demonstrating that values higher than 18 are most specific for the contact aureole. The vertical dashed lines indicate the various class boundaries that were used for level slicing the image.

The diversity image (Fig.5a) enables the selection of areas with the highest diversity in land use, which are most typical for the contact area. All pixels with a diversity value above 101 are reset (Fig.5b) to 1 (black), all other pixels to 0 (white). Again, the high diversity pixels are not uniquely confined to the contact aureole, but also occur in the granite terrain. Therefore it has to be decided which black pixels

are likely to correspond with contact aureole. By analogy to the way the classified TM image was handled, this decision can be based on the concentration of black pixels. After contouring the image with a 50*50 kernel, the result was level sliced (Plate 3) into four classes: 1-2(blue), 3-7(green), 8-36(yellow) and 37-85(red). In this way the interpretability of the results is strongly improved, as the diagram demonstrates that high diversity is more frequent in the contact aureole than in the granite terrain.

The classified radiometric data can be used to map the granite contact by calculating the boundaries between areas classified as granite and areas classified as sediment. It is however likely that a certain degree of misclassification occurred, as relatively small areas classified as granite occur in the sedimentary terrain and vice versa. In order to avoid granite boundaries being drawn along misclassified sediments and granites, a criterion is needed that enables to decide which pixels are misclassified. These pixels can subsequently be corrected. An obvious criterion for misclassification is the dimension of a specific group of classified pixels, as smaller areas of a given class are more likely to be misclassified than larger ones. Areas with an extension below a desired threshold can be removed by passing a median filter over the classified image. A median filter is in fact a special rank-order filter, that replaces the central value in a kernel by the median of all values in the kernel. When the size of filter is small, only small areas will be replaced by the class value of the surrounding pixels. The effect of increasing the size of the filter is that larger areas will be regarded as misclassified and reset to the class of the surrounding pixels, which is demonstrated by passing a 25*25 and a 127*127 median filter over the classified image (Table 3). Best results for the study area are obtained with the 127*127 filter (Plate 4c). Only areas classified as granite and metasediment that are larger than 8065 pixels remain intact. On the basis of this image the granite boundaries are established.

Fieldwork reveals that the contact aureole is normally narrower than 2.5km. In order to identify rocks that are possibly contact metamorphic, pixels at less than 2.25km distance from the contact are mapped by calculating a corridor around the granite contact (plate 4d). However, it would not be realistic to assume that within this corridor all pixels are equally likely to represent contact metamorphic rocks, because the larger the distance to the constructed contact, the smaller the probability is that contact metamorphic rocks are present. Therefore the corridor is subdivided into three zones. As the minimum width of the aureole is approximately 750m, and the average width of the contact aureole in the study area is 1500m, the zone is divided in the distance classes; 0-750m, 750-1500m and 1500-2250m. Naturally, the width of the corridor can be varied. It will be clear that not removing small misclassified areas prior to calculation of the corridors will have the effect creating multiple corridors across the entire image, and thus complicating the information content and reducing the interpretability.

Contact metamorphic rocks are predominantly classified as metasediments, but are simultaneously characterized by a magnetic signature similar to the granitic intrusion. Therefore the combined magnetic and radiometric data can be used to detect contact metamorphic rocks, by finding those pixels that are classified as sedimentary rock, and have the magnetic signature of granitic rocks. With respect to the magnetic signature, the contact metamorphic rocks are similar to the granitic rocks in two aspects: 1) the absolute value of the magnetic field in the contact zone is similar to that in the granite; 2) the relief of the magnetic field in the contact zone is flat. The second feature it is expected to be present in other contact metamorphic zones and in other regions, for reasons described above. The first feature may be more specifically related to this area and vary in other situations. Therefore sedimentary rocks that only have a flat field are distinguished from those that additionally have the same magnetic value as the granites near the contact. Areas in green (Plate 5b) represent sediments with a low magnetic relief. Areas in red additionally have a magnetic value identical to that of the granites.

6.6 INTEGRATION OF THE RESULTS

To this point, a number of maps have been obtained, each of which contains information about the possibility that contact metamorphic rocks are present at a certain location. By adding up these components (Plates 2,3,4d and 5b), all contained information is combined into a map which enables prediction where contact metamorphic rocks are most likely to be present.

Before joining maps, weights should be assigned to each individual component. One could want to assign weights to each different dataset as a whole, but the importance of each piece of information is hard to assess. For example, in the case of exposed granites the information obtained from radiometric data may be more significant, while in the case of hidden intrusions, the magnetic and TM data may be more significant. It rather is recommended to assign weights to the different classes within each component, as in that case the weights reflect the decisions made during the various phases of data interpretation. The quality of the final prediction is thus inherited from the steps that were taken during the interpretation of each data set. As demonstrated for the results of TM-interpretation (Plates 2,3), a measure of the quality is the ratio %contact:%granite + sediment for each contour value. This ratio can be used as a weight factor. The weights that were assigned to each class in this case are the average ratios for each class. The weights obtained in this way for the various components are listed in Table 4. The result (Plate 6a) shows that the pixels with a high contact probability are all predicted in or near to the contact aureole as mapped in the field. Highest probabilities are found in the widest part of the aureole. The map very clearly demonstrates that the strength of this type of data-integration is that misclassifications, derived for some reason from the interpretation of one dataset are evident. They already had low weights and additionally they are not confirmed by other datasets, and thus end up with low probabilities in the final map.

Table 4. Internal weights for each of the four maps that were joined into a probability map (Plate 5).

contact soils (plate 1c)			Distance (plate 3d)		
<u>Class</u>	<u>weights</u>		<u>Class</u>	<u>weights</u>	
(1-3)	a 4.75	b 1	(0-750)	5.4	1
(4-18)	9.46	2	(750-1500)	5.8	2
(19-44)	51.8	3	(1500-2250)	4.1	3

Diversity (plate 2c)			Magnetics (plate 4b)		
<u>Class</u>	<u>weights</u>		<u>Class</u>	<u>weights</u>	
(1-2)	a 0.95	b 1	"green"	2.3	1
(3-7)	1.50	2	"red"	9.2	2
(8-36)	4.75	3			
(37-85)	39.5	4			

a: weights for each class are computed using the average of the ratio described in the text for each class. **b:** weights are determined by the number of classes that were distinguished.

6.7 DISCUSSION

The map presented in Plate 6a is just one example of a combined interpretation of remotely sensed datasets. The result may be improved by involving other datasets, e.g. lineament maps or topographic maps (Goossens, 1991), or by refining the decision criteria. It seems that the result (Plate 6a) is satisfactory for this particular situation and does not require significant improvement. It is however likely that for other areas the decision criteria will be different. The main difficulty with flexible integrated interpretation of datasets is to express the uncertainty whether a piece of information is useful, less useful or not useful; whether a decision is right, "less right" or wrong.

For this area it is known exactly where the granites and where the sediments are located. Therefore we know when misclassification occurs. But in the case of hidden granite bodies, or in relatively unknown areas, the discarding of useful data, during decision-making as to the usefulness of information, must be avoided. For example, in the case of the classified radiometric data this may mean that one does not want to filter out small areas before calculating a corridor, but wants to distinguish between corridors around large surfaces and around smaller surfaces. This means in fact giving the corridor a weight that represents the surface of the area that it surrounds.

The weights assigned to the various classes were based on the degree of matching between the interpretation and the existing ground knowledge. It will often be the case in regional exploration

surveys, that hardly any ground reference is available. The weights thus cannot be derived in the way described above, but could for example depend on the number of classes that are distinguished. This is demonstrated by Plate 6b. The weights simply corresponded with the number of classes in each component (Table 4). The two maps are very similar, implying that, as long as the risk of misinterpretation during the processing of the data is translated into weights, different ways of processing, with different filters or thresholds can be tested and compared easily, even if no or very little ground information is available. When, in the course of a survey, the knowledge about local geological conditions increases, the decision model can interactively be updated and the value of the predictions will increase.

6.8 SUMMARY AND CONCLUSIONS

Some major problems that continue to hamper efficient and successful involvement of remotely sensed datasets in mineral exploration, were identified: 1) The basic relation between geology and the original data is often obscured by complicated data manipulation, which makes understanding of the output a difficult task; 2) The risk of removing possibly important information during the interpretation is normally high and needs to be controlled; 3) The decision criteria as to whether misclassification occurred are often arbitrary and need to be quantified; 4) Error- and quality assessments are often subjective and therefore not reproducible under different circumstances.

Using a well documented study area with granite related mineralization, a methodology has been developed to overcome these complications. This methodology supplies the necessary flexibility for successful application in less well documented areas.

In summary, this study demonstrates that remote sensing and data integration are valuable tools for identification of target areas in mineral exploration, provided that a basic understanding is available concerning the variations in remotely sensed data that can be expected in relation to the geological features one is searching for.

6.9 REFERENCES

- Amor JM, Artiega J, Cienfuegos I, Ortega E, Palero F (1989) Image processing and graphic integration: new tools to save time and costs in mineral exploration. Proc. Mineral exploration programmes, Nov. 13-15, Madrid, Spain.
- Bea F 1982, Sobre el significado de la cordierita en los granitoides del batolito de Ávila (Cistema Central Español). Bol. Geol. Miner XCIII; 59-67.
- Billiton 1983. El proyecto de Scheelita de Los Santos (Salamanca, España) Internal report Billiton International Metals.

- Bonham-Carter GF, Agterberg FP, Wright DF 1990. Weights of evidence modelling; a new approach to mapping mineral potential. In: Agterberg FP, Bonham-Carter GF (eds.). Statistical applications in the Earth Sciences. Geol.Surv.Canada. Paper 89-9; 69-78.
- Buchan KL, Schwartz EJ 1985. Determination of the maximum temperature profile across dike contacts using remanent magnetization and its applications; In: Halls HC, Fahrig FW (eds). Mafic dyke swarms, Geol.Ass.Canada Spec.Paper 34; 221-227.
- Diez Balda MA 1982. El Complejo Esquisto-Grauváquico, las series Paleozoicas y la estructura Hercínica al sur de Salamanca. PhD-thesis Univ. Salamanca.
- Fabbri AG (1984) Image processing of geological data. Computer methods in geosciences. van Nostrand Reinhold Company, New York. 244pp
- Franklin SE, Gillespie RT 1990. Methods and applications of image analysis using integrated data sets. In: Agterberg FP, Bonham-Carter GF (eds.). Statistical applications in the Earth Sciences. Geol.Surv.Canada. Paper 89-9; 69-78.
- Goossens MA 1991. Integration of remote sensing data and ground data as an aid to exploration for granite related mineralization, Salamanca province, W-Spain. Proceedings Eighth Thematic Conference on Geologic Remote Sensing, Denver, USA;393-406.
- Harris J 1990. Clustering of gamma ray spectrometer data using a computer image analyses system. In:Agterberg FP, Bonham-Carter GF (eds.). Statistical applications in the earth sciences. Geol.Surv.Canada. Paper 89-9; 69-78.
- Lorenc M, Saavedra J 1985. Estudio geológico del plutonismo ácido-básico y su entorno metamórfico en el área Guijuelo-Bercimuelle (SE de Salamanca). Bol.Geol.Miner XCVI; 62-73.
- Mather P.M 1987. Computer processing of remotely sensed images, Wiley&Sons, New York; 349 pp.
- Mellinger M In: Agterberg FP, Bonham-Carter GF (eds.). Statistical applications in the Earth Sciences. Geol.Surv.Canada. Paper 89-9; 69-78.
- Pellitero E. Carácteres petrogenéticos y metalogenéticos de los yacimientos de wolframita de la Provincia de Salamanca 1980. PhD-thesis Univ. Salamanca.
- Ugidos JM 1974. Los granitos biotíticos + cordierita de Bejar y areas adyacentes. Bol.Geol.Miner.LXXXV; 214-222.
- Rheault MM, Simard R, Keating P, Pelletier MM 1990. Mineral exploration: digital image processing of LANDSAT, SPOT, magnetic and geochemical data. In: Agterberg FP, Bonham-Carter GF (eds.). Statistical applications in the Earth Sciences. Geol.Surv.Canada. Paper 89-9; 69-78.
- Richards JA 1986. Remote sensing Digital image analysis. Springer, Berlin; 276 pp.
- Rottura A, Bargossi GM, Caironi V, d'Amico C, Maccarone E 1989. Petrology and geochemistry of the late-hercynian granites from the Western Central System of the Iberian Massif. Eur.J.Miner. 1; 667-683.
- Saavedra J, Garcia A 1974. Estudio geoquímico de algunos granitos de la Provincia de Salamanca. Bol.Geol.Miner. LXXXV; 182-192.

- Schwartz EJ, Buchan KL 1989. Identifying types of remanent magnetization in igneous contact zones. *Phys.Earth Planet.Inter.*, 58; 155-162.
- Speer JA 1981. The nature and magnetic expression of isograds in the contact aureole of the Liberty Hill pluton, South Carolina. *Geol.Soc.Amer.Bull.* 92, Part I:603-609.
- Villadeval M, Saavedra J, Pelleiro E 1980. Scheelite en el contacto granítico Monleón-Los Santos (Salamanca). Consideraciones genéticas. *Tecniterrae* 37; 29-33.

CHAPTER 7

A BLIND TEST OF THE DATA INTEGRATION METHODOLOGY

7.1 ABSTRACT

The data integration methodology, developed in the foregoing part of this thesis is tested on a regional scale. The knowledge obtained for the Los Santos study area served as a basis for the interpretation of the data. The complexity of the data handling increased, not only due to the absence of regional ground knowledge, but also because a variety of factors was encountered that complicated the interpretation of the remote sensing data. It is demonstrated that the proposed methodology is sufficiently flexible indeed to overcome these complications. On the produced probability maps, most of the known mineral deposits are located within or near high probability zones. A number of locations can be selected that require additional fieldwork, either because they are promising exploration targets, or because they left us with unanswered questions during the interpretation of the data.

7.2 INTRODUCTION

In the previous chapter (CHAPTER 6) a data integration methodology is developed to map potentially mineralized parts of the contact metamorphic aureole. It was demonstrated how very specific geochemical (CHAPTER 2,3 and 4), pedological and geomorphological (CHAPTER 5) features related to granite intrusion, magma fractionation and mineralization could be recognized and enhanced using airborne radiometric, airborne magnetic and Thematic Mapper data. As the methodology was developed in a small, very extensively documented, test area, it has probably become rather fine-tuned to the specific situation around the Los Santos tungsten deposit.

One of the scopes of this investigation was however to present a technique for the prediction of granite related mineralization that is flexible enough to deal with complications that arise when applied to poorly known areas. Under such circumstances the interpretation of remotely sensed data will certainly be considerably more complex, and therefore the investigation would not be complete without testing the methodology in a much larger area. In this chapter an integrated analysis of airborne radiometric, magnetic and Thematic Mapper data is performed for a large area, using the knowledge obtained in the study area around Los Santos as a basis for the interpretation of the data. The aims of this chapter are: 1) to determine what sort of complications can be expected if the methodology is applied to a much larger area; 2) to test whether known mineralization could have been predicted using this technique and; 3) to investigate whether, with the use of the developed methodology, new locations can be recommended for future exploration.

7.3 PROCEDURE

The procedure of data analysis and integration is essentially the same as described in CHAPTERS 5 and 6, and for explanation of the processing sequence we refer to these chapters.

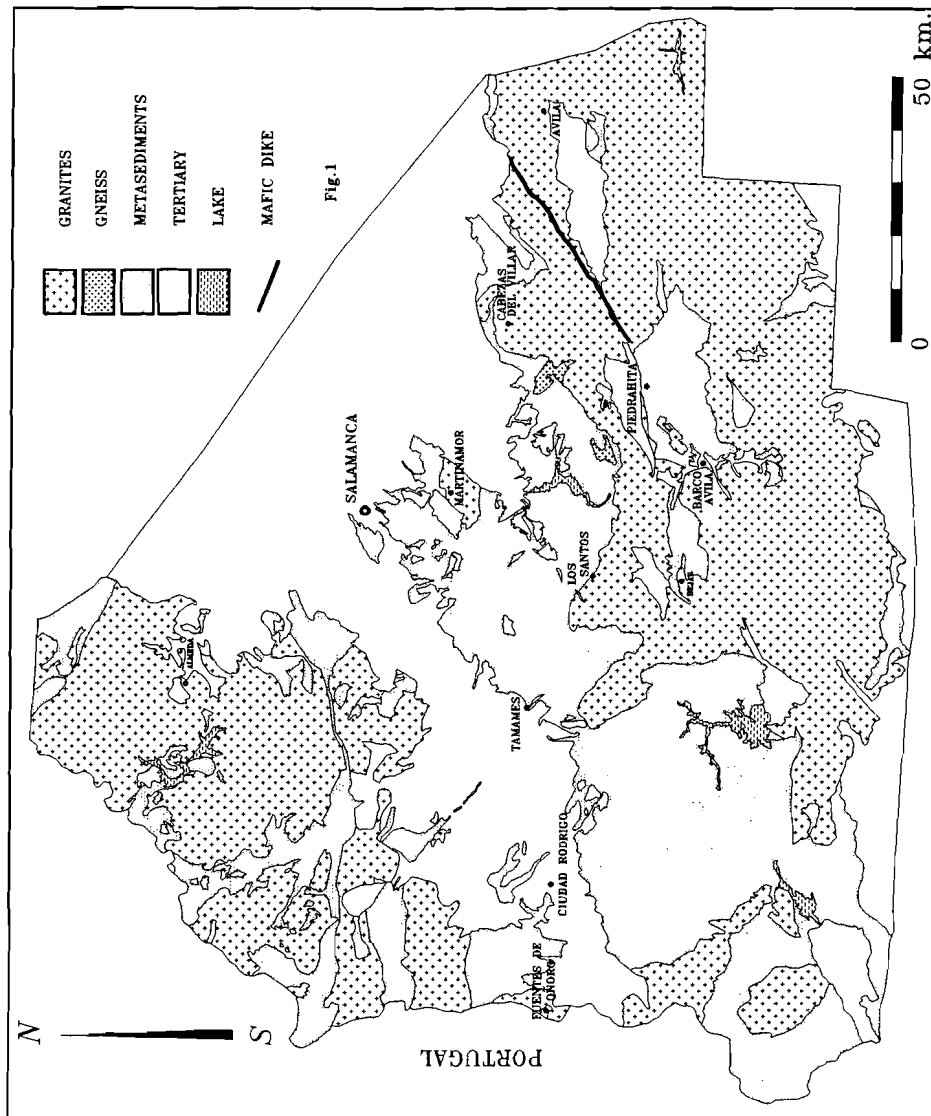


Fig. 1. Simplified regional geological map of the investigated area.

The area investigated in this chapter covers a surface of approximately 13,000 km². A simplified geological map, showing intrusive rocks, metamorphic sediments and Tertiary cover, is presented in Fig.1.

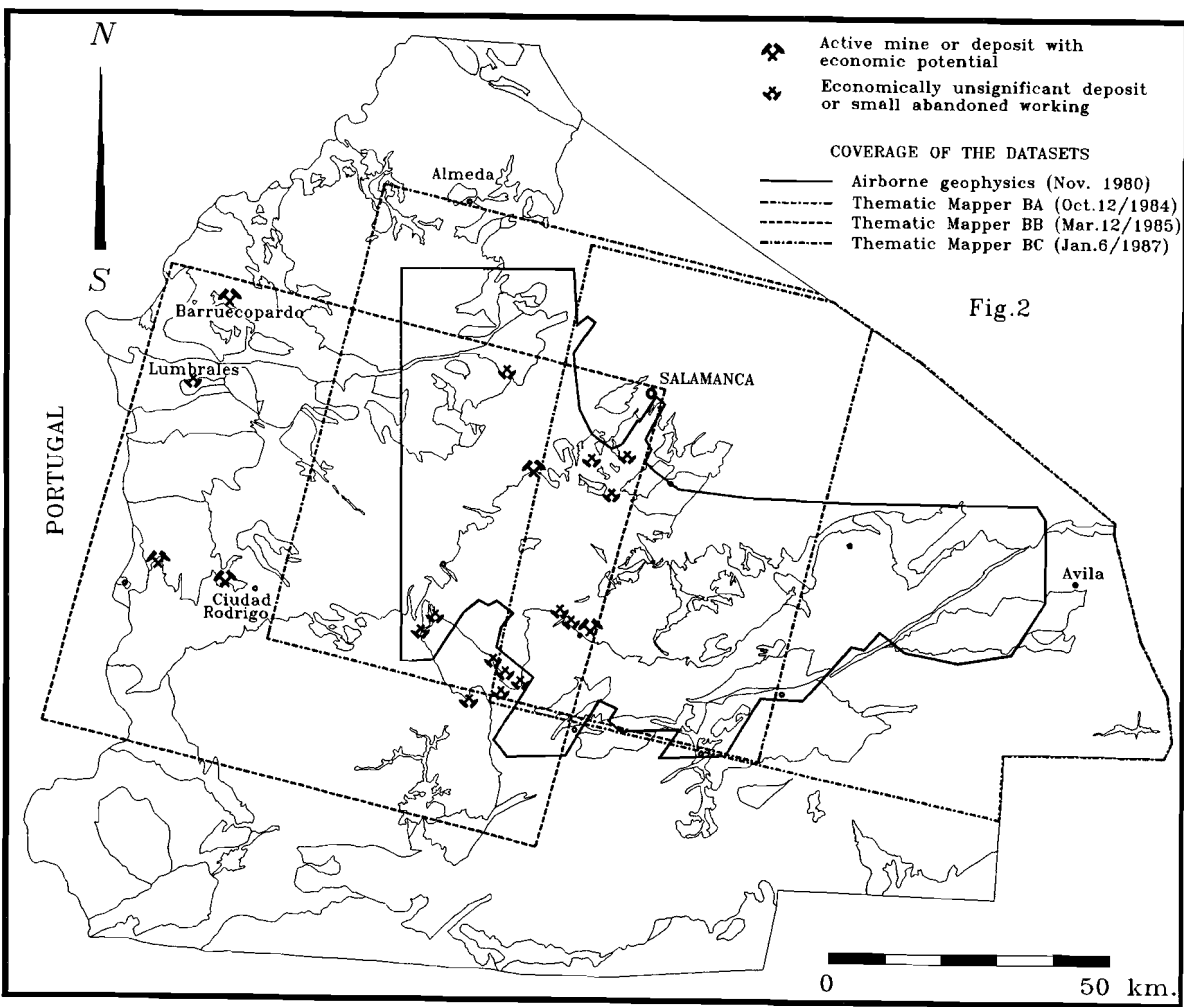


Fig.2. Coverage of the Thematic Mapper scenes and of the airborne geophysical dataset. Locations of the more significant mineral deposits in the region are indicated with crossed hammers.

This map was digitized from a 1:200.000 geological compilation (Carnicero 1983), and used as overlay for the various data sets. Apart from this map we have no knowledge about the area.

Three Thematic Mapper scenes of different seasons, autumn (BA, Fig.2), winter (BC) and spring (BB) were used in order to examine the variation in information content as a result of changing seasonal conditions. No summer image was available, which is unfortunate, as the spectral contrast between the various surface materials is usually the best with high sun elevation angles. Due to hardware limitations, the TM images had to be subsampled to a pixel size of 90m, since otherwise the data sets would be too large to handle.

The airborne geophysical data in this case (K,U,Th and TC) were the original flight line data, in contrast to the study area for which digitized contour maps were used (CHAPTER 6). The original flight data were not available at the time that the pilot study was carried out. The flight line data were gridded to a pixel size of 180m. All data sets were georeferenced to UTM zone 30, ellipsoid Hayford.

The coverage of the three TM scenes and of the airborne data sets is shown in Fig.2, together with the locations of known mineralization, which are compiled from various sources (SGE 1976, JCL 1986, IGME, 1987). For the specific mineral content of each individual deposit we refer to the sources given above. Most deposits contain either tin or tungsten. Some deposits, mostly the uneconomic smaller ones, contain uranium, lead, zinc, copper or gold. The map in Figure 2 is not pretending to be complete, as the number of small showings that have been exploited to a greater or lesser degree in the past, is at least three times higher (Garcia Sanchez, pers.comm). These are not mapped, as they are economically unsignificant, and their relation with granite intrusion is not established.

7.4 THEMATIC MAPPER DATA

The October (BA) and March (BB) scenes are cloud free. The January (BC) scene contained few clouds, but so much the more haze, which lowered the spectral contrast considerably, especially in the visible part of the spectrum. Although the sun elevation angle for the October and March images is similar, better spectral contrast seemed to be present in the October image.

The Thematic Mapper images were used to map kaolinite rich soils and zones with high diversity in land use, as these were found to be typical for the contact metamorphic area near Los Santos.

Mapping of kaolinite soils

Kaolinite rich soils were mapped in the various TM-scenes using the band ratio masking sequence described in CHAPTER 5. Before calculating the band ratios, an atmospheric correction was performed (CHAPTER 5).

The thresholds for the various band ratio images, that were used to isolate the most "kaolinitic" pixels, were established visually by trying to obtain optimum discrimination of the known kaolinitic zone near Los Santos (table 1).

Table 1. Threshold values used for masking Thematic Mapper ratio images.

BA (Oct.12/1984)

$[(TM3/TM4)/(TM5/TM7)]*200$	< 76
$[TM2/TM7]*300$	> 103
$[TM3/TM4]*200$	< 176

BB (Mar.12/1985)

$[(TM3/TM4)/(TM5/TM7)]*200$	< 100
$[TM2/TM7]*300$	> 105
$[TM3/TM4]*200$	< 165

BC (Jan.6/1987)

$[(TM3/TM4)/(TM5/TM7)]*200$	< 72
$[TM2/TM7]*300$	> 124
$[TM3/TM4]*200$	< 170

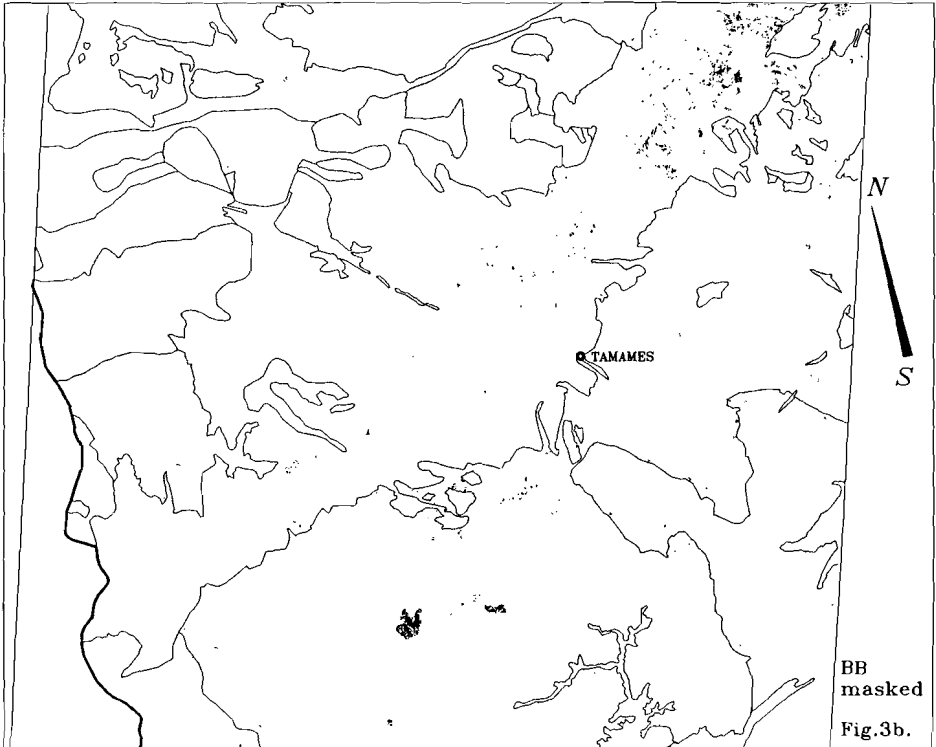
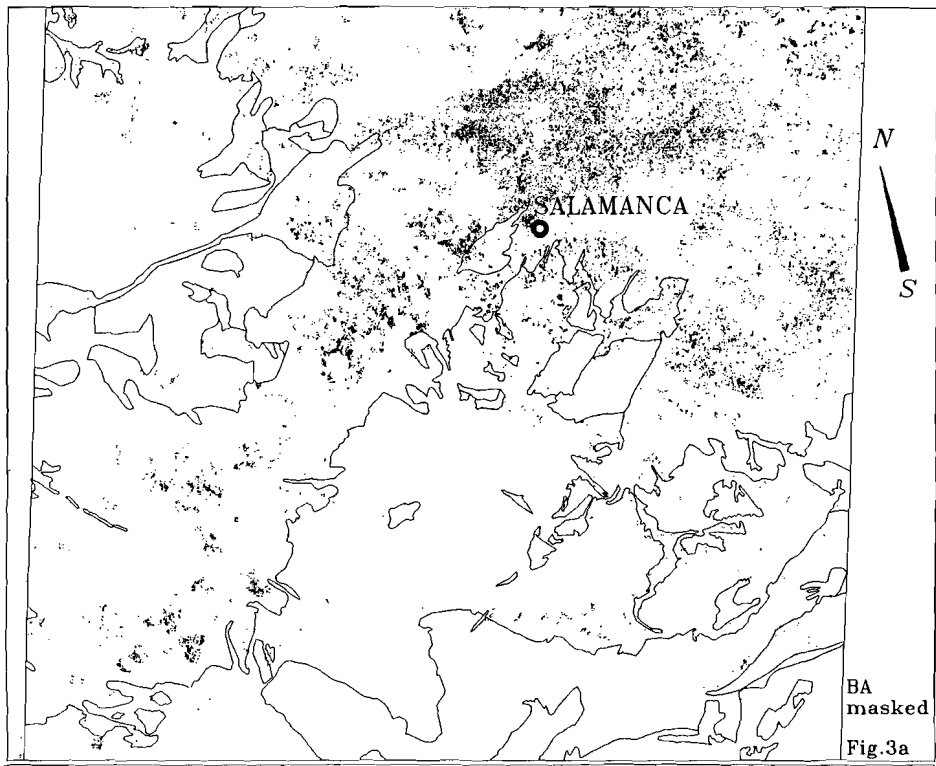
< :pixels with value below threshold were reset to zero

> :pixels with value above threshold were reset to zero

The results of the masking procedure indicate that Tertiary soils are spectrally very similar to the kaolinitic soils, regardless the acquisition date of the TM-scene (Fig. 3a-c). Additionally, in the January scene (BC), many classified pixels are located within the granite terrain. Best discrimination of the kaolinitic zone near Los Santos appears to be obtained from the October image.

As argued in CHAPTER 6, the discrimination of kaolinitic pixels can be improved by subsequently carrying out a supervised classification, using the kaolinite pixels near Los Santos, that result from the masking procedure, as training samples. The supervised classification routine, part of the ILWIS software only allowed a maximum of four input bands. Therefore for each TM scene two classifications are presented, with different band combinations. The first classification for all three scenes was carried out using TM3,TM4,TM5 and TM7, while for the second classification different combinations of bands and band ratios were used (Table 2). The averages and standard deviations of the training set for each input band show that the highest average values for training pixels in the first classification are obtained for the October scene, lowest values for the January scene. In general it can be said that the higher reflection intensities of a particular scene are, the better one can discriminate between subtle spectral differences. Therefore, the best classification results are expected from the October image.

The Mahalanobis Distance (MD), used as threshold for the classification, determines both the quality of the classification and the amount of classified pixels (CHAPTER 6). Increasing the Mahalanobis distance increases the number of classified pixels, but simultaneously decreases the accuracy of the classification, and consequently a useful result has to be a compromise between accuracy and the amount of obtained information. It was necessary to experiment with different MD's in order to come to satisfying results: a reasonable amount of classified pixels, and adequate discrimination of the kaolinite



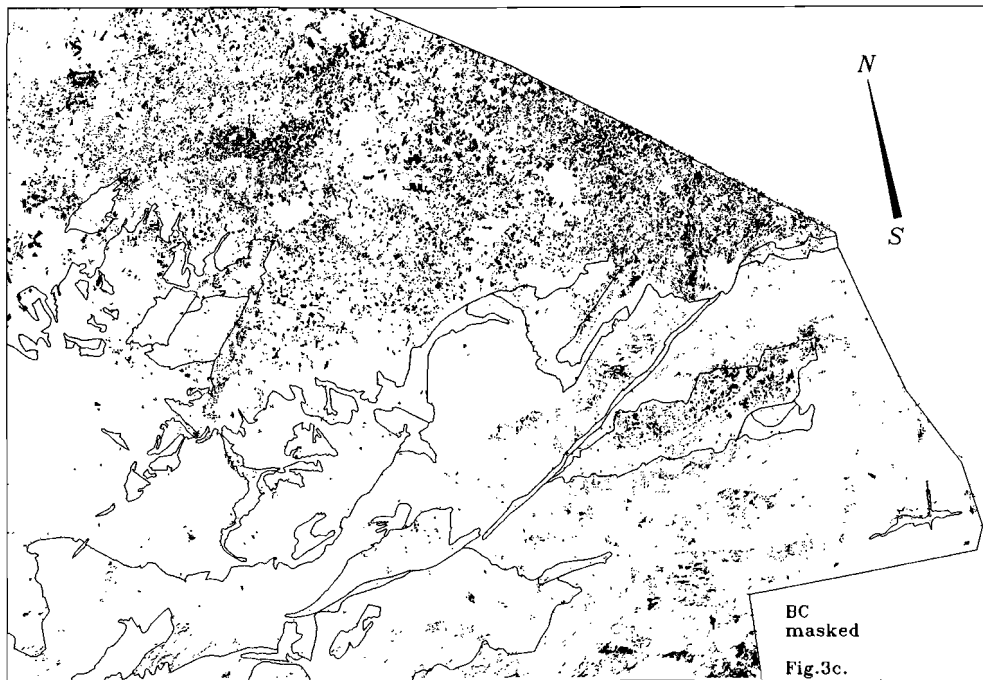


Fig.3. Pixels that are identified as kaolinite soils, using the masking procedure, in the three TM scenes:
a) October(BA); b) March(BB) and; c) January(BC). Geological outlines are shown.

Table 2. Averages and standard deviations for training classes used for maximum likelihood classification of kaolinitic soils.

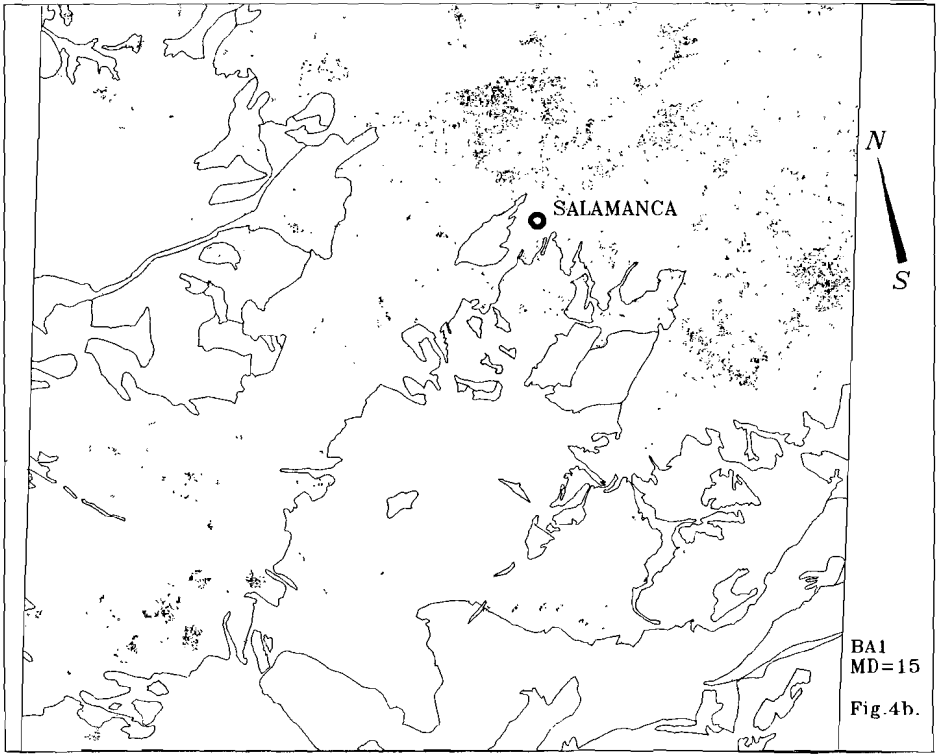
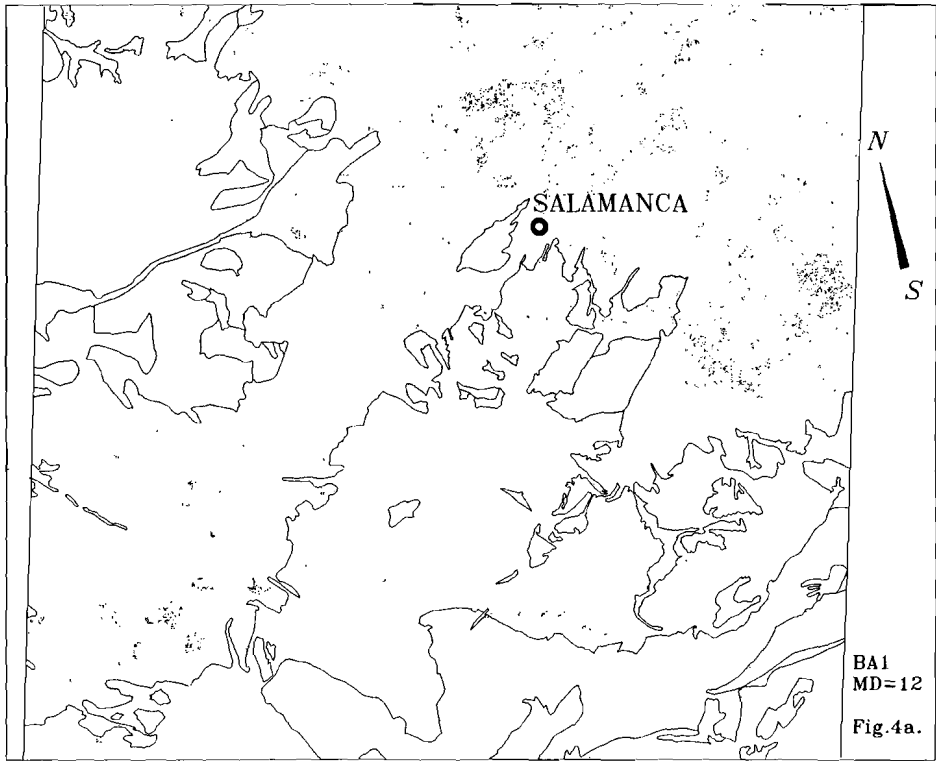
BA1:			BA2:		
Band	Average	Std.	Band	Average	Std
TM3	38.7	3.2	(TM2/TM5)*500	169	6.1
TM4	42.3	3.8	(TM4/TM7)*200	129	6.3
TM5	112.6	9.3	TM3	38.7	3.2
TM7	66.8	5.4	TM4	42.3	3.8

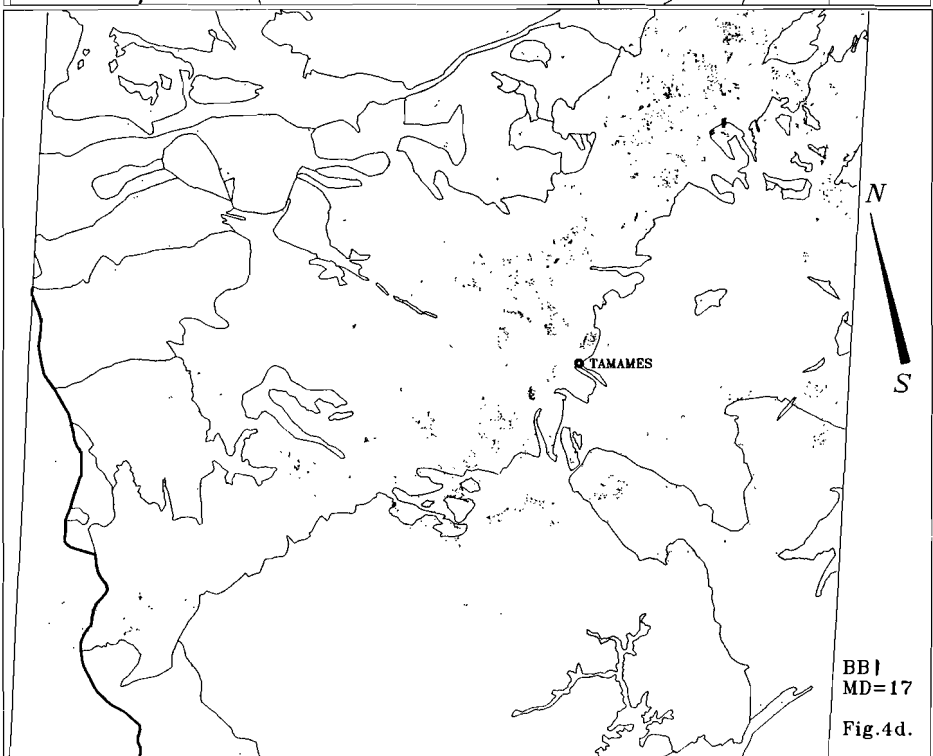
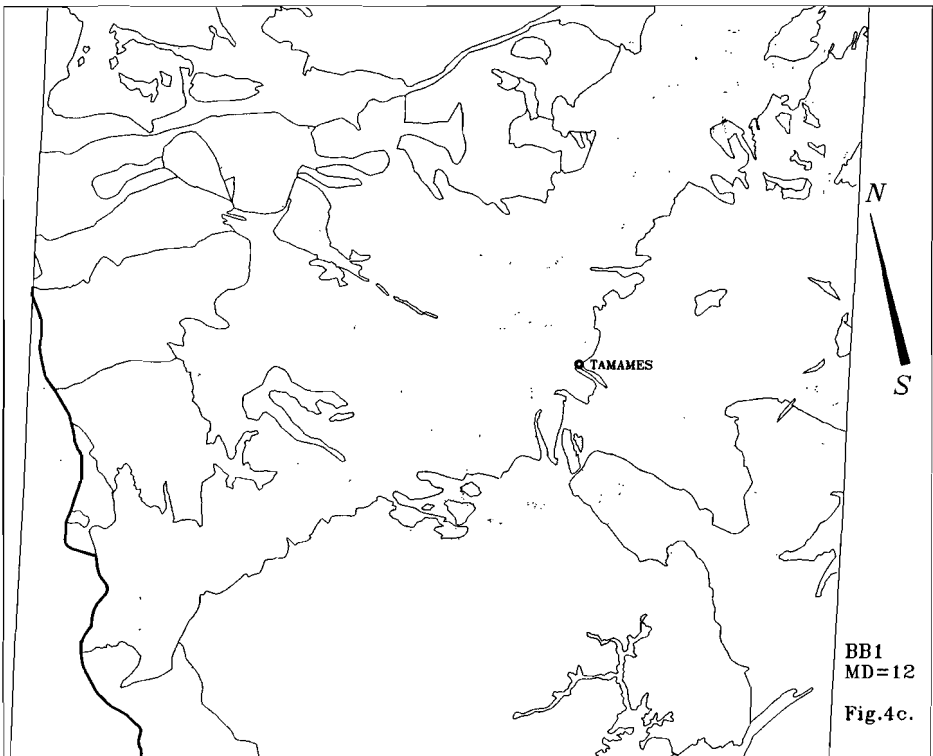
BB1:			BB2:		
Band	Average	Std	Band	Average	Std
TM3	29.1	3.8	(TM3/TM4)*200	162.9	6.9
TM4	36.3	4.1	(TM5/TM7)*100	116.2	11.7
TM5	98.6	10.7	(TM3/TM7)*200	93.6	17.3
TM7	56.3	7.6	(TM4/TM5)*200	68.94	9.7

BC1:			BC2:		
Band	Average	Std	Band	Average	Std
TM3	27	1.8	(TM2/TM7)*150	116	5.7
TM4	29.6	2.7	(TM3/TM4)*200	184	10.6
TM5	57.2	3.6	(TM4/TM5)*150	77	4.1
TM7	29.0	2.5	(TM4/TM7)*60	61.9	5.0

BA1 and BA2: October image; BB1 and BB2: March image; BC1 and BC2: January image.

pixels near Los Santos (Figs. 4a-f). The quality of the classifications is hard to assess, as we have no knowledge about the regional soil mineralogy, except for the Los Santos study area, and therefore it can only be estimated by comparing the results with those for the study area (Chapter 5).





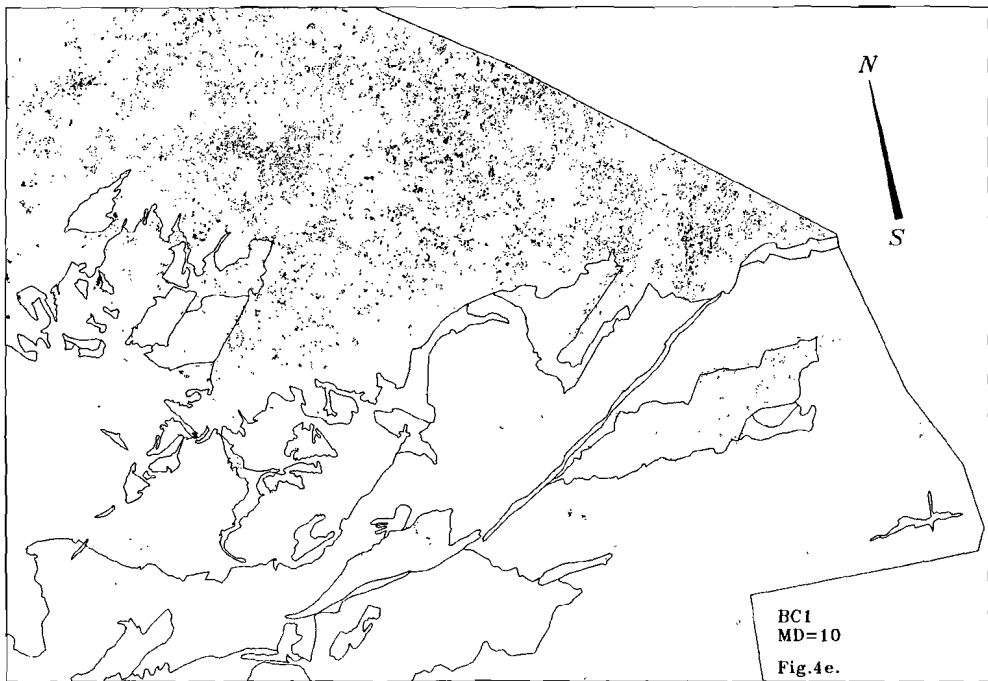


Fig.4a-f. Results of first supervised classification (with TM3, TM4, TM5 and TM7) of kaolinitic soils (black pixels), using different Mahalanobis distances (MD), fo the three TM scenes: a,b) October; c,d) March; e,f) January.

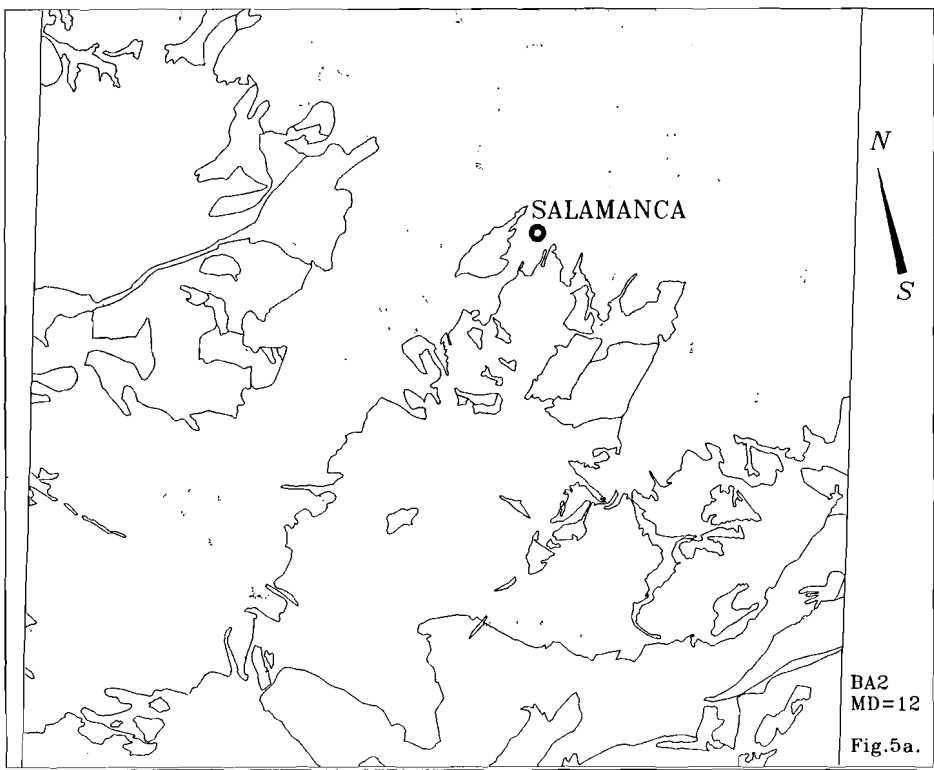


Fig. 5a.

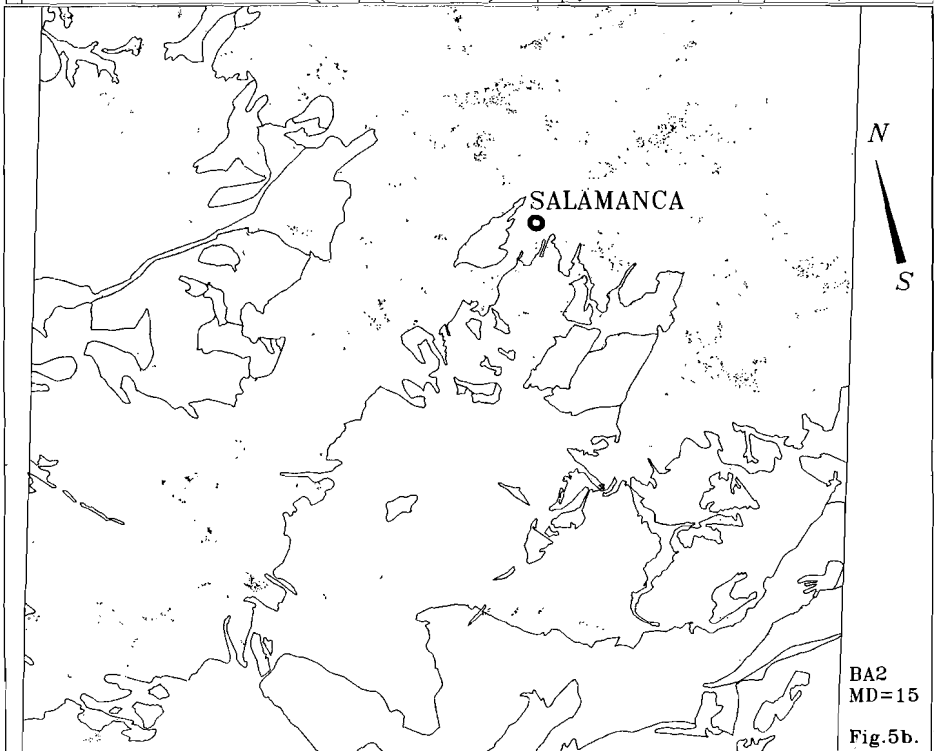


Fig. 5b. 137

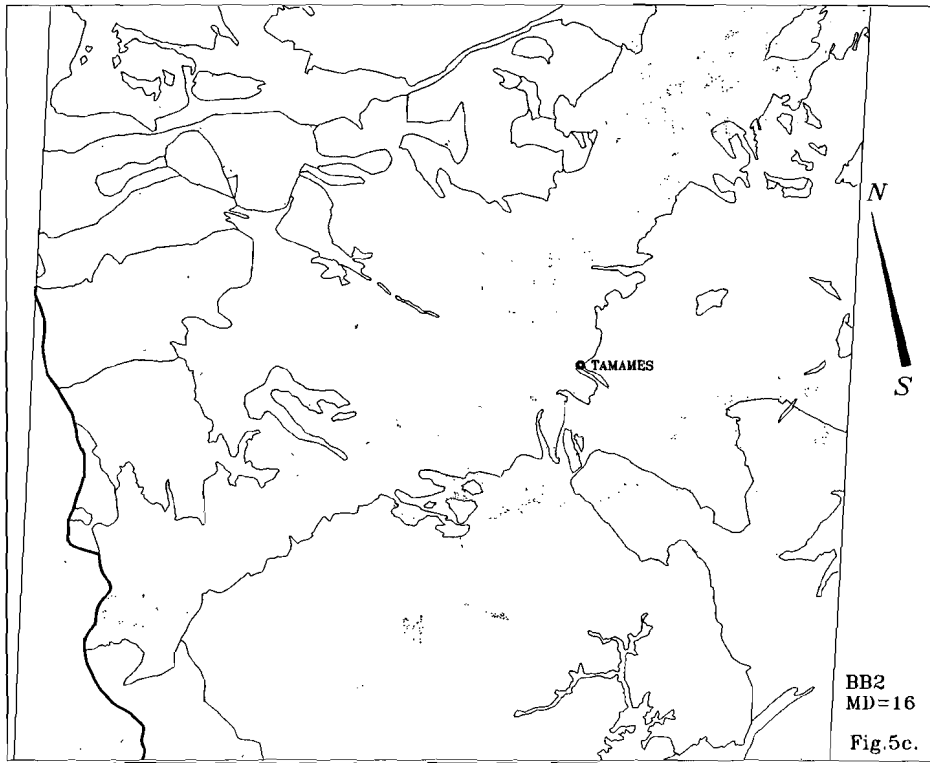


Fig.5c.

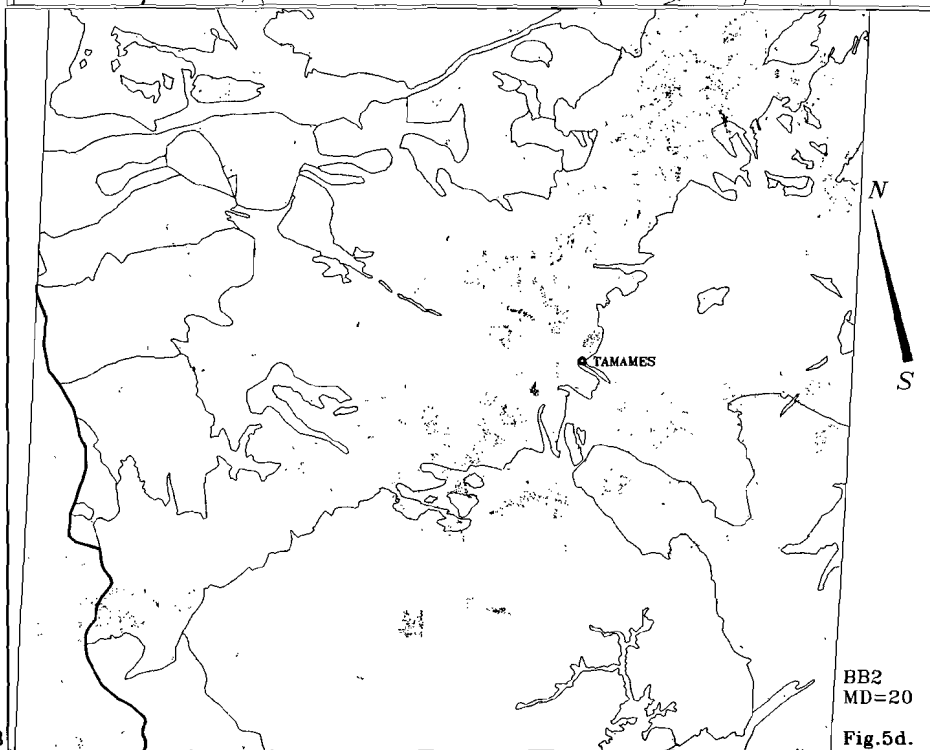


Fig.5d.

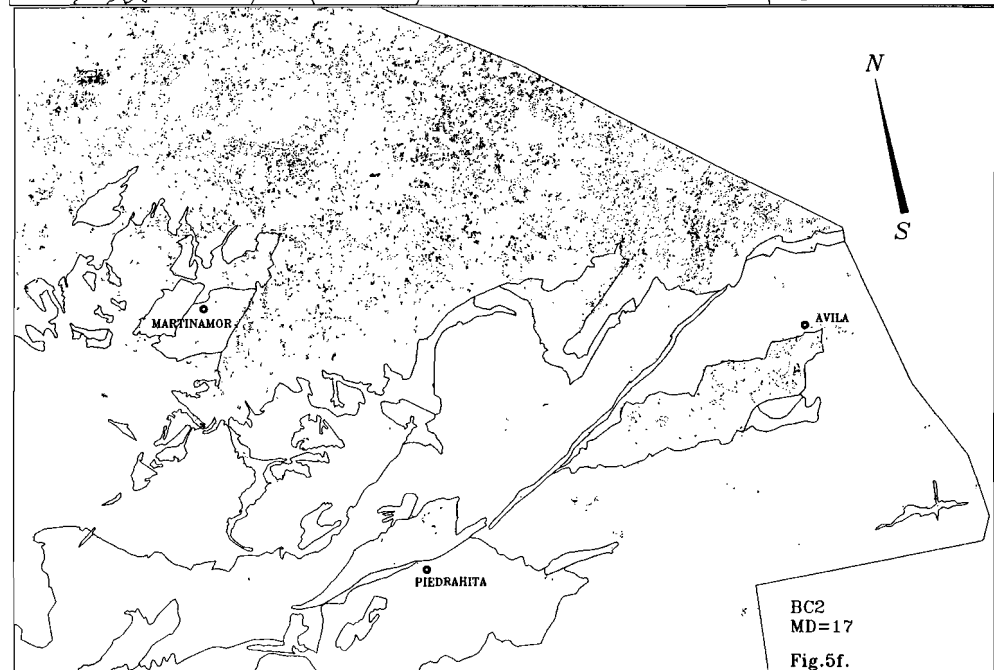
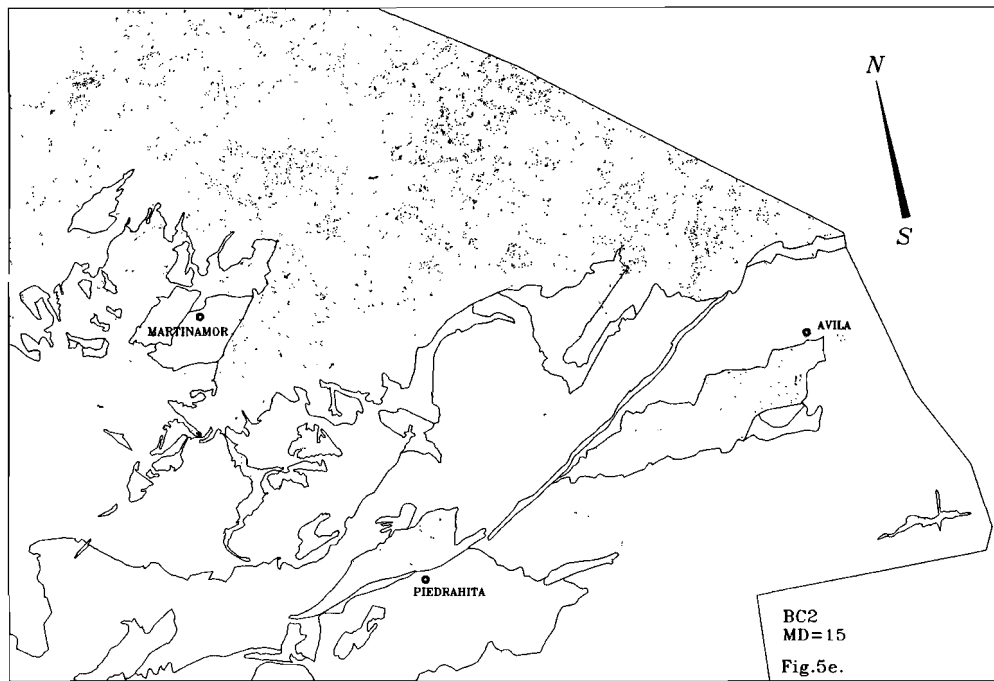


Fig.5a-f. Results of second supervised classification of kaolinitic soils (black pixels), using different Mahalanobis distances (MD), fo the three TM scenes: a,b) October; c,d) March; e,f) January.

Compared to the results of the masking procedure (Fig.3), the results are considerably improved by the addition of the classification step, as most of the "contact"pixels near Los Santos are preserved, while the amount of classified pixels in both the Tertiary terrain and granite terrain is strongly reduced. This is particularly well illustrated for the January image (BC). It is interesting to note in the March scene (BB), that a cluster of black pixels located within the metasedimentary terrain in the masked image (Fig.3b), has entirely disappeared.

Classification with combinations of band ratios, or combinations of band ratios and original TM bands does not yield significantly different classification results (Figs.5a-f).

For each scene one classified image was selected for further processing: BA2 (MD = 15); BB1 (MD = 17) and BC1 (MD = 12). Isolated single pixels were removed from the classified image by passing a 5*5 rank order over the image, using a threshold of 24 (Figs.6a-c). These were subsequently contoured using a 15*15 kernel, and divided into 4 frequency classes (Plates 7a-c).

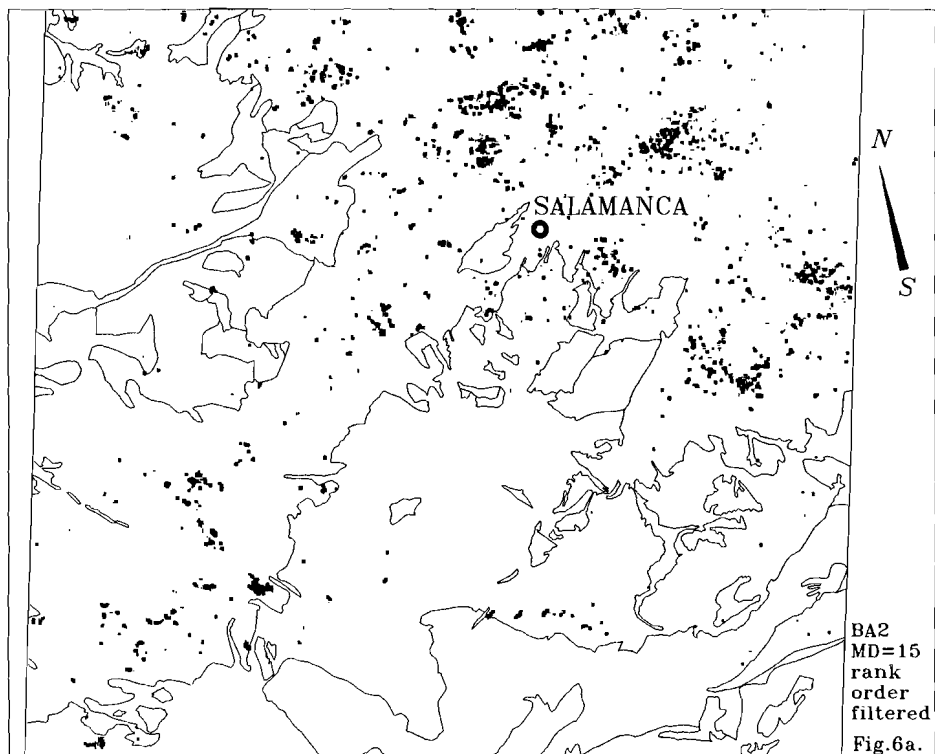
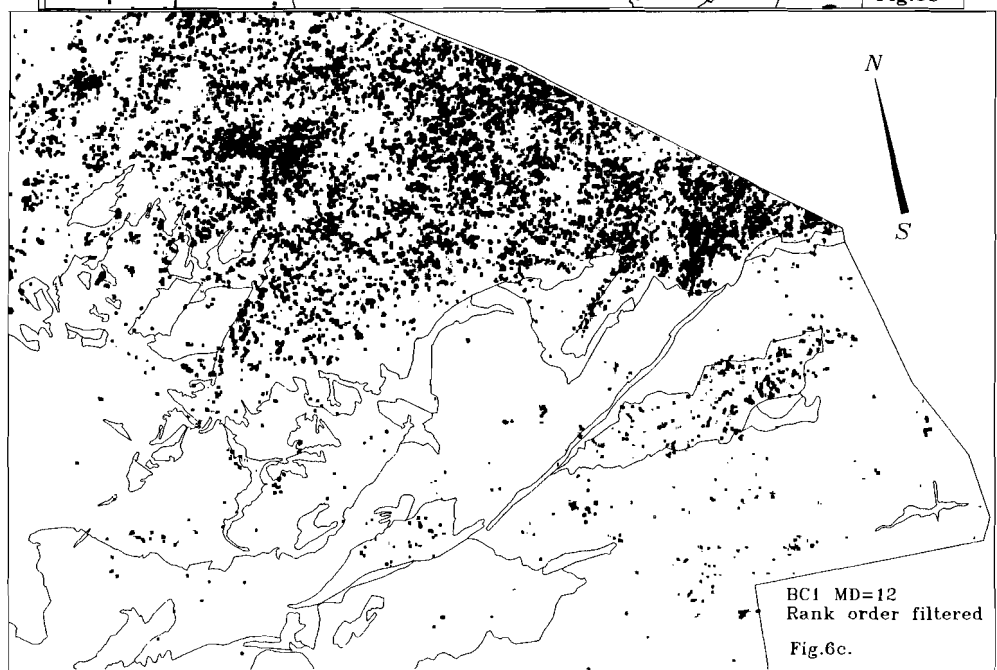
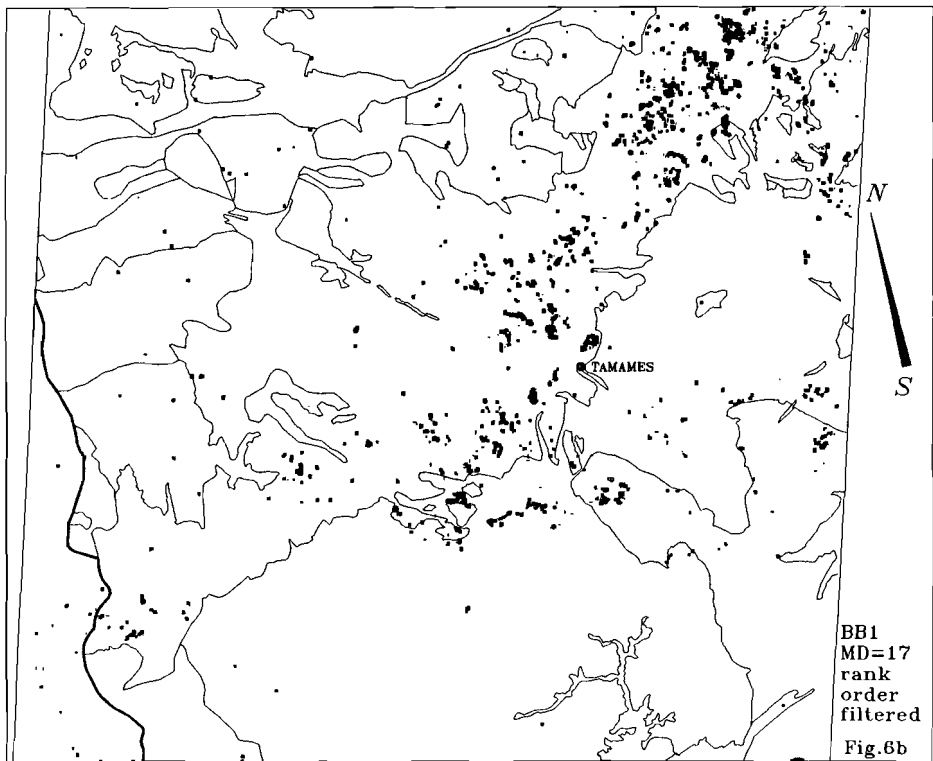


Fig.6a-c. Result of rank order filtering of classified TM images: a) October scene, classification 2, MD=15; b) March scene, classification 1, MD=17; c) January scene, classification 1, MD=12.



In contrast to what was found for the study area in CHAPTER 5, the highest frequency class appears to be most characteristic for the Tertiary soils in all images, while the kaolinitic soils near los Santos yield slightly lower frequencies. This might be a useful feature to distinguish between Tertiary soil and contact metamorphic soil, as is particularly well illustrated by the January scene (Plate 7c). The contour maps shown in Plate 7 enable another, possibly important observation, which was not made in the previous chapters: The kaolinite soils, typical for the mineralized contact zone near Los Santos do not occur along the full extent of all granite contacts, suggesting that extensive development of kaolinitic soils during the weathering of contact metamorphic rocks not only depends on the degree of contact metamorphism, but also on the degree of hydrothermal interaction on these rocks. This requires additional study.

Land use Mapping

The contact metamorphic zone near los Santos is distinguished from the regional metasediments by a higher diversity in land use (CHAPTER 5). In order to map the variation in land use, a 15*15 diversity filter was passed over the TM3/TM4 ratio images of October, January and March. The resulting images were divided into 5 frequency intervals (Plate 8a-c). These plates very clearly reveal that the diversity in land use strongly changes during the various seasons. Furthermore, it is obvious that high diversity is not a feature unique for the contact metamorphic aureole, but is also associated with a number of other features:

October: The Los Santos contact is characterized by diversities > 101, while a major part of the Tertiary, the metasediments and the granites are characterized by diversities < 101. The east-west high diversity zone in the Tertiary near Salamanca, which further eastward bends to the south, exactly follows the course of river Tormes. It is no surprise that high diversity in land use is found near the river, as water for irrigation and sprinkling is plentyful available; An east-west high diversity zone about 10 Km north of Los Santos corresponds with a quartzitic formation; A high diversity zone west of Los Santos corresponds with a mountainous area with steep quartzite ridges.

March: The diversity image is quite similar to that of October, except for the fact that diversities > 101 are more abundant in the Tertiary terrain, while in the metasediments and granites the diversity is generally lower compared to October.

January: The Tertiary terrain is characterized by higher diversities than the other mapping units. The contact zone near Los Santos is hardly noticeable. This image could be particularly useful for mapping the Tertiary terrain.

In summary it can be said that discrimination of contact metamorphic rocks on the basis of the land use is most adequate using the October scene. The diversity in land use could provide a good mapping tool if the variation of land use, due to seasonal differences, is better studied.

7.5 AIRBORNE GEOPHYSICAL DATA

The airborne geophysical data (magnetics, radiometric potassium, thorium, uranium and Total Count) are used to map granitic and metasedimentary rocks, to identify the granite contact, and to identify metasedimentary rocks that are possibly contact metamorphic.

Radiometric data

The granitic rocks generally have higher contents in radioelements than the sedimentary terrain, of which the clearest example is provided by potassium (Plate 9). In CHAPTER 6 it was demonstrated that the most effective way to map the intrusive rocks is to perform a supervised classification, using the combined radiometric data set.

A first supervised classification was carried out using three granite training classes, as the granite intrusion is strongly zoned (CHAPTER 2,3,4,6), and one metasediment class. All training samples were selected in the original study area near Los Santos. The statistics of the training classes are listed in Table 3. The red pixels in the classified image (Plate 10) correspond with granodiorite, yellow with slightly more felsic granodiorites, while blue corresponds with monzogranites. Green corresponds with metasedimentary terrain. The positions of the training samples are indicated in black. The location of classified granite and metasediment corresponds rather well with the geological map, except for granite class 3 (monzogranite). Parts of the Tertiary and small parts of the metasedimentary terrain are also classified as monzogranite.

Table 3. Statistics of training classes used for supervised classification of the radiometric data sets.

Class	U (ppm)		Th (ppm)		K (%)		Tc	
	X	STD	X	STD	X	STD	X	STD
Granite1	4.81	0.71	16.0	0.73	2.42	0.14	3.14	0.18
Granite2	4.05	0.67	13.2	0.69	2.13	0.12	2.67	0.12
Granite3	3.65	0.95	10.4	0.99	2.15	0.15	2.32	0.17
Metasediment	3.99	0.89	9.94	0.87	1.71	0.19	2.03	0.23
Tertiary1	3.01	0.82	7.29	0.79	2.19	0.14	2.01	0.13
Tertiary2	2.67	0.59	8.06	0.86	1.06	0.15	1.26	0.14

A second classification was carried out, adding two training classes in the Tertiary terrain to the sample set. The first class is sampled in the Tertiary that was classified as granite, while the second was selected in the Tertiary zone southwest of Salamanca. The latter class was added because it would be very useful if the Tertiary could be mapped. This would help to decide which soils, classified in the TM image as kaolinite, in fact are Tertiary soils.

The results of the second classification form an improvement compared to the first classification in the sense that Tertiary soils can be distinguished (Plate 11a). However this time some of the granites in the

north-west corner are also classified as Tertiary. These are apparently granites that have a lower Th and U-content than the other granites (Table 3).

The binary diagram of the potassium content of the training samples against their thorium content (Plate 11a), clearly demonstrates that the two Tertiary classes are radiometrically totally different. Perhaps this has to do with different origins of the soil material. It might be that the first class is derived from granites, while the second is derived from metasediments. Alternatively it might be that the first class overlies granitic rocks, as also the granites near Martinamor partly have a similar radiometric signature. Additional fieldwork would be required to explain this difference.

Some experimenting with additional training classes indicates that the classification could be further refined. However, it is not our aim to reproduce the geological map, but rather to map granites and sediments as good as possible on the basis of the knowledge obtained in the study area around Los Santos. Therefore it is decided to continue the data processing with the image obtained by the second classification.

Small areas, which are probably misclassified, are removed with a median filter, prior to calculation the granite contact (see CHAPTER 6). The size of the median filter used is 15*15 pixels, implying that areas with a size below 113 pixels are replaced by the class of the surrounding pixels.

The filtered image (Plate 11b) is used to construct the position of the granite contacts.

In order to define sedimentary rocks that are possibly contact metamorphic, the distance within the sedimentary rocks to the classified granite contact is calculated (Plate 11c). As it is very unlikely that contact metamorphic rocks occur at a distance greater than 3000m from the intrusive contact, all pixels at greater distance have been reset to zero.

With this image, there is something very remarkable: if we look at the granite contact between Los Santos and Cabezas de Villar (see Fig.1) the shape of the classified contact is identical to that on the geological map, but it is shifted approximately 2km to the north. The same seems to be the case with the boundary of the Tertiary (Class 2, Plate 11b) in the north-west corner of the image, and perhaps also with the Tertiary just north of Los Santos. This suggests either that the coordinates of the airborne data set are incorrect, or that the coordinates of the digitized geological map are wrong. The latter possibility is unlikely, since, when the geological map is overlain on a TM image, the boundaries of the lakes match correctly. Unfortunately there is no way to check the quality of the coordinate system of the airborne data set.

Magnetic data

The gridded residual airborne magnetic data are presented in Plate 12a. This image very clearly illustrates the disturbing effect of the levelling errors, due to the absence of cross flight lines.

In order to reduce the effects of levelling errors, the flight line data were corrected using a cosine filter, which removes frequencies related to the flight line spacing. The filtering was done using GEOSOFT software. The filtered flight line data are regridded (Plate 12b), demonstrating that the effects of levelling

errors seem to have been removed. It is important however to realize that the filtering may have introduced new errors.

The shift of the airborne data to the north, suggested on the basis of the radiometric data, seems to be confirmed by the magnetic data, if we look at the magnetic response of the large mafic dike, near Avila. This dike, which consists of gabbro, is presumably vertical, as it shows a straight intersection with the topography along its full extent (approx. 500km, Garcia de Figuerola and Carnicer 1973). The positive magnetic anomaly related to such a dike, should on the northern hemisphere, occur south of the dike (Bredewout pers.comm.), while in this image it is located north of the dike.

As discussed in the previous chapter, contact metamorphic rocks near Los Santos are recognized by two different magnetic features: 1) they have a low magnetic relief and; 2) they have the same magnetic field as the adjoining granites.

As we want to determine which sedimentary rocks have a low magnetic relief, the magnetic relief image was calculated for those rocks that were classified as metasedimentary or Tertiary on the basis of the radiometric data, using a 13*13 diversity filter. With this filter, a high magnetic relief will be translated into high diversity values, while a low magnetic relief will result in low diversities (Plate 12c).

Based on the situation around Los Santos it is decided that pixels with a diversity value below 35 may represent contact metamorphic rocks (Plate 12d, green). The pixels that additionally have a residual magnetic field between -225 and -235 nanotesla are indicated in red.

7.6 DATA INTEGRATION

So far a number of maps are generated that contain information whether granite related mineralization may be present or not. This study however demonstrates very clearly that the situation is much more complicated than was the case for the study area near Los Santos, as in none of the maps the classified pixels are unique features for the contact aureole. For example high diversity in land use is not only mapped in the contact aureole, but also in the Tertiary terrain. The same is the case for kaolinite pixels. Therefore the integration step is even more important than was the case for the study area. True contact pixels will be enhanced, since they should appear in more than one map, while pixels that for some other reason are classified as contact metamorphic in one map only will not be enhanced. In this way we can distinguish between pixels that are probably correctly classified and those that are likely to be misclassified.

In CHAPTER 6 the importance of assigning weights to the different classes within each single map was discussed, and two different methods were suggested for determining these weights for any particular map.

Table 4. Weights assigned to the various classes within each map.

BA(Kaolinite)	a*	b*	c*	BA(Diversity)	a*	b*	c*
1-10	5.7	1	1	1-63	0.33	1	0
11-30	12.6	2	2	64-79	0.41	2	0
31-89	32.85	3	6	80-89	0.69	3	0
>89	0	4	1	90-101	1.03	4	1
				>101	4.72	5	4
BB(Kaolinite)	a*	b*	c*	BB(Diversity)	a*	b*	c*
1-10	1.75	1	1	1-63	0.47	1	0
11-39	2.53	2	2	64-79	0.47	2	0
40-83	2.19	3	3	80-89	1.6	3	1
>83	0	4	1	90-101	3.39	4	2
				>101	4.72	5	3
BC(Kaolinite)	a*	b*	c*	BC(Diversity)	a*	b*	c*
1-20	2.11	1	1	1-63	0.31	1	0
21-42	2.25	2	2	64-79	1.35	2	0
43-105	6.89	3	3	80-89	1.53	3	2
>105	0	4	1	90-101	0.8	4	1
				>101	0	5	0
Magnetic map	a*	b*	c*	Distance map	a*	b*	c*
"Green"	0.93	1	1	2251-3000m.	0.05	1	1
"Red"	1.6	2	2	1501-2250m.	0.69	2	2
				751-1500m.	2.4	3	3
				1-750m.	4.3	4	4

* a: ratio method; b: number of classes; c: final weight.

The first method was to calculate, in the study area near Los Santos, the ratio between the surface percentage of the contact aureole that is covered by a certain class, and the surface percentage of the remaining area that is covered by the same class (Table 4, column a).

The second method was much simpler, as the weight is determined by the number of classes in a certain map (Table 4, column b). The actual weights assigned to the various classes (Table 4 column c) are, although mainly based on a combination of the two methods, also influenced by number of additional factors:

- 1) The highest class in the kaolinite map would get a weight of 0 according to the first method, as it does not occur in the contact aureole of the study area. It could however be that in other contact zones these high frequencies do occur, and therefore it was given a weight 1.
- 2) If the weights assigned to kaolinite map BA would be conform the ratio method, they would probably dominate too much in the integrated image, as they are very high compared to weights used in the other maps. Therefore these values have been divided by 5.
- 3) The lowest classes in the diversity maps are assigned the weight 0, as they are not typical for contact metamorphic rocks.
- 4) The distance map was divided in four classes, each with a width of 750m (see CHAPTER 6). The weights of the classes between 1500 and 3000m. would have been 0 according to the ratio method. However, this would mean that pixels at a greater distance than 1500m would be lost, which would be a waste of potentially useful information.

The maps resulting from the data integration are shown in Plates 13a-f.

BA: (Plate 13a,b) The mineralized area near Los Santos is well identified by high probabilities (7-16). Other areas showing probabilities of 7 or higher, that correspond with known mineralization are: south of Salamanca, near the village of Martinamor; West of Salamanca and; south of Tamames. The other zones with high probabilities do not correspond with known mineralization. It is curious that the Tertiary east of Martinamor has such a high probability. It is recommended that these high probability areas are checked out in the field.

As it is most likely that mineralization occurs within sedimentary rocks, we have produced a second map that only gives the probabilities within the metasedimentary rocks (Plate 13b), which facilitates the interpretation.

BB: (Plate 13c,d) This image indicates essentially the same areas as the previous, but there are higher probabilities in the Tertiary. The mineralized zone near Martinamor is clearer in this image. The probability map for the metasedimentary rocks is given in Plate 13d.

BC: (Plate 13d,e) The difference between this map and the previous ones is small: Los Santos is slightly less pronounced, while a number of interesting locations appear along the eastward extension of the contact near Los Santos. The Martinamor zone comes out slightly better compared to BA, but less clear compared to BB.

7.7 DISCUSSION AND CONCLUSIONS

In this chapter the data integration methodology developed in the foregoing part of this thesis was tested on a very large area, using the knowledge obtained in the Los Santos study area as a basis for the interpretation of the data. The only extra ground reference available was a 1:200.000 scale geological map. As was expected, the interpretation of the data was more complex, not only because our ground knowledge was so limited, but also because in the large area a number of additional factors were encountered, that complicate the interpretation of the data:

- 1) The spectral signature of Tertiary soil is very similar to that of the soils overlying contact metamorphic rocks;
- 2) Due to seasonal variations, the successful discrimination of kaolinitic soils is dependent on the acquisition date of the TM scene;
- 3) The degree of development of kaolinitic soil may not only be related to the degree of contact metamorphism, but also to the degree of hydrothermal interaction;
- 4) High land use diversity is not unique for the contact metamorphic zone;
- 5) Due to seasonal variations the results of Land use diversity mapping depend strongly on the acquisition dat of the TM scene;
- 6) The coordinate system of the airborne data is probably incorrect, causing a shift of the data of at least 2km northwards;
- 7) Radiometric discrimination of granites is complicated due to the similarity between some granite types and parts of the Tertiary terrain;
- 8) The quality of the magnetic data set is strongly reduced due to serious levelling problems. These errors can be partly removed, but this may simultaneously introduce new errors.

In conclusion, a number of remarks can be made:

- I: Based on the knowledge obtained in the pilot study area near Los Santos, the remote sensing data for a much larger area were analyzed and integrated into maps that predict the presence of granite related mineralization in this region.
- II: The fact that most of the known mineralization does occur in high probability zones, indicates a good quality of these maps.
- III: Therefore the methodology is sufficiently flexible indeed to deal adequately with the additional uncertainties and complications that are encountered when the scale is enlarged from a pilot investigation to a regional survey.
- IV: Based on these results a number of areas can be selected that require additional fieldwork, either because they are promising exploration targets, or because they left us with questions during the interpretation of the data. One of these areas would certainly be the Tertiary zone east of Salamanca. Another area worth a visit, would for example be the cluster of kaolinitic pixels, located within the sedimentary rocks (Figure 3b), that disappeared during the subsequent classification step.

7.8 REFERENCES

- Carnicer A (1983). *Syntesis Geológica del Basamento (zona del centro-oeste Español)*. Departamento de Petrología Universidad de Salamanca.
- García de Figuerola LC, Carnicer A (1973). El extremo noreste del Gran Dique del Alentejo-Plasencia. *Stud.Geol.* VI; 65-71.
- IGME (1987). *Mapa Minero de Espana*. Published by: Instituto Geológico Y Minero de Espana, Madrid.
- JCL (1986). *Estudio geológico-minero en el área de la Peña de Francia-Miranda del Castañar (Salamanca)*; Junta de Castilla y León, unpubl.rep.
- SGE (1976). *Mapa Militar de Espana 1:200.000, 3-5, 3-6, 4-5, 4-6*. Published by: Servicio Geográfico del Ejército



Plate 1. RGB colour composite image of TM1, TM3, TM4 (12 October 1987). The granite contact and the approximate boundary of the contact aureole are indicated in red. Hammers indicate the position of the Los Santos tungsten mine.

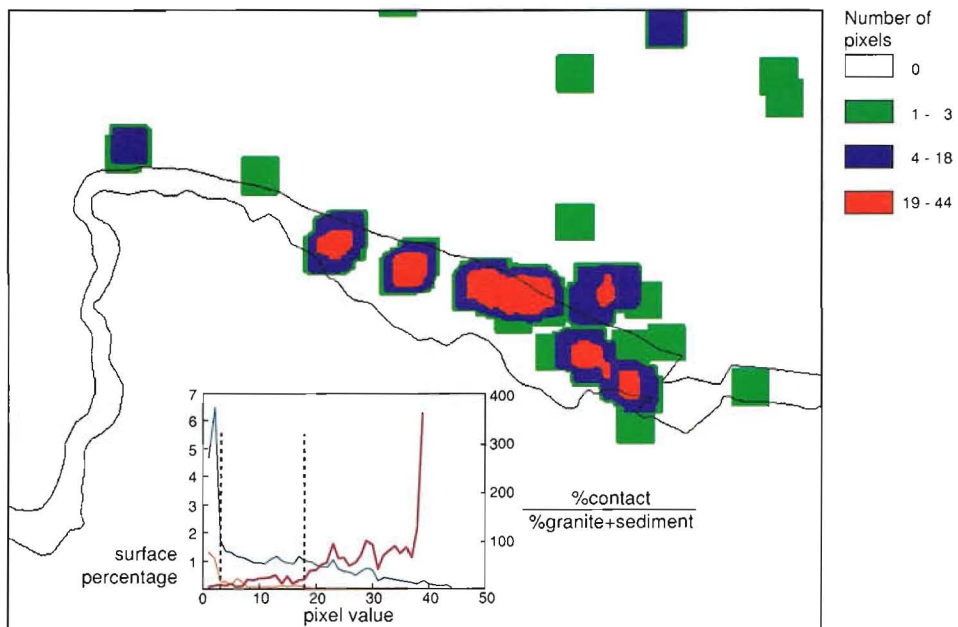


Plate 2. Results of contouring the "kaolinite" pixels in the image presented in Fig. 4b (Chapter 6). The contoured image is sliced into three frequency classes.

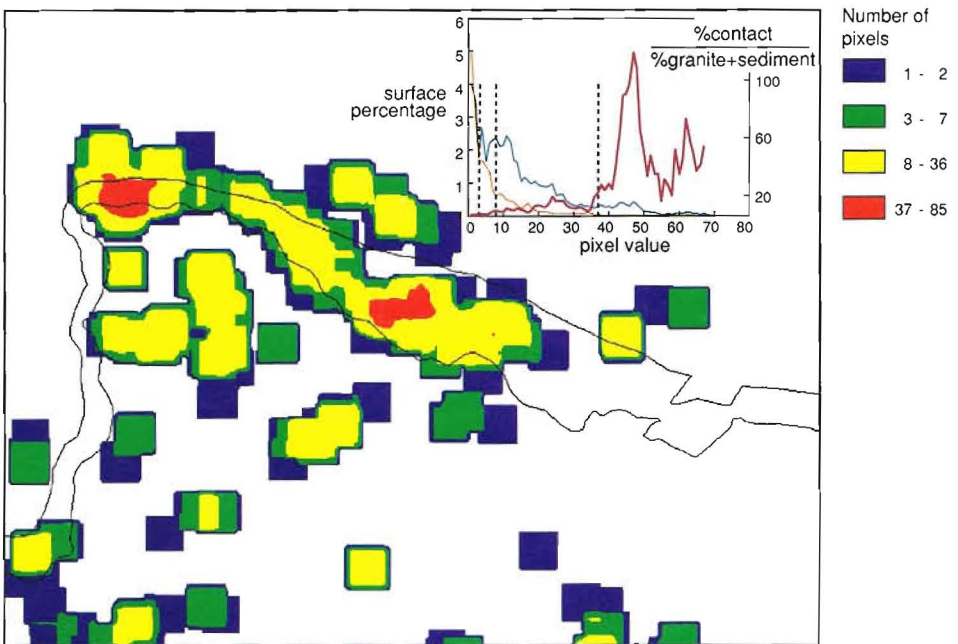


Plate 3. Result of contouring the "high diversity" pixels in the image presented in Fig.5b (Chapter 6) with a 50*50 kernel. The contoured image is sliced into four classes.

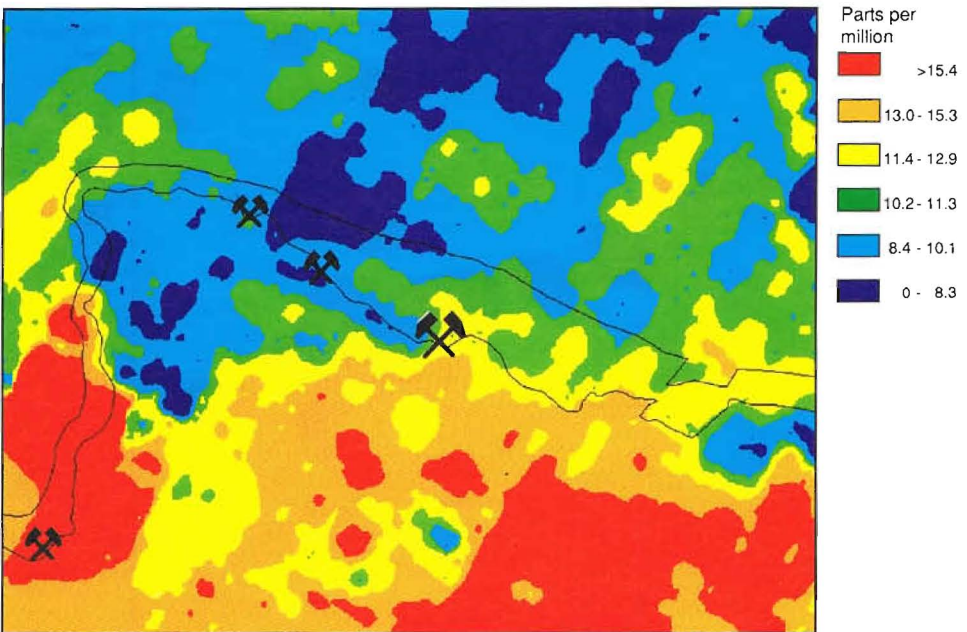


Plate 4a. Level sliced image of airborne radiometric eTh (ppm)

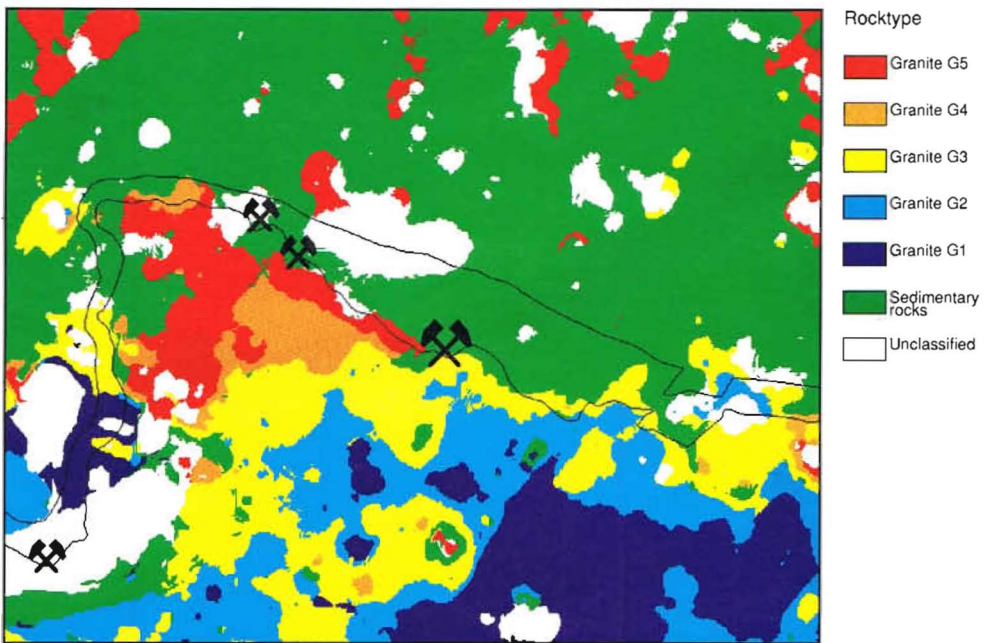


Plate 4b. Result of maximum likelihood classification of airborne radiometric datasets, (Th, U, K), using a Mahalanobis Distance of 100. G1 corresponds with the most granodioritic, G5 with the most monzogranitic rocks.



Plate 4c. Result of smoothing the classified image presented in Plate 4b, using a 127*127 median filter, in order to correct for misclassified areas.

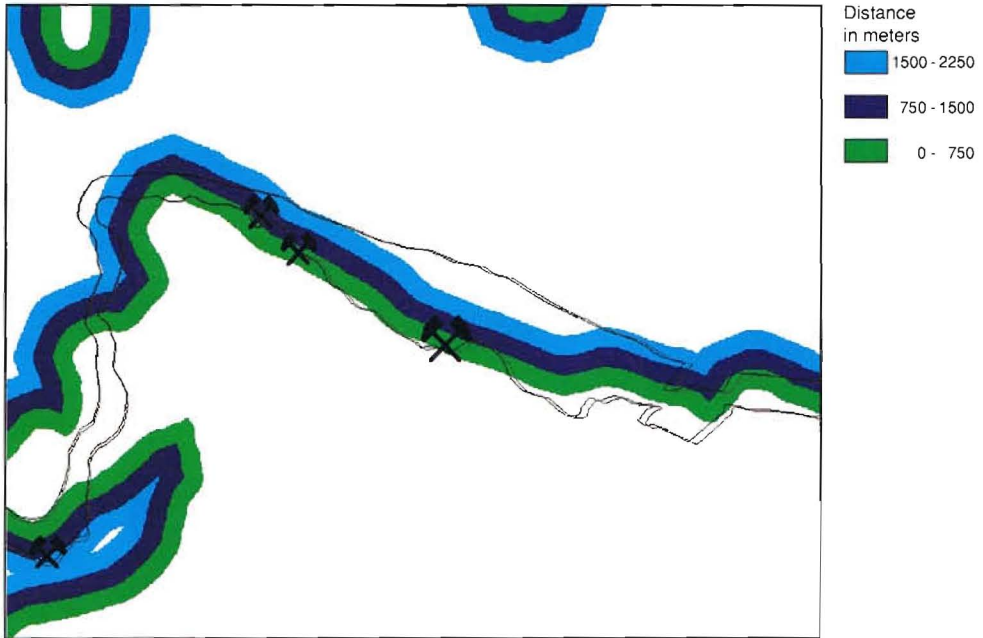


Plate 4d. Corridor of 2.25km around granite boundary, predicting the presence of contact metamorphic rocks. The granite boundary is calculated using the image presented in Plate 4c. The corridor is subdivided into three distance classes.

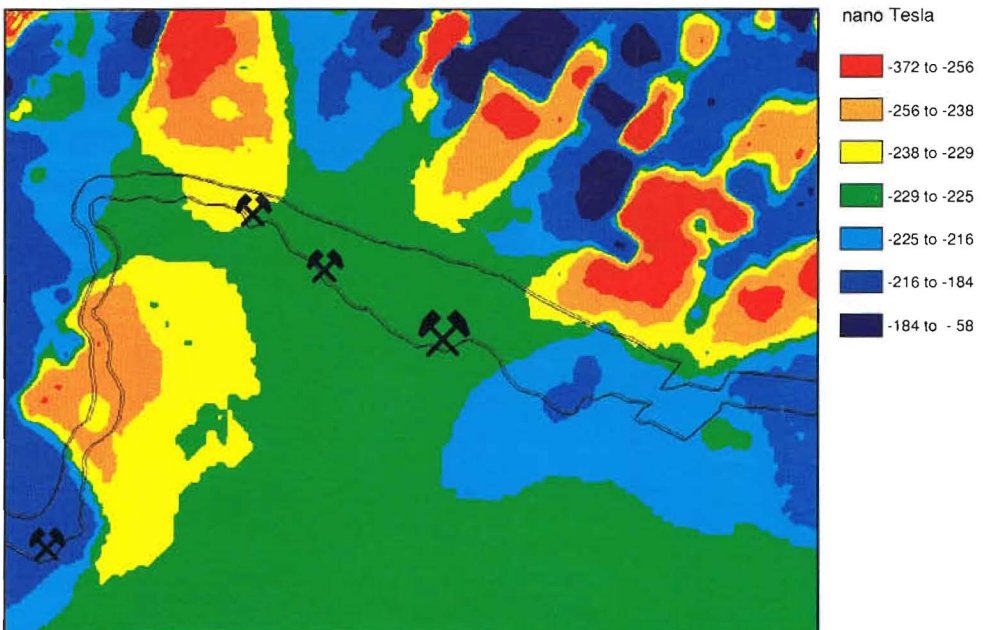


Plate 5a. Level sliced image of residual airborne magnetic field. NE-trending linear features are predominantly an effect of levelling errors.

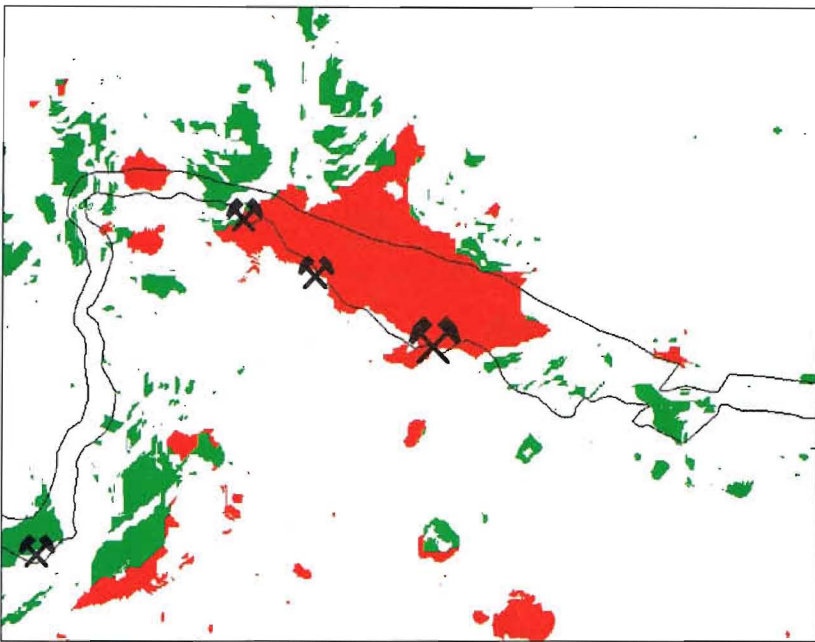


Plate 5b. Classified metasediments with magnetic properties similar to the granitic rocks, which therefore may be contact metamorphic. Green pixels represent sediments with a flat magnetic relief; Red areas additionally have the same residual magnetic value (-225 to -229nT) as the granites.

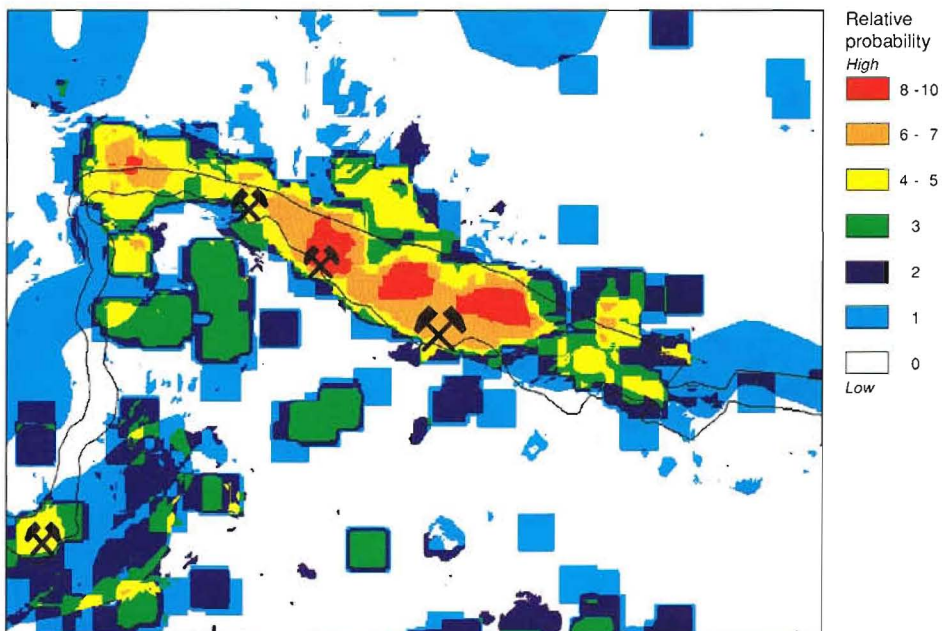


Plate 6a. Map that predicts the presence of contact metamorphic rocks. This map is the sum of the images presented in Plates 2,3,4d and 5b, using the weights given in Table 4 (Chapter 6), column a.

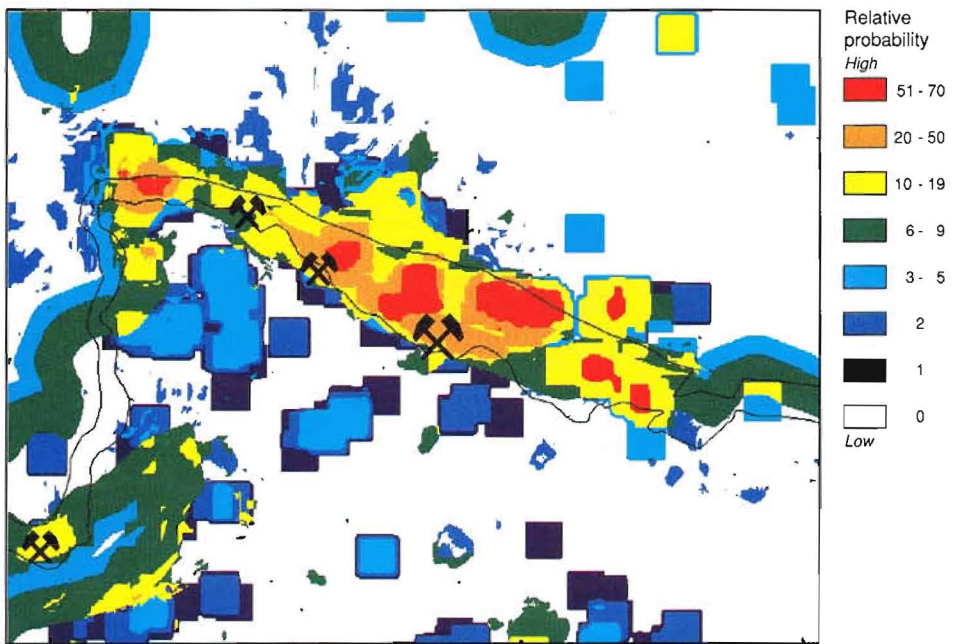


Plate 6b. Map that predicts the presence of contact metamorphic rocks, using the weights given in Table 4, column b.

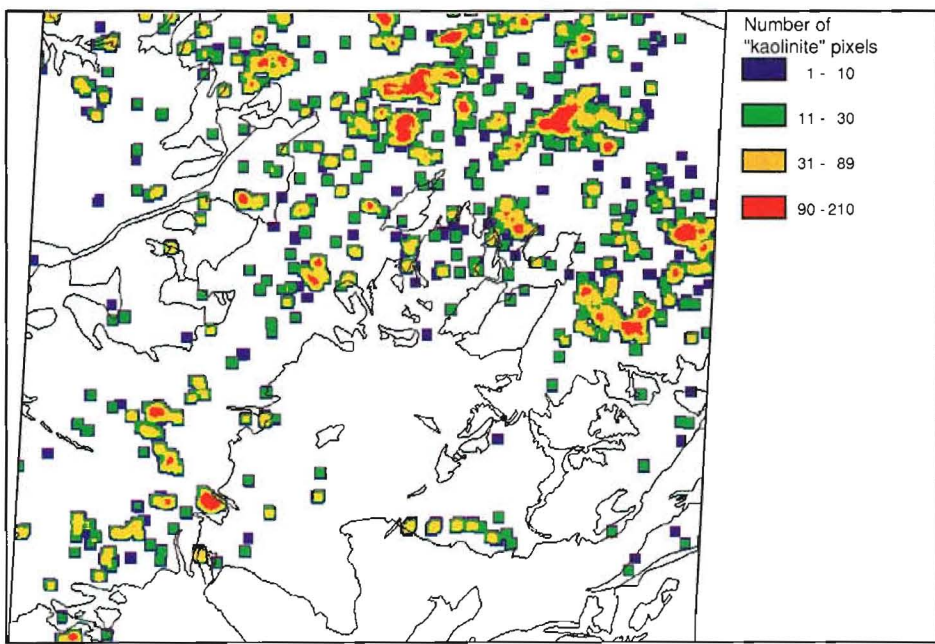


Plate 7a. Results of contouring the kaolinite map presented in Fig.6a (Chapter 7), using a 15*15 kernel. October scene.

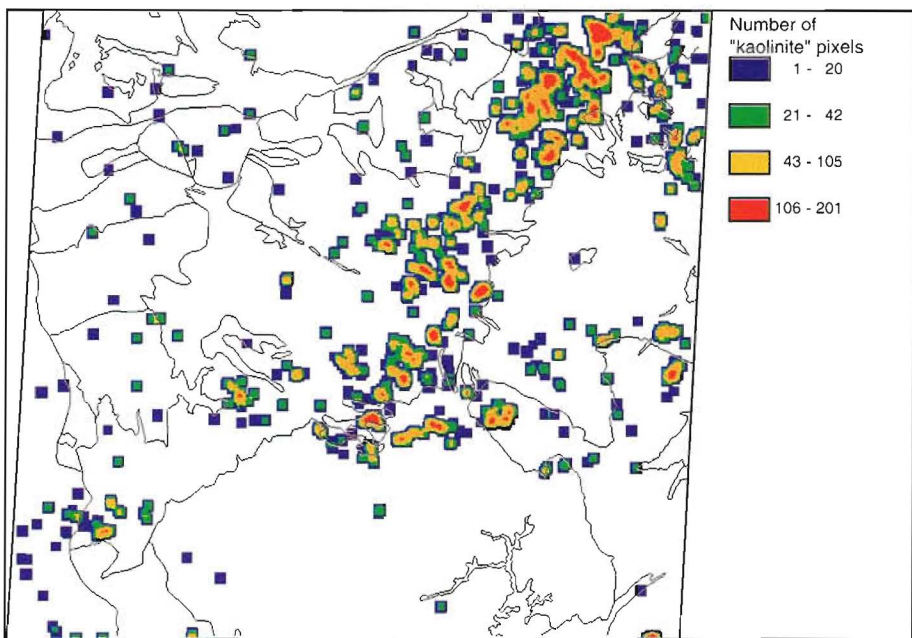


Plate 7b. Results of contouring the kaolinite map presented in Fig.6b (Chapter 7), using a 15*15 kernel. March scene.

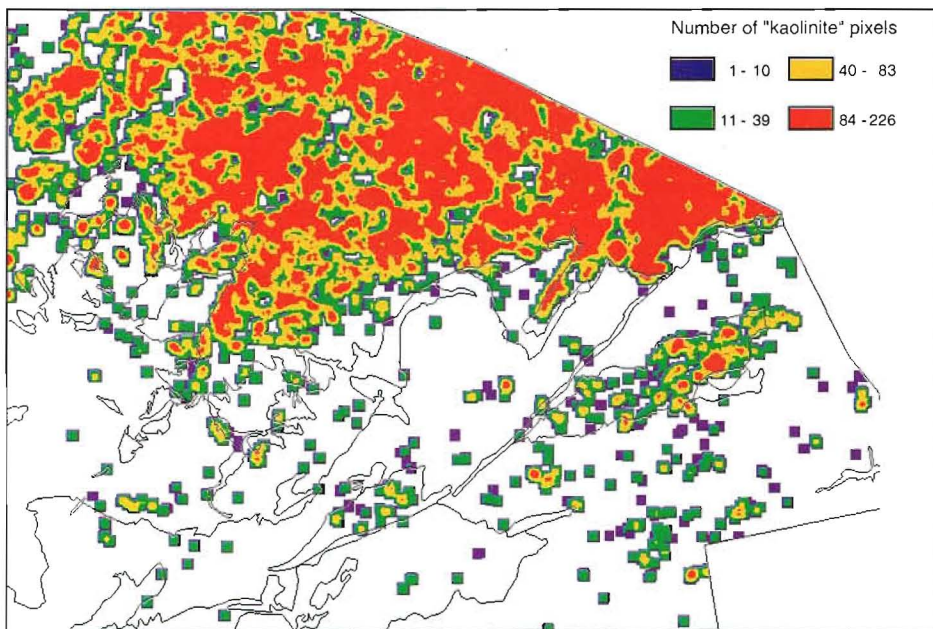


Plate 7c. Results of contouring the kaolinite map presented in Fig.6c (Chapter 7), using a 15*15 kernel. January scene.

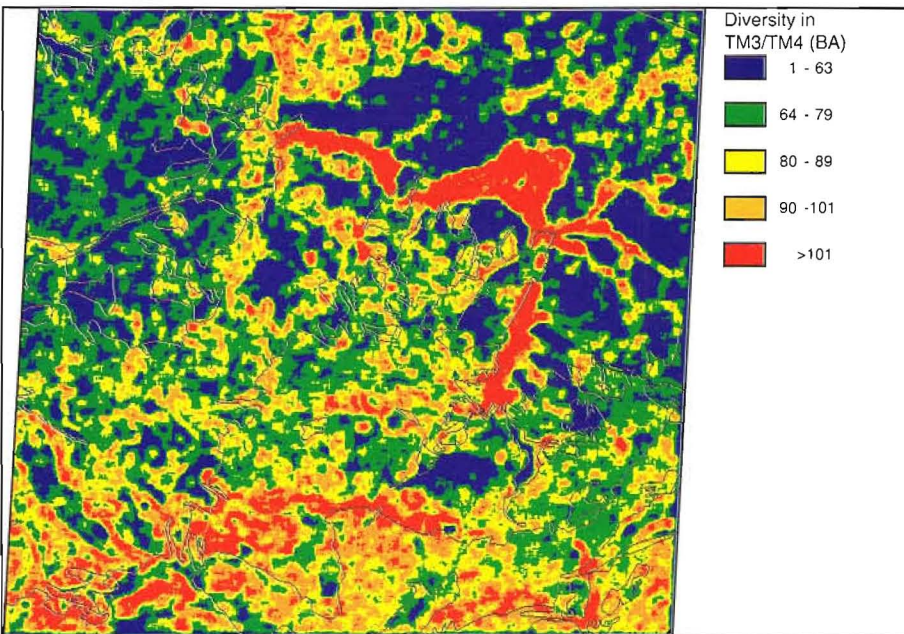


Plate 8a. Land use diversity map, resulting from diversity filtering of TM3/TM4 ratio image (October scene).

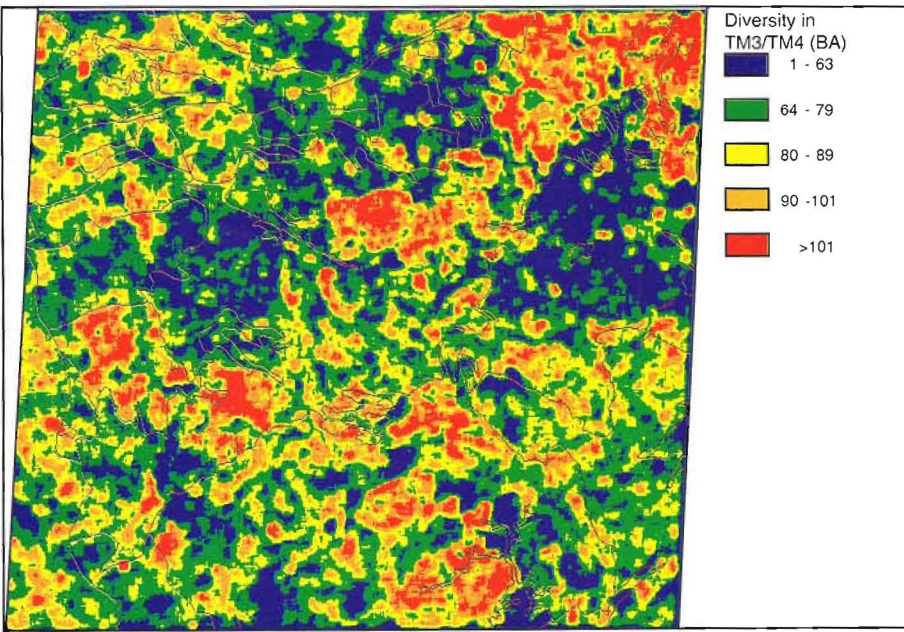


Plate 8b. Land use diversity map, resulting from diversity filtering of TM3/TM4 ratio image (March scene).

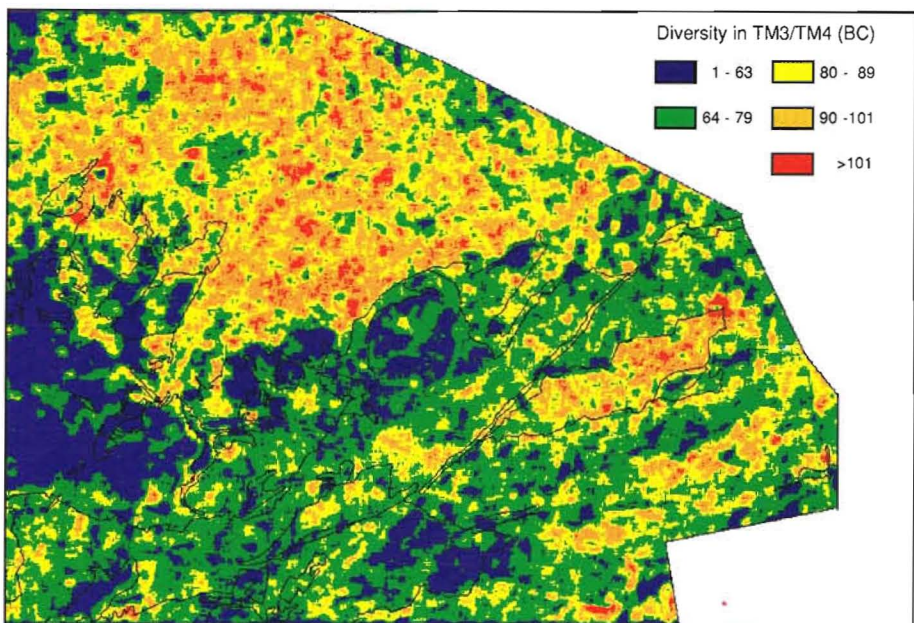


Plate 8c. Land use diversity map, resulting from diversity filtering of TM3/TM4 ratio image (January scene).

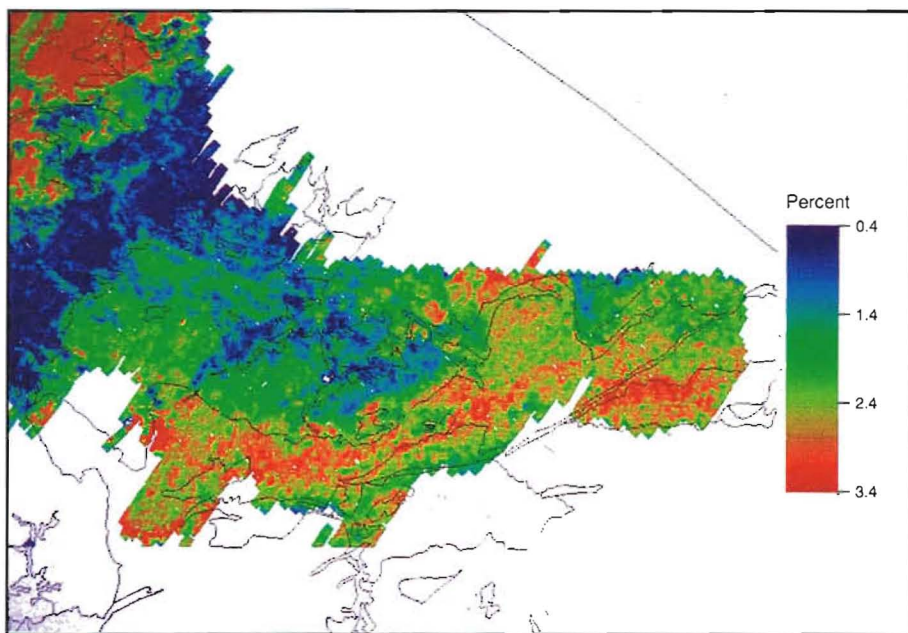


Plate 9. Airborne radiometric Potassium Image.

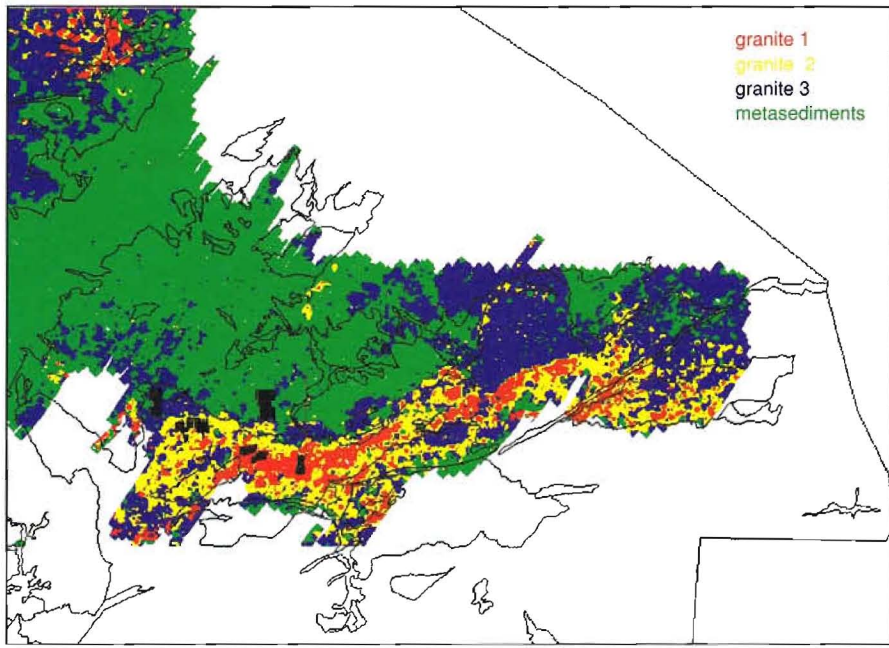


Plate 10. Results of supervised classification of airborne radiometric data (K_2O , Th, U and Total Count), distinguishing three granite classes and one metasediment class. Locations of training samples are indicated in black.

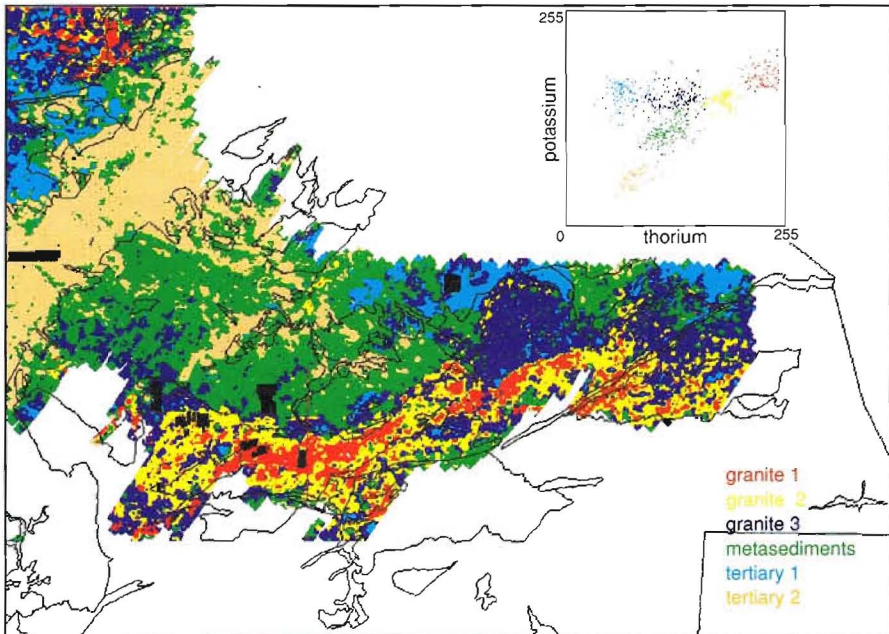


Plate 11a. Results of supervised classification of airborne radiometric data, distinguishing three granite classes, one metasediment class and two Tertiary cover classes. Locations of training samples are indicated in black. The diagram presents the variation in potassium and thorium for the six training classes.

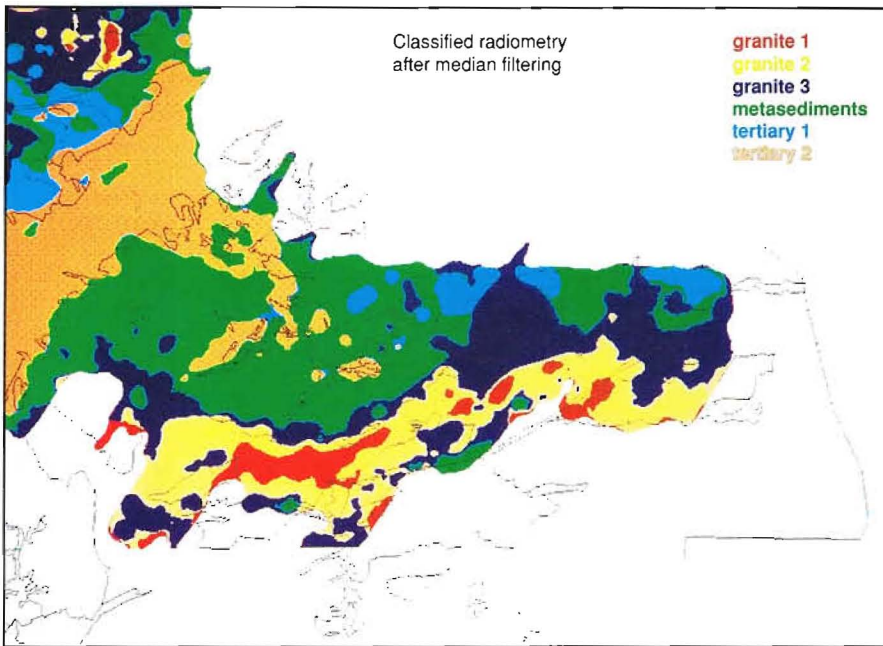


Plate 11b. Result of passing a 15*15 median filter over the classified image presented in Plate 11a. Classified areas with a surface smaller than 113 pixels are replaced by the value of the surrounding class.

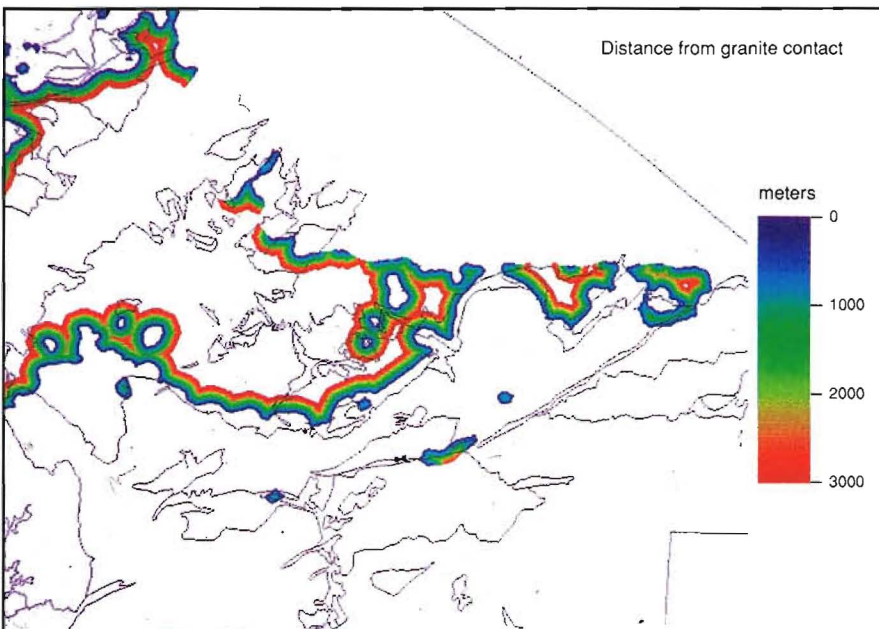


Plate 11c. Distance to the granite contact. The granite contact is constructed using the smoothed image presented in Plate 11b.

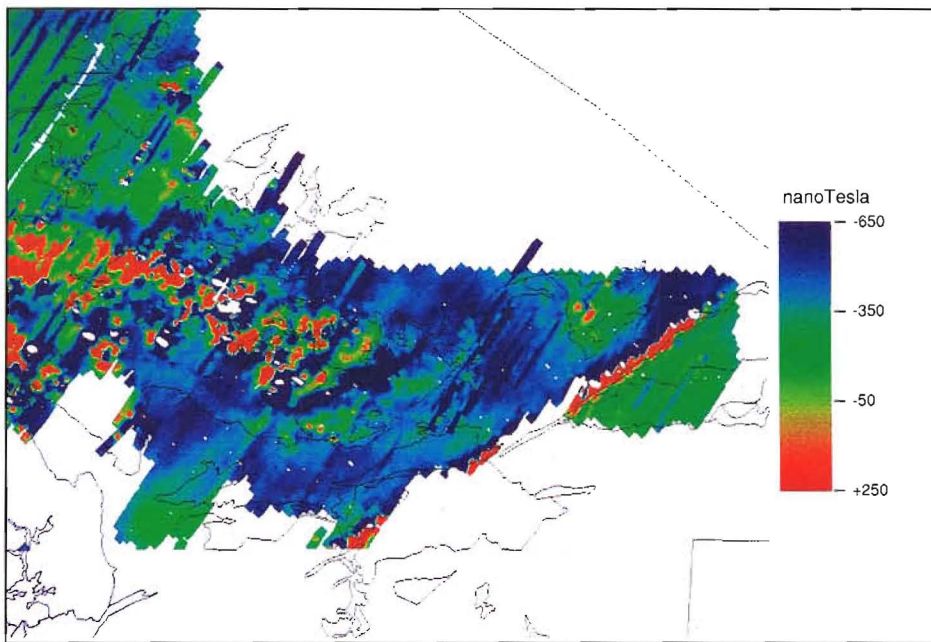


Plate 12a. Image of raw residual airborne magnetic data.

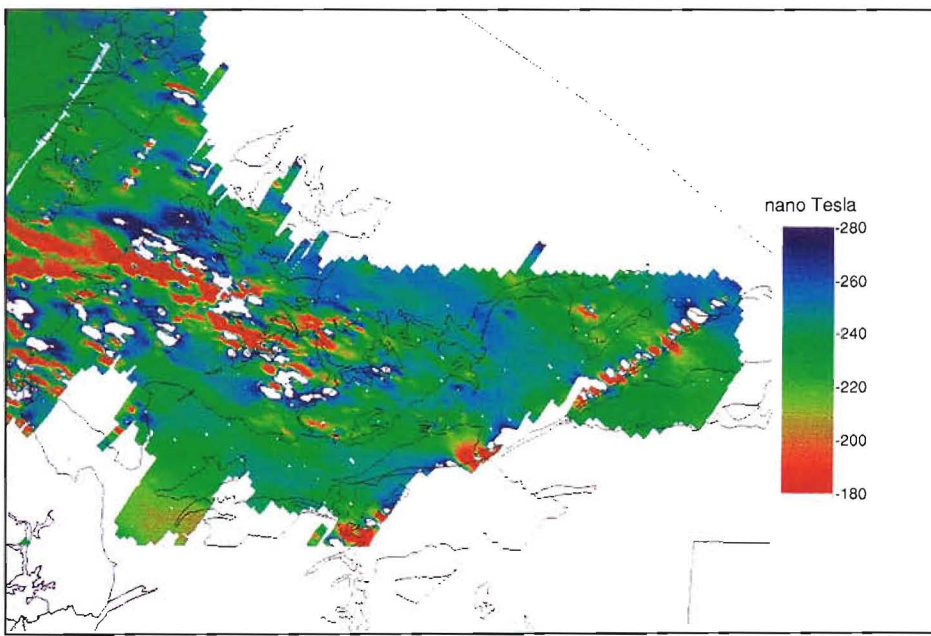


Plate 12b. Residual airborne magnetic data after cosine filtering of the original flight line data. This was done in order to remove the levelling errors.

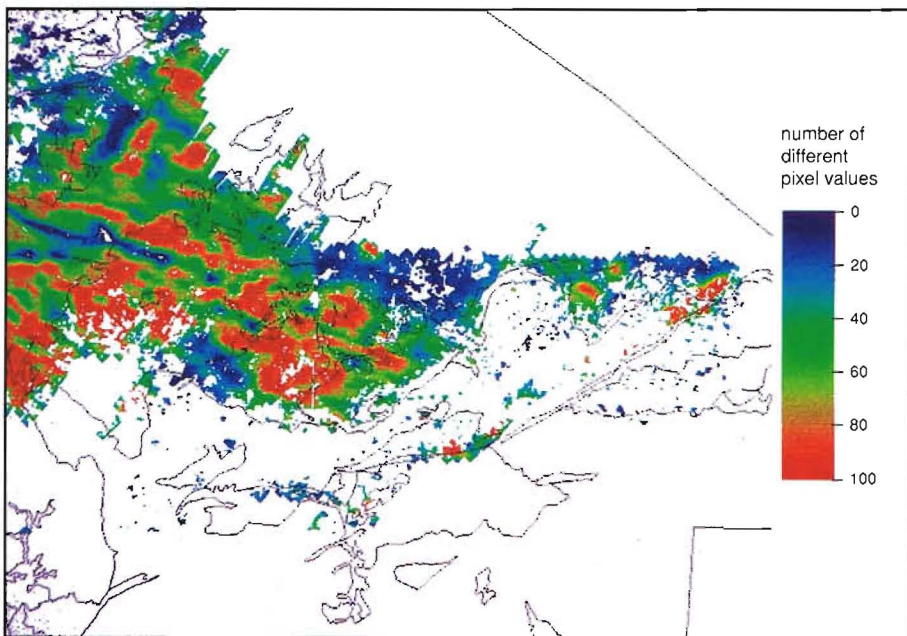


Plate 12c. Magnetic relief in areas classified, on the basis of the radiometric data, as metasedimentary rocks.

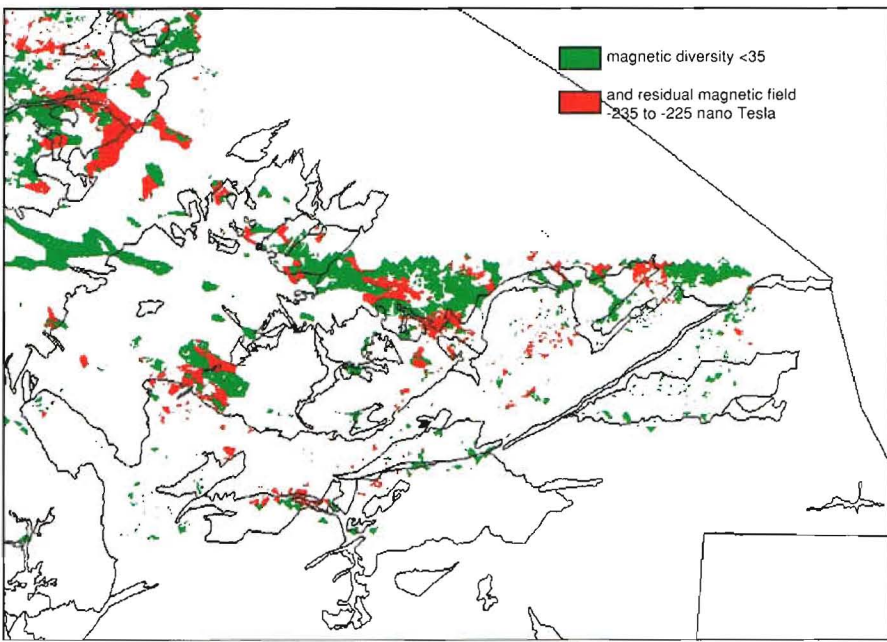


Plate 12d. Classified metasedimentary rocks, whose magnetic signature suggests contact metamorphism.

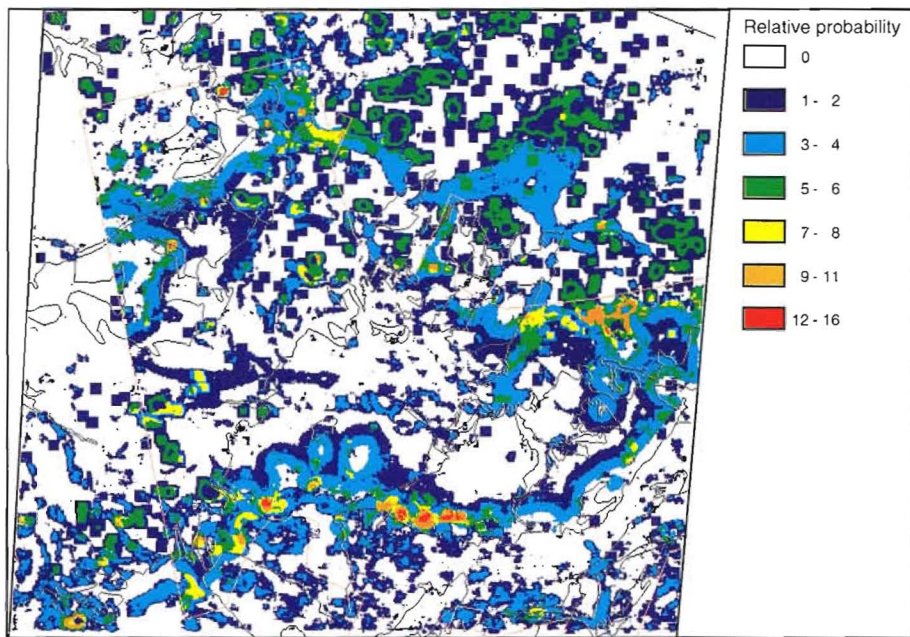


Plate 13a. Probability map for the area covered by the October scene; Orange coloured lines indicate the boundaries of the airborne geophysical data set.

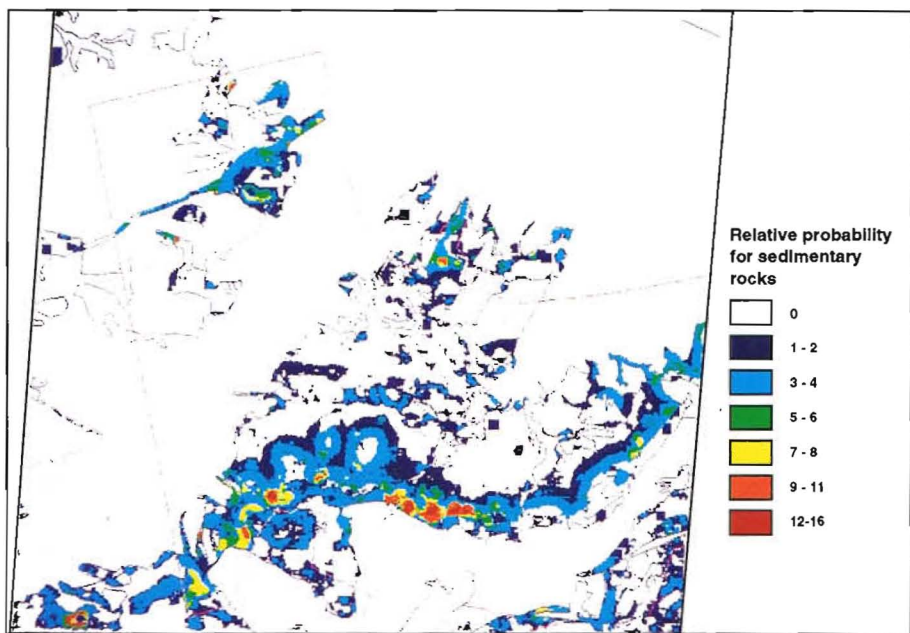


Plate 13b. Probability map for the area covered by the October scene, exclusively for metasedimentary rocks.

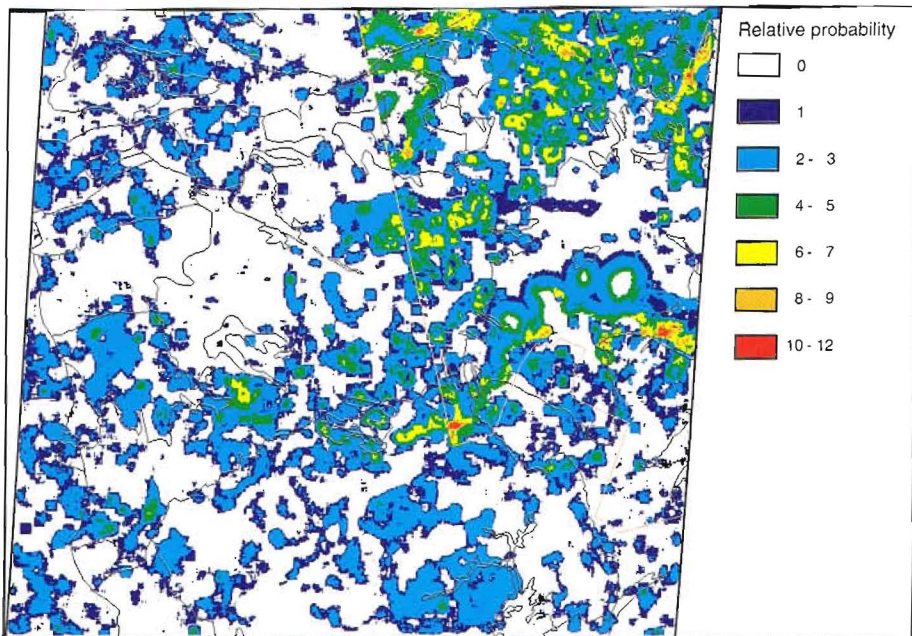


Plate 13c. Probability map for the area covered by the March scene.

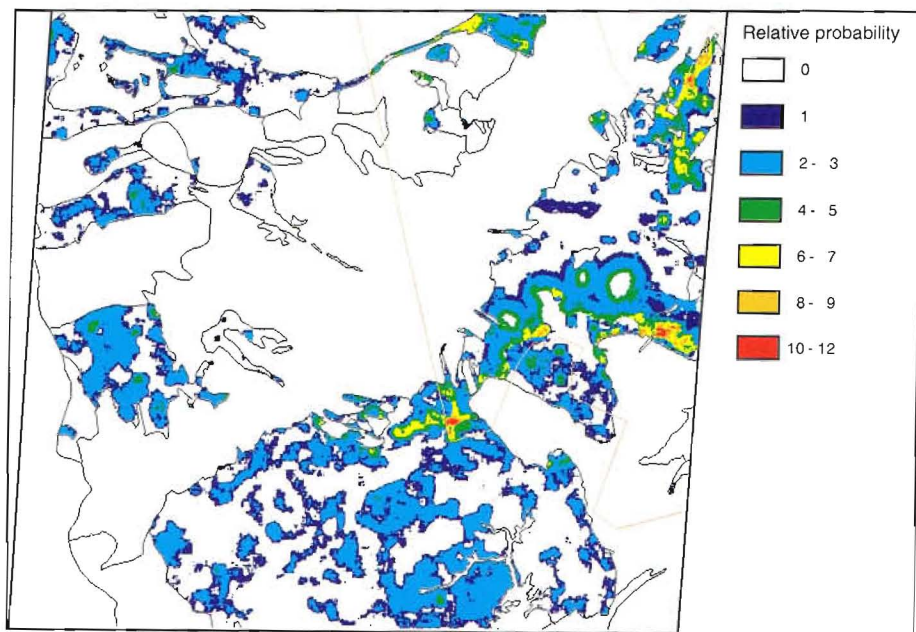


Plate 13d. Probability map for the area covered by the March scene, exclusively for metasedimentary rocks.

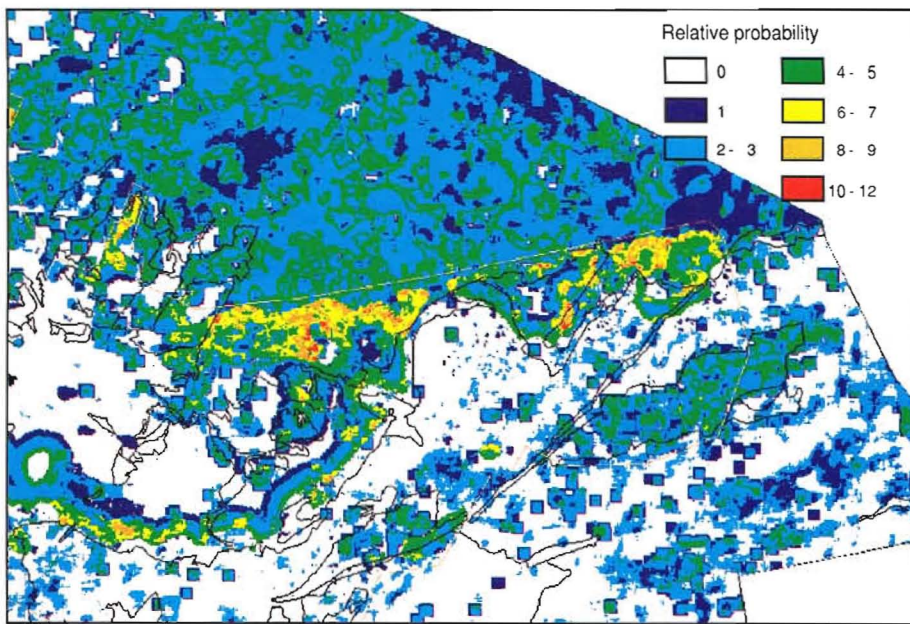


Plate 13e. Probability map for the area covered by the January scene.

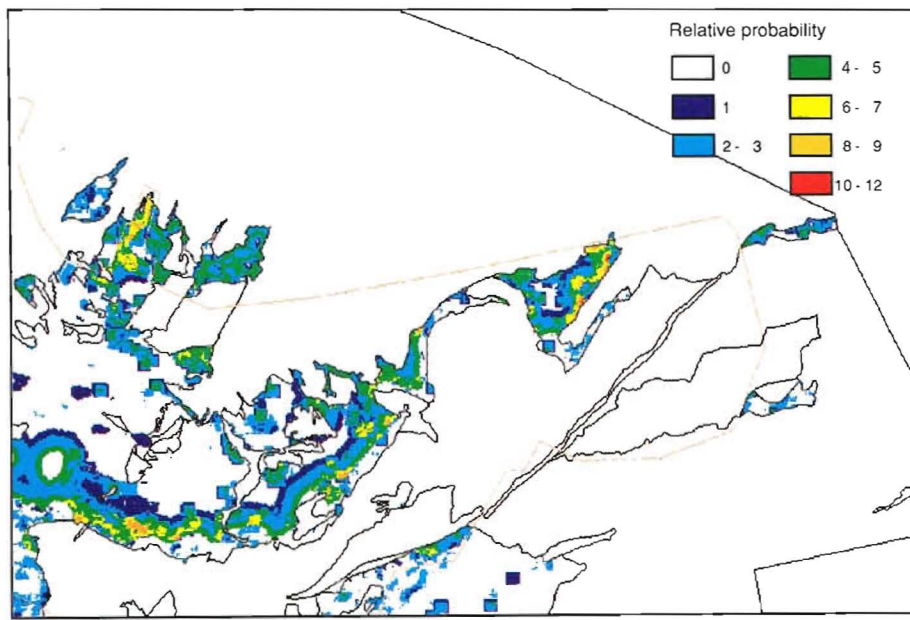


Plate 13f. Probability map for the area covered by the January scene, exclusively for metasedimentary rocks.